

NO-A187 248

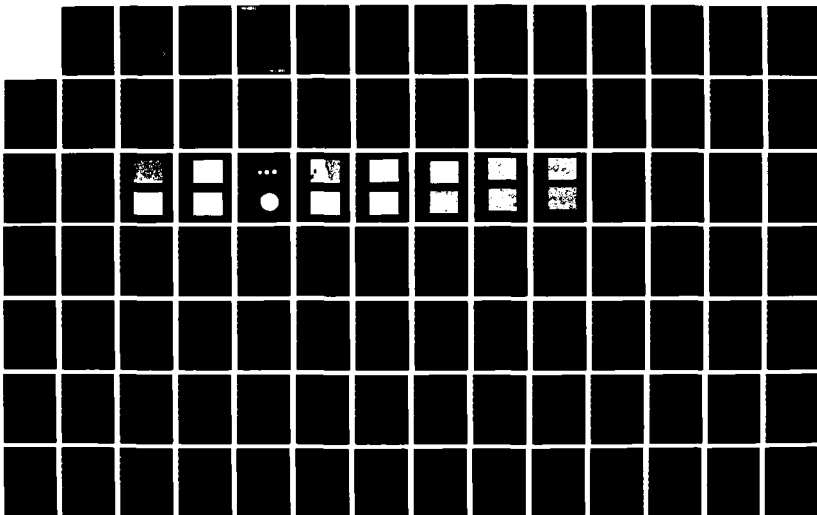
RESEARCH ON HIGH-SPECIFIC-HEAT DIELECTRICS(U)
CERAMPHYSICS INC WESTERVILLE OH W N LAWLESS ET AL.
11 MAY 87 AFOSR-TR-87-1452 F49620-86-C-0049

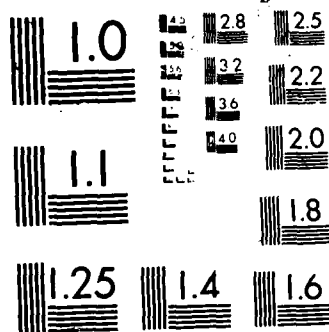
1/2

UNCLASSIFIED

F/G 11/2

ML





2

CeramPhysics, Inc.

921 Eastwind Drive, Suite 110

Westerville, Oh 43081

DTIC FILE COPY

AFOSR-TR. 87-1452

Final

~~ANNUAL~~ TECHNICAL REPORT

AFOSR Contract F49620-86-C-0049

Research on High-Specific-Heat Dielectrics

May 11, 1987

DTIC
ELECTE
OCT 29 1987
S R H D

87 10 14 322

AD-A187 248

I SUMMARY

A. Introduction

This Annual Report details a program of research on composite spinel ceramic materials with enormous specific heat maxima in the temperature range 5-20 K carried out by CeramPhysics, Inc., Ohio State University, Pennsylvania State University, and West Virginia University. In this section the main advances and accomplishments of the year are summarized and the organization of the rest of the report outlined.

We start with a brief review of the interpretation of these spinel materials developed in our previous research. The results obtained so far have suggested an attractive picture for the ordering phenomena in the B-site spinels, CdCr_2O_4 and ZnCr_2O_4 . The results have shown that at least two types of magnetic correlations are present, antiferromagnetic and paramagnetic, and that frustration and the presence of strong spin-lattice coupling play an important role in the anomalously large specific heats and thermal conductivities.

A basic examination⁶ of the structure of the spinel phases of CdCr_2O_4 and ZnCr_2O_4 revealed an interesting pattern among the B-site spinels, suggesting that additional systems of considerable interest might be made by filling in a table of materials constructed by replacing the A-site atom (Zn or Cd) by isoelectronic atoms or mixtures of atoms. In addition the transitions in these materials were seen to have a peculiar nature in which the spins order weakly in a lattice which has a high degree of frustration. This has great importance for our understanding of these systems, since it means that large numbers of spins can remain unordered below the transition, resulting in anomalously large specific heats, and furthermore, that distortions of the

SECURITY CLASSIFICATION OF THIS PAGE
UNCLASSIFIED

ADA187248 (C)

REPORT DOCUMENTATION PAGE

1a. REPORT SECURITY CLASSIFICATION Unclassified		1b. RESTRICTIVE MARKINGS None	
2a. SECURITY CLASSIFICATION AUTHORITY		3. DISTRIBUTION/AVAILABILITY OF REPORT Approved for public release, distribution unlimited	
2b. DECLASSIFICATION/DOWNGRADING SCHEDULE			
4. PERFORMING ORGANIZATION REPORT NUMBER(S)		5. MONITORING ORGANIZATION REPORT NUMBER(S) AFOSR-TR- 87 - 1452	
6a. NAME OF PERFORMING ORGANIZATION CeramPhysics, Inc.	6b. OFFICE SYMBOL (If applicable) LF	7a. NAME OF MONITORING ORGANIZATION Air Force Office of Scientific Research	
6c. ADDRESS (City, State, and ZIP Code) 921 Eastwind Drive, Suite 110 Westerville, Ohio 43081		7b. ADDRESS (City, State, and ZIP Code) Bldg. 410 Bolling AFB DC 20332-6448	
8a. NAME OF FUNDING/SPONSORING ORGANIZATION AFOSR	8b. OFFICE SYMBOL (If applicable) LF	9. PROCUREMENT INSTRUMENT IDENTIFICATION NUMBER F49620-86-C-0049	
8c. ADDRESS (City, State, and ZIP Code) Bldg. 410 Bolling AFB DC 20332-6448		10. SOURCE OF FUNDING NUMBERS PROGRAM ELEMENT NO. 1011007 PROJECT NO. 2301 TASK NO. H7 WORK UNIT ACCESSION NO.	
11. TITLE (Include Security Classification) Research on High Specific Heat Dielectrics			
12. PERSONAL AUTHOR(S) Lawless, W.N. and Clark, C.F., (CeramPhysics, Inc.); Patton, B.R., (Ohio State Univ.); Kahol, P.K. and Dalal, N.S., (W.Virginia Univ.); Snrout, T. (Pennsylvania State Univ.)			
13a. TYPE OF REPORT Annual FINAL	13b. TIME COVERED FROM 1986, Apr TO 1987, June	14. DATE OF REPORT (Year, Month, Day) 1987, May 10	15. PAGE COUNT 188
16. SUPPLEMENTARY NOTATION 01 30			
17. COSATI CODES FIELD GROUP SUB-GROUP		18. SUBJECT TERMS (Continue on reverse if necessary and identify by block number) SPINELS, ceramic, magnetocaloric spins	
19. ABSTRACT (Continue on reverse if necessary and identify by block number) This Annual Report details a program of research on composite spinel ceramic materials with enormous specific heat maxima in the temperature range 5-20 K. The results obtained so far have suggested an attractive picture for the ordering phenomena in the B-site spinels, CdCr_2O_4 and ZnCr_2O_4 . Significant progress in characterizing and controlling the fabrication of the spinel materials has been made. Pure powders, compacted disks, as well as the 9/1 columbite composite have been made and characterized. Magnetocaloric experiments reveal no trace of hysteresis, which means that the phenomena involved in the low temperature transitions in the Zn and Cd spinels must involve second order transitions. Adiabatic demagnetization cooling above T_j and also at low temperatures is indicative of paramagnetic spins, while a region of demagnetization heating just below T_j .			
20. DISTRIBUTION/AVAILABILITY OF ABSTRACT <input checked="" type="checkbox"/> UNCLASSIFIED/UNLIMITED <input checked="" type="checkbox"/> SAME AS RPT <input checked="" type="checkbox"/> DTIC USERS		21. ABSTRACT SECURITY CLASSIFICATION UNCLASSIFIED	
22a. NAME OF RESPONSIBLE INDIVIDUAL BALLS L SMITH		22b. TELEPHONE (Include Area Code) (202) 762-4902	22c. OFFICE SYMBOL LF

UNCLASSIFIED

19. ABSTRACT (continued)

seems to indicate antiferromagnetic ordering. Measurements have also discovered an amazing anomaly in the dielectric constant at the antiferromagnetic transition.

The susceptibility measurements on the pure spinel powder reveal no low temperature paramagnetic Curie tail, implying that all the spins are well ordered by $T \approx 0.2 T_N$. On the other hand the grains reacted with 10% columbite reveal a low temperature paramagnetic tail. Comparison of the measured susceptibility with a mean-field Currie-Weiss law above T_N , and a Curie law at low temperature seems to imply that, at low temperatures at least, the number of paramagnetic spins N_p is a small fraction of the anti-ferromagnetic spins N_{af} , of order 1% in the Cd spinel and 0.1% in the Zn spinel.

Theoretical Monte Carlo calculations have found that the spinel lattice with spins only at the B sites has a magnetic transition at a relatively low temperature. The magnetization is linear in field in good agreement with experiment. The calculated low field susceptibility shows a modest cusp at an ordering temperature $T_N \approx J$, where J is the nearest neighbor anti-ferromagnetic exchange interaction.

→ Key points

lattice, which remove the frustration, can couple strongly to the spins, thus leading to dielectric anomalies and large thermal conductivities due to spin energy being transported through the spin-phonon interaction.

B. Current Work

Recent and interesting new work has been done under this proposal on the properties of the B-site spinels, CdCo_2O_4 and ZnCo_2O_4 . In this summary, we focus on 1) recent advances in the fabrication and structural characterization of various ceramic phases of CdCo_2O_4 and ZnCo_2O_4 (section III), 2) experimental research on the magnetocaloric properties of the B-site spinels and the experimental discovery of a significant dielectric anomaly at T_N , which reveals a novel coupling of the spin and lattice (section IV), 3) experimental work on the magnetization and susceptibility which reveal an antiferromagnetic transition at $T_N \approx 8\text{-}11\text{K}$ (section V), 4) theoretical results for a) the properties of the ideal spinel lattice and b) the properties of the tetragonally distorted lattice obtained from Monte Carlo computer simulations on the frustrated spinel spin lattice (section VI), and 5) an overall picture for the phenomena occurring in these fascinating materials which integrates the numerous results listed above (section VII). We describe each of these accomplishments in more detail in the following:

1) Significant progress in characterizing and controlling the fabrication of the spinel materials CdCo_2O_4 and ZnCo_2O_4 has been made. Pure powders, compacted disks, as well as the 9/1 columbite composite have been made and characterized. The fabrication experiments in section III give clear evidence that the spinel powder of nominal grain size 10 microns reacts with the columbite component to produce paramagnetic spins at low temperatures. The same ceramic material can be made in several different ways, with about 10%

addition of the columbite phase. SEM evidence indicates that the spinel and columbite phases remain distinct, forming a composite of the two different substances, with grain sizes of order 10μ , consistent with earlier thermodynamic determinations at CeramPhysics.

2) The magnetocaloric experiments reported in section IV reveal no trace of hysteresis, which means that the phenomena involved in the low temperature transitions in the Zn and Cd spinels must involve second order transitions. Adiabatic demagnetization cooling above T_N and also at low temperatures is indicative of paramagnetic spins, while a region of demagnetization heating just below T_N seems to indicate antiferromagnetic ordering. These results are consistent with the thermodynamic relation which requires that the sign of the temperature change (heating or cooling) upon adiabatic demagnetization depends on the sign of the temperature derivative of the susceptibility. Measurements have also discovered an amazing anomaly in the dielectric constant at the anti-ferromagnetic transition. This data clearly shows that the ordering of the frustrated spin system has an enormous effect on the structure of the lattice. We recall that the pattern in the B-site spinel single crystals is toward a slight tetragonal distortion of the high temperature cubic phase below the magnetic transition.⁶ We know of no other case of such a strong coupling between the magnetic and the lattice degrees of freedom in any material. The present measurements are the first to find an anomaly at low temperatures. A theory was developed (section VI) which gives both a qualitative explanation as well as quantitative agreement with this anomaly.

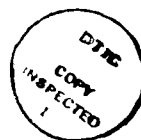
3) The susceptibility measurements described in section V on the pure spinel powder reveal no low temperature paramagnetic Curie tail, implying that all the spins are well ordered by $T \approx 0.2 T_N$. On the other hand the grains reacted with 10% columbite reveal a low temperature paramagnetic tail. Comparison of the measured susceptibility with a mean-field Curie-Weiss law above

T_N , and a Curie law at low temperature seems to imply that, at low temperatures at least, the number of paramagnetic spins N_p is a small fraction of the anti-ferromagnetic spins N_{af} , of order 1% in the Cd spinel and 0.1% in the Zn spinel.

4) Finally, the theoretical Monte Carlo calculations reported in section VI have found that the spinel lattice with spins only at the B sites has a magnetic transition at a relatively low temperature. The magnetization is linear in field in good agreement with experiment. The calculated low field susceptibility shows a modest cusp at an ordering temperature $T_N \approx J$, where J is the nearest neighbor anti-ferromagnetic exchange interaction.

In conclusion, it is clear that a wide variety of experimental and theoretical work on the frustrated B-site spinels, CdCr_2O_4 and ZnCr_2O_4 has begun to produce a coherent picture for the very interesting behavior of these systems. A magnetic transition of anti-ferromagnetic character, incomplete ordering of the spins, and strong coupling to the lattice degrees of freedom are all well established. Further work is required to pin down the origins and parameters

of these novel phenomena.



Accession For	
NTIS GRA&I	<input checked="" type="checkbox"/>
DTIC TAB	<input type="checkbox"/>
Unannounced	<input type="checkbox"/>
Justification	
By	
Distribution/	
Availability Codes	
Dist	Avail and/or Special
A-1	

II. INTRODUCTION AND BACKGROUND

In the late 70's, Wright Patterson AFB began funding a series of applied programs aimed at developing dielectric insulation systems incorporating enthalpy stabilization for the superconductors NbTi and Nb₃Sn (WPAFB Contracts #F33615-80-C-2202, -82-C-2227, -82-C-2229, and -84-C-2418). These programs were based on new materials which are two-phase, spinel + columbite ceramics and which sinter at ~ 1300°C. The columbite phase, although minor, must be present for the spinel phase to densify, and these ceramics have huge specific heats at low temperatures.

In the Summer of '83, research on the physics of these new materials was begun by CeramPhysics, Inc. and the Physics Dept. at the Ohio State Univ. under a subcontract to AFOSR Contract #F49620-82-C-0129. This research is summarized in Eckels et al. (1985), and this Annual Report documents the continuation of this research by CeramPhysics, Inc., Ohio State Univ., Pennsylvania State Univ., and W. Virginia Univ.

The columbite mineralizers CdNb₂O₆ and ZnNb₂O₆ must be present for the spinels CdCr₂O₄ and ZnCr₂O₄ to densify in the ceramic, and the optimum spinel:columbite molar ratio is 9:1. The thrust of the previous research has been to understand the enormous specific heat maxima in these spinels at low temperatures rather than the ceramic-formation phenomena.

Specific heat data, 1.5-40 K, were measured on these 9:1 ceramics and on ceramic samples of the CdNb₂O₆ and ZnNb₂O₆ mineralizers over broad temperature ranges. Next, the specific heats of the columbites were fitted to Schottky and Einstein functionals, and these fitted data were then used to correct the 9:1 ceramics specific heat data to determine the specific heats of the spinel phases.

The separated specific heat data for the CdCr₂O₄ and ZnCr₂O₄ spinels are shown in Fig. 2-1(a) where the data are plotted as C/T^3 to illustrate the non-Debye contributions at the lowest temperatures. We point out that these specific heat maxima are

equivalent to the specific heat of water at room temperature; hence, the applied interest in enthalpy stabilization.

These specific heat data were decomposed into Debye, Schottky, and magnetic contributions, and the entropies of these contributions in CdCr_2O_4 are shown in Fig. 2-1(b). These contri-

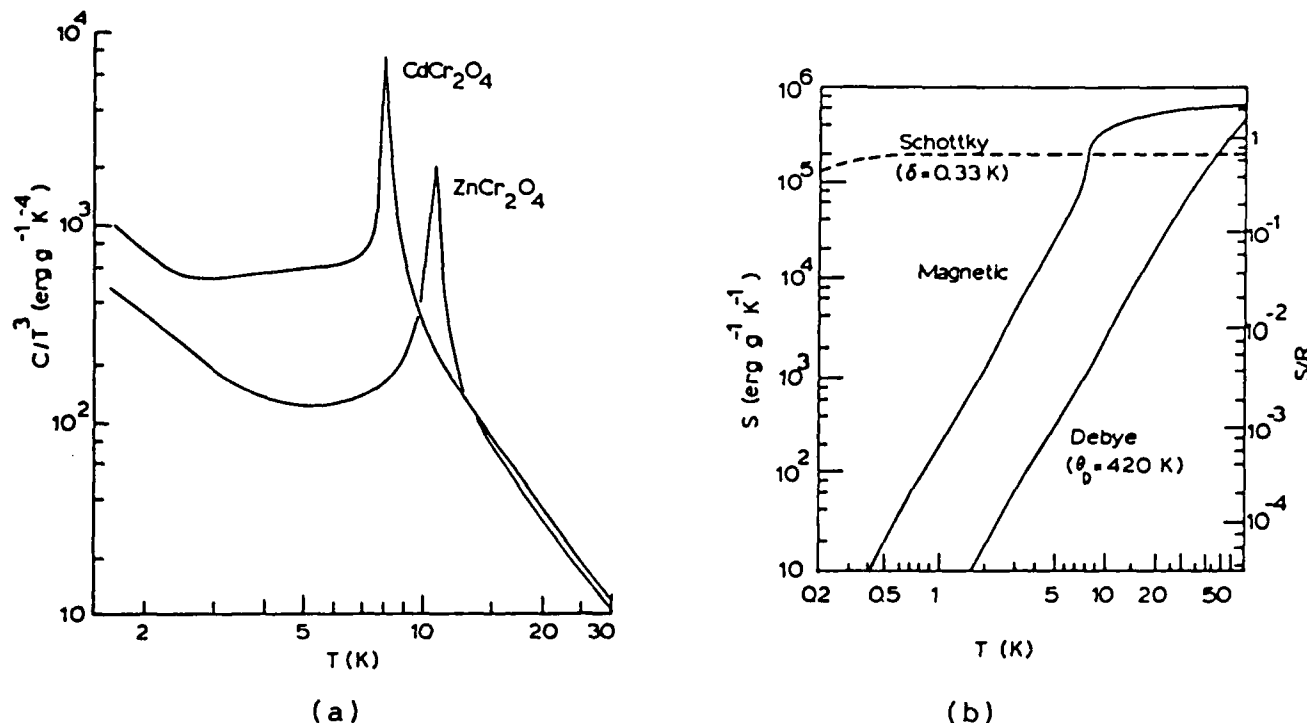


Figure 2-1. (a) Specific heats of the new spinels; (b) Contributions to the specific heat of CdCr_2O_4 .

butions were determined by the following procedure based on the data in Fig. 2-1(a):

1. The high-temperature data [i.e., $T > 2T_N$, where T_N is the peak temperature in Fig. 2-1(a)] were fitted to the general Schottky term, and these fittings yielded the Debye temperatures, $\theta_D = 420$ and 463 K for the cadmium and zinc spinels, respectively. These θ_D - values are in excellent agreement with predictions of the Lindemann relation.
2. The low-temperature data (i.e., $T < T_N/2$) follow a Schottky term very well with two-level splittings of 0.33 and 0.37 K for the cadmium and zinc spinels. However, these fits

yielded unrealistically small θ_D 's (e.g., ~ 100 K), and it was concluded that antiferromagnetic spin waves are contributing a T^3 term which is indistinguishable from the T^3 Debye acoustic background.

3. Adopting the more realistic Debye temperatures allows a determination of the spin-wave parameters,

$$\begin{aligned} J's/c_a^{1/3} &= 5.94 \times 10^{-16} \text{ erg (CdCr}_2\text{O}_4) \\ &= 9.65 \times 10^{-16} \text{ erg (ZnCr}_2\text{O}_4) \end{aligned}$$

4. Finally, the determination of the parametric data above allows the separation of the specific heat contributions and, by integration, the entropy of these contributions, as illustrated in Fig. 2-1(b). The magnetic entropies of the two spinels determined from these analyses are

$$\begin{aligned} S_M/R &= 2.340 \text{ (CdCr}_2\text{O}_4) \\ &= 1.434 \text{ (ZnCr}_2\text{O}_4) \end{aligned}$$

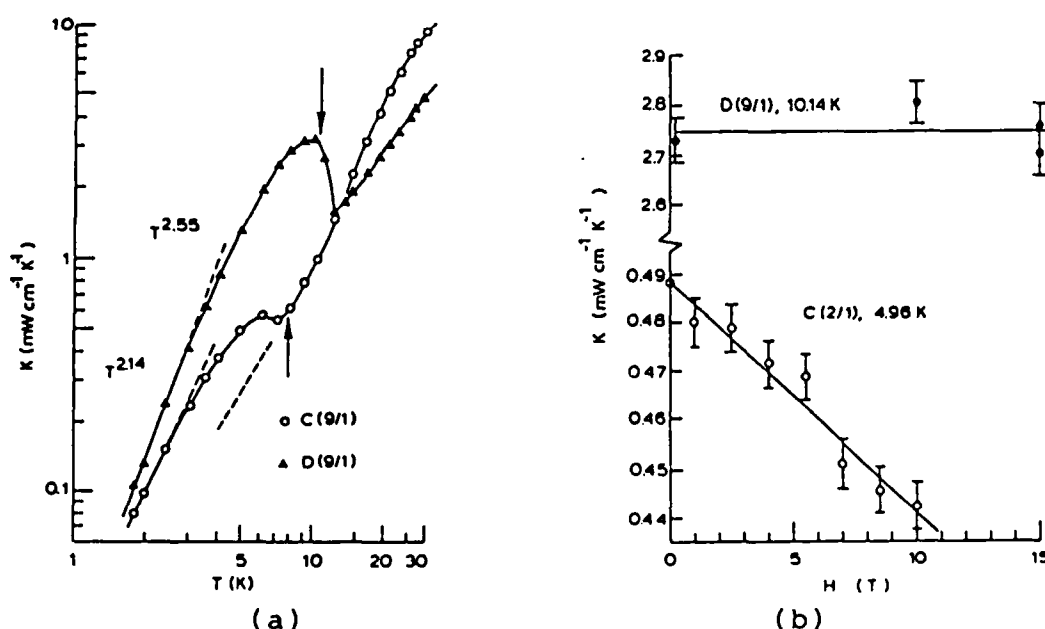


Figure 2-2. Thermal Conductivity data on the spinels, (a) As a function of temperature; (b) In magnetic fields. Here C(9/1) and D(9/1) refer to the Cd- and Zn-spinels, respectively.

The thermal conductivities of the spinels display "jumps" associated with the (antiferromagnetic) transitions as shown in Fig. 2-2(a). The magnetic-field dependence of these anomalies was measured just below T_N , and these data are shown in Fig. 2-2(b). Surprisingly, the anomaly in ZnCr_2O_4 is unaffected, but in CdCr_2O_4 a magnetic field "quenches" the anomaly as shown schematically by the dashed curve in Fig. 2-2(a). This excess thermal conductivity in CdCr_2O_4 is $\approx 0.23 \text{ mW cm}^{-1} \text{ K}^{-1}$, or roughly half the zero-field thermal conductivity at 5 K.

By far the most intriguing measurements previously made on the spinels have been the magnetocaloric measurements at $T < T_N/2$. Both spinels display adiabatic-demagnetization cooling and adiabatic-magnetization heating, and these caloric effects are perfectly reversible. The measured ΔT data up to 10 T are shown in Fig. 2-3, and we point out that these are very large effects because the specific heats of these spinels are large at 3-5 K.

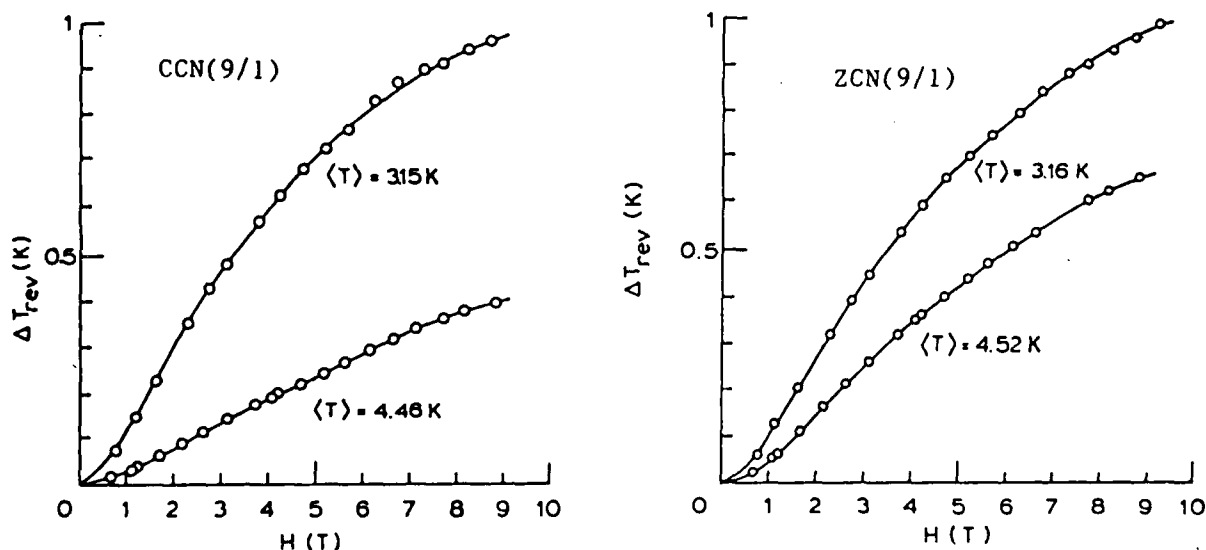


Figure 2-3. Reversible magnetocaloric effects in the new spinels at $T < T_N/2$. Here CCN(9/1) and ZCN(9/1) refer to the 9:1 spinel + columbite ceramics.

The measurements in Fig. 2-3 led naturally to measurements of the magnetization of the spinels at 4.2 K, and these data are shown in Fig. 2-4. Here it was found that both spinels act as

perfect paramagnets and display no hysteretic effects.

A self-consistent picture began to emerge from these measurements: Namely, the specific heat peaks in Fig. 2-1(a) appear due to an antiferromagnetic spin ordering as evidenced by the T^3 antiferromagnetic spin-wave contribution below about 3 K. These ordered spins do not affect the magnetization, Fig. 2-4. However, several degrees of freedom remain below T_N , and these paramagnetic spins cause the reversible magnetocaloric effects.

Actually, there is competition between the ordered spins and the disordered spins in the magnetocaloric effects because the former spin system would show demagnetization heating, the latter system, demagnetization cooling. There may be different spin-phonon relaxation rates involved which cause the dominance of the latter effects associated with the paramagnetic spin system.

It is puzzling that both the specific heat maxima at T_N and the magnetocaloric effects below T_N are so large (i.e., the energetics associated with these phenomena are very large, ~ 0.1 - 1 J/g).

A very simple approach was tried theoretically here; namely, a two-spin model where some fraction of the Cr^{3+} spins partake in the antiferromagnetic ordering at T_N , the balance of the spins remain unordered, and coupling between the spin systems is ignored. Using $s = 3/2$, it was found from the magnetic entropy S_M above that 84 and 52% of the spins order at T_N in CdCr_2O_4 and ZnCr_2O_4 , respectively. From the spin-wave specific heat contributions above, we have for the exchange constants,

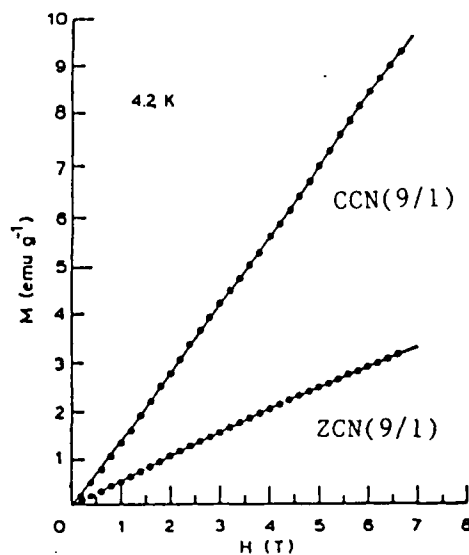


Figure 2-4. Magnetization data at 4.2 K on the new spinels.

$$\begin{aligned} J/k &= 3.42, \text{ CdCr}_2\text{O}_4, \\ &= 4.72, \text{ ZnCr}_2\text{O}_4. \end{aligned}$$

From the Schottky specific heat terms well below T_N , we find for the two-level splitting,

$$\begin{aligned} \delta &= 0.59 \text{ K}, \text{ CdCr}_2\text{O}_4, \\ &= 0.37 \text{ K}, \text{ ZnCr}_2\text{O}_4, \end{aligned}$$

where these terms are ascribed to the unordered spins.

This simple model yields reasonable parameter values from the specific heat data, but the model cannot explain the magnetic properties. From the magnetization data, Fig. 2-4, the model indicates that the spin densities in CdCr_2O_4 are three times larger than in ZnCr_2O_4 , but the magnetocaloric data indicate just the opposite from this simple model.

The more basic theoretical approach started with a basic examination of the structure of the spinel phases of CdCr_2O_4 . This study revealed an interesting pattern among the B-site spinels, which suggests that additional systems of considerable interest might be made by filling in a table of materials constructed by replacing the A-site atom (Zn or Cd) by isoelectronic mixtures of Cu and In, or Ag and In. In addition, the transitions in these materials were seen to have a peculiar nature in which the spins order weakly in a lattice which has a high degree of frustration. This has great importance for our understanding of these systems, since it means that large numbers of spins can remain unordered below the transition, resulting in anomalously large specific heats and magnetocaloric effects. Furthermore, distortions of the lattice, which remove the frustration, can couple strongly to the spins, thus leading to large thermal conductivities due to spin energy being transported through the spin-phonon interaction.

The first attempt to understand the theoretical properties of these systems was to derive the Hamiltonian describing the interaction of the spins on the spinel lattice sites. From this

we extracted a simple model in which we kept only two possible sublattice magnetizations, an antiferromagnetic one which orders at the transition, and a ferromagnetic one coupled to it, which is polarized in a magnetic field, giving rise to spin-flop like effects. In the mean-field approximation, this model already gives interesting effects, including a temperature dependent magnetization linear in field and a magnetic field dependent specific heat which increases with field. These results are in good qualitative agreement with the experimental data and confirm the basic correctness of our approach. The next step was to examine the renormalization effects due to fluctuations, which led to the novel feature that the non-ordering spins give rise to a large contribution to the specific heat even well below the ordering temperature of the antiferromagnetic spins. This is not possible in a simpler system with only one order parameter, again

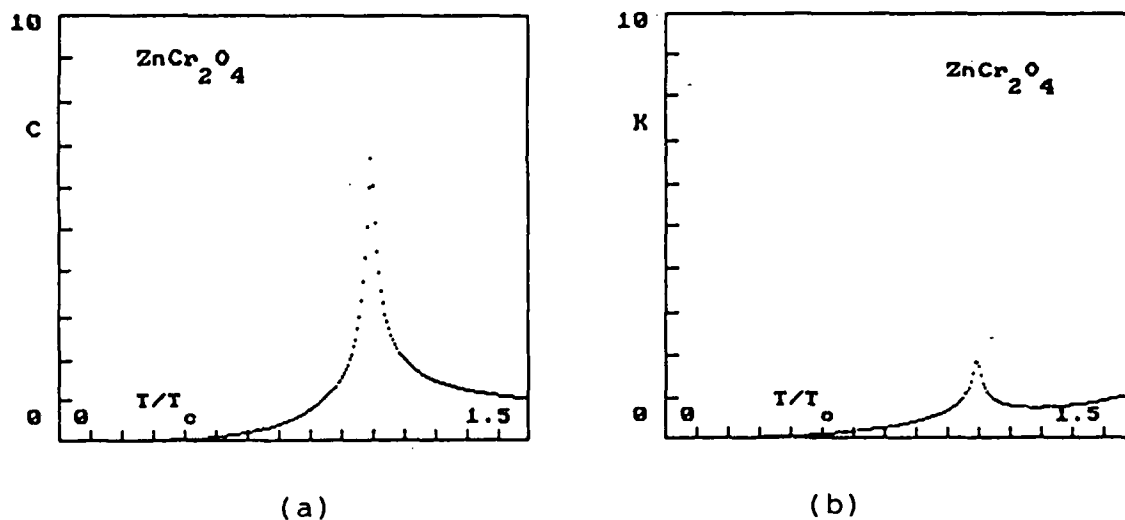


Figure 2-5. Example of theoretical fits to specific heat (a) and thermal conductivity (b) data for ZnCr_2O_4 .

suggesting our model has correct general properties. Detailed results were obtained in the gaussian fluctuation approximation for the specific heat as a function of temperature and magnetic field both above and below the transition. Finally, a theory for the thermal conductivity in this class of materials was developed. The thermal conductivity depends on both the specific

heat and the scattering rate, which we showed involved, in addition to the usual phonon and antiferromagnetic spin wave contributions, a spin fluctuation term which limits the thermal conductivity in the vicinity of the transition. Fits were made to the specific heat and thermal conductivity data using the same set of fitting parameters, which revealed that the peak in the thermal conductivity at the transition arises from the peak in the specific heat, but that it is typically a factor of about three smaller due to the spin scattering at the transition. An example of the theoretical fits for the ZnCr_2O_4 spinel are shown in Fig. 2-5.

The research reported in this Annual Report was based on the above experimental and theoretical findings and represents a continuation of this previous research.

Our broad goals in the present research are as follows:

1. To investigate the ceramic formation of these new spinel + columbite materials (i.e., Why must the columbite phase be present for densification?) and to explore ceramic fabrication of the pure spinels (Pennsylvania State Univ.).
2. To extend the magnetocaloric measurements of Fig. 2-3 over broad temperature ranges for both the spinel + columbite ceramics and for the pure spinel ceramics (CeramPhysics).
3. To extend the specific heat measurements of Fig. 2-1 to the pure spinel ceramics (CeramPhysics).
4. To measure magnetic susceptibility data on these materials over broad temperature ranges and in magnetic fields (W. Va. Univ.).
5. To pursue EPR measurements, including electron nuclear triple resonance measurements, on these spinel systems (W. Va. Univ.).
6. To pursue Monte Carlo simulations of the spinel lattice, including frustratin and variable boundary conditions, and to couple these calculations to Ginzberg-Landau theory. Renormalization group theory will be employed

near the phase transition.

III. CERAMIC PREPARATION STUDIES

3.A Introduction

A key to the understanding of the thermal, dielectric, magnetocaloric, and magnetic susceptibility measurements performed in this program is the crystal chemistry and ceramic fabrication of the CdCr_2O_4 and ZnCr_2O_4 spinel materials. A portion of this program was devoted to this topic. In earlier CeramPhysics studies, it was found that dense ceramics of the CdCr_2O_4 or ZnCr_2O_4 spinels could only be fabricated by the addition of at least 10 mole percent of the respective (CdNb_2O_6 or ZnNb_2O_6) columbites. Ceramic compositions with various spinel/columbite ratios were the basis of earlier studies. Several of these existing ceramic samples were thoroughly characterized by x-ray diffraction and scanning electron microscopy, in order to better understand the crystal chemistry of these materials. It was hoped that if an understanding of the crystal chemistry and densification mechanisms of the spinel-columbite ceramics could be obtained, fabrication methods could be established to allow for the preparation of more phase-pure spinel ceramics, with improved thermal properties. Ceramic preparation studies were also performed in order to prepare dense samples of the pure spinel ceramics. These efforts were aimed at supplying improved ceramic samples for thermal and magnetic measurements.

3.B Spinel-Columbite Ceramics (CeramPhysics Samples)

3.B.1 X-Ray Diffraction Studies

X-ray diffraction and SEM studies were performed on previously synthesized spinel-columbite ceramics (both calcined powders and sintered disks) with spinel/columbite ratios varying from 1/1 to 11/1. X-ray diffraction results are presented in Table 3.1; the phases found for each of the samples are listed in order of decreasing relative amount. The results for the $\text{CdCr}_2\text{O}_4/\text{CdNb}_2\text{O}_6$ samples (Table 3.1a) confirmed the multi-phase nature of these ceramics. With low ratios ($<5/1$) of spinel to columbite, the major phase in the ceramic was pyrochlore $\text{Cd}_2\text{Nb}_2\text{O}_7$, with lesser amounts of spinel CdCr_2O_4 , columbite CdNb_2O_6 , and Nb_2O_5 . As the spinel/columbite ratio increased, the amount of pyrochlore decreased, and the amounts of spinel and columbite

increased. Spinel CdCr_2O_4 was the dominant phase with spinel/columbite ratios of 5/1 and greater. With high spinel/columbite ratios (9/1), the pyrochlore phase was not observed.

X-ray diffraction patterns of the $\text{ZnCr}_2\text{O}_4/\text{ZnNb}_2\text{O}_6$ samples (Table 3.1b) were much simpler. Spinel ZnCr_2O_4 was the dominant phase for all of the ceramics (ratios of 3/1 to 9/1). Columbite ZnNb_2O_6 phase was the only other phase in these samples (except for a trace of excess Nb_2O_5 detected in the 5/1 sample. The amount of columbite decreased as the spinel/columbite ratio was increased, as expected.

Additional ceramic samples were studied by x-ray diffraction, and gave interesting results. The compositions were $\text{Cd}_5\text{Zn}_7\text{Cr}_{20}\text{Nb}_4\text{O}_{52}$ and $\text{Cd}_7\text{Zn}_5\text{Cr}_{20}\text{Nb}_4\text{O}_{52}$; the intent here was to form a 50/50 solid solution of CdCr_2O_4 and ZnCr_2O_4 spinels, with a 10 percent mineralizer of the ZnNb_2O_6 and CdNb_2O_6 columbites, respectively. As shown by the data in Table 3.1c, the spinel solid solution was not formed. For each composition, the same three phases were formed: spinel ZnCr_2O_4 , columbite CdNb_2O_6 , and CrNbO_4 . This suggests that the ceramic solid solution of these two spinels will be difficult (if not impossible) to fabricate.

3.B.2 Microstructure

X-ray diffraction of the CeramPhysics samples revealed that most of the ceramics consisted primarily of two phases, the respective Cd or Zn spinels and columbites. SEM backscattered and x-ray fluorescence analyses of the sintered ceramic sample of the 5/1 $\text{CdCr}_2\text{O}_4/\text{CdNb}_2\text{O}_6$ composition are presented in Figure 3.1. The SEM (backscatter mode) micrograph (Figure 3.1a) reveals the coexistence of two phases, with the major phase being light in contrast and a minor phase evident as round, greyish spots, which appear to be precipitates. X-ray fluorescence analyses (Figures 3.1b, c, and d) indicate that the major phase is rich in Cd and Cr, and is probably the CdCr_2O_4 spinel phase. The grey areas are rich in Nb and deficient in Cr, suggesting that this phase is CdNb_2O_6 .

The microstructure of the $\text{ZnCr}_2\text{O}_4/\text{ZnNb}_2\text{O}_6$ samples were studied by both optical and scanning electron microscopy. Optical microstructures of polished faces of three sintered ceramic disks with spinel/columbite ratios of 3/1, 5/1, and 7/1 are presented in Figure 3.2. Two types of microstructures

are clearly indicated, with a core-like structure at the center of the disks. It is important to note that the core size increases with decreasing spinel/columbite ratio. Higher magnifications of the 7/1 sample were studied by SEM, and are shown in Figure 3.3. The SEM (backscatter mode) micrograph (Figure 3.3a) revealed that both the outer ring and inner core are composed of two phases, evident as grey (low contrast) and light (bright contrast) areas. The outer ring is composed primarily of the grey areas with isolated regions rich in the light phase. The inner core is also composed of a mixture of the of two phases, but with a finer distribution than the outer ring. X-ray fluorescence revealed that the samples are uniform in Zn (Figure 3.3b), the light areas are rich in Nb and deficient in Cr (Figure 3.3c), and the grey areas are rich in Cr and deficient in Nb (Figure 3.3d). These results suggest that the inner core is composed of a fine mixture of the ZnCr_2O_4 spinel and ZnNb_2O_6 columbite phases, whereas the outer ring is rich in spinel with isolated columbite-rich regions.

3.B.3 Initial Conclusions

The XRD and SEM characterization studies on the CeramPhysics spinel/columbite ceramic samples revealed contrasting phase constitutions and microstructures between the Cd and Zn spinel/columbite compositions. However, the results these studies did not offer any conclusive evidence as to how the columbite affects the sintering behavior of the spinel ceramics, or why it is necessary to enhance densification. Further studies were thus warranted.

3.C Ceramic Studies (Penn State)

3.C.1 Pure CdCr_2O_4 and ZnCr_2O_4 Spinel

In order to understand how the additions of the columbites (CdNb_2O_6 and ZnNb_2O_6) were necessary to densify the respective CdCr_2O_4 and ZnCr_2O_4 spinel ceramics, the single phase spinel ceramic powders were fabricated and sintering studies were performed. Reagent grade oxides (CdO , ZnO , and Cr_2O_3) were batched to the stoichiometric spinel compositions, vibratory milled in nalgene jars with alcohol and zirconia grinding media, and dried. Samples of the two spinel compositions were calcined at various temperatures, and x-ray diffraction was used to monitor the formation of the spinel phase. It was

found that the CdCr_2O_4 spinel was formed by calcination at 950°C for four hours, while the formation of the ZnCr_2O_4 spinel required a calcination temperature of 1050°C .

Disks were prepared from the two spinel powders, and a sintering study was performed. The disks were placed on zirconia setters and sintered at various temperatures for one hour. The results of this sintering study are presented in Table 3.2. It was found that neither of the two spinels could be densified to near their theoretical densities of 5.79 and 5.30 g/cc, for CdCr_2O_4 and ZnCr_2O_4 , respectively. The maximum densities achieved for the the spinel samples were 4.4 g/cc (76 percent of theoretical) for the CdCr_2O_4 spinel ceramic sintered at 1290°C , and 3.8 g/cc (72 percent of theoretical), for the ZnCr_2O_4 spinel ceramic sintered at 1650°C . It was interesting to note that below 1350°C , the fired disks experienced a weight gain of between 1 and 2 percent. The origin of this weight gain is yet unknown, as the fired disks remained single phase spinel by XRD. For sintering temperatures above 1350°C , weight loss due to volatilization of CdO or ZnO was observed; the weight loss was very pronounced in the CdCr_2O_4 spinel sample sintered at 1350°C and was accompanied by a substantial decrease in density. Such weight loss is typically expected, as both ZnO and especially CdO are volatile at these high temperatures.

The inability to densify the two spinel ceramics can be attributed to the volatilization of CdO and ZnO at the high sintering temperatures that are required for these spinel ceramics. If the volatilization of CdO or ZnO could be prevented, then densification of the ceramics would occur. In order to prevent weight loss, the spinel disks were sintered in a CdO- or ZnO-rich atmosphere, by burying the disks in a sintered powder (or sand) of their own composition. For the ZnCr_2O_4 samples, this technique was effective in preventing ZnO loss, and dense ceramics (90 percent of theoretical) were achieved, although extremely high sintering temperatures (1600°C) were required. The SEM microstructure of a 90 percent dense ZnCr_2O_4 sample, sintered at 1600°C for four hours, is shown in Figure 3.4, and compared with the SEM microstructure of the analagous Zn spinel/columbite (9/1) sample sintered at 1350°C . The grain structure size of the 1600°C sintered ZnCr_2O_4 sample was non-uniform but with a large grain size (4 to 12 microns); conversely, the Zn spinel/columbite (9/1) sample had a much more uniform microstructure and smaller grain size (about 1-2 microns).

Sintering the CdCr_2O_4 spinel disks using the "sand" method to control CdO loss was effective, but no appreciable difference density was achieved. However, with a sintering temperature of 1350°C , the weight loss was reduced from 13 to less 1 percent. The "sand" technique was ineffective for preventing CdO loss with sintering temperatures above 1350°C , and resulted in lower densities. Thus, dense samples (90 percent of theoretical) of CdCr_2O_4 could not be prepared. The SEM microstructure of the CdCr_2O_4 sample sintered at 1300°C for 0.5 hours in a CdO -rich atmosphere is compared with that of the analogous Cd spinel/columbite (9/1) sample, in Figure 3.5. The CdCr_2O_4 sample had a uniform microstructure with a grain size of about 2 microns, and a significant amount of porosity. The Cd spinel/columbite (9/1) sample had a non-uniform microstructure with grain sizes ranging from 4 to 8 microns, but with less porosity.

3.C.2 Modified Spinel Compositions

Stoichiometry and/or other compositional variations often are important factors in determining whether a particular ceramic powder will densify. A study was undertaken to determine whether compositional modifications would affect the sintering behavior of the spinel ceramics. It was hoped that the results of this study would improve the understanding of how the columbite additions enhance the sintering in these spinels.

Various compositional modifications were made to the pre-calcined spinel powders. After additions such as CdO , ZnO , or Nb_2O_5 were mixed with the appropriate spinel (by vibratory milling followed by drying), disks were prepared and sintering studies were carried out. Sintering results (weight loss and density) and x-ray diffraction data are presented in Table 3.3. Note that when both CdO and Nb_2O_5 , or ZnO and Nb_2O_5 , were added simultaneously, the amounts corresponded to an addition of 10 mole percent columbite. As shown by the data in Table 3.3, excess additions of ZnO to ZnCr_2O_4 , or CdO to CdCr_2O_4 , did not enhance densification. However, enhanced densification was achieved in all cases of excess Nb_2O_5 , regardless of whether ZnO or CdO was also added. For the case of ZnCr_2O_4 , a 1 weight percent addition of Nb_2O_5 was sufficient to improve the densification of the spinel ceramics, whereas a 10 mole percent addition of columbite corresponds to more than 13 weight percent. The best density were achieved with a 5 weight percent Nb_2O_5 addition (4.95

g/cc (93% of theoretical). For the case of CdCr_2O_4 , a 5 weight percent Nb_2O_5 addition resulted in a sintered spinel ceramic with a density of 5.0 g/cc. It was found that if CdO loss was prevented, by using a closed crucible and a CdO -rich atmosphere source powder (CdCr_2O_4 sand), further densification to 5.3 g/cc (91% theoretical) could be achieved.

X-ray diffraction data of the sintered samples of the ZnCr_2O_4 spinel with the various ZnO and/or Nb_2O_5 additions indicated that the major phase was spinel, and a trace amount of columbite ZnNb_2O_6 was detected. For the case of CdCr_2O_4 spinel with additions of CdO and/or Nb_2O_5 , the spinel was again the major phase, but minor amounts of several other phases were detected: columbite CdNb_2O_6 , pyrochlore $\text{Cd}_2\text{Nb}_2\text{O}_7$, CrNbO_4 , Cr_2O_3 , and Nb_2O_5 . The microstructures of sintered disks of the Cd and Zn spinels with 7 percent additions of Nb_2O_5 , are presented in Figure 6. The microstructure of the CdCr_2O_4 spinel sample indicated a larger grain size than the ZnCr_2O_4 sample, though both samples displayed non-uniform grain structures, with grain sizes ranging from 1 to 5 microns.

It is likely that the mechanism responsible for enhanced densification of the spinel ceramics caused by excess Nb_2O_5 is identical to that of the columbite additions. Although there are no existing phase diagram data for the CdCr_2O_4 and ZnCr_2O_4 systems, a possible explanation for the enhanced sintering can be inferred from existing phase diagrams of the $\text{CdO-Nb}_2\text{O}_5$ and $\text{ZnO-Nb}_2\text{O}_5$ systems. These phase diagrams are shown in Figure 3.7. Liquid phases are present in the $\text{CdO-Nb}_2\text{O}_5$ system at temperatures as low as 1350°C , and in the $\text{ZnO-Nb}_2\text{O}_5$ system at temperatures below 1300°C . It is possible that the presence of chromium further reduces these liquidus temperatures. The presence of a liquid phase at temperatures in range where a liquid phase is present would suggest that the Nb_2O_5 enhances the sintering of the spinel ceramics through a liquid-phase sintering mechanism. It is unfortunate that no phase diagram data exist for either of the spinel- Nb_2O_5 systems. To verify the existence of a liquid-phase sintering mechanism, differential thermal analysis (DTA) was carried out on a sample of CdCr_2O_4 -9% Nb_2O_5 powder. The DTA pattern is presented in Figure 3.8. An endothermic peak was observed at a temperature of 1297°C , confirming the presence of a liquid phase at this temperature. This endothermic peak was not observed in pure CdCr_2O_4 powder. This result strongly suggests that liquid-phase sintering is the mechanism whereby the Nb_2O_5 (or columbite) enhances the sintering of the spinel ceramics.

3.D Summary of Results of Ceramic Studies

The results of the ceramic studies performed in this investigation are summarized below:

- 1) X-ray diffraction and microstructural analyses of the original CeramPhysics ceramics with various spinel/columbite ratios were performed. Different microstructures were observed between the Cd and Zn analogues of the spinel/columbite ceramics.
- 2) Pure CdCr_2O_4 could not be densified (in air) to greater than 80% of theoretical, because of excessive CdO loss. The densification did not improve significantly when CdO loss was limited by sintering in a CdO-rich atmosphere. It was also impossible to densify pure ZnCr_2O_4 by sintering in air, due to ZnO volatilization. However 90 percent dense ZnCr_2O_4 ceramics with large grain size (about 10 microns) could be prepared by sintering at 1600°C in a ZnO-rich atmosphere.
- 3) Densification of the ZnCr_2O_4 ceramics could be improved by a one weight percent, instead of the 13 weight percent columbite (ZnNb_2O_6) addition that has previously been used. Similarly, CdCr_2O_4 ceramics could be densified by a 5 weight percent addition of Nb_2O_5 .
- 4) The improved sintering behavior caused by the columbite or Nb_2O_5 additions was the result of a liquid phase, which appears to be present. This conclusion is supported by incomplete phase diagram data which suggest the presence of low-temperature eutectics in the $\text{CdO-Nb}_2\text{O}_5$ and $\text{ZnO-Nb}_2\text{O}_5$ systems.

Table 3.1a

X-ray Diffraction Analysis of Spinel:Columbite Composition.
 $(\text{CdCr}_2\text{O}_4):\text{CdNb}_2\text{O}_6$ - CeramPhysics

Composition	Phases Present
CCN (1/1) (#592)	$\text{Cd}_2\text{Nb}_2\text{O}_7$ (Pyrochlore), Spinel, Columbite, Nb_2O_5
CCN (3/1) (cal. powder 1050°C-2hr)	Pyrochlore, Spinel, Nb_2O_5
CCN (5/1) (#571)	Spinel, Pyrochlore, Columbite, Cr_2O_3
CCN (7/1) (#563)	Spinel, Pyrochlore, Columbite
CCN (9/1) (#312+6.75% Fe)	Spinel, Columbite, Pyrochlore
CCN (9/1) (#352)	Spinel, Columbite, Cr_2O_3
CCN (11/1) (CPI-13 powder)	Spinel, Cr_2O_3 , CdO, Columbite (Note: incompletely reacted)

Note: All samples were sintered disks unless
otherwise stated.

Table 3.1b

X-ray Diffraction Analysis of Spinel:Columbite Compositions.
($\text{ZnCr}_2\text{O}_4\text{:ZnNb}_2\text{O}_6$) - CeramPhysics

Composition	Phases Present
ZCN (3/1) (#251)	Spinel, Columbite
ZCN (5/1) (#302)	Spinel, Columbite + Trace Nb_2O_5
ZCN (7/1) (#301)	Spinel, Columbite
ZCN (9/1) (#559)	Spinel, Columbite
ZCN (9/1) (#557)	Spinel, Columbite

Table 3.1c

X-ray Diffraction Analysis of Solid Solution Spinel:Columbites.

Composition	Phases Present
$\text{Cd}_5\text{Zn}_7\text{Cr}_{20}\text{Nb}_4\text{O}_{52}$	ZnCr_2O_4 Spinel, CdNb_2O_6 Columbite, CrNbO_4
$\text{Cd}_7\text{Zn}_5\text{Cr}_{20}\text{Nb}_4\text{O}_{52}$	ZrCr_2O_4 Spinel, CdNb_2O_6 Columbite, CrNbO_4

Sintering Study of ZnCr_2O_4 and CdCr_2O_4 Disks.

Composition	Sintering Condition	Wt Change %	Density g/cc
ZnCr_2O_4	1290°C/1 hr	+1-2%	3
	1340°C/1 hr	+1-2%	3
	1420°C/1 hr	-0.6%	3.4
	1550°C/1 hr	-2%	3.7
	1650°C/1 hr	-3%	3.8
CdCr_2O_4	1290°C/1 hr	+1%	4.4
	1350°C/1 hr	-13%	3.0

Table 3.3
XRD and sintering results of Modified
 $ZnCr_2O_4$ and $CdCr_2O_4$ spinels

Composition	Sintering Conditions	Weight Change(%)	Density (g/cc)	Phases Present
$ZnCr_2O_4$ + 2wt% ZnO	1300°C/1hr	--	3.2	-----
$ZnCr_2O_4$ + 3.33% ZnO + 10.86% Nb_2O_5	1300°C/1hr 1350°C/1hr	+0.3 0	4.80 4.85	Spinel, tr.columbite Spinel, tr.columbite
$ZnCr_2O_4$ + 1% Nb_2O_5 + 3% Nb_2O_5 + 5% Nb_2O_5 + 7% Nb_2O_5 + 9% Nb_2O_5	1350°C/1.5hrs. 1350°C/1.5hrs. 1350°C/1.5hrs. 1350°C/1.5hrs. 1350°C/1.5hrs.	<0.5 <0.5 <0.5 <0.5 <0.5	4.70 4.80 4.95 4.87 4.80	----- ----- Spinel, tr.columbite ----- -----
$CdCr_2O_4$ + 4% CdO	1300°C/1hr	--	3.7	-----
$CdCr_2O_4$ + 4.4% CdO + 9.11% Nb_2O_5	1320°C/0.5hr. 1320°C/0.5hr. (*)	-7% -0.5%	4.7 5.15	Spinel, columbite Pyrochlore, tr. $CrNbO_4$
$CdCr_2O_4$ + 5% Nb_2O_5	1320°C/0.5hr. 1320°C/0.5hr.	-7% -0.2%	5.0 5.3	Spinel, tr.columbite Spinel, Pyrochlore, tr.columbite, tr. Nb_2O_5 tr. Cr_2O_3

(*) Disks fired in closed crucible with $CdCr_2O_4$ atmosphere powder (sand).

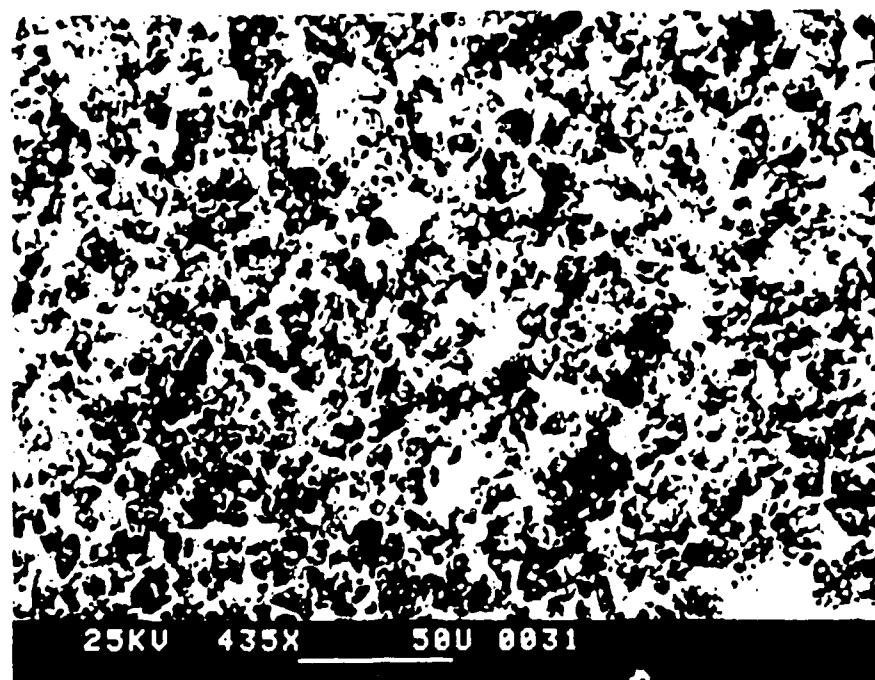


Figure 3.1a. SEI backscattered micrograph of $\text{CdCr}_2\text{O}_4\text{-CdHb}_2\text{O}_6$ (5/1).

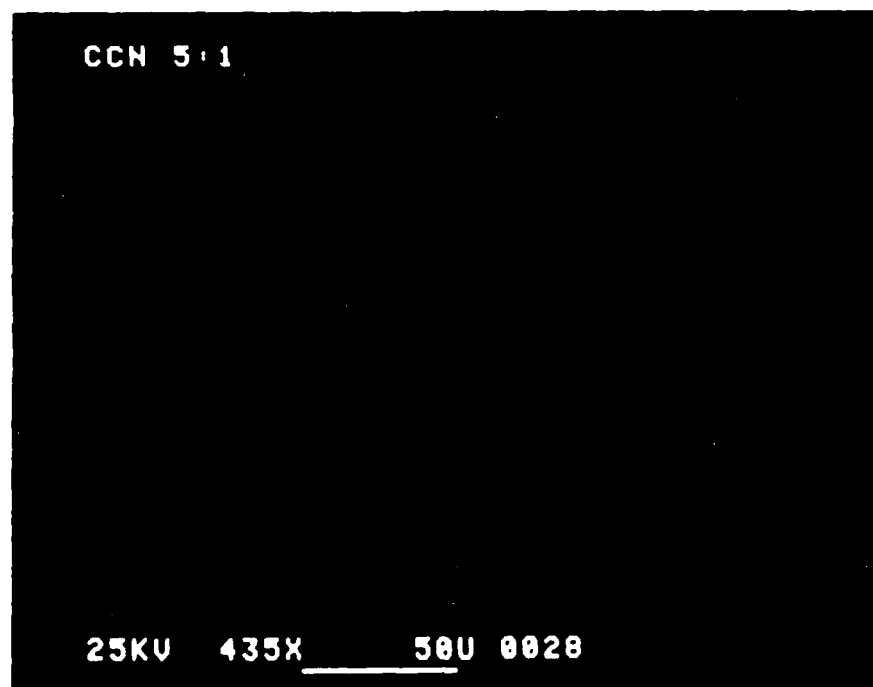


Figure 3.1b. X-ray fluorescence of Cd in $\text{CdCr}_2\text{O}_4\text{-CdHb}_2\text{O}_6$ (5/1).

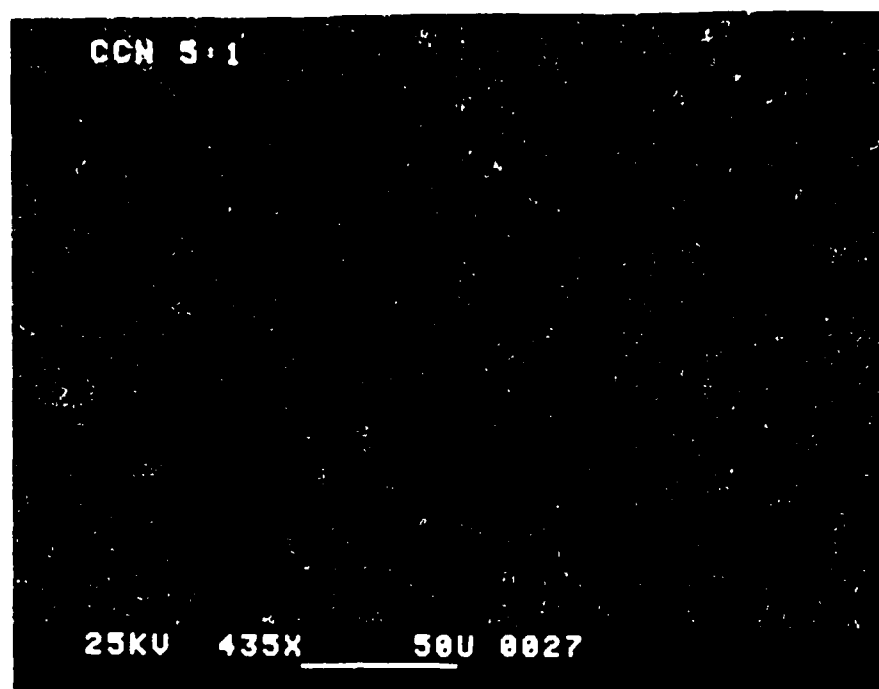


Figure 3.1c. X-ray fluorescence of Cr in $\text{CdCr}_2\text{O}_4\text{-CdNb}_2\text{O}_6$ (5/1).

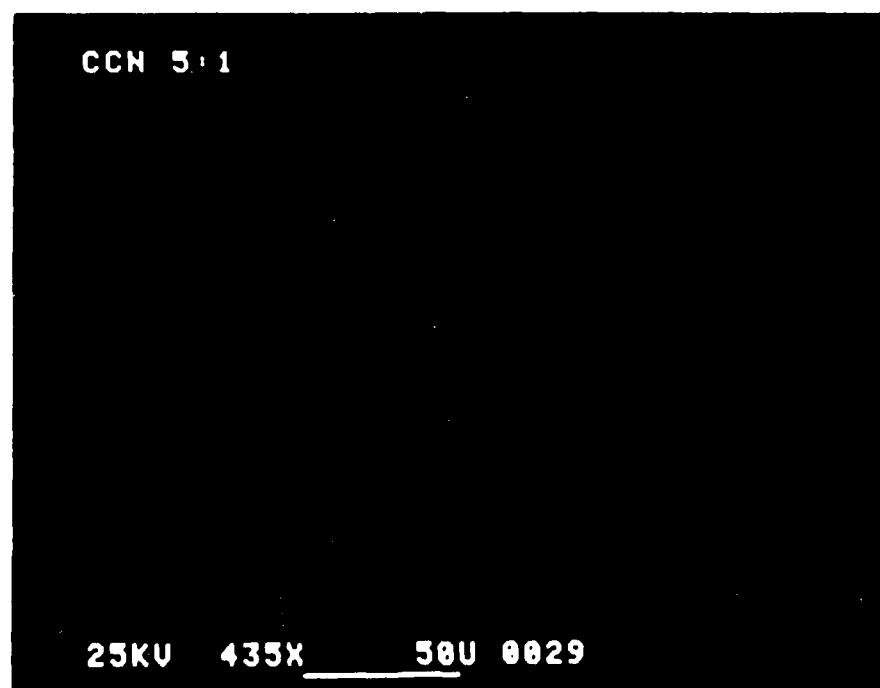


Figure 3.1d. X-ray fluorescence of Nb in $\text{CdCr}_2\text{O}_4\text{-CdNb}_2\text{O}_6$ (5/1).



Figure 3.2a. Optical macrostructure of ZnCr₂O₄-ZnNb₂O₆ disks (3/1), (5/1), (7/1) left to right, respectively.

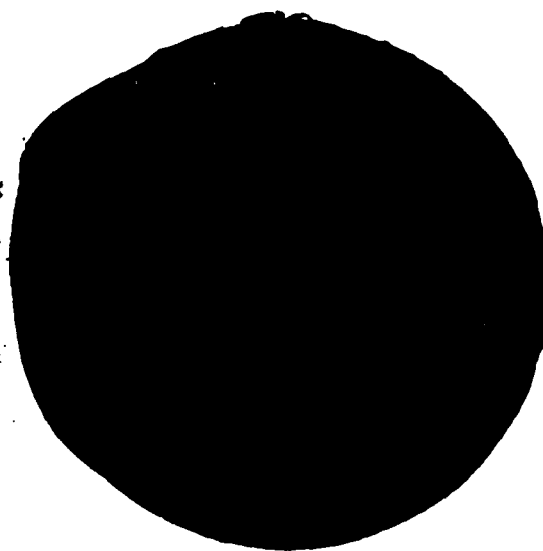


Figure 3.2b. Optical macrostructure of ZnCr₂O₄-ZnNb₂O₆ (7/1) at magnification (x8).

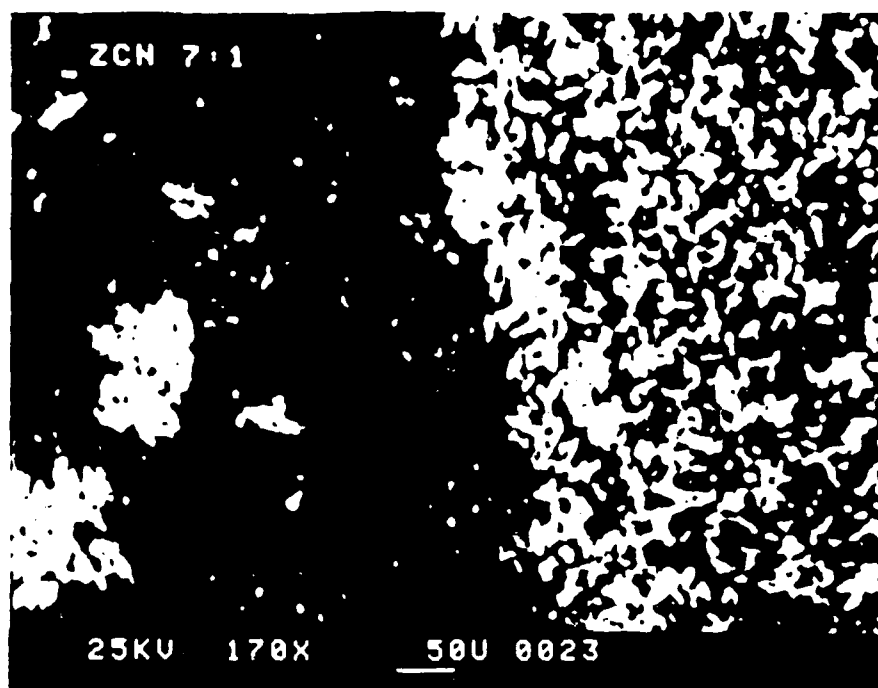


Figure 3.3a. SEM backscattered micrograph of $\text{ZnCr}_2\text{O}_4\text{-ZnNb}_2\text{O}_6$ (7/1) (core on the right).

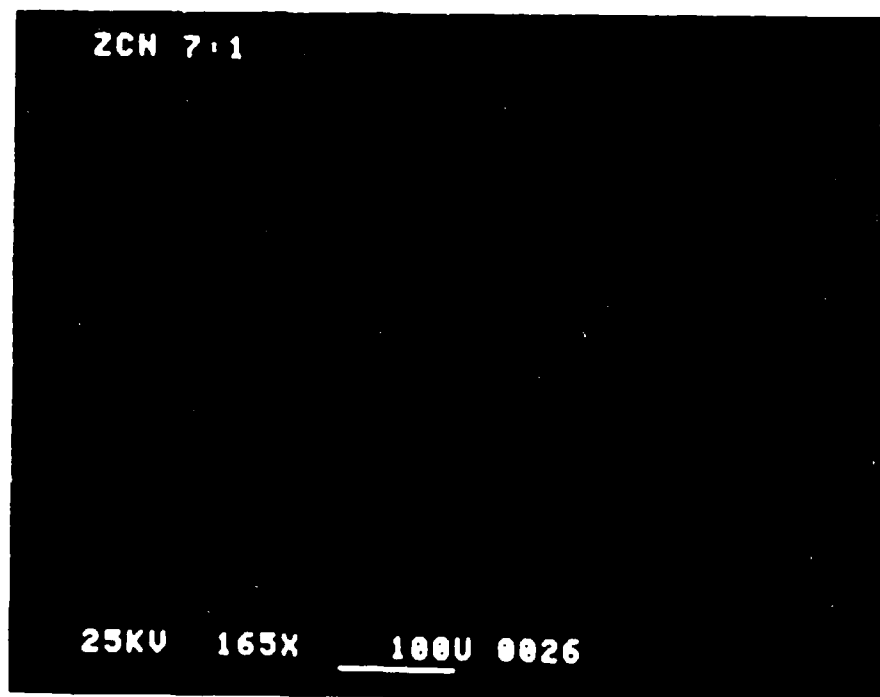


Figure 3.3b. X-ray fluorescence of Zn in $\text{ZnCr}_2\text{O}_4\text{-ZnNb}_2\text{O}_6$ (7/1).

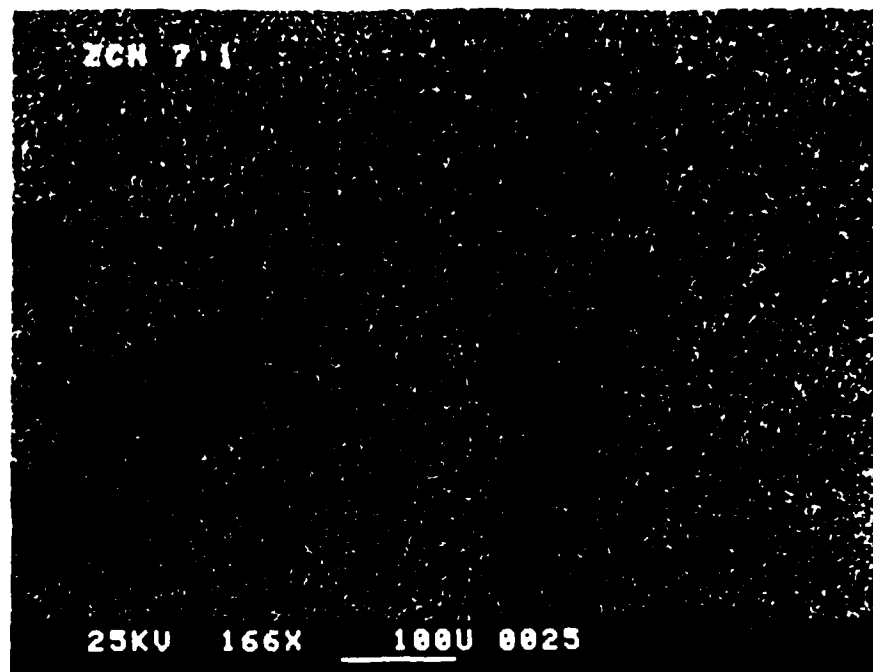


Figure 3.3c. X-ray fluorescence of Cr in $\text{ZnCr}_2\text{O}_4\text{-ZnNb}_2\text{O}_6$ (7/1) (core on the right).

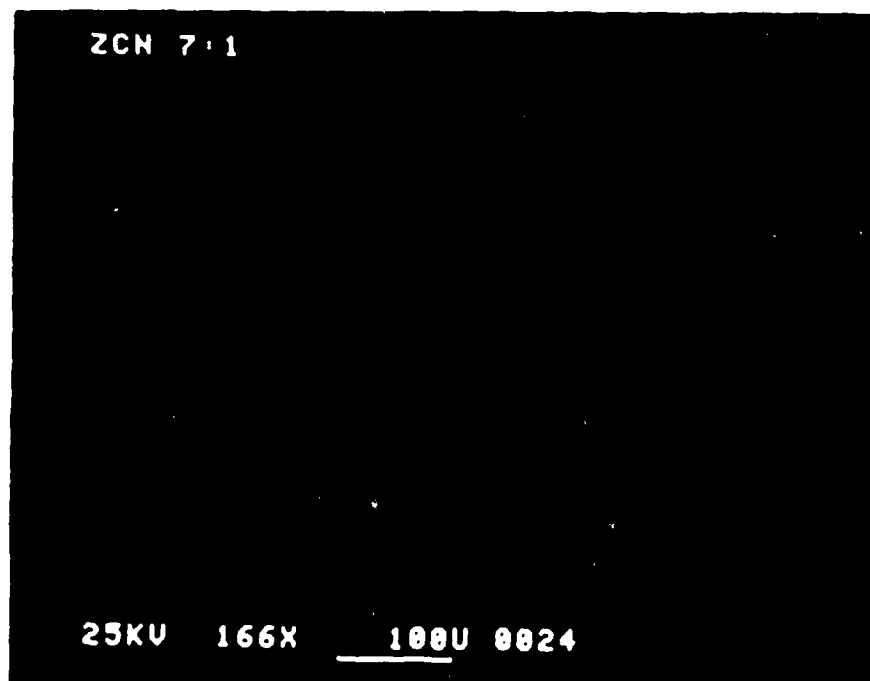


Figure 3.3d. X-ray fluorescence of Nb in $\text{ZnCr}_2\text{O}_4\text{-ZnNb}_2\text{O}_6$ (7/1) (core on the right).

ZnCr_2O_4
1600°C/4 hrs.

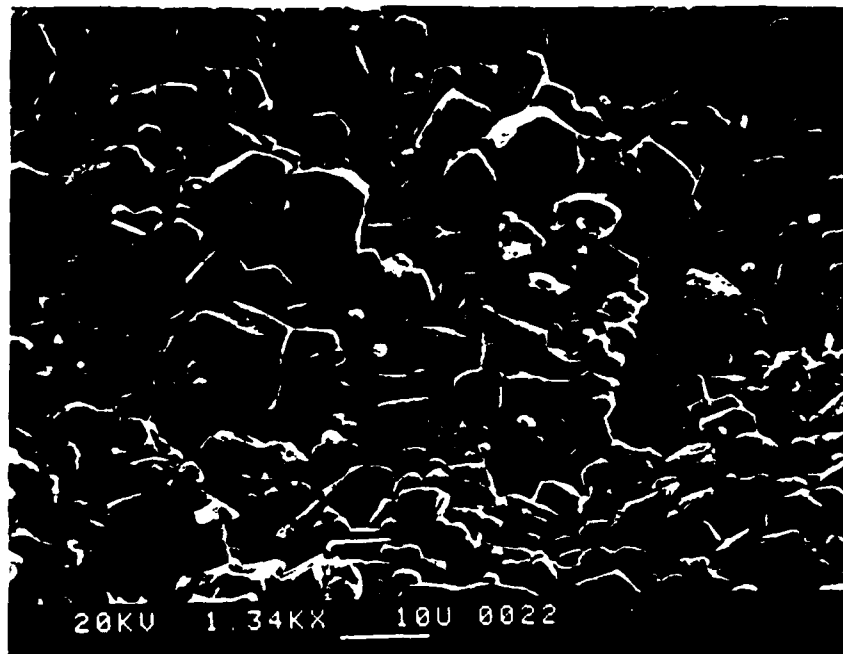


Figure 3.4a. Microstructure of ZnCr_2O_4 sample, sintered in ZnCr_2O_4 sand at 1600°C for 4 hrs.

$\text{ZnCr}_2\text{O}_4/\text{ZnNb}_2\text{O}_6(9/1)$

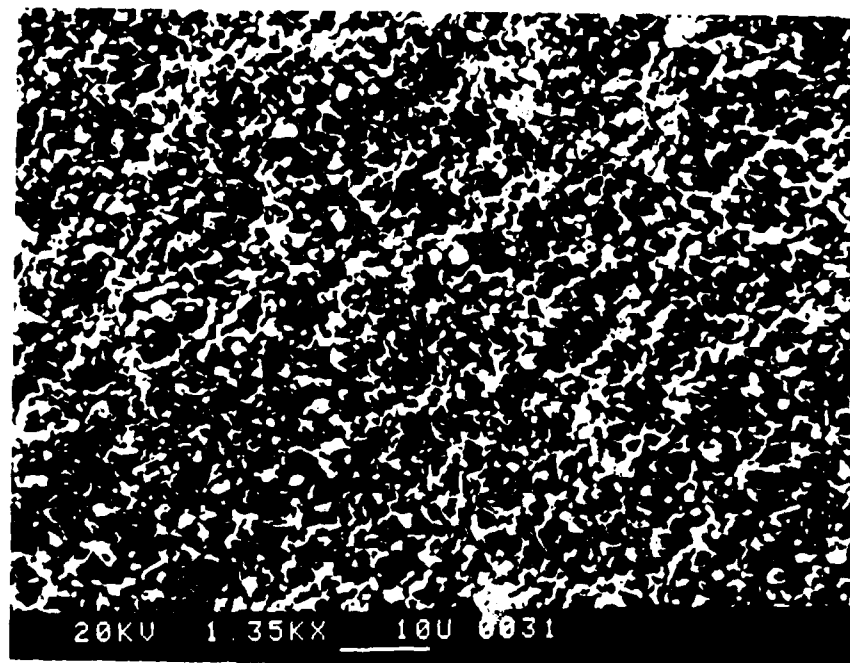


Figure 3.4b. Microstructure of $\text{ZnCr}_2\text{O}_4/\text{ZnNb}_2\text{O}_6(9/1)$ sample, sintered at 1300°C for 1 hr.

CdCr₂O₄
1300°C/0.5

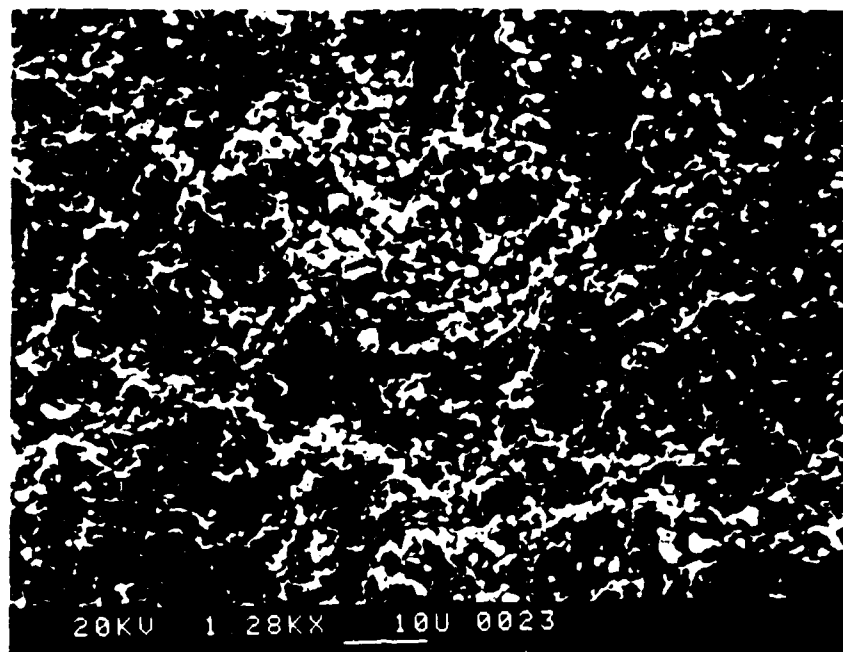


Figure 3.5a. Microstructure of pure CdCr₂O₄ sample sintered in CdCr₂O₄ sand at 1300°C for 0.5 hrs.

CdCr₂O₄/CdNb₂O₆ (9/1)
06751E

(PI312)

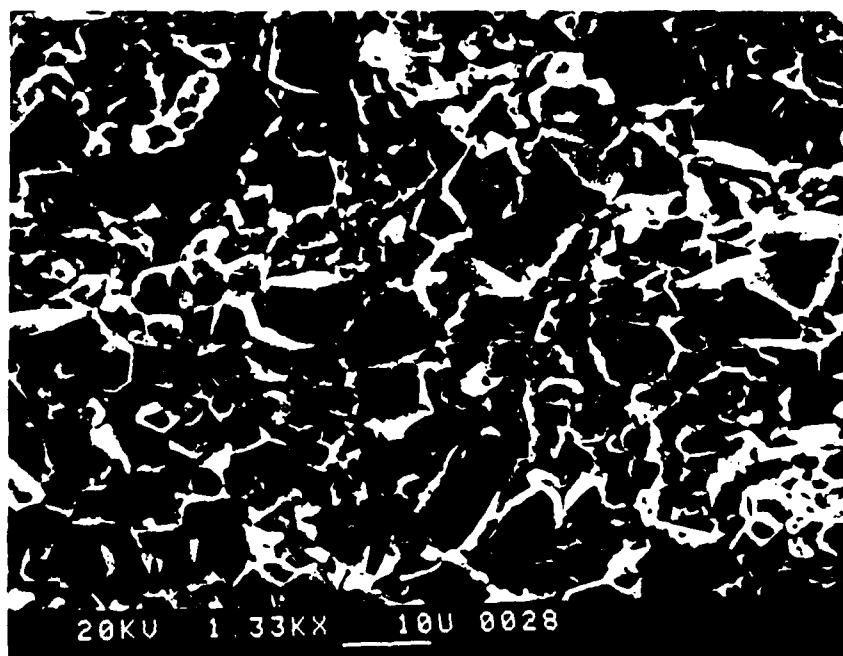


Figure 3.5b. Microstructure of CdCr₂O₄/CdNb₂O₆ (9/1) sample sintered at 1300°C for one hour.

*CdCr₂O₄ 7% Nb₂O₅
in sand
1320°C
0.5 hr*

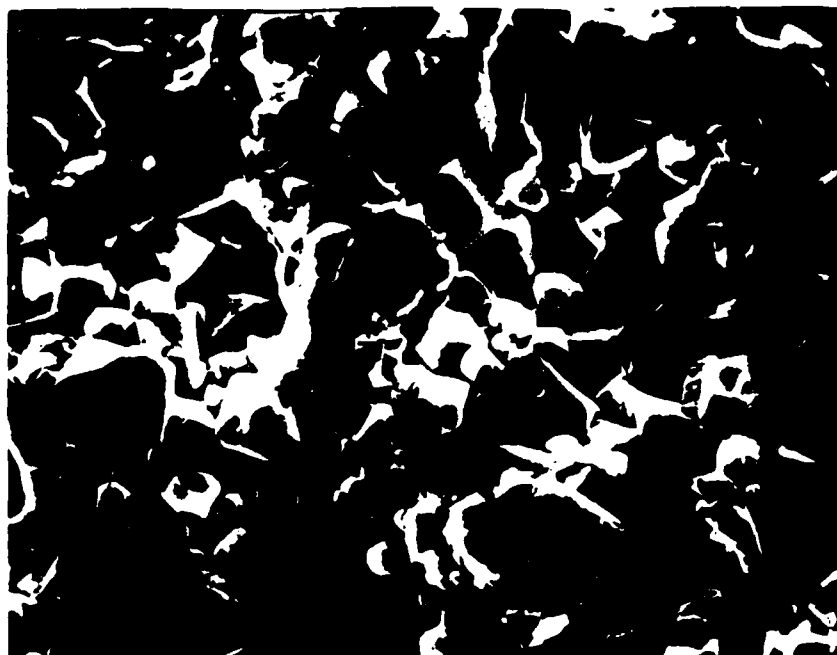


Figure 6a. Microstructure of $\text{CdCr}_2\text{O}_4/7\% \text{Nb}_2\text{O}_5$ sample sintered at 1320°C for 0.5 hours (in CdCr_2O_4 sand).

*ZnCr₂O₄ 7% Nb₂O₅
in sand
1350°C
1.5 hr*

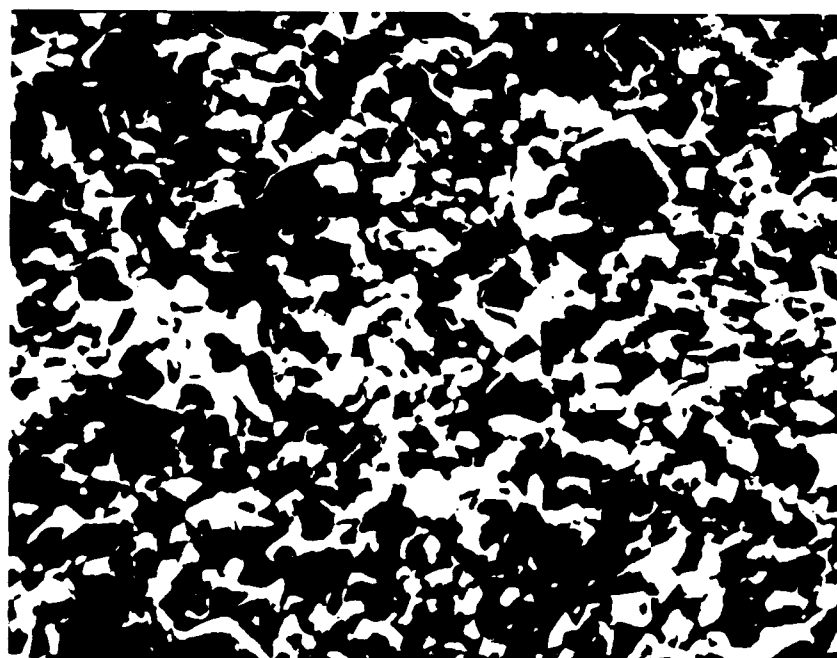


Figure 6b. Microstructure of $\text{ZnCr}_2\text{O}_4/7\% \text{Nb}_2\text{O}_5$ sample sintered at 1350°C for 1.5 hours.

(1 cm bar = 5 microns)

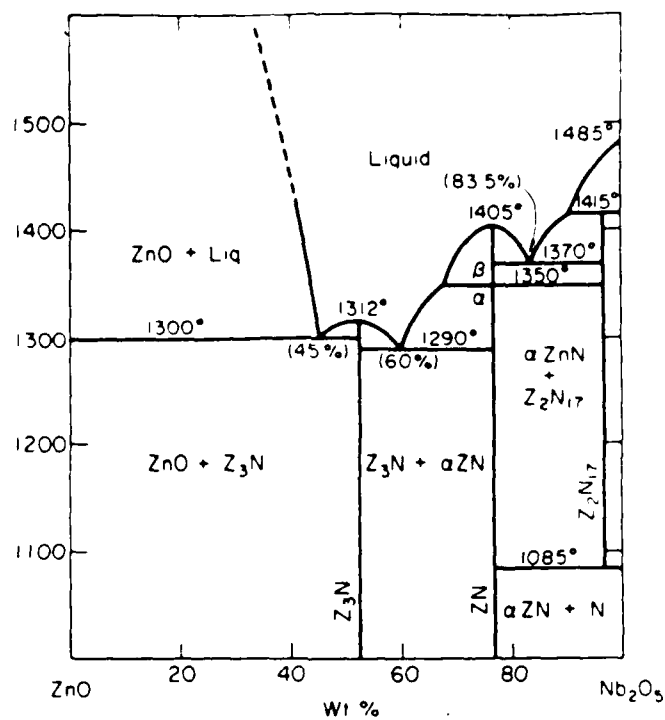


Figure 3.7a. System $\text{ZnO-Nb}_2\text{O}_5 \cdot \text{Z}_3\text{N} = \text{Zn}_3\text{Nb}_2\text{O}_8$, $\text{ZN} = \text{ZnNb}_2\text{O}_6$, $\text{Z}_2\text{N}_{17} = \text{Zn}_2\text{Nb}_{34}\text{O}_{87}$.

CdO-Nb₂O₅

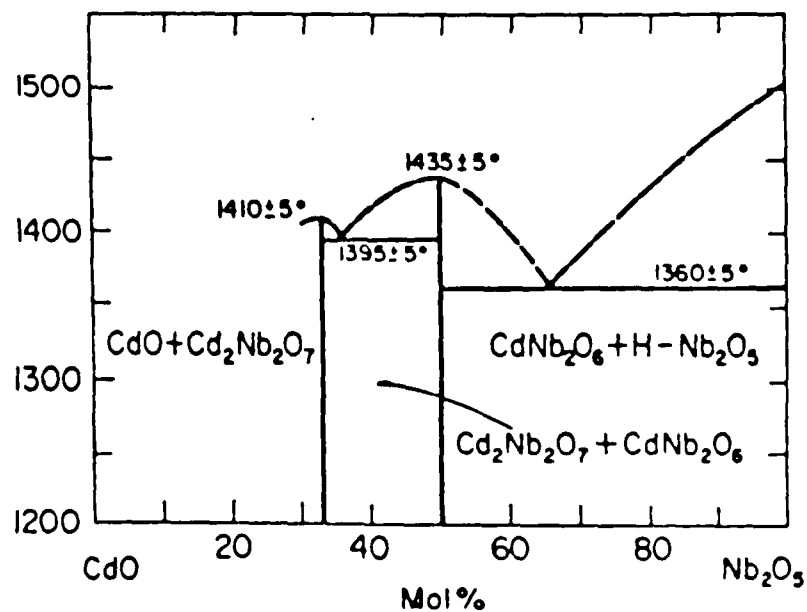


Figure 3.7b. CdO-Nb₂O₅ phase diagram.

8.00

CDCR204+9%NB2O5

WT: 0.00 mg

SCAN RATE: 20.00 deg/min

ATMOSPHERE: ARGON 40 cc/min

ENDO

DEGREES

4.00

0.00

PEAK FROM 1150
TO 1350
ONSET, 1273.8
PEAK HEIGHT, -4.22
MIN, 1296.7

100.00 220.00 340.00 460.00 580.00 700.00 820.00 940.00 1060.00 1180.00 1300.00

KCZ/BJ FILE: GZ287.DT

TEMPERATURE (C)

DTA

DATE: 87/03/11 TIME: 11:34

Figure 3.8. DTA pattern of CdCr_2O_4 -9% Nb_2O_5 powder.

IV. SPECIFIC HEAT, MAGNETOCALORIC, AND DIELECTRIC CONSTANT MEASUREMENTS AT LOW TEMPERATURES

This Section is devoted to experimental research on the specific heat, magnetocaloric, and dielectric constant properties of CdCr_2O_4 - and ZnCr_2O_4 - containing ceramics at low temperatures and in intense magnetic fields. All measurements here were made on dense or semi-dense ceramic pellets, and the nomenclature used below is as follows:

CCN(9/1) = Mixture of 10 mole% CdNb_2O_6 , 90 mole% CdCr_2O_4 ,
fully dense, fine grain size

ZCN(9/1) = Zinc analog of CCN(9/1)

CdCr_2O_4 = Pure CdCr_2O_4 , 74% dense, fine grain size

ZnCr_2O_4 = Pure ZnCr_2O_4 , 72% dense, fine grain size

This Section is organized along the following lines: First, the dielectric-constant data will be presented, followed by the specific heat data. Next, the specific heat data will be analyzed. Thirdly, the magnetocaloric data will be presented, and lastly these data will be analyzed.

A. Dielectric Constant Measurements

Dielectric measurements of CCN(9/1) and ZCN(9/1) disks have been made at low temperatures. Each sample had sputtered gold electrodes and was a disk approximately one centimeter in diameter and one millimeter thick. The measurements were made in a dielectric probe where the lead capacitance was on the order of a tenth of a picofarad (about 1% of the measured values).

Dielectric constant versus temperature data for each sample are shown in Fig. 4-1. In each case the dielectric constant peaks above the temperature at which the specific peaks occur [8 K and 10.7 K for CCN(9/1) and ZCN(9/1), respectively]. The specific-heat-peak temperatures are shown as the vertical arrows.

From Fig. 4-1, it appears that the slope of the dielectric constant increases at the specific-heat-peak temperatures. To

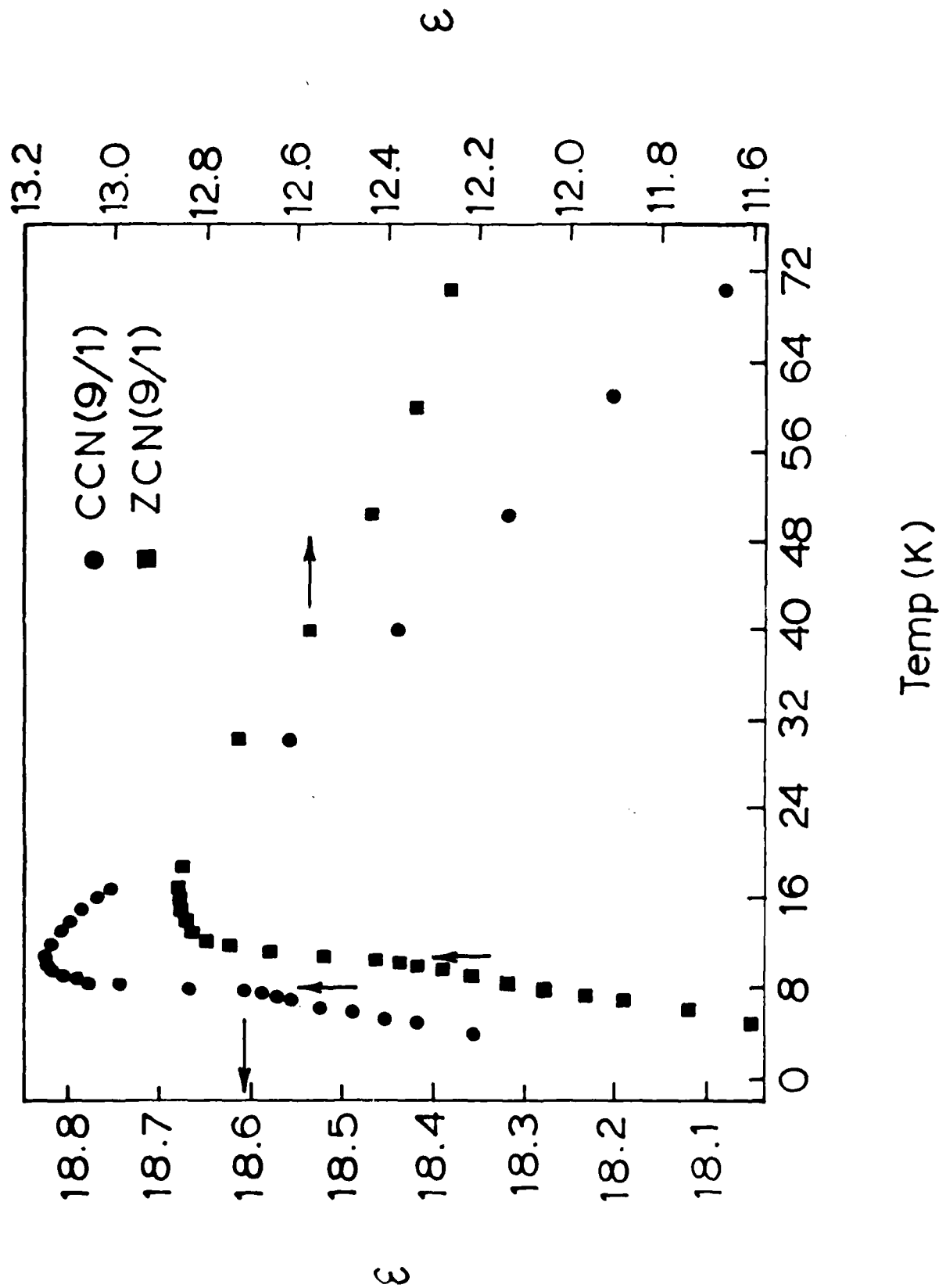


Figure 4-1. Dielectric constant measurements (1 kHz) on CCN(9/1) and ZCN(9/1) in the neighborhood of the specific heat maxima (arrows).

test this observation, the average slope ($\Delta\epsilon/\Delta T$) was calculated between each pair of data points and is plotted in Fig. 4-2(a) where the temperature of each point is the average temperature in that interval. Figure 4-2(a) clearly shows the dramatic increases in the slopes very near the specific-heat-peak temperatures.

Figure 4-2(b) shows the variation in the dielectric constant as a function of frequency at constant temperature near the peaks of each material (8.01 K and 10.55 K, respectively). Both sets of data are normalized to the dielectric constant at 200 Hz. Although both changes are small, the ZCN(9/1) changes are much larger than the CCN(9/1) changes.

Following the discovery of sharp maxima in $\Delta\epsilon/\Delta T$ at the temperature of the specific heat maximum for both CCN(9/1) and ZCN(9/1), Fig. 4-2(a), a decision was made to pursue these measurements on the pure materials and in intense magnetic fields.

Figure 4-3 shows the original dielectric data for CCN(9/1) and the new dielectric data for pure CdCr_2O_4 in zero field. The latter sample was a disk that was only 54% of theoretical density, and the data have been corrected for this low density following a formula given by Niesel (1952). The pure material has a smaller dielectric constant than the CCN(9/1) and does not have the rapid rise associated with the spinel/columbite mixture. At first glance, it appears there might be a small structure in the pure CdCr_2O_4 data at 8 K, but upon repetition of the measurements across this region (not shown) it became clear that this apparent structure is near the noise level and is probably not present. Except for the broad maximum, the dielectric constant of the pure material is distinctly different from that of CCN(9/1).

Figure 4-4 shows similar data for ZCN(9/1) and pure ZnCr_2O_4 where again the pure material data have been density-corrected (70% of theoretical). Here the pure material does show slight structure; i.e., a small, comparatively broad rise in the dielectric constant between 6 and 8 K. There is no broad peak

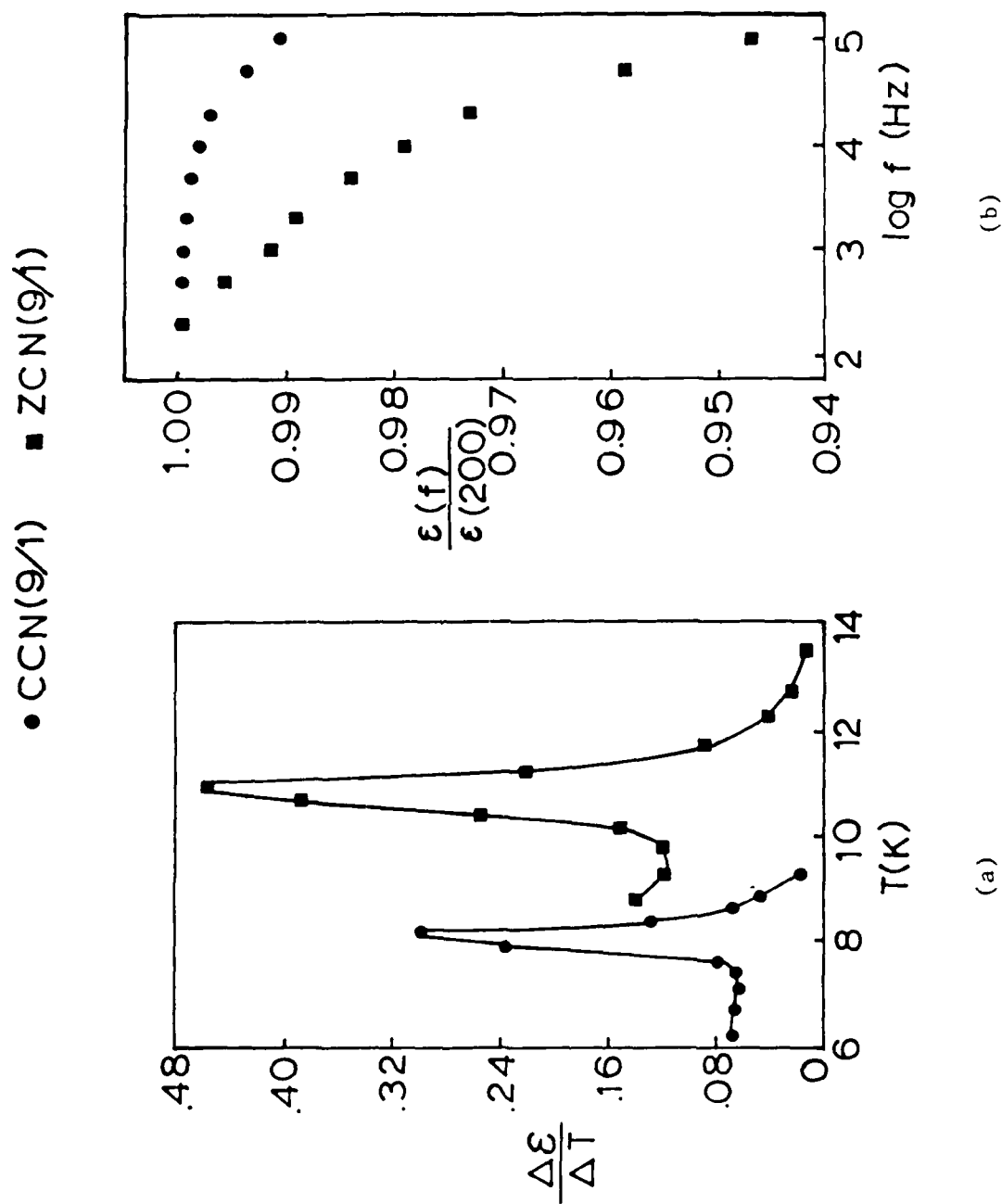


Figure 4-2. (a) Variation of the derivative $\Delta \epsilon / \Delta T$ with temperature in the neighborhood of the specific heat maxima. (b) Frequency dependence of ϵ near the temperature of the specific heat maxima.

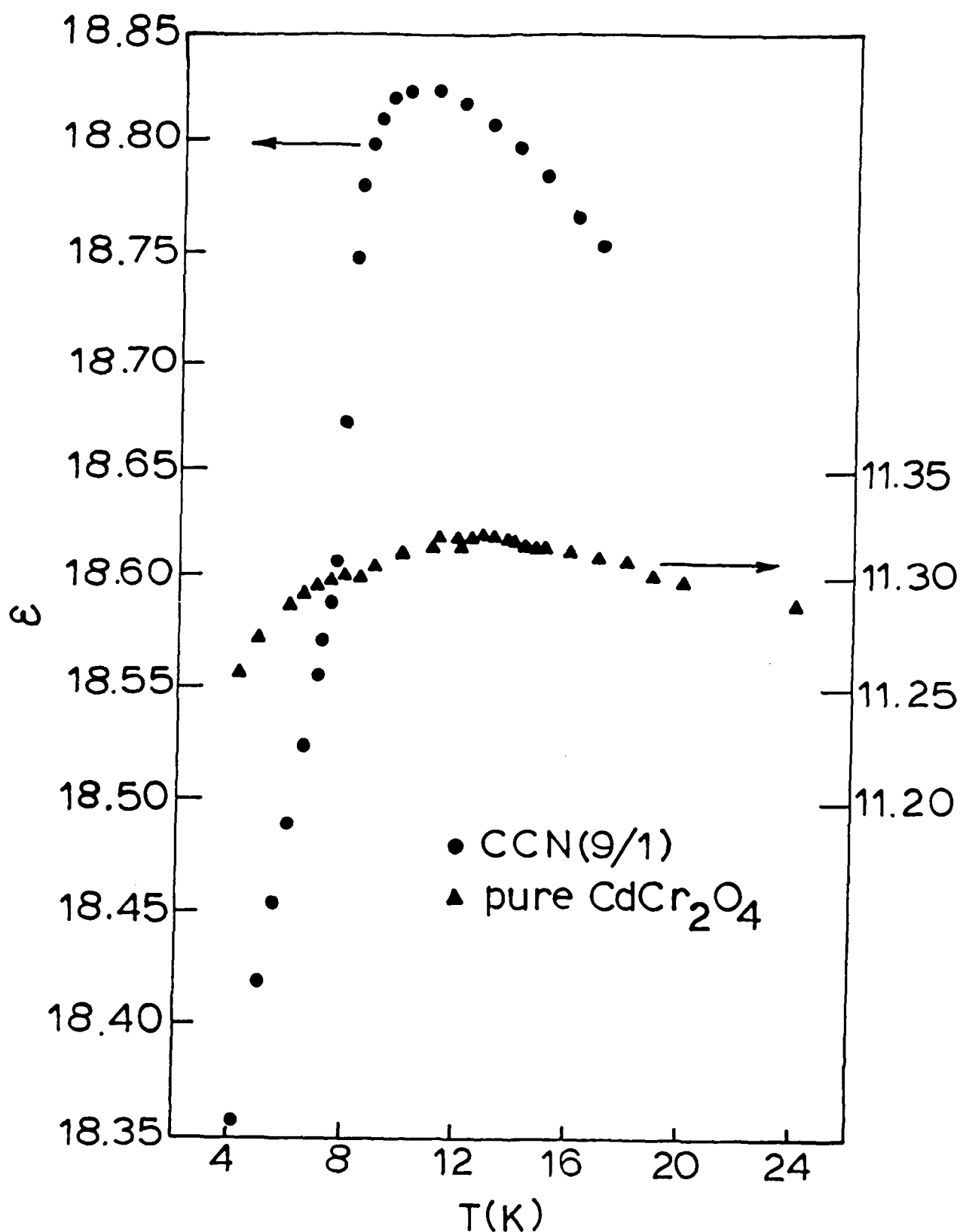


Figure 4-3. Comparison of dielectric data measured on CCN(9/1) and CdCr_2O_4 . The absence of structure in the data for the latter material correlates with a similar lack of structure in the specific heat data (see Fig. 4-9).

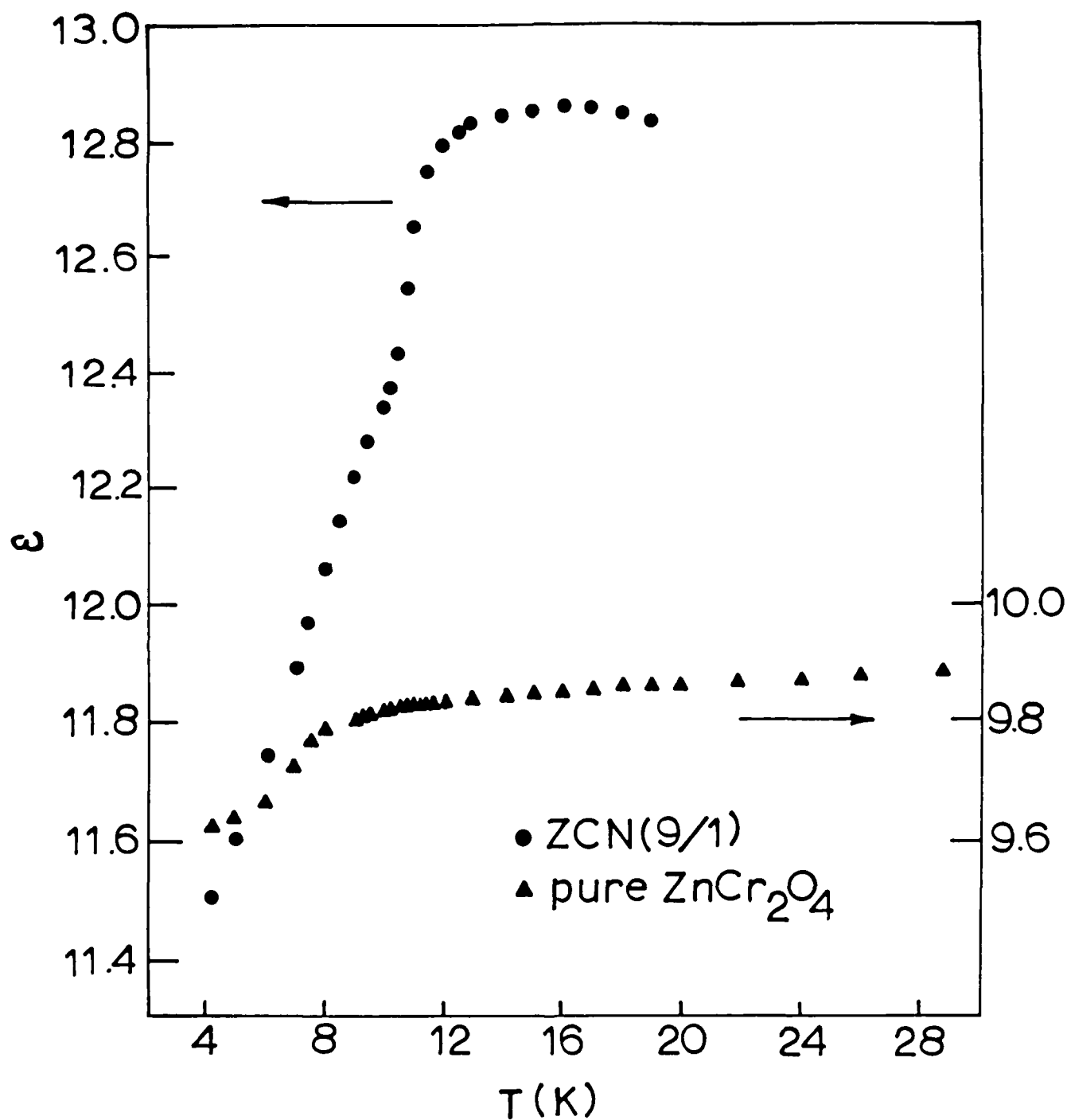


Figure 4-4. Comparison of dielectric data measured on ZCN(9/1) and ZnCr₂O₄. The structure in the latter data is small, but this material exhibits a substantial maximum in the specific heat (see Fig. 4-10).

above this rise as in ZCN(9/1). The anomalous rise in the dielectric constant coincides with the peak in the specific heat for the spinel + columbite samples. There is no correlation in either of the pure materials between the specific heat data and dielectric constant data (see Figs. 4-9 and -10 below).

The three materials which show dielectric structure [i.e., CCN(9/1), ZCN(9/1) and ZnCr_2O_4] were measured at the National Magnet Laboratory at MIT. In each case, the following procedure was followed. At zero field, the dielectric constant was measured as a function of temperature through the range of the dielectric structure. Then at a constant temperature slightly below the maximum in $\partial\epsilon/\partial T$ the dielectric constant was measured as a function of H-field. Holding the field constant at 15 T, another temperature sweep was made over the same temperature range as above.

At zero field, the temperatures were held constant using a capacitance-temperature controller sensing a field-independent capacitance thermometer (Lawless, 1971) in the probe. This thermometer was calibrated in zero field against a germanium thermometer during the first sweep. Then at $H \neq 0$, the controller could be set to the same known temperature points.

In the following data, it will be noted that the absolute dielectric constants are slightly higher in each case compared to the original data of Figs. 4-3 and 4-4. This is due to a slightly larger lead capacitance in the MIT probe ($\sim 0.1 - 0.2$ pF). No correction was made for this effect. In each case, the samples were identically the same, and the dielectric constants of the pure spinels were corrected as above for density.

Figures 4-5, 4-6, and 4-7 show the results of these measurements where in each figure the main graph shows the results of the two temperature sweeps at 0 T and 15 T and the inset shows the field dependence of the change in dielectric constant at constant temperature. For both the pure ZnCr_2O_4 and the CCN(9/1), the dielectric constant is consistently higher across the full temperature range, while the dielectric constant of ZCN(9/1) at 15 T compared to 0 T is first above at low

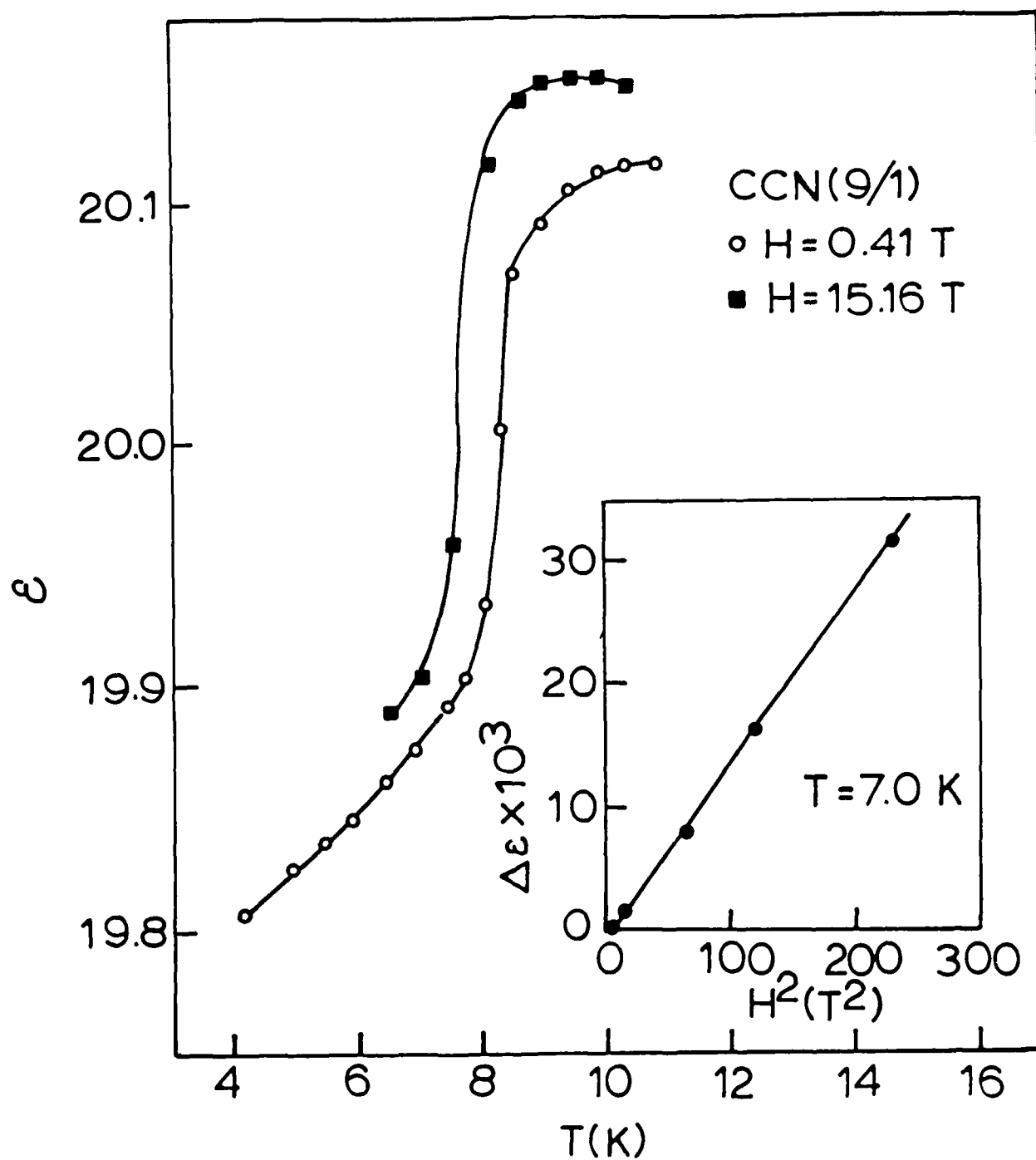


Figure 4-5. Magnetic field dependence of the dielectric constant of CCN(9/1) in the neighborhood of the specific heat maximum at 8 K.

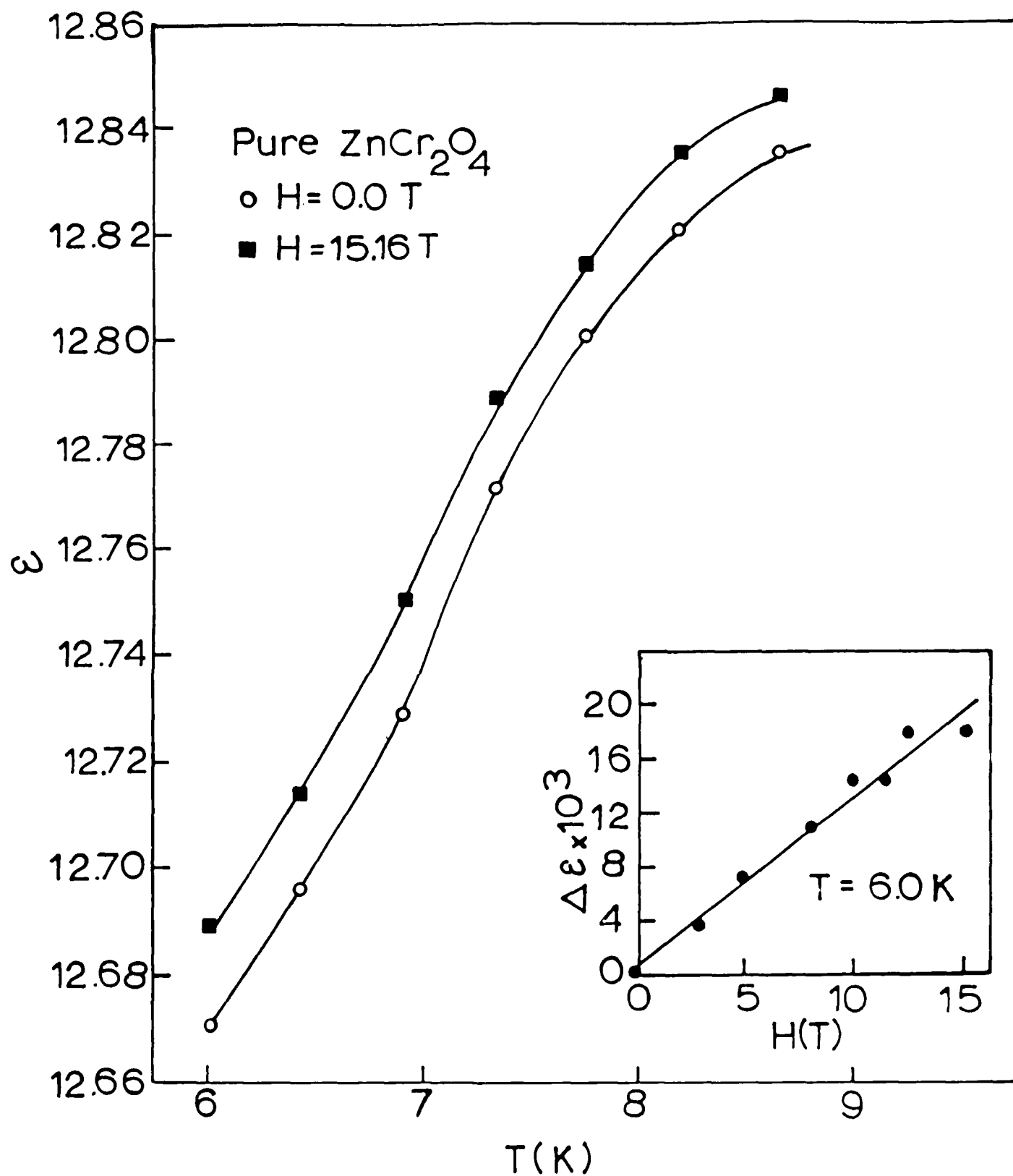


Figure 4-6. Magnetic field dependence of the dielectric constant of ZnCr_2O_4 .

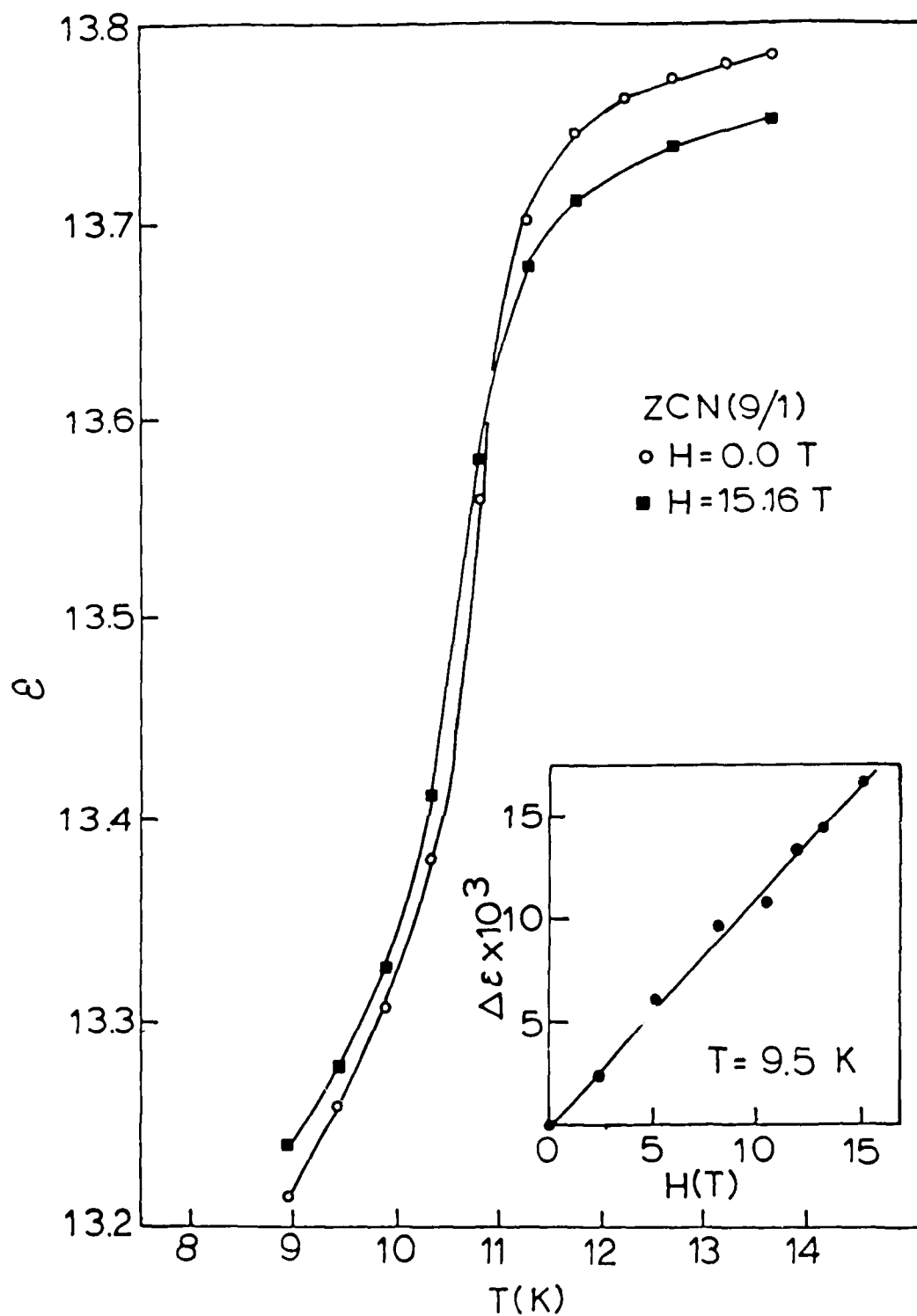


Figure 4-7. Magnetic field dependence of the dielectric constant of ZCN(9/1) in the neighborhood of the specific heat maximum.

temperatures, then below at high temperatures. The inset graphs indicate that $\Delta\epsilon$ in CCN(9/1) is proportional to H^2 while $\Delta\epsilon$ in both of the Zn samples is proportional to H with the slope approximately the same in both cases [1.09×10^{-3} (1/T) for ZCN(9/1) and 1.26×10^{-3} (1/T) for pure ZnCr_2O_4].

The derivatives $\Delta\epsilon/\Delta T$ for the temperature sweeps in a magnetic field are plotted in Fig. 4-8 as a function of temperature for both of the spinel/columbite samples. The peak in $\Delta\epsilon/\Delta T$ in ZCN(9/1) has not shifted in field while the peak for CCN(9/1) has shifted by approximately 0.5 K. From previous work, it has been found that the temperatures of the specific heat peaks of CCN(9/1) and ZCN(9/1) do not shift in field.

It is an open question what role the columbite phase plays in each case; it is possible that denser samples of the pure spinels would more closely mimic the spinel/columbite behavior. This possibility is suggested by Figs. 4-3 and 4-4 where the more dense (70%) ZnCr_2O_4 showed structure closer to the 9/1 samples than the less dense (54%) CdCr_2O_4 .

One possibility to consider is a magnetic phase transition occurring in the spinel component accompanied by a volume change which in turn applies a pressure to the columbite phase changing the dielectric constant of the columbite phase by electrostriction. The dielectric changes are then only indirectly probing the phase transition in the spinel. To analyze this situation, consider the free energy of the columbite phase as a function of polarization P and hydrostatic pressure, p , in the Ginzburg-Landau-Devonshire formalism,

$$A(P,p) = \frac{1}{2}\chi_0 P^2 + \frac{1}{4}\xi P^4 + \dots + \frac{1}{2}(Q_{11} + 2Q_{12})pP^2 + \dots$$

where Q_{11} and Q_{12} are electrostrictive coefficients. For $P = 0$,

$$\chi_p = 4\pi/\epsilon_p = \partial^2 A / \partial P^2 = \chi_0 + (Q_{11} + 2Q_{12})p + \dots$$

Therefore,

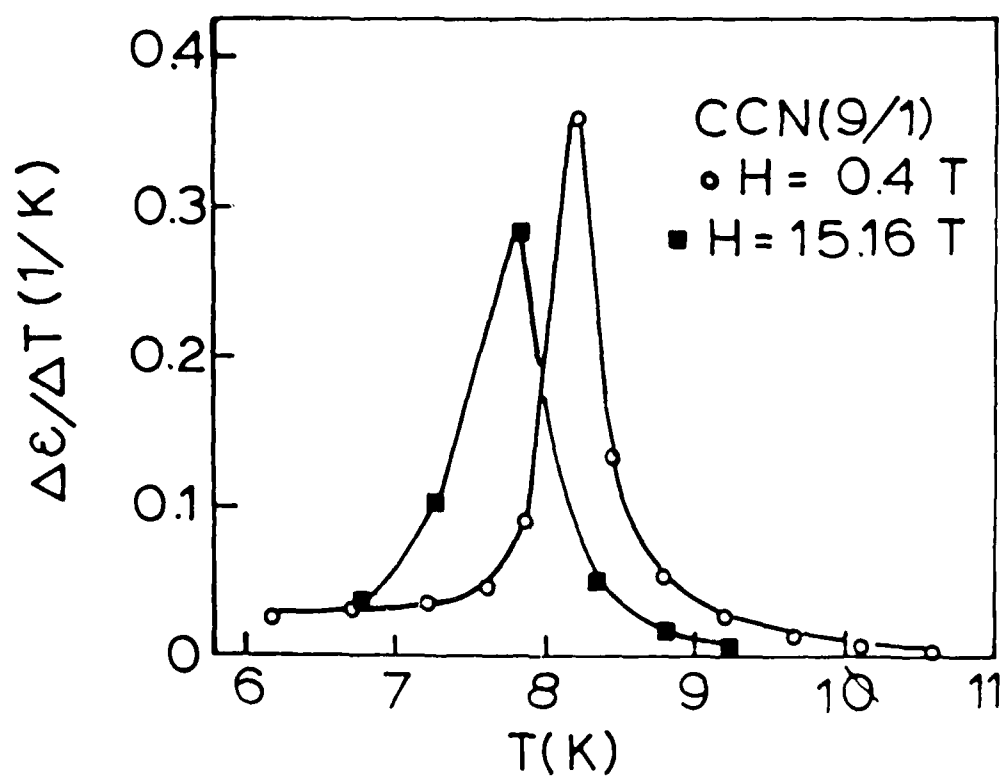
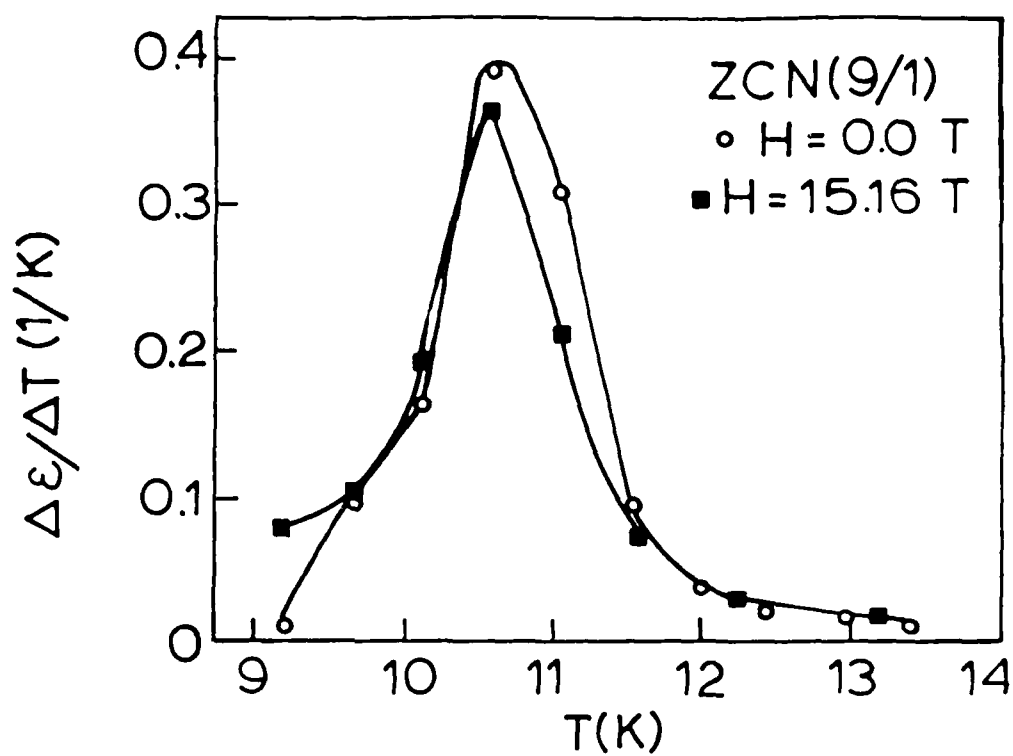


Figure 4-8. Magnetic field dependence of the maxima in $\Delta\epsilon/\Delta T$ for CCN(9/1) and ZCN(9/1).

$$4\pi/\epsilon_p = 4\pi/\epsilon_o + qp \quad (4-1)$$

where $q = Q_{11} + 2Q_{12}$ and the subscripts on ϵ refer to pressure. Here, p in Eq.(4-1) is the pressure exerted on the columbite phase by the spinel phase.

Now consider three general types of phase transitions in the spinel phase and use Eq.(4-1) to predict the behavior of $\epsilon(T)$. In a first-order transition the pressure will be a step function with a cut-off at the transition temperature T_N . From Eq.(4-1), ϵ will also change in a step pattern. Although there is a sudden rise in the dielectric constant of both (9/1) mixtures, this model does not explain either the maxima in ϵ in the (9/1) samples nor the rise in ϵ in the pure $ZnCr_2O_4$ sample.

Next consider a second-order transition with

$$p \propto (T_N - T)^{1/2}.$$

Using Eq.(4-1),

$$\partial\epsilon_p/\partial T \propto \epsilon_p^2/(T_N - T)^{1/2}.$$

Here $\partial\epsilon/\partial T$ stays finite at T_N because of the presence of higher order terms in the free energy expansion. Again, this case does not correspond to the experimental results.

The third case is a distributed phase transition with mechanical relaxation where approximately

$$p \propto \exp[-\alpha(T_N - T)^2]$$

Then, using Eq.(4-1):

$$\partial\epsilon/\partial T \propto (T_N - T) \exp[-\alpha(T_N - T)^2].$$

In this case an extremum occurs in ϵ at $T = T_N$, and a change in sign is predicted for $\Delta\epsilon/\Delta T$ at $T = T_N$.

None of these cases fits the experimental observations, and we are left with the conclusion that the columbite phases in CCN(9/1) and ZCN(9/1) probably do not play a role in these

dielectric anomalies. Consequently, these dielectric anomalies are associated with a coupling between the optic modes and spin systems within the spinel phase.

B. Specific Heat Measurements

As mentioned in Section III above, compacted disks of the pure spinel powders were successfully formed at 1290°C for 1 hr in the case of CdCr_2O_4 , 1650°C for 1 hr for ZnCr_2O_4 . Weight changes were negligible ($\sim +1$ and -3% , respectively).

Specific heat samples were prepared as follows: Two disks of CdCr_2O_4 were first grooved across the diameter, and these grooved faces were then bonded together to form the basic sample. Similarly for ZnCr_2O_4 . The grooved faces thus formed a slot for the insertion of a carbon-chip thermometer. A generous amount of copper foil was used in the sample assembly (e.g., between bonded faces, on the disk periphery, etc.) to provide good thermal diffusion, as later proved to be the case in the actual experiments. Nonetheless, the specific heats of the disks were large enough that the addenda contributions were very small ($< 5\%$) despite the copper-foil additions.

The densities of the starting disks were as follows:

CdCr_2O_4 : 4.359 ± 0.009 ($74.4 \pm 0.1\%$ of theoretical)

ZnCr_2O_4 : 3.865 ± 0.021 ($72.0 \pm 0.4\%$ of theoretical),

using the NBS XRD densities (5.862 and 5.367, respectively). It is worth noting that the density of a free powder is ~ 65 - 68% (sphere close-packing), so the densification of these disks is only marginally larger than that of the free powders. It should also be pointed out that these disks proved surprisingly hard to cut, despite the marginal densification.

Specific heat data were measured 2-34 K by the dynamic pulse technique in the adiabatic calorimeter, and the two samples were measured simultaneously.

Specific heat data, C vs. T , for the CdCr_2O_4 disk are shown in Fig. 4-9 compared to the specific heat of $\text{CCN}(9/1)$. In the

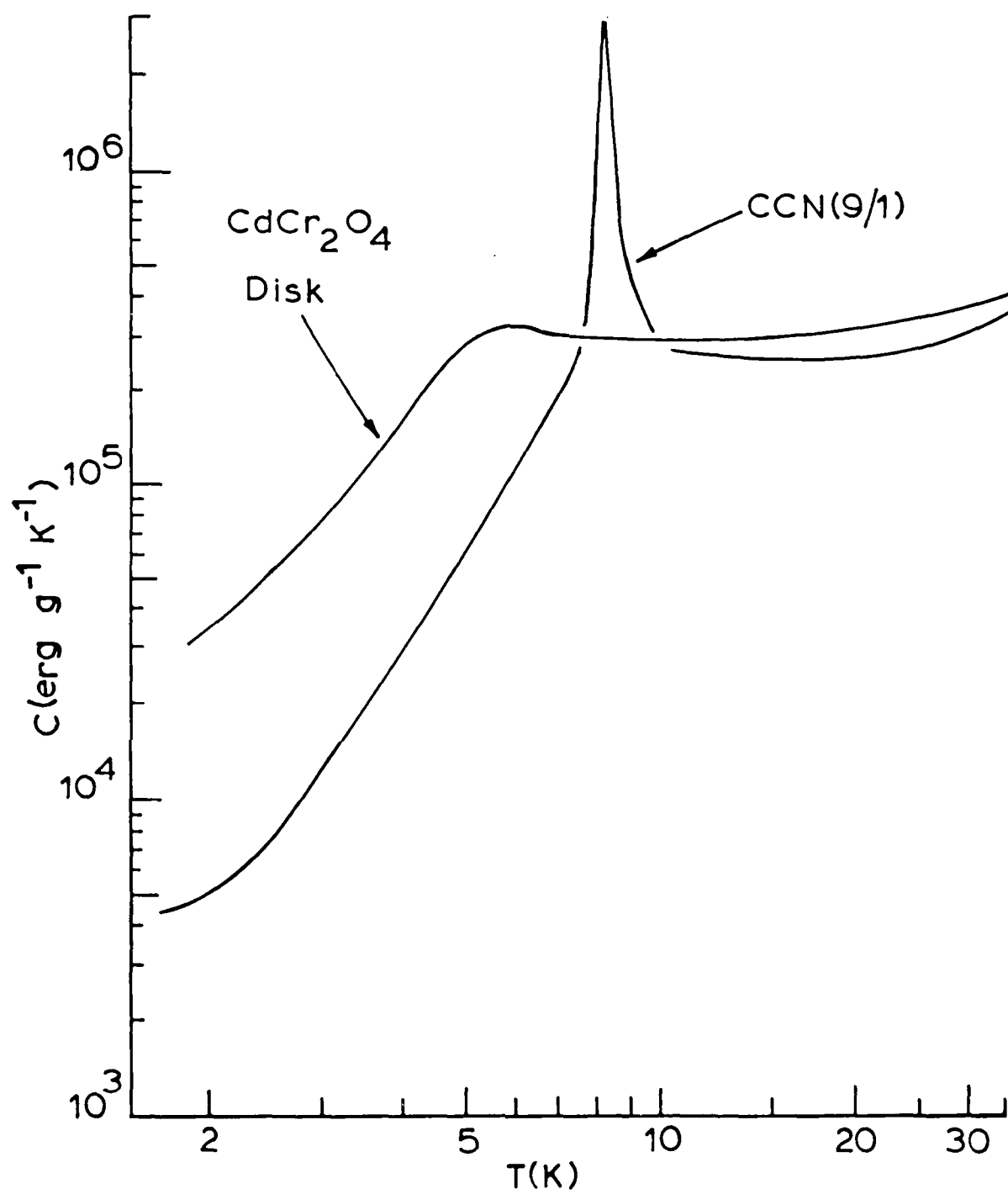


Figure 4-9. Comparative specific heat data for CdCr_2O_4 and $\text{CCN}(9/1)$.

spinel disk, a small, broad maximum in C occurs at 5.8 K, in good agreement with the χ -data in Fig. 5-x below. However, this maximum is smaller and much broader than the C-maximum in CCN(9/1) at 8.0 K in Fig. 2-1.

The corresponding specific heat data for the ZnCr_2O_4 spinel and ZCN(9/1) are shown in Fig. 4-10. Here a different picture emerges, as the spinel disk has a distinct peak in C at 9.7 K, compared to the C-peak in ZCN(9/1) at 10.5 K. The temperature of the C-maximum for the ZnCr_2O_4 spinel is in good agreement with the χ -data in Fig. 5-y below.

The behavior of C/T^3 often provides useful insights, and in Figs. 4-11 and 4-12 are shown C/T^3 -data for the CdCr_2O_4 and ZnCr_2O_4 materials, respectively. In both of these plots are shown data for the disks measured here plus separated data for the spinel phases in CCN(9/1) and ZCN(9/1) from Fig. 2-1. In all cases in Figs. 4-11 and 4-12, there is a rapid rise in C/T^3 with decreasing temperature at the lowest temperatures, and this has previously been attributed to a Schottky term due to free spins. Using this interpretation, one would say from Fig. 4-11 that the density of free spins in the CdCr_2O_4 compacted disk is $\sim 6-7$ times larger than for the spinel phase in CCN(9/1). However, this picture does not agree with the χ -data in Fig. 5-x below. From Fig. 4-12 for the ZnCr_2O_4 materials, one would speculate that the density of free spins in the ZnCr_2O_4 compacted disk is ~ 2 times larger than for the spinel phase in ZCN(9/1), and this interpretation is not necessarily out of line with the χ -data in Fig. 5-y below.

It is interesting to observe how large the specific heat of the CdCr_2O_4 disk really is at the lowest temperatures. We previously determined a reliable Debye temperature for spinel CdCr_2O_4 , $\theta_D = 420$ K, and this means that the Debye limit is $(C/T^3)_D = 6.55 \text{ erg g}^{-1} \text{ K}^{-4}$. From Fig. 4-11 for the CdCr_2O_4 disk at the lowest temperatures, $C/T^3 \approx 3 \times 10^3$ -- i.e., the Debye contribution is only $\sim 0.2\%$.

It is difficult to reconcile the C-data reported here and the χ -data. First, given the very slight densification of these

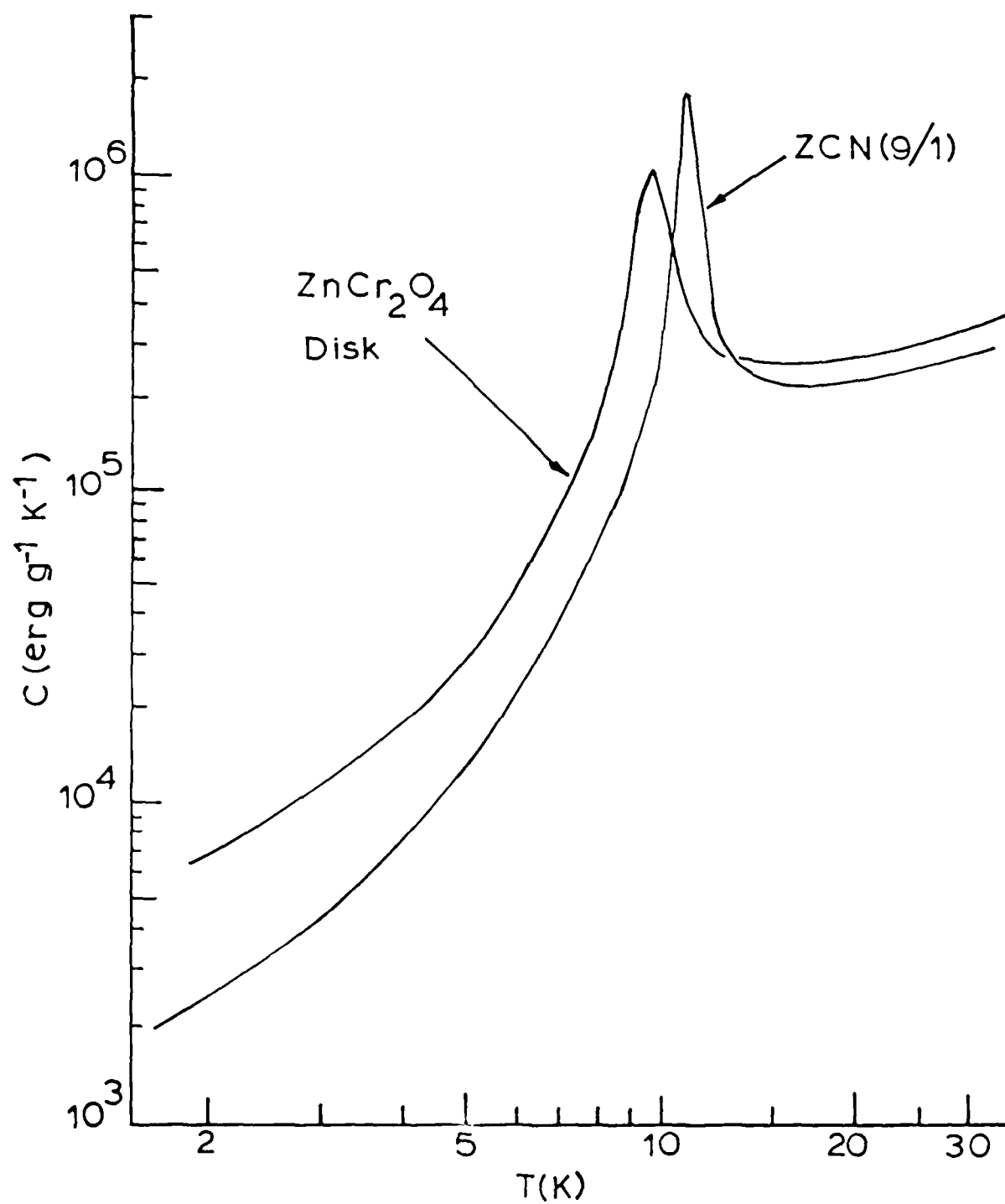


Figure 4-10. Comparative specific heat data for ZnCr_2O_4 and $\text{ZCN}(9/1)$.

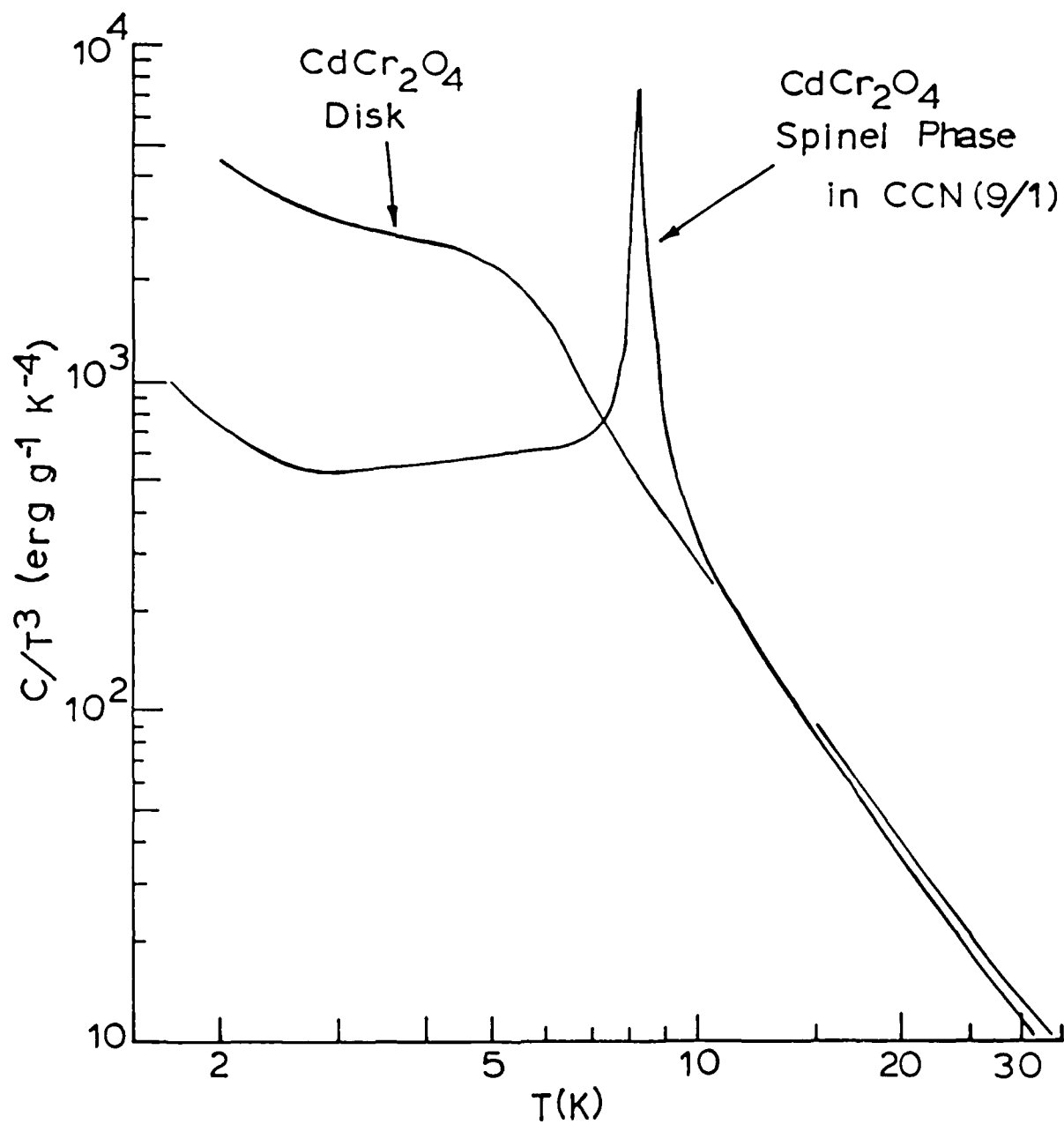


Figure 4-11. Comparative specific heat data plotted as C/T^3 for CdCr_2O_4 and for the CdCr_2O_4 phase in $\text{CCN}(9/1)$.

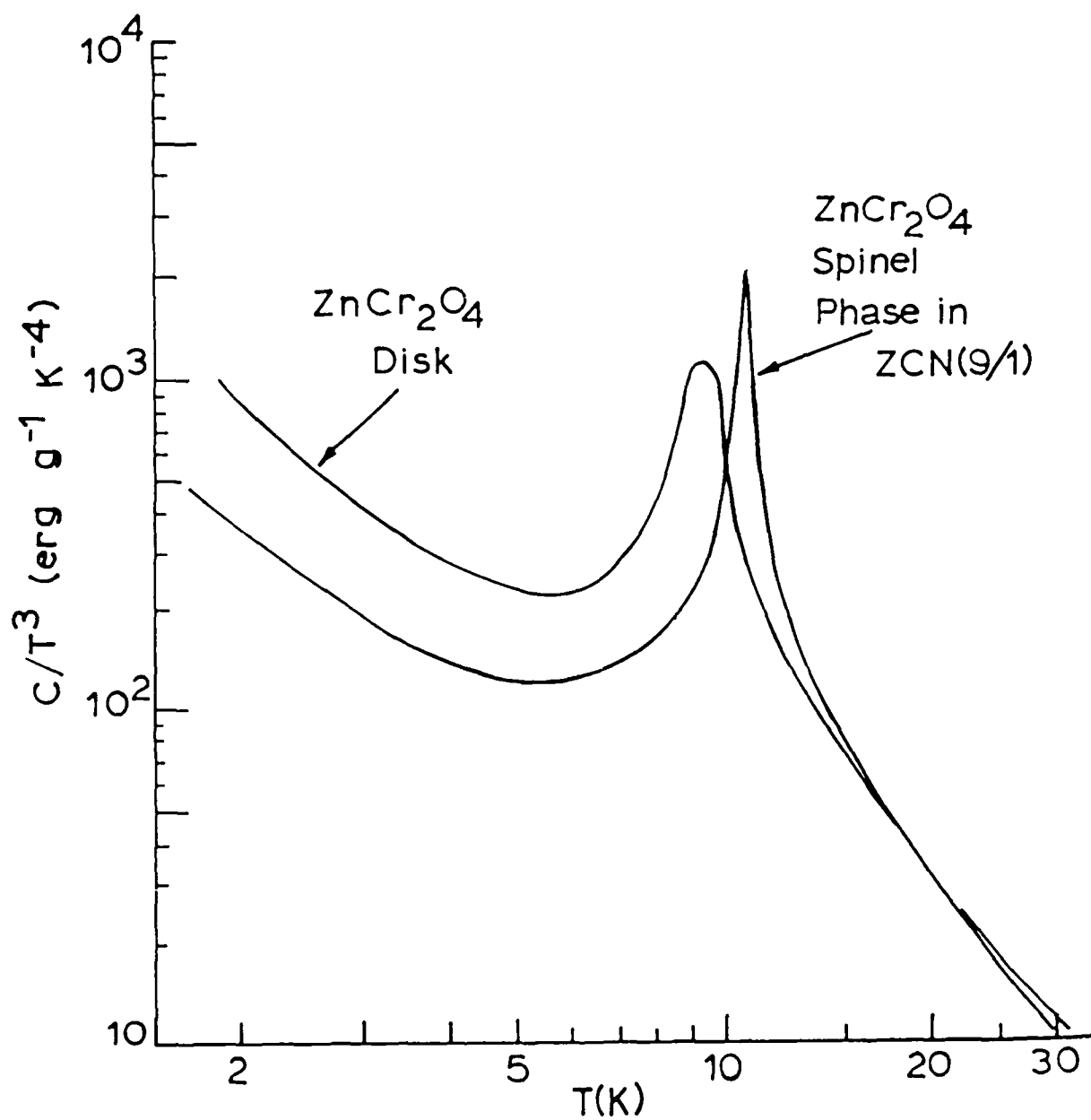


Figure 4-12. Comparative specific heat data plotted as C/T^3 for ZnCr_2O_4 and for the ZnCr_2O_4 phase in ZCN(9/1).

spinel disks, it is reasonable to consider these disks and the respective powders as being essentially identical (e.g., same surface area). Going further, the grain sizes in the powder and disk are most likely also identical, for the same reason. Electron microscope studies are needed here. The broad C-peaks in Figs. 4-9 and 4-10 may be due to short correlation lengths in the disks, since it is believed that the spinel grains in CCN(9/1) and ZCN(9/1) are quite large ($\sim 10\mu\text{m}$) and have long correlation lengths, leading to sharp C-peaks.

However, the χ -data in Section V below consistently show that the density of free spins increases as the surface area decreases (e.g., powders have few free spins). On the other hand, the very large value of C/T^3 for the CdCr_2O_4 disk at the lowest temperatures in Fig. 4-11 suggests a very large density of free spins.

Magnetic Field Dependence. The magnetic field dependence of the specific heats of the CdCr_2O_4 and ZnCr_2O_4 disks were measured in a field of 10 T at the National Magnet Laboratory. A so-called drift technique developed by CeramPhysics was used in these measurements (Lawless et al., 1982).

Magnetic-field-dependent specific heat data in the neighborhood of T_N for the CdCr_2O_4 and ZnCr_2O_4 disks are shown in Figs. 4-13 and 4-14, respectively, at $H = 10$ T and $H = 0$. In the paramagnetic regions, the 10 T field decreases the specific heat of CdCr_2O_4 by $\sim 35\%$, Fig. 4-13, and this is thermodynamically consistent with the magnetocaloric phase diagram shown in Fig. 4-24 below. That is, based on simple entropy arguments, magnetization heating requires that a magnetic field suppresses the specific heat.

However, a magnetic field increases the specific heat of ZnCr_2O_4 , Fig. 4-14, and this is thermodynamically inconsistent with the magnetocaloric data in Fig. 4-30 below.

Our interpretation here is that the carbon-chip thermometer on the ZnCr_2O_4 sample probably shifted in calibration in the 10 T field, leading to the inconsistent results in Fig. 4-14. Along

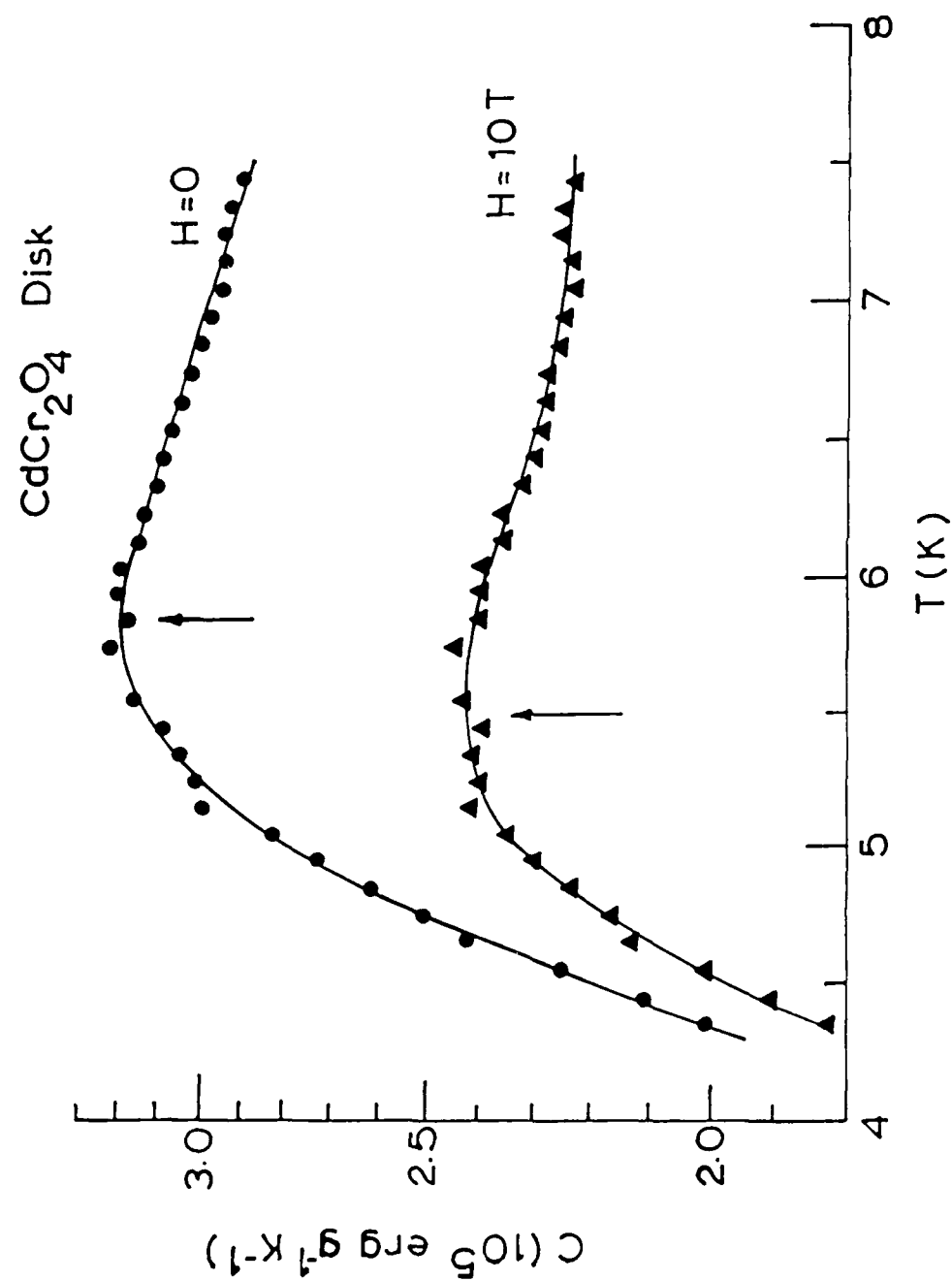


Figure 4-13. Specific heat of CdCr_2O_4 at $H = 0$ and $H = 10 \text{ T}$.

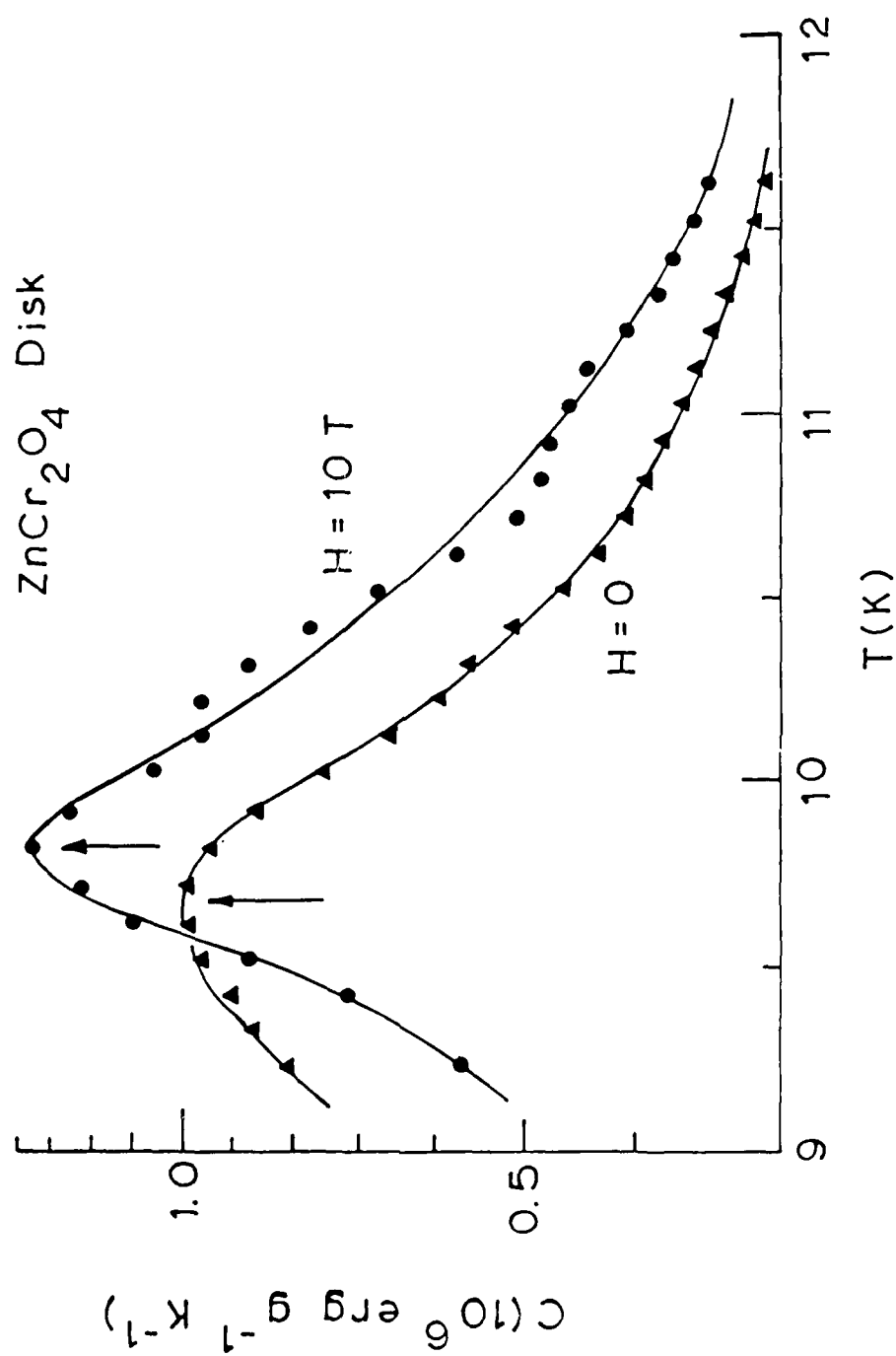


Figure 4-14. Specific heat of ZnCr_2O_4 at $H = 0$ and $H = 10 \text{ T}$.

this line, this thermometer was observed to shift in calibration during the magnetocaloric measurements (see below). Further support for this interpretation comes from the fact that a field suppresses T_N for an antiferromagnetic transition, as in Fig. 4-13, whereas the opposite is seen in Fig. 4-14.

This interpretation would seem to cast some doubt on the ZnCr_2O_4 magnetocaloric measurements below; however, there are major differences in the two experiments. First, calibration points were taken at practically all magnetocaloric set points, and there was internal consistency amongst the sets of magnetocaloric data. And second, magnetocaloric measurements involved ΔT 's.

Data Analyses. We now consider phenomenological analyses of the specific heat data for the pure spinels shown in Figs. 4-9 through 4-12 for comparison with similar analyses of the data for the spinel phases in CCN(9/1) and ZCN(9/1) (Eckels et al., 1985). To review, the spacing of quantized energy levels gives rise to a so-called Schottky specific-heat term. For a two-level system where δ is the energy separation, for example, the high-temperature ($T \gg \delta$) form of the Schottky term is

$$C_{\text{Sch}} = nRg_0g_1(g_0 + g_1)^{-2} (\delta/T)^2 \quad (4-2)$$

where g_0 and g_1 are the degeneracies of the two levels, and n is the number of level systems per formula weight. The form of Eq.(4-2), $C_{\text{Sch}} \propto T^{-2}$, is correct for the general Schottky term, and in the Debye limit for the lattice contribution (i.e., $C_l \propto T^3$) a plot of

$$CT^2 = mT^5 + b \quad (4-3)$$

is a straight line where m is related to the Debye temperature (θ_D) and $b \neq 0$ is the coefficient of the Schottky term.

A subtlety enters the m -coefficient in Eq.(4-2), as follows: If an antiferromagnetic transition occurs, then at temperatures

below T_N a T^3 spin-wave contribution to the specific heat is present, and in Eq.(4-3) $m = m_D + m_{sw}$, where m_D is related to the Debye temperature and m_{sw} is the coefficient of the spin-wave term. For a ferromagnetic transition, the spin-wave contribution varies as $T^{3/2}$.

Thus, these Schottky analyses of specific heat data yield a great deal of information: (1) The b -coefficient in Eq.(4-3) yields data for $n\delta^2$ from Eq.(4-2), given certain assumptions regarding g_0 and g_1 ; and (2) The m -coefficient in Eq.(4-3) yields information on both the Debye temperature and the presence of antiferromagnetic spin waves.

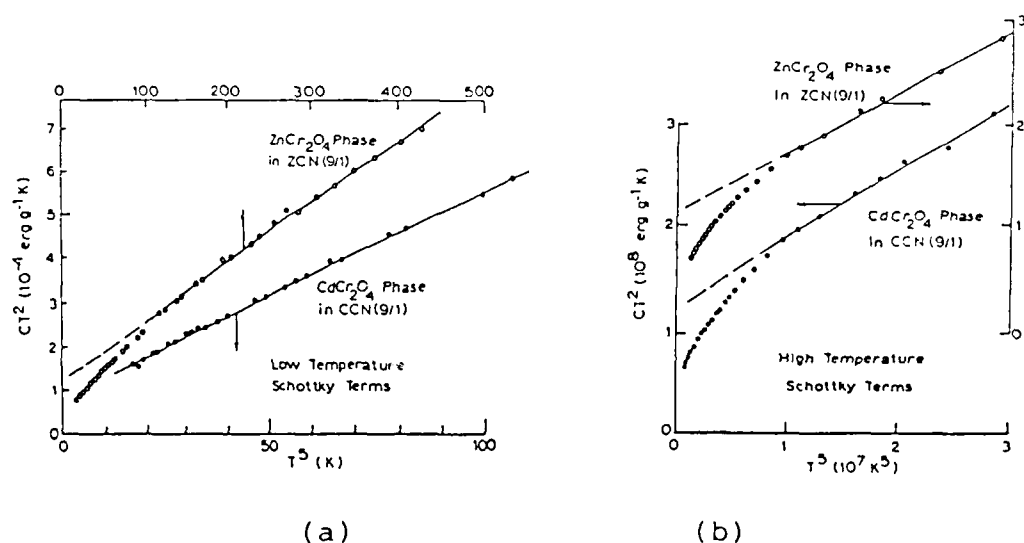


Figure 4-15. Schottky analyses at (a) low and (b) high temperatures for the spinel phases in the spinel + columbite densified ceramics CCN(9/1) and ZCN(9/1).

Examples of these types of Schottky analyses have previously been performed for the CdCr_2O_4 and ZnCr_2O_4 spinel phases in the densified ceramics CCN(9/1) and ZCN(9/1), respectively, and these analyses are reproduced in Fig. 4-15 (Eckels *et al.*, 1985). Analyses at $T > T_N$, Fig. 4-15(b), are not complicated by spin-wave terms, whereas at $T < T_N$, Fig. 4-15(b), this complication may enter. Excellent fits to Eq.(4-3) are obtained in Fig. 4-15 with $b \neq 0$ (note that the deviations at the lower temperatures are due to the $T \gg \delta$ approximation), and we note in particular

that the excellent $T < T_N$ fits in Fig. 4-15(a) are strong evidence for antiferromagnetic transitions. We shall return below to the details of these fits.

Returning to Figs. 4-11 and 4-12, we note that the behavior of C/T^3 is basically the same at $T > T_N$ for the spinels whether in the compacted disks or as the spinel phases in the densified spinel + columbite ceramics. Likewise, at $T < T_N$ there is a marked rise in C/T^3 with decreasing temperature in all cases. Therefore, by analogy with the data in Fig. 4-15, Schottky analyses at $T < T_N$ and $T > T_N$ were carried out for the specific heat data measured on the compacted disks of CdCr_2O_4 and ZnCr_2O_4 and these data are shown in Figs. 4-16 and 4-17, respectively. Once again, excellent plots according to Eq.(4-3) are obtained.

The results of least-squares fittings of the data for all materials are summarized in Table 4-1. In all these analyses, the assumption $g_0 = g_1$ in Eq.(4-2) has been made.

Table 4-1
Schottky Analyses, Eq.(4-3)*

Quantity	<u>CdCr_2O_4</u>		<u>ZnCr_2O_4</u>	
	In CCN(9/1)	Disk	In ZCN(9/1)	Disk
m (High-T)	6.546	6.546	5.875	6.765
m (Low-T)	470.6	2764	136.1	2182
θ_D (High-T)	420	420	463	442
θ_D (Low-T)	101	56	162	139
$n\delta^2$ (High-T)	1679	2168	1264	1377
$n\delta^2$ (Low-T)	0.109	0.761	0.135	0.637
$\frac{n_s C_a}{k/2Js}^3$	1.57×10^{-3}	9.30×10^{-3}	3.66×10^{-4}	6.11×10^{-3}

*Units are consistent with the specific heat in units of $\text{erg g}^{-1} \text{K}^{-1}$; note also that $g_0 = g_1$ in Eq.(4-2).

Also included in Table 4-1 are data for the spin-wave specific heat term,

$$C_{sw} = n_s R C_a (k/2Js)^3 T^3 \quad (4-4)$$

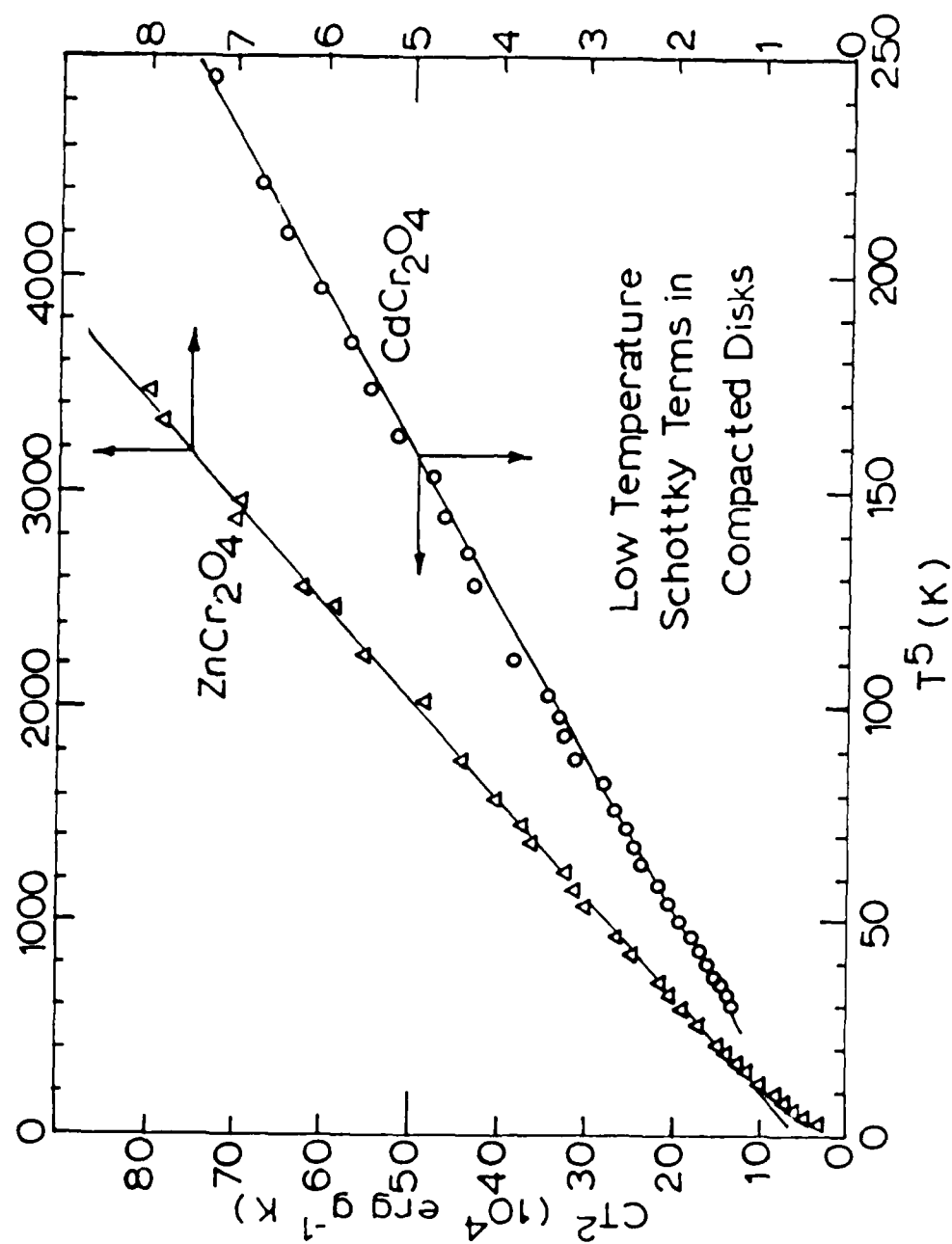


Figure 4-16. Schottky fits to the $T < T_N$ specific heat data for CdCr_2O_4 and ZnCr_2O_4 according to Eq. (43).

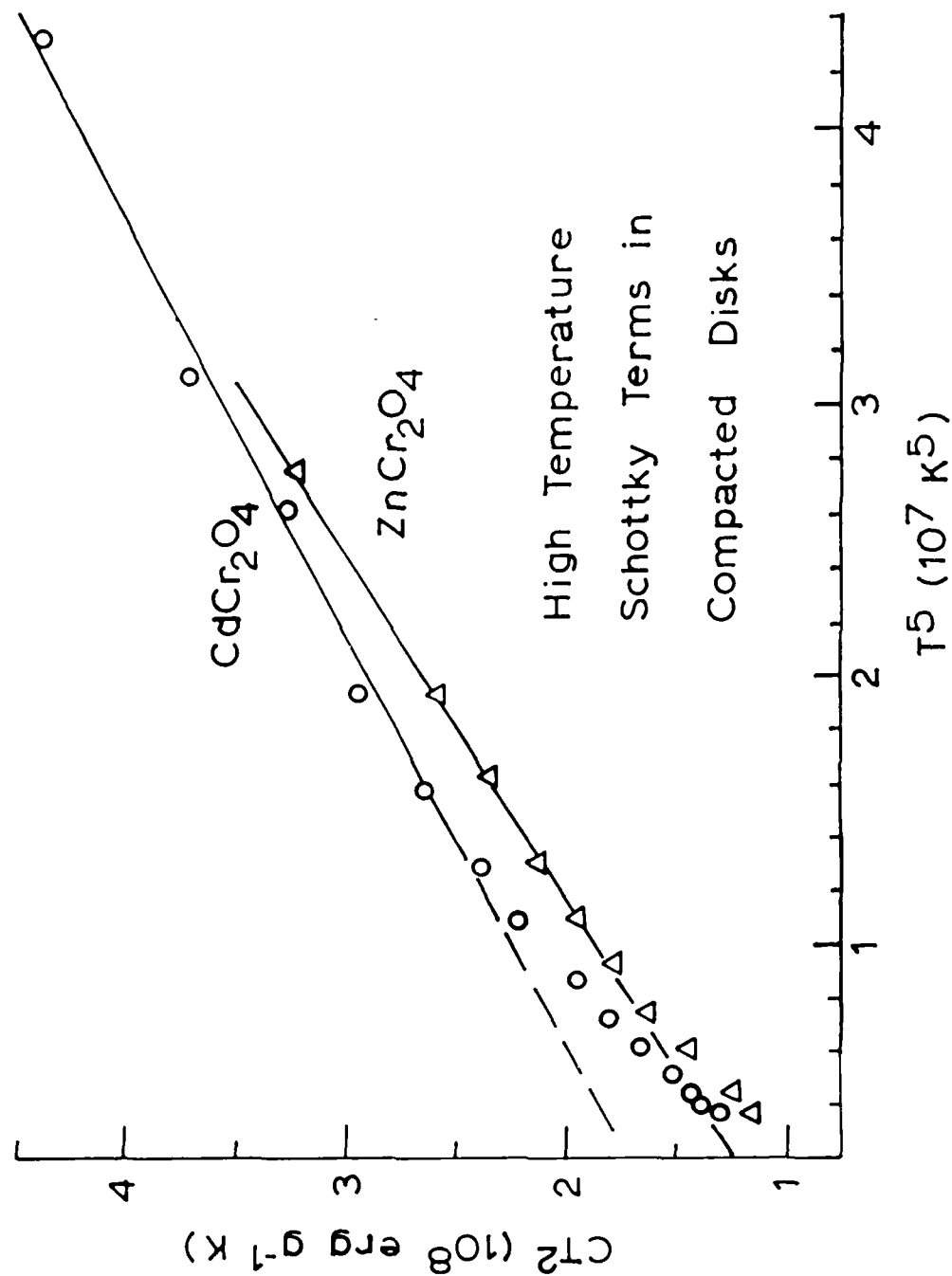


Figure 4-17. Schottky fits to the $T > T_N$ specific heat data for CdCr_2O_4 and ZnCr_2O_4 according to Eq.(4-3).

computed from the differences in the m -coefficients [i.e., $m = m_D + m_{sw} = m_D + n_s R C_A (k/2Js)^3$], where n_s is the density of spin waves.

A rather staggering amount of experimental data analyses are summarized in Table 4-1, and these results fall into several separate categories, as follows:

Debye Temperatures. The agreement between the θ_D 's for the spinels from the high-temperature analyses are very good (exact in the case of CdCr_2O_4). For comparison, the Lindemann equation relates θ_D to other properties.

$$\theta_D \approx B(T_m/MV^{2/3})^{1/2} \quad (4-5)$$

where T_m is the melting point, M is the molecular weight, V is the molecular volume, and B is constant (≈ 115). Adopting 1800°C melting points for both spinels, we find from Eq.(4-5) that

$$\begin{aligned} \theta_D (\text{CdCr}_2\text{O}_4) &= 414 \text{ K} \\ \theta_D (\text{ZnCr}_2\text{O}_4) &= 469 \text{ K} \end{aligned}$$

in remarkably good agreement with the data in Table 4-1 [Note in this regard that changing T_m by $\pm 200^\circ\text{C}$ in Eq.(4-5) changes θ_D by only $\pm 5\%$]. We also point out that these θ_D 's are large enough to justify the T^3 approximation for the lattice specific heats implicit in Fig. 4-17.

The Debye temperatures in Table 4-1 from the low-temperature Schottky analyses are clearly too small, and this is firm evidence for antiferromagnetic spin waves.

Schottky Terms, $T > T_N$. The Schottky specific heat term in the paramagnetic phase ($T > T_N$) is due to the spins that partake in the transition at T_N , and it seems reasonable to assume that δ is the same for, say, ZnCr_2O_4 in both the compacted disk and as the spinel phase in the spinel + columbite densified ceramic.

This argument can be generalized further by observing that whatever the form of the actual Schottky term, the high-temperature expansion will always have the functional form, $C_{Sch} \propto n/T^2$, where n is the density of contributing spins. Thus, δ^2 becomes a constant of proportionality which is assumed the same for the two forms of $ZnCr_2O_4$ (and $CdCr_2O_4$). Proceeding along this line, the ratio of the $n\delta^2$ values should correspond to the ratio of spin densities in the two forms, and from Table 4-1 we find:

Table 4-2	
Paramagnetic Spin Densities, $T > T_N$	
Spinel	$n(\text{Disk})/n(\text{spinel} + \text{columbite})$
$CdCr_2O_4$	1.29
$ZnCr_2O_4$	1.09

There is satisfactory agreement between the contributing spin densities in the two forms of $ZnCr_2O_4$ in Table 4-2 (i.e., $\sim \pm 5\%$), and along this line we note the similarities in the specific heat maxima in Fig. 4-10 where the two curves appear shifted by about 1-2 K. On the other hand, the magnetocaloric ΔT_r phase diagram at 10 T in Fig. 4-31 below for the two forms of $ZnCr_2O_4$ suggests that the spin density in the compacted disk is ~ 2 times larger than the spinel + columbite ceramic. However, the magnetocaloric data reflect the total spin density whereas the $T > T_N$ Schottky term reflects the spins partaking in the transition at T_N .

For $CdCr_2O_4$, the Table 4-2 data indicate that about 30% more spins partake in the transition in the compacted disk than in the spinel:columbite ceramic.

Schottky Terms, $T < T_N$. Below the transition it is reasonable to assume that the free spins give rise to the Schottky term. Proceeding as above, we find for the ratio of free-spin densities:

Table 4-3

<u>Free Spin Densities, $T < T_N$</u>	
<u>Spinel</u>	<u>$n(\text{Disk})/n(\text{Spinel} + \text{Columbite})$</u>
CdCr_2O_4	6.98
ZnCr_2O_4	4.72

Here, we find a wide disparity in the free-spin densities between the two forms of both CdCr_2O_4 and ZnCr_2O_4 . The origin of these disparities is simply the very large differences between the specific heats of the compacted disks and the spinel + columbite ceramics in Figs. 4-9 and 4-10.

Our interpretation of these $T < T_N$ Schottky terms may be incorrect, for two complementary reasons: (1) The susceptibility data clearly show that the spinel + columbite ceramics have much larger free spin densities compared to the powders (see Section V); and (2) The magnetocaloric phase diagrams below support these susceptibility data.

The question then is the origin of these $T < T_N$ Schottky terms, since in the simple model of the two-spin systems the correlated spins contribute the T^3 spin-wave term, and the uncorrelated spins contribute the Schottky term. Possibly a third spin system is involved as suggested by some of the susceptibility data in Section V.

Spin-Wave Densities. As a final exercise, we consider the densities of the spin waves, n_s , from Table 4-1, as given by the ratios of $n_s C_a (k/2Js)^3$, and we recall that these densities come from the m -coefficients in Eq.(4-3) and are independent of the Schottky terms. Proceeding as above, we find

Table 4-4

<u>Spin Wave Densities</u>	
<u>Spinel</u>	<u>$n_s(\text{Disk})/n_s(\text{spinel} + \text{columbite})$</u>
CdCr_2O_4	5.92
ZnCr_2O_4	16.7

Here also we find a wide disparity in n_s from the two forms of these spinels. Recalling that n_s is also the density of antiferromagnetically correlated spins and that these spins give rise to magnetization cooling (see below), the Table 4-4 data suggest that such cooling phenomena should be much more pronounced in the compacted disks than in the spinel + columbite ceramics -- but this is not borne out in the magnetocaloric phase diagrams below. Along this line, however, we do note from Table 4-1 that the quantity $n_s C_a (k/2Js)^3$ is larger for $CdCr_2O_4$ than for $ZnCr_2O_4$, and magnetization cooling is always seen in the $CdCr_2O_4$ materials but not in the $ZnCr_2O_4$ materials, as we shall see shortly.

The data and analyses reported here support the earlier findings on the CCN(9/1) and ZCN(9/1) ceramics and lead to a clear picture of the specific heat properties of these spinels at temperatures well removed from T_N :

1. The lattice modes in $CdCr_2O_4$ and $ZnCr_2O_4$ are well characterized by Debye temperatures of 420 and about 450 K, respectively, in excellent agreement with the predictions of the Lindemann equation.
2. The excellent low-temperature Schottky fits leave little doubt regarding the presence of antiferromagnetic spin waves.
3. From the high-temperature Schottky fits, there is good agreement for the density of contributing spins in the two forms of $CdCr_2O_4$ (and $ZnCr_2O_4$).

Attempts have been made here to estimate the ratios of free spin densities below T_N and of antiferromagnetic spin waves between the two forms of $CdCr_2O_4$ and of $ZnCr_2O_4$. However, these estimates depend critically on the assumptions that δ , g_0 , g_1 , J , etc. are the same in the two forms, whereas in fact the stress conditions most probably are not the same.

C. Magnetocaloric Measurements

Measurements of magnetocaloric effects under adiabatic

conditions were performed over broad temperature ranges (2-20 K) and magnetic field ranges (< 15 T) on samples of CCN(9/1), ZCN(9/1), CdCr_2O_4 , and ZnCr_2O_4 . These were the same samples used for the specific heat measurements above.

Magnetocaloric measurements are a sensitive test of the contributing spin systems for the simple reason that uncorrelated spins give rise to magnetization heating, antiferromagnetically correlated spins give rise to magnetization cooling, and ferromagnetically correlated spins give rise to hysteretic effects.

There are several experimental details involved in these measurements (e.g., thermal time constants, addenda corrections, magnetoresistive effects in thermometry, etc.). These details have been adequately discussed previously (Eckels et al., 1985) and in Interim Reports and will not be discussed here.

In addition, a voluminous amount of magnetocaloric data were measured here, as reported in Interim Reports, and rather than present all these data in this Annual Report, we shall present selected and summary data.

Data Measured on CCN(9/1) and CdCr_2O_4 . Considering the Cd spinel materials first, the magnetocaloric ΔT_r data for CCN(9/1) measured above and below T_N are shown in Figs. 4-18 and 4-19, respectively. These are the reversible ΔT -components; the hysteretic components while small ($< 5\%$) have been separated out.

In a narrow temperature range around T_N (i.e., $7.5 < T < 9$), CCN(9/1) displays magnetization cooling; at all other temperatures CCN(9/1) displays magnetization heating. We note in particular in Fig. 4-18 that a $\Delta T \propto H$ relation is followed (inset), and at the lowest temperature $\Delta T/T \sim 100\%$.

Data at the lowest temperatures for CdCr_2O_4 are shown in Fig. 4-20, and here, in contrast to CCN(9/1), a significant hysteretic component is found which indicates a presence of ferromagnetically correlated spins. In addition, the data in Fig. 4-20 show a dependence on the ramp rate; that is, 40 s ramp rates were employed except for the 4-s rates indicated in Fig.

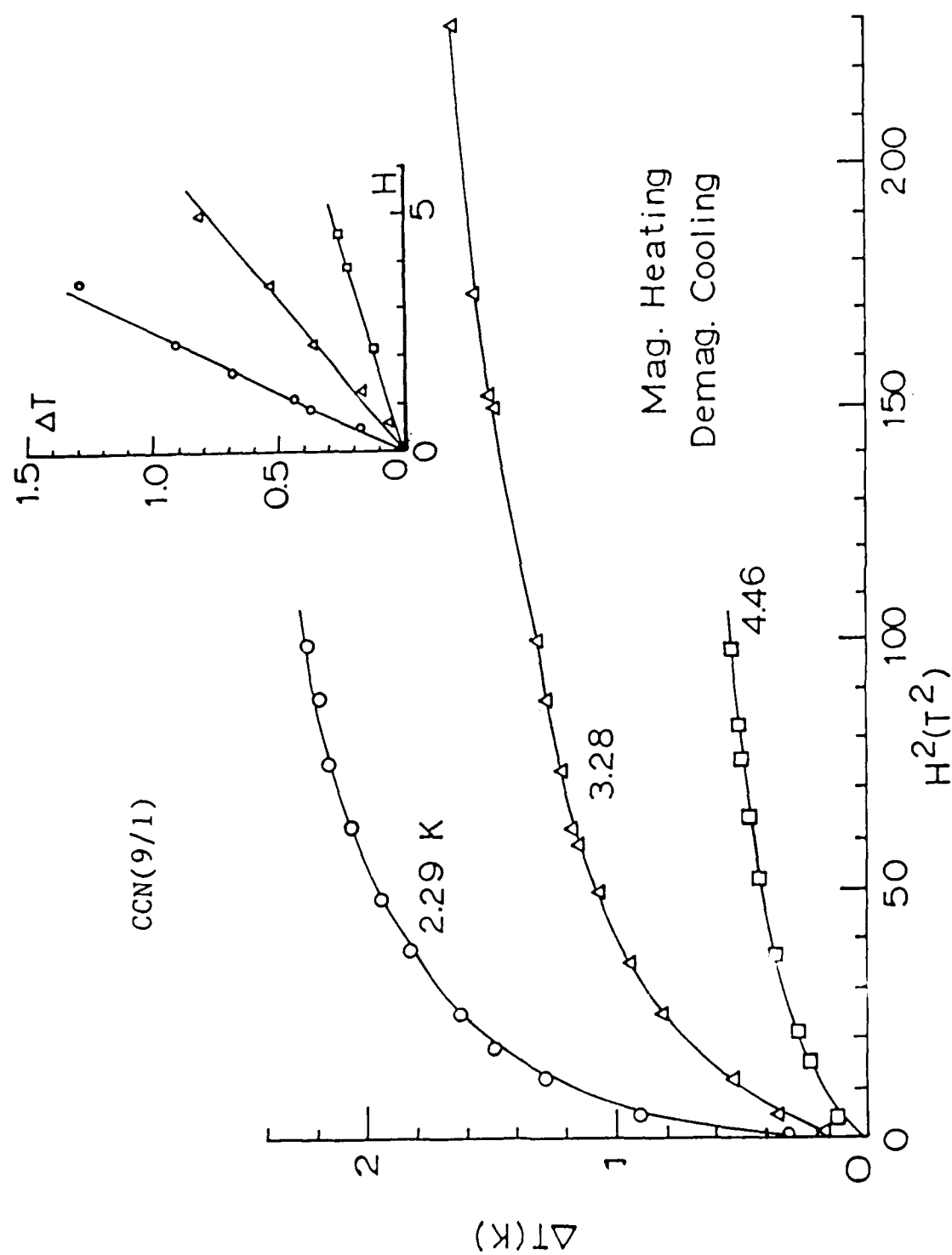


Figure 4-18. Magnetocaloric data measured on CCN(9/1) below $T_N = 8.0$ K. Non-hysteretic magnetization heating is exhibited. A linear $\Delta T_f \propto H$ relation is suggested (inset).

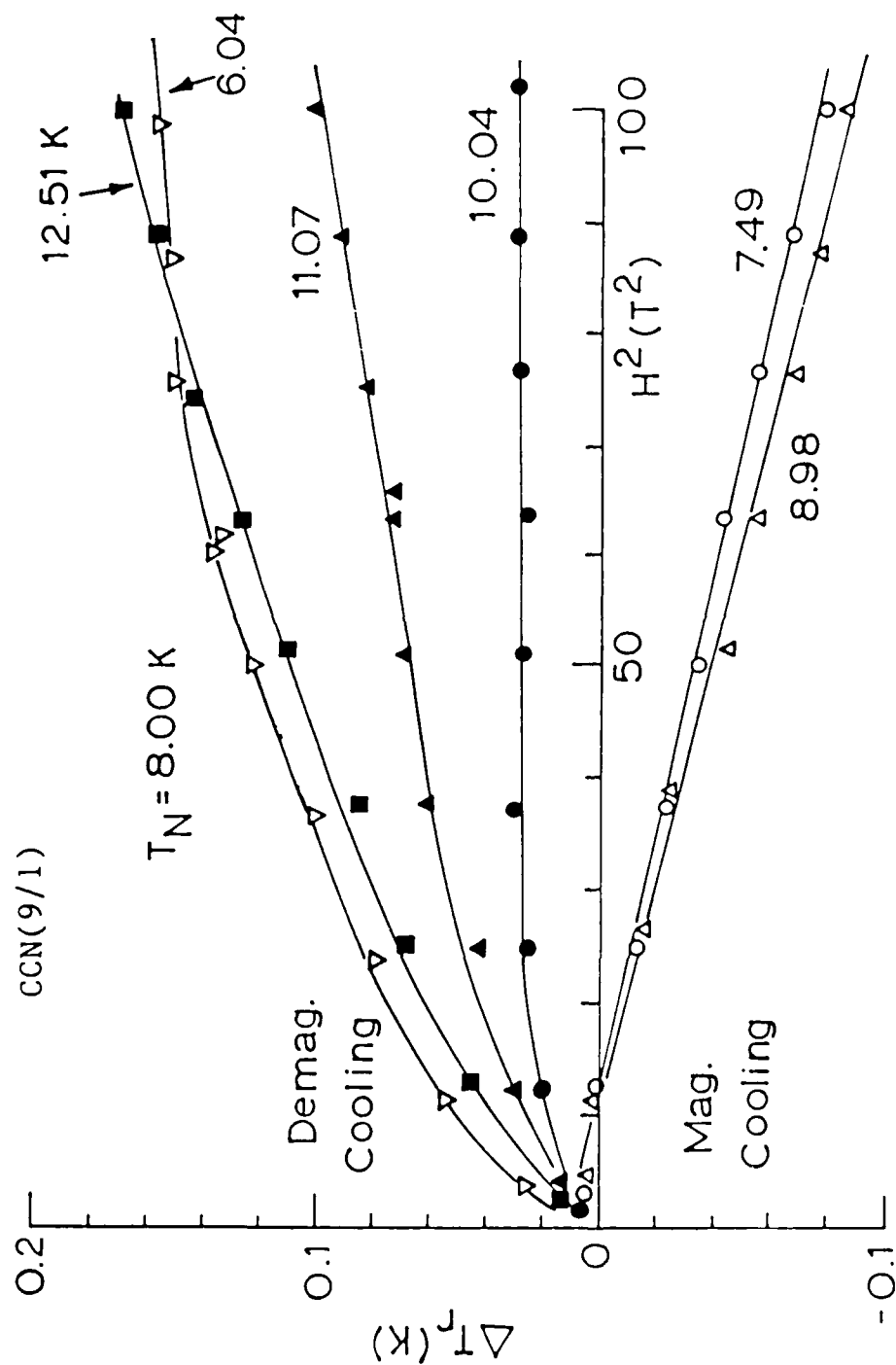


Figure 4-19. Magnetocaloric data measured on CCN(9/1). Non-hysteretic behavior is found, and near T_N magnetization cooling is exhibited.

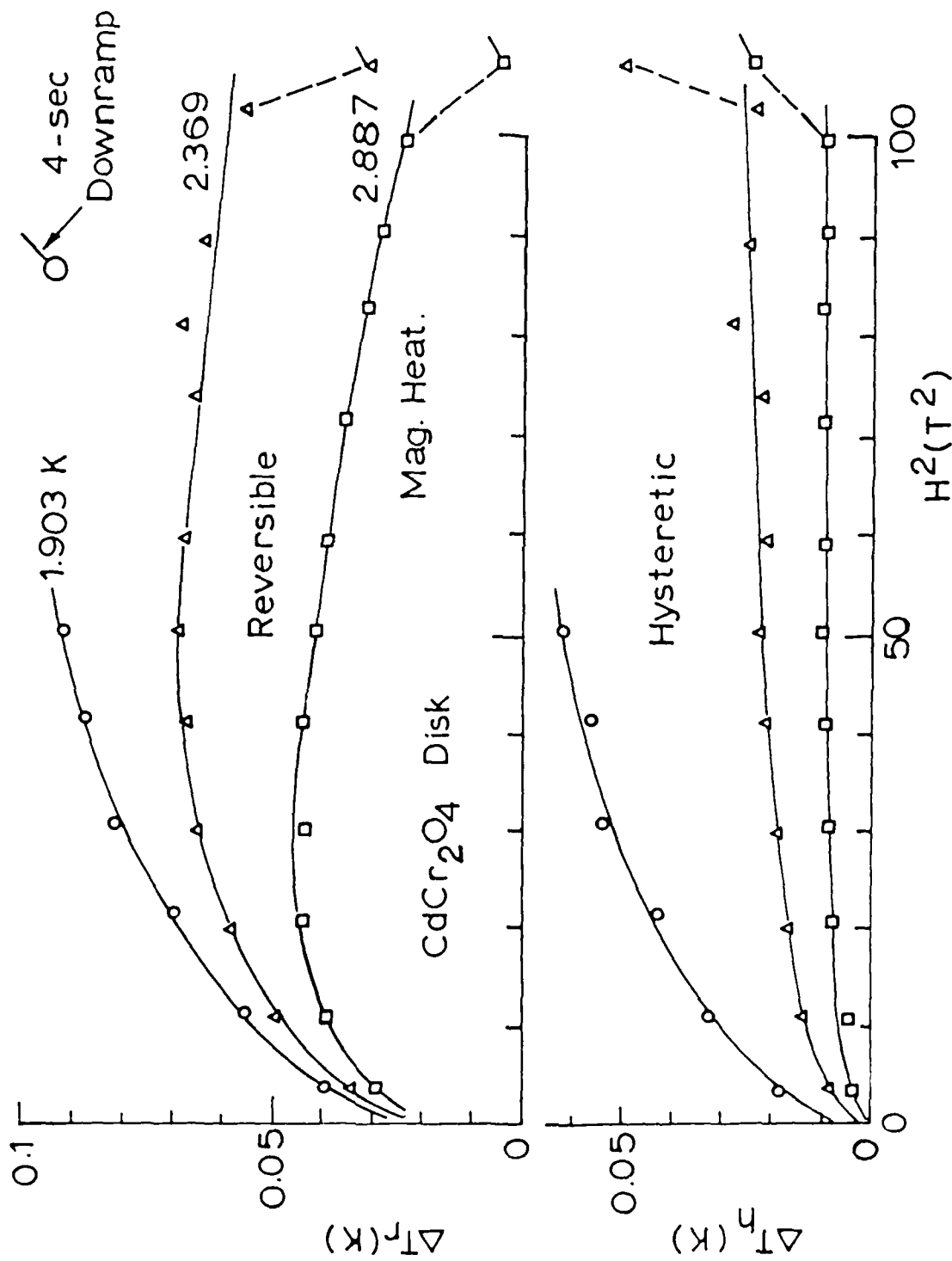


Figure 4-20. Magnetocaloric data measured on $CdCr_2O_4$ at the lowest temperatures. In contrast to CCr_2O_4 , a significant hysteresis component is found, and the data depend on the ramp rate.

4-20.

An unexpected discovery in CdCr_2O_4 is shown in Fig. 4-21 -- namely, a field-induced change from magnetization heating to magnetization cooling. The hysteretic components seen in Fig. 4-20 are negligible at the temperatures in Fig. 4-21, and these latter data are not sensitive to the ramp rate. Note in this regard that the CCN(9/1) data in Fig. 4-18 and 4-19 do not show even a hint of this crossover behavior.

A crossover magnetic field for CdCr_2O_4 can be seen in Fig. 4-21 (i.e., that field where $\Delta T_r/\Delta H$ changes sign), and the dependence of this crossover field on temperature is shown in Fig. 4-22. As seen, the minimum crossover field occurs at about 4.8 K.

Magnetocaloric data for CdCr_2O_4 at temperatures where only magnetization heating is seen are shown in Fig. 4-23, and here also there is no dependence on the ramp rate.

Finally, in Fig. 4-24 is shown a field-temperature phase diagram for reversible magnetocaloric effects in CdCr_2O_4 , and in Fig. 4-25 are shown combined phase diagrams for CCN(9/1) and CdCr_2O_4 .

The phase diagrams in Fig. 4-25 are very similar and appear offset in temperature by the difference in the T_N 's (indicated). However, at temperatures well below T_N the phase diagrams diverge, indicating a much larger density of free spins in CCN(9/1) compared to CdCr_2O_4 .

Data Measured on ZCN(9/1) and ZnCr_2O_4 . Following the same organization of the data as for the Cd spinel materials above, the magnetocaloric data for ZCN(9/1) above and below T_N are shown in Figs. 4-26 and 4-27, respectively. We note that ZCN(9/1) displays nonhysteretic magnetization heating at all temperatures, and at the lowest temperature in Fig. 4-26 the magnetocaloric effect is not as large as in CCN(9/1), Fig. 4-18.

Complementary data measured on ZnCr_2O_4 are shown in Figs. 4-28 and 4-29, respectively. As with the ZCN(9/1) data in Figs. 4-26 and 4-27, nonhysteretic magnetization heating occurs at all

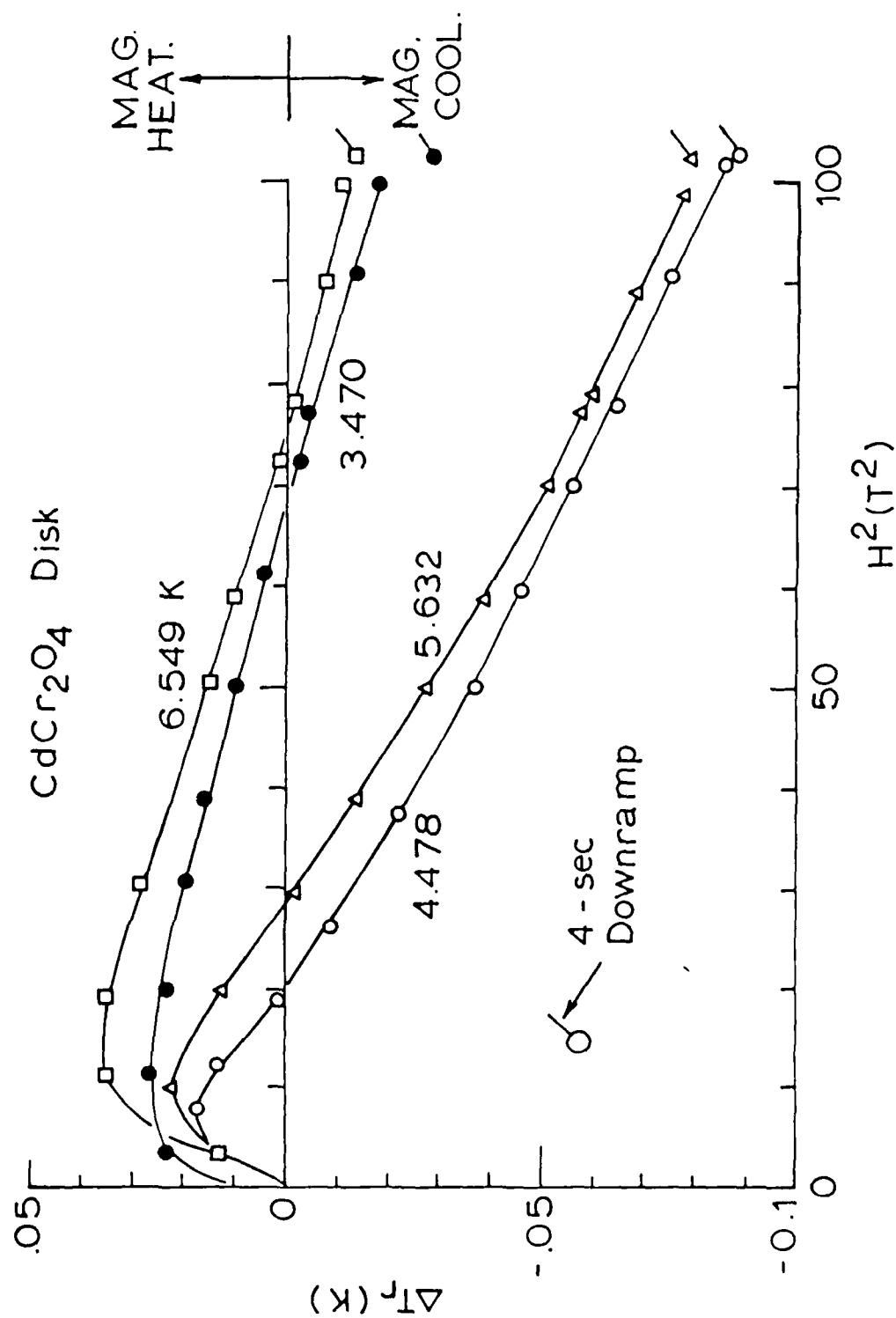


Figure 4-21. Magnetocaloric data on CdCr_2O_4 showing the field-induced change from magnetization heating to cooling.

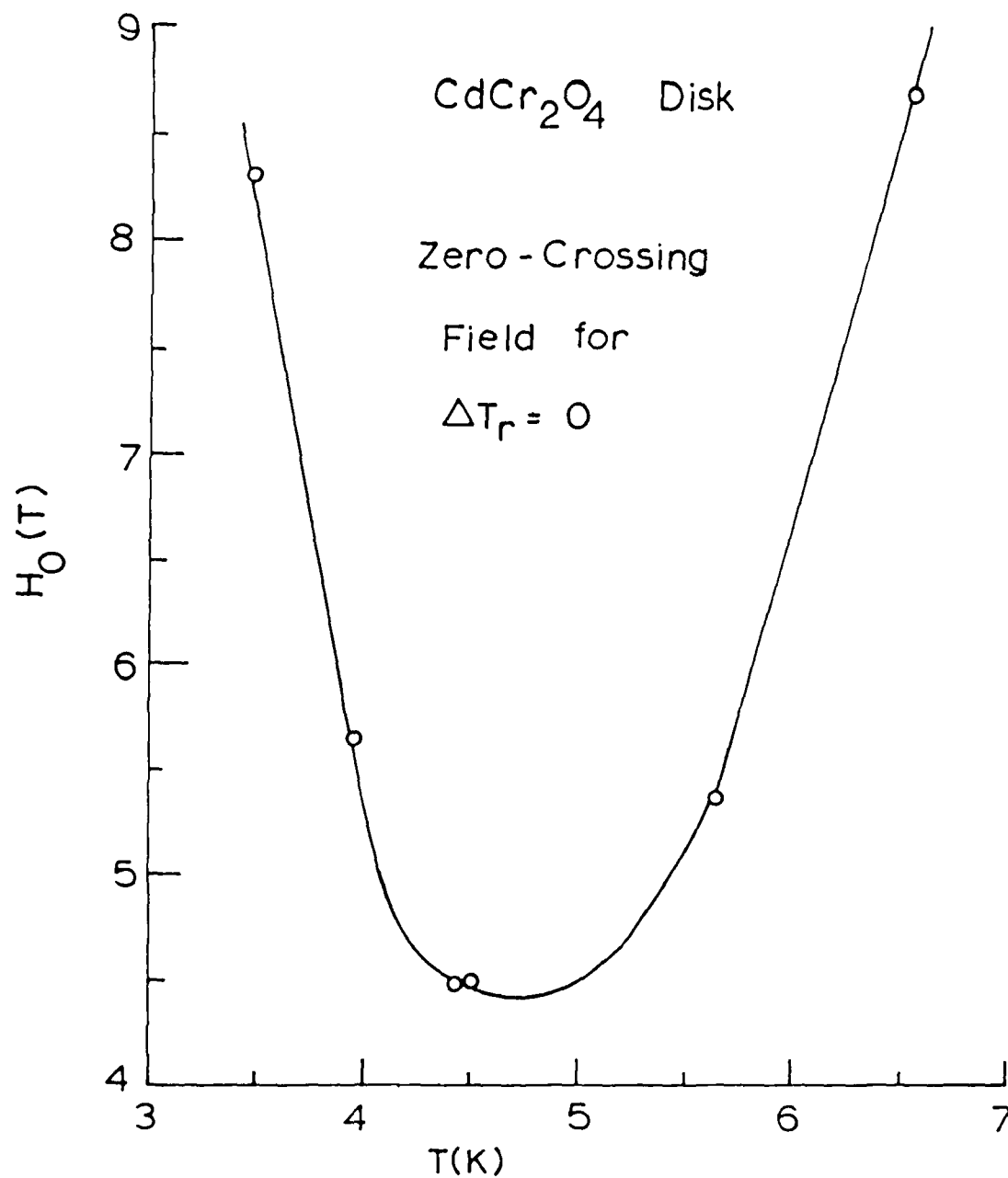


Figure 4-22. Dependence of the crossover magnetic field on temperature for CdCr₂O₄. At this field the magnetocaloric effects, $\Delta T_r / \Delta H$, change sign.

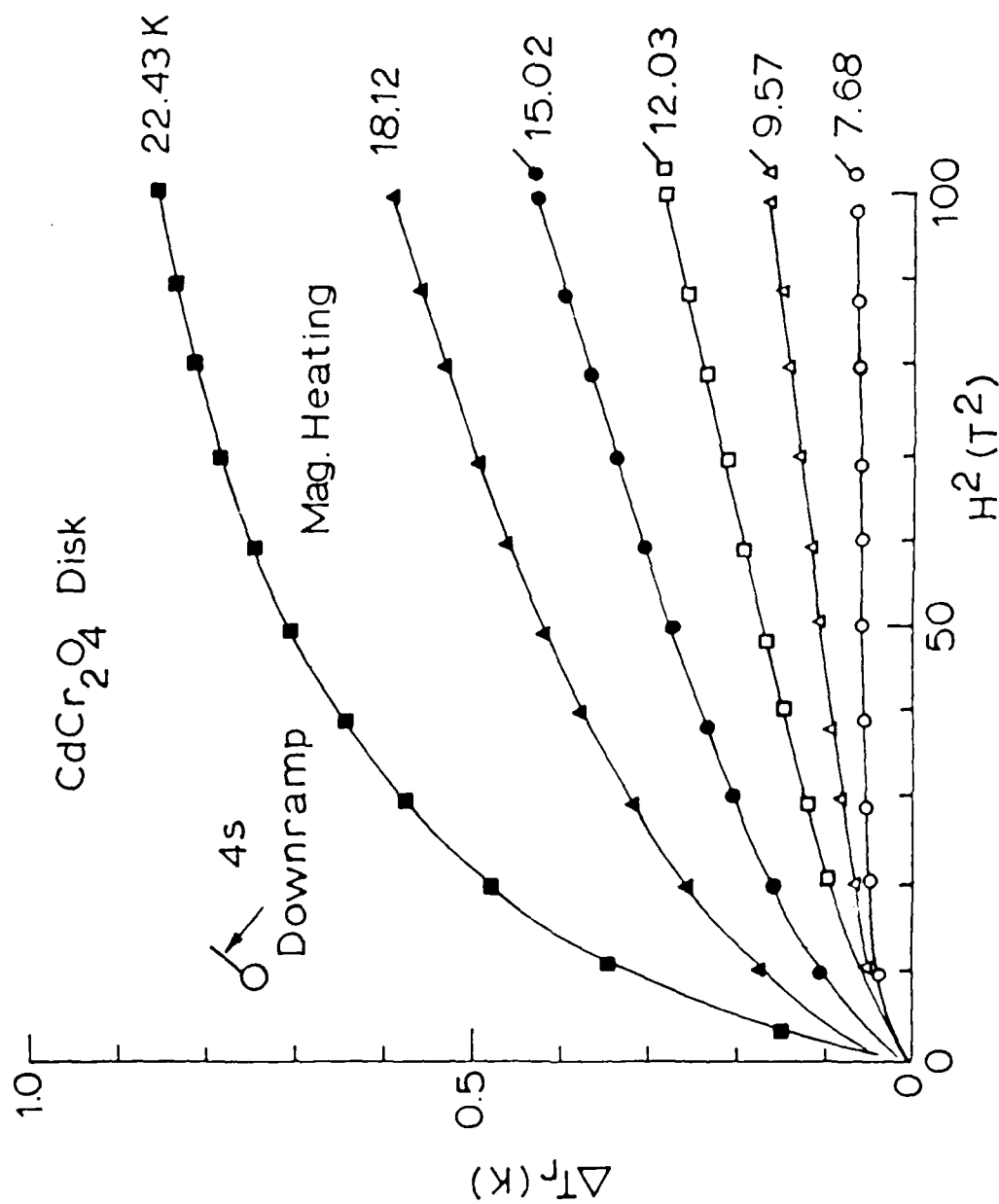


Figure 6-23. Magnetocaloric data for CdCr_2O_4 at temperatures where only magnetization heating is observed (for $H \lesssim 10$ T).

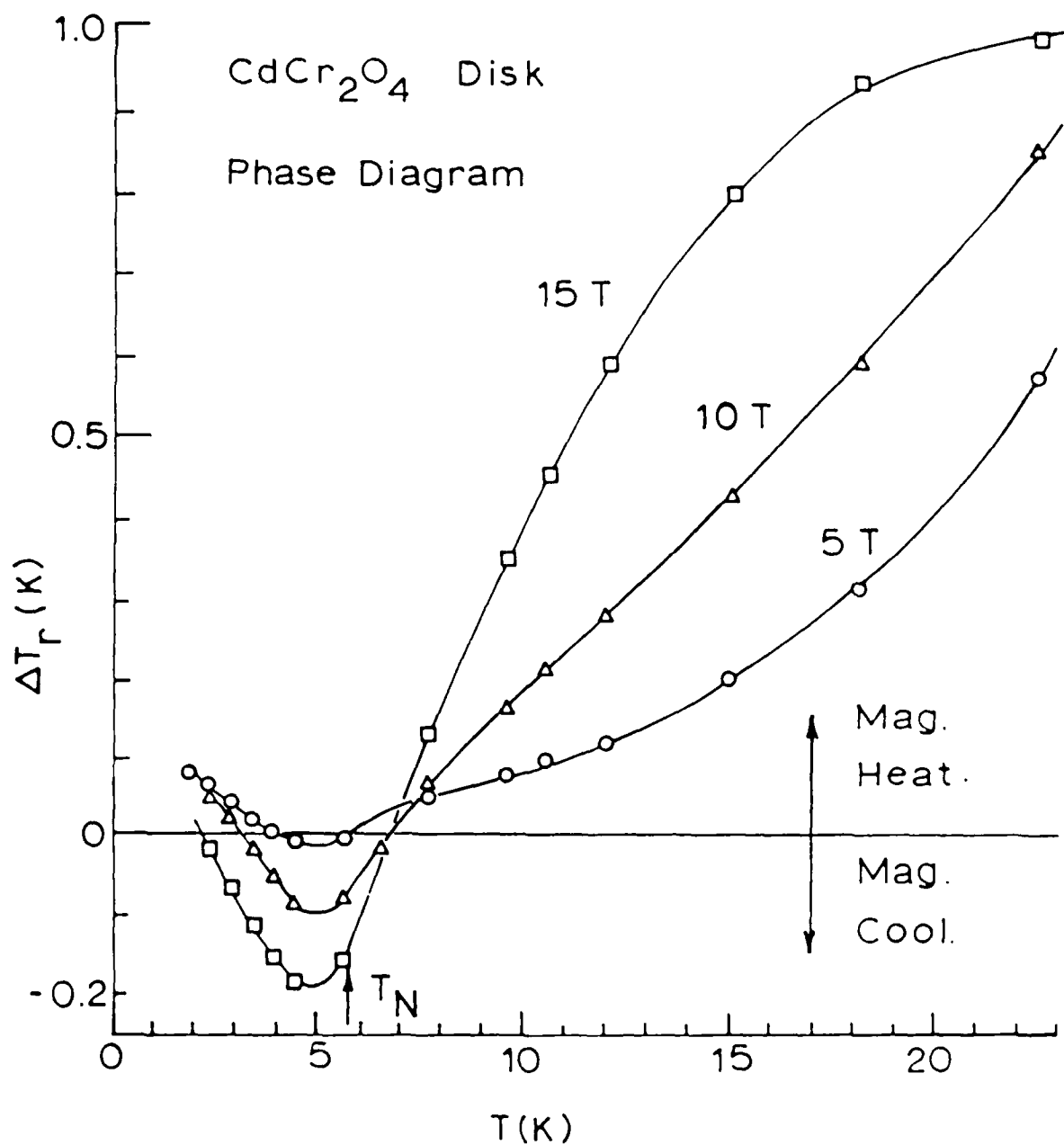


Figure 4-24. Temperature-magnetic field phase diagram for reversible magnetocaloric effect in CdCr_2O_4 .

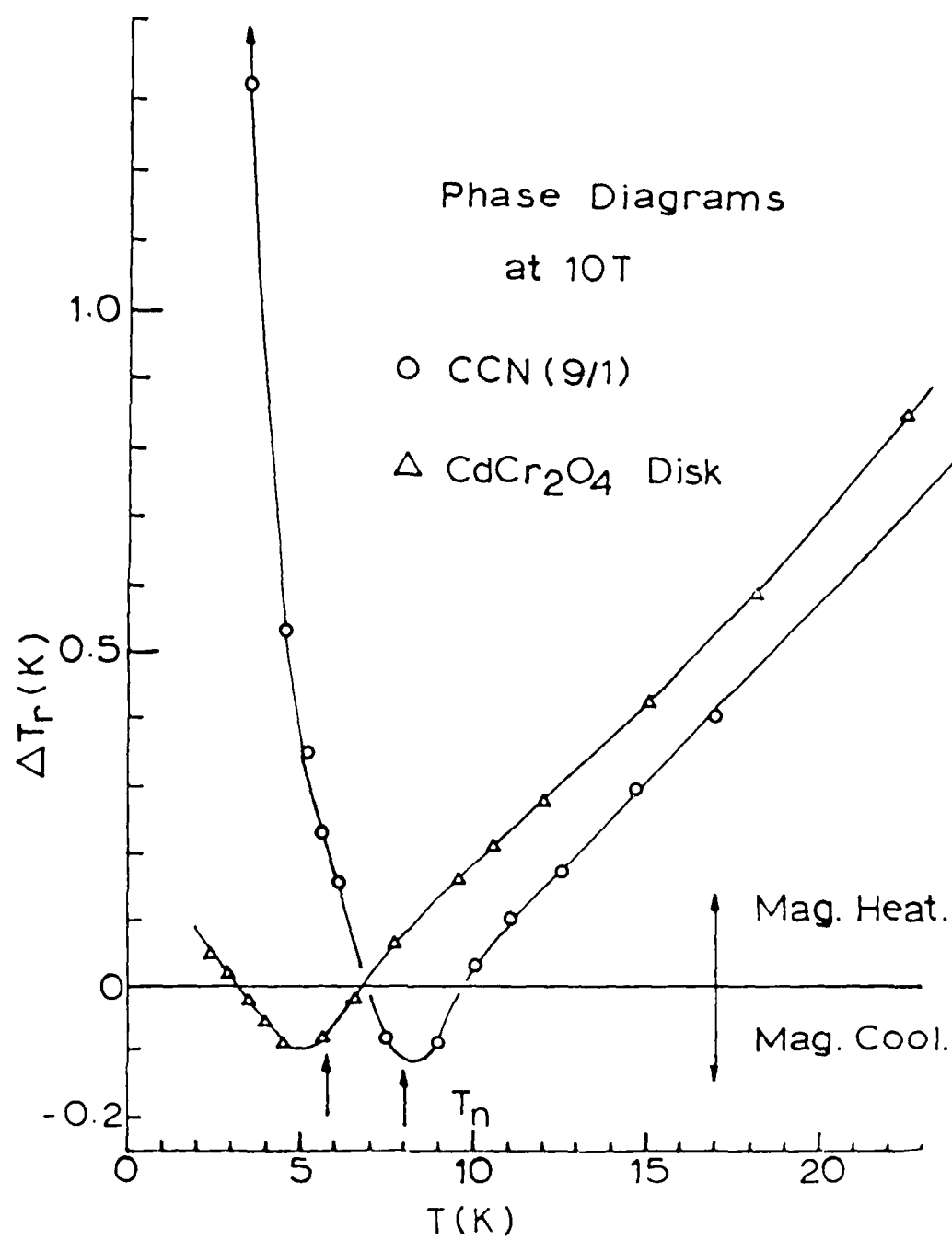


Figure 4-25. Combined magnetoclastic phase diagrams for CCN(9/1) and CdCr₂O₄.

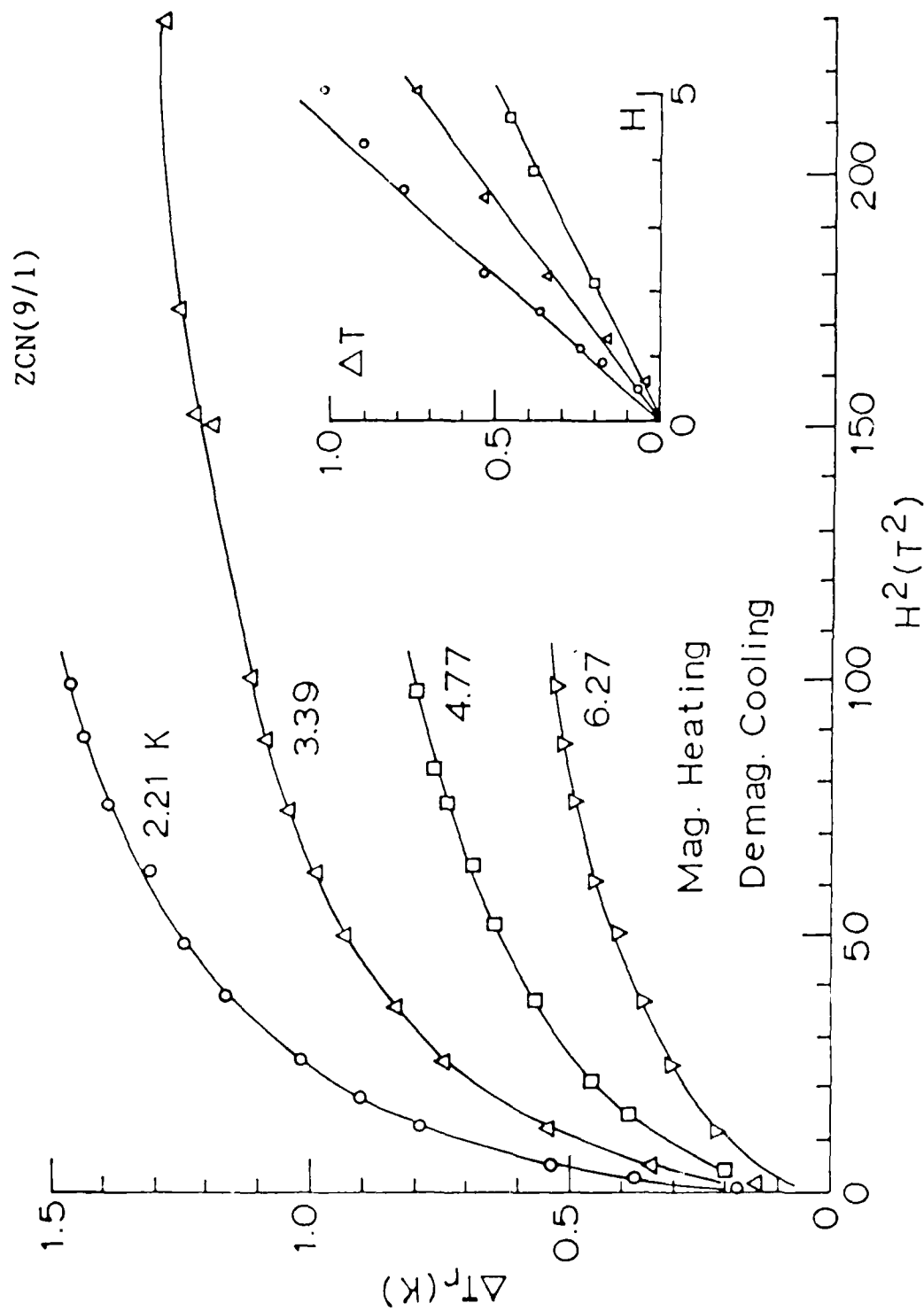


Figure 4-26. Magnetocaloric data measured on ZCN(9/1) below T_N . Non-hysteretic magnetization heating is found, and a linear $\Delta T_r \propto H$ relation is suggested (inset).

ZCN(9/1)

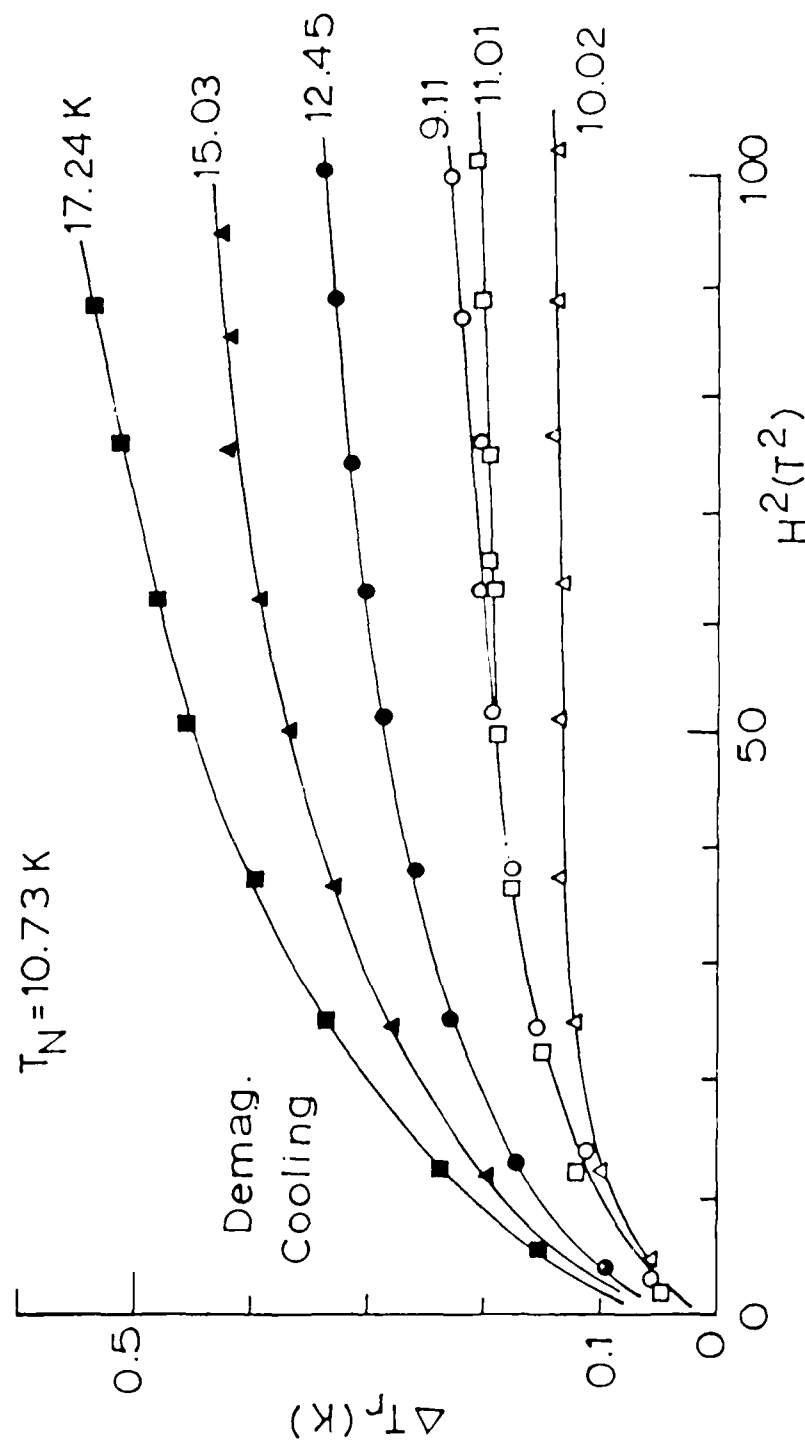


Figure 4-27. Magnetocaloric data measured on ZCN(9/1) at and above T_N . Nonhysteretic magnetization heating is found.

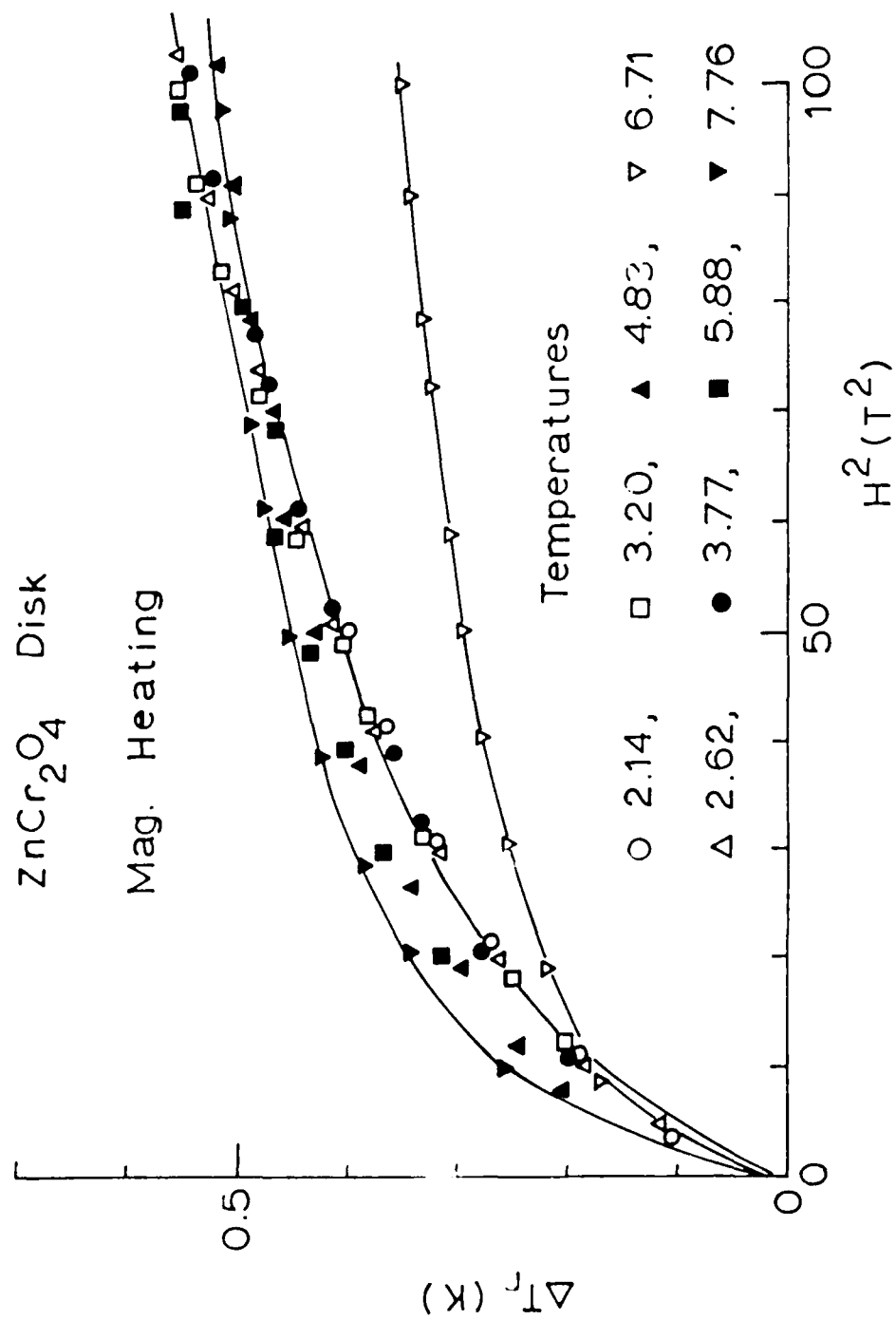


Figure 4-28. Magnetocaloric data on ZnCr_2O_4 at temperatures below T_N .
Nonhysteretic magnetization heating is observed.

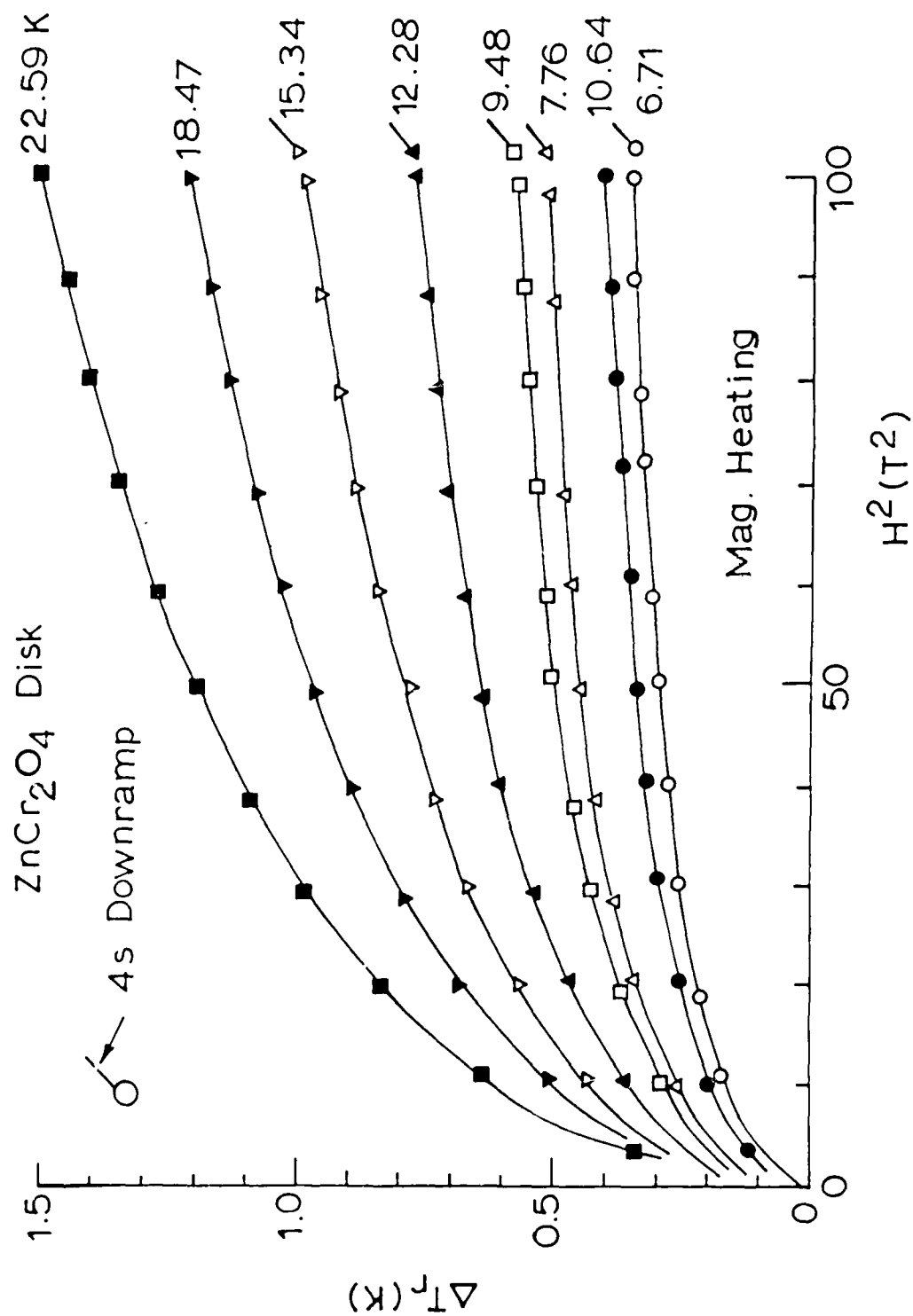


Figure 4-29. Magnetocaloric data on ZnCr₂O₄ at temperatures above T_N . Nonhysteretic magnetization heating is observed, independent of the ramp rate.

temperatures, independent of the ramp rate.

The temperature-magnetic field phase diagram for ZnCr_2O_4 is shown in Fig. 4-30, and T_N is indicated. Combined magnetocaloric phase diagrams for $\text{ZCN}(9/1)$ and ZnCr_2O_4 are shown in Fig. 4-31.

The combined data in Fig. 4-31 for the Zn spinels are quite dissimilar compared to the combined data for the Cd spinels in Fig. 4-25. The data in Fig. 4-31 do not scale above T_N based on the difference in T_N 's, as the data in Fig. 4-25 do. However, as with $\text{CCN}(9/1)$, the $\text{ZCN}(9/1)$ material has a much larger density of free spins at the lowest temperatures compared to the pure spinel.

"Accidental" Magnetocaloric Event. During the course of magnetocaloric measurements on $\text{CCN}(9/1)$ and $\text{ZCN}(9/1)$, an inadvertent collapse of the magnetic field occurred during up-ramp, and the measured behavior of the samples during this event may provide important clues regarding the spin systems in these materials.

The temperature-time and magnetic field-time records for this event are shown in Fig. 4-32.

The Fig. 4-32 data reveal two interesting features: (1) The sum result of the event was to heat the samples far above the reservoir temperature, $\text{CCN}(9/1)$ in particular; (2) Following the field collapse, an instantaneous cooling occurred followed by a heating process with a characteristic time ~ 1 -2 sec.

These results might be understood in terms of the the model of two spin systems: The uncorrelated spins instantaneously demagnetization-cool with a very rapid spin-phonon relaxation time; and the correlated spins demagnetization-heat with a long spin-phonon relaxation time. The explanation then is that on field collapse the uncorrelated spins first cooled the lattice phonons to a very low temperature, followed by the correlated spins slowly heating the phonon field back to the reservoir temperature or higher.

The question, of course, is what happened to the entropy in the uncorrelated spin system since clearly when the field is

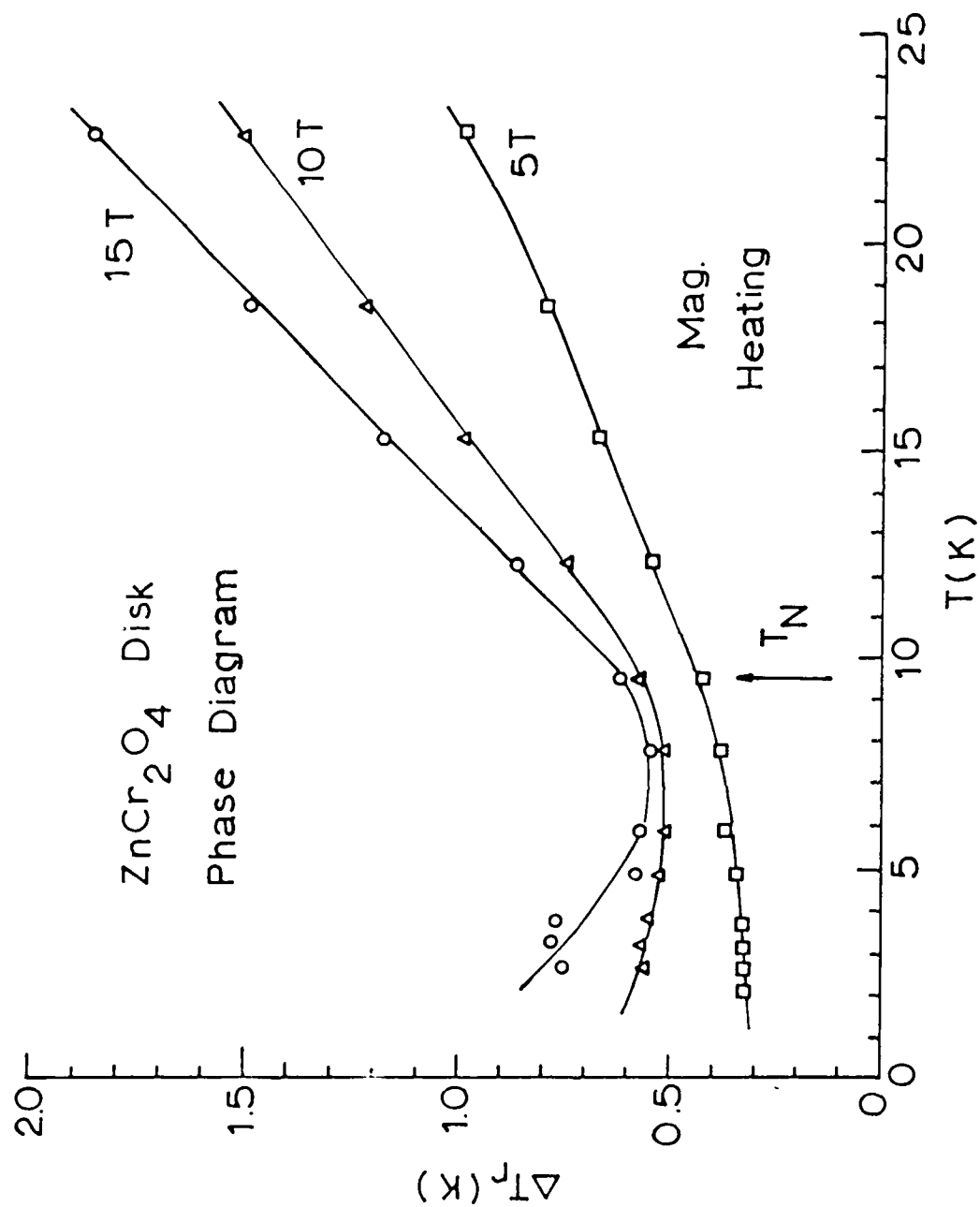


Figure 4-30. Temperature-magnetic field phase diagram for ZnCr_2O_4 showing magnetization heating at all temperatures; T_N is indicated.

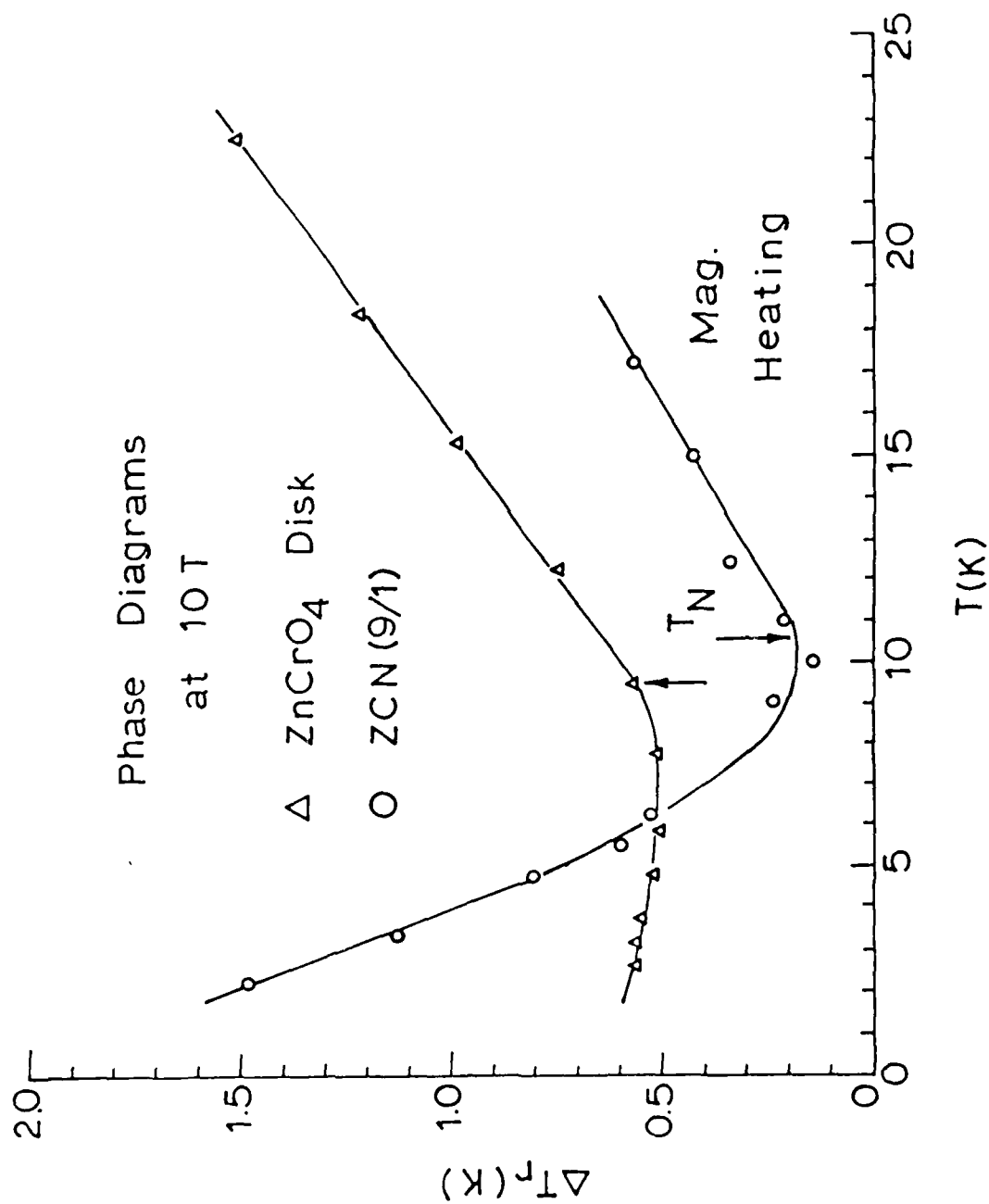


Figure 4-31. Combined phase diagrams for ZnCr_2O_4 and ZnCrO_4 .

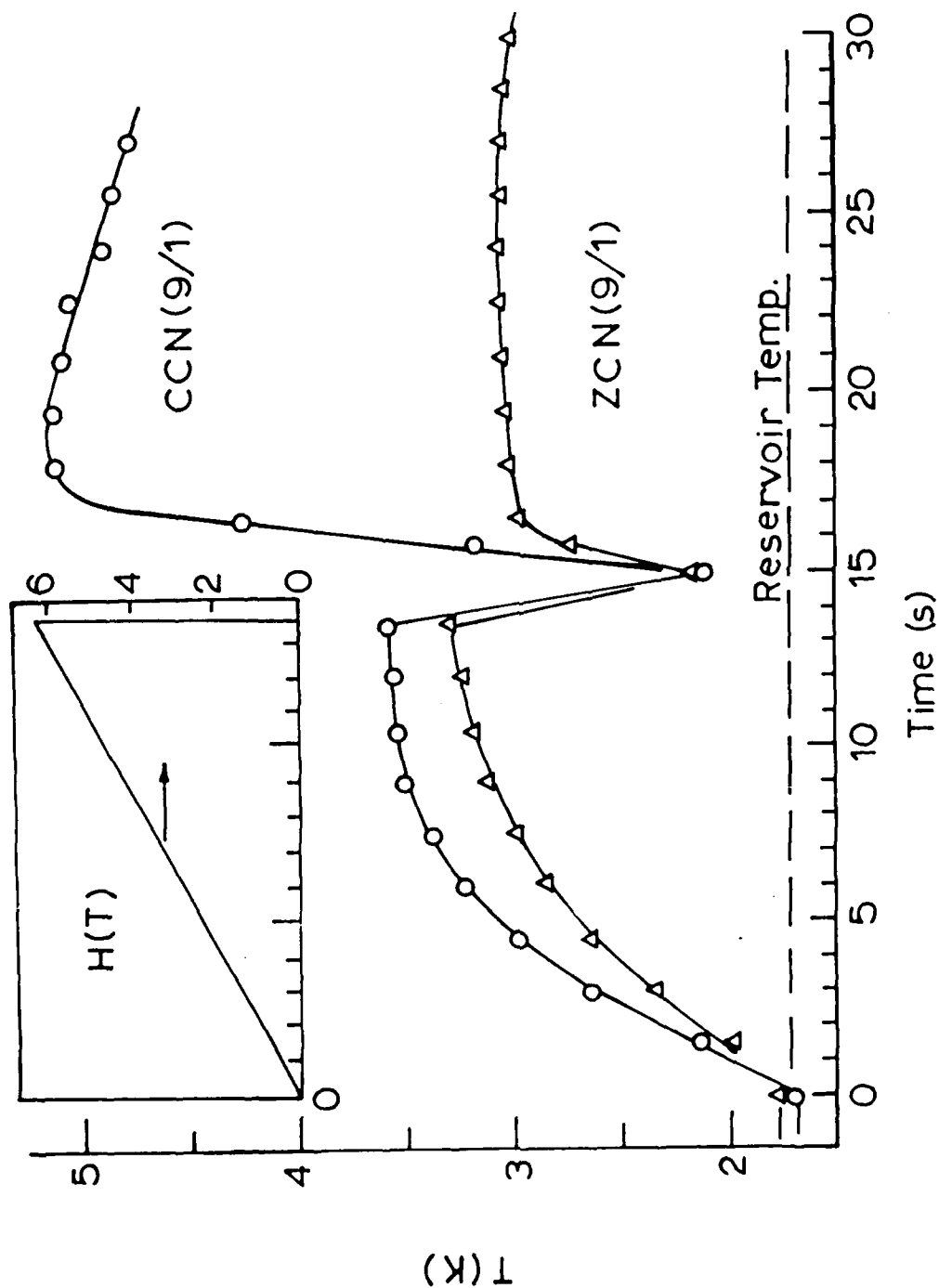


Figure 4-32. Accidental field-collapse, 6.5 ± 0 T, during up-ramp and the observed magnetocaloric behavior of CCN(9/1) and ZCN(9/1).

slowly ramped down the net effect is demagnetization cooling back to the reservoir temperature. The answer here may lie in the zero-field splitting of the uncorrelated spins which ultimately limits how low in temperature this spin system can cool and therefore limits the recoverable (i.e., reversible) entropy. Under slow-ramp conditions the spin systems are presumably in equilibrium with each other and the phonon field so that zero-field-splitting effects aren't seen.

In any case, this accidental event seems to lend additional weight to the notion of two spin systems in these spinels. Also, it's interesting to observe that the effect of the correlated spins in ZCN(9/1) in Fig. 4-32 is weaker than in CCN(9/1), and this reflects the behavior seen above (Figs. 4-18 and 4-26).

D. Magnetothermal Data Analyses

In the above sections, a large amount of specific heat and magnetothermal data have been reported on materials composed of the spinels CdCr_2O_4 and ZnCr_2O_4 . We now take up analyses of these data based on the TdS equation for magnetic insulators. Additionally, we will give estimates of the densities of free spins in these materials. We begin with the TdS equation for magnetic insulators,

$$\text{TdS} = mC_H dT + \mu_O mT (\partial M / \partial T)_H dH \quad (4-6)$$

where m is the sample mass and C_H is the specific heat at field. Next, guided by the linear $M - H$ characteristic in Fig. 2-4, we write

$$M = \chi H, \quad (4-7)$$

and substituting in Eq.(4-6) for adiabatic conditions, we have

$$(C_H/T)dT = -\frac{1}{2}\mu_O(d\chi/dT)dH^2. \quad (4-8)$$

The specific heat measurements on these materials in intense

magnetic fields have not revealed a strong field dependence. Approximately $C_H \approx C_O$, we have upon integration that

$$\mu_O(dx/dT) = -2\Delta S_O/H^2 \quad (4-9)$$

where ΔS_O is the change in the zero-field entropy on adiabatically ramping $0 \rightarrow H$. Thus, by this convention, if magnetization heating occurs ($\Delta S_O > 0$), then $dx/dT < 0$.

It will prove useful to review the elementary dependence of dx/dT on $\chi(T)$, and this is shown in Fig. 4-33. T_N can be defined by the maximum in dx/dT , as shown. At the lowest temperatures, the presence of free spins causes χ to rise rapidly (dashed curve), and this in turn will cause dx/dT to plunge rapidly, as shown.

In arriving at Eq.(4-9), the most serious approximation is that of a linear paramagnet, Eq.(4-7), and it is instructive to consider the corrections to this approximation. In the most general case, we have the Landau-type expansion,

$$M = \chi H + \xi H^3 + \zeta H^5 + \dots \quad (4-10)$$

Substituting in Eq.(4-8) and rearranging, we have

$$\mu_O(dx/dT) = -2\Delta S_O/H^2 + \mu_O\left[\frac{1}{2}(d\xi/dT)H^2 + \frac{1}{3}(d\zeta/dT)H^4\right]. \quad (4-11)$$

We note two features from Eq.(4-11): First, even in the case of a nonlinear paramagnet, if ξ and ζ are temperature-independent then Eq.(4-11) reduces to Eq.(4-9). And second, under isothermal conditions (i.e., dx/dT is constant), if $\Delta S_O/H^2$ is not constant

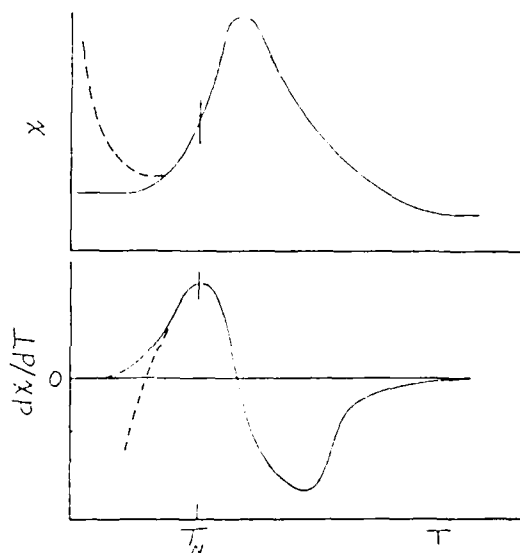


Figure 4-33. Sketch of the variation in dx/dT due to the idealized change of χ with temperature.

then the importance of the higher terms in Eq.(4-11) is clearly indicated. We shall see below that these considerations become important in interpreting the phenomenological results.

Finally, anticipating that ΔS_o tables will be generated, another interesting analysis of the data becomes possible. Namely, the maximum entropy available in a free-spin system is simply

$$\Delta S_m = n_p R \ln (2s + 1) \quad (4-12)$$

where n_p are the number of free spins per formula weight (e.g., $n_p = 2$ in the high-temperature, paramagnetic phase of CdCr_2O_4) and s is the spin value. If we now assume that at some sufficiently large field strength all of these free spins are aligned, then upon demagnetization the temperature change of the sample is due to the randomization of these spins. Stated differently,

$$\Delta S_o = n_p R \ln (2s + 1) \quad (4-13)$$

where ΔS_o is the entropy change of the sample, as above. In this fashion, the free-spin density, n_p , can be estimated from the very high field magnetocaloric data.

The first step in these analyses was to develop ΔS_o -tables from the four sets of zero-field specific heat data in Figs. 4-9 and 4-10. This was done by numerically integrating the experimental C_o/T data, and then these data were smoothed for greater accuracy. Next, a code was written for converting a $T_1 \rightarrow T_2$ magnetocaloric event on $0 \rightarrow H$ up ramp to the ratio $\Delta S_o/H^2$ according to Eq.(4-9). The average temperature of the event is $(T_1 + T_2)/2$, and only the reversible ΔT 's were considered. In this fashion, two types of phase diagrams were generated for each of the four samples: (1) $\mu_o dx/dT$ vs. T at constant H ; and (2) $\mu_o dx/dT$ vs. H at constant T . In the former type of diagram, the data are limited to $H = 5$ and 10 T because complete data sets were unavailable at other field levels, in particular at lower

field levels.

CdCr₂O₄ Disk. The magnetothermal phase diagrams for the compacted CdCr₂O₄ disk are shown in Fig. 4-34. The $\mu_0 \, d\chi/dT$ vs. T diagram in Fig. 4-34(a) at 5 and 10 T show that field-dependent magnetization cooling, $d\chi/dT > 0$, is observed at and below T_N , as discussed previously.

We note here that for an ideal Curie magnet $\chi \propto T^{-1}$, so in some temperature range $d\chi/dT \propto -T^{-2}$, as illustrated in the idealized sketch in Fig. 4-33. The Fig. 4-34(a) data do not reflect this up to 23 K; otherwise, these Fig. 4-34(a) data follow the idealized behavior in Fig. 4-33 and indicate that a free-spin contribution exists below about 3 K.

The $\mu_0 \, d\chi/dT$ vs. H magnetothermal phase diagram in Fig. 4-34(b) is shown for temperatures below and above T_N ; at both temperatures magnetization heating is observed. For both temperatures, $d\chi/dT$ decreases rapidly as H decreases, so little quantitative agreement can be expected with the low-field χ -data in Section V below.

The $d\chi/dT$ -data at 3.47 K in Fig. 4-34(b) involve contributions from both correlated and uncorrelated spins. However, at 10.6 K one expects all the spins to be uncorrelated, and here the non-constancy of Eq.(4-9) is clearly seen. The higher-order terms in Eq.(4-11) are needed to explain these data, but this was not pursued due to the lack of data at lower H-values in Fig. 4-34(b). Note in this regard that the measurement of magnetocaloric data at lower H-values is subject to the experimental constraint of resolving the associated small temperature changes in intense magnetic fields.

Finally, from Fig. 4-34(b) it appears that saturation occurs by about 15 T.

CCN(9/1). The $\mu_0 \, d\chi/dT$ vs. T magnetothermal phase diagram for CCN(9/1) is shown in Fig. 4-35(a), and this diagram closely resembles that of CdCr₂O₄ in Fig. 4-34(a) given the shift in the T_N -values. Note also that the scales (i.e., magnitudes) of the

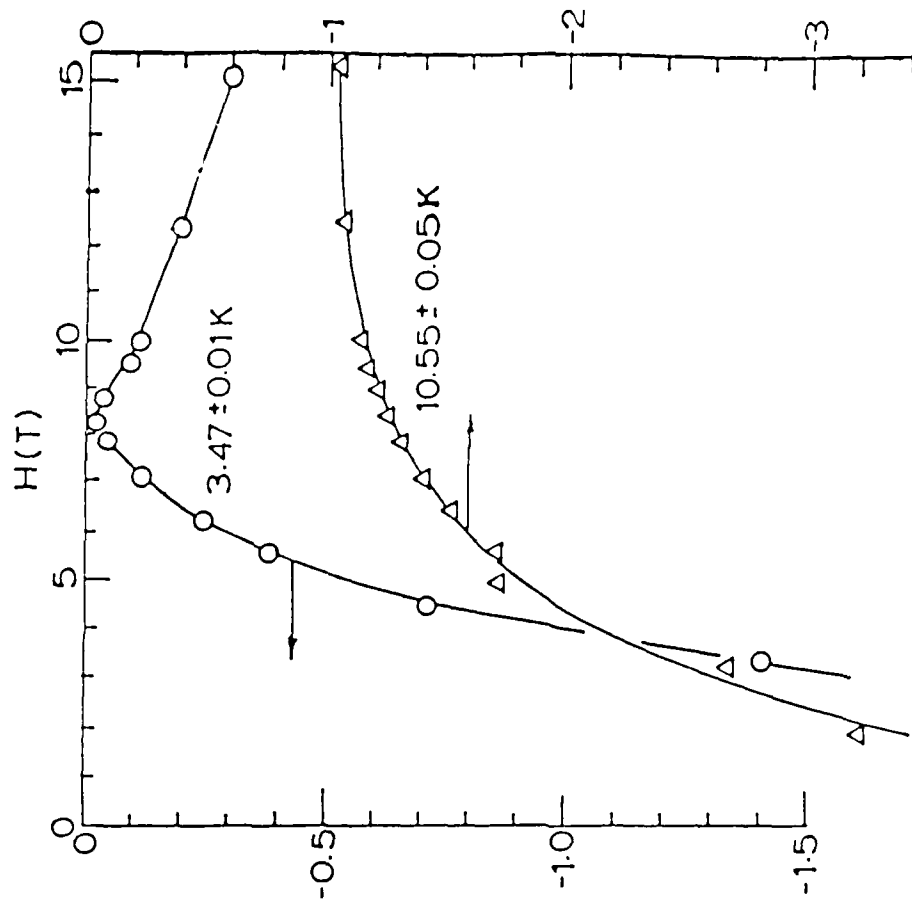
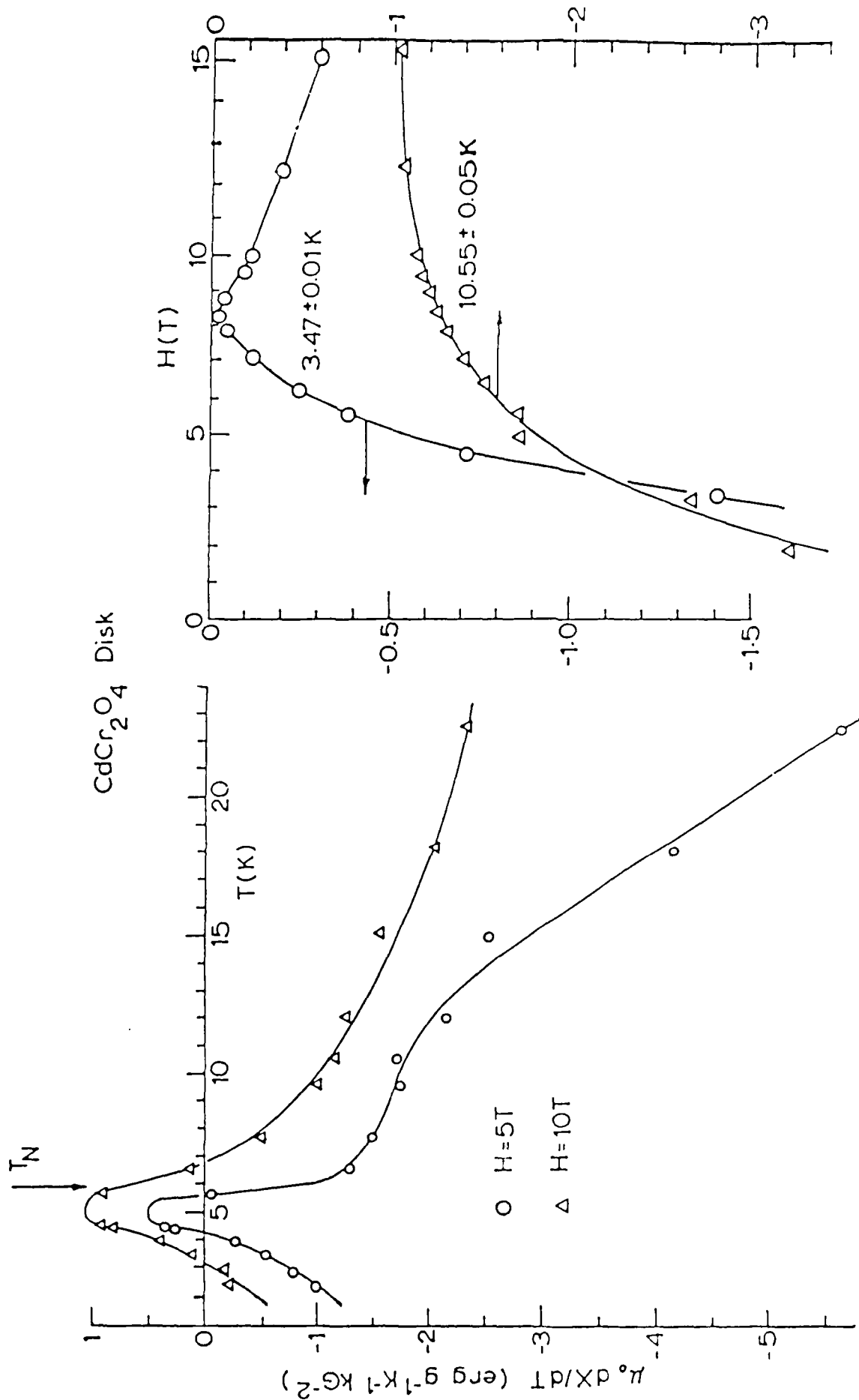


Figure 4-34. Magnetothermal phase diagrams for CdCr_2O_4 according to Eq.(4-9) as functions of: (a) Temperatures, and (b) Magnetic field.

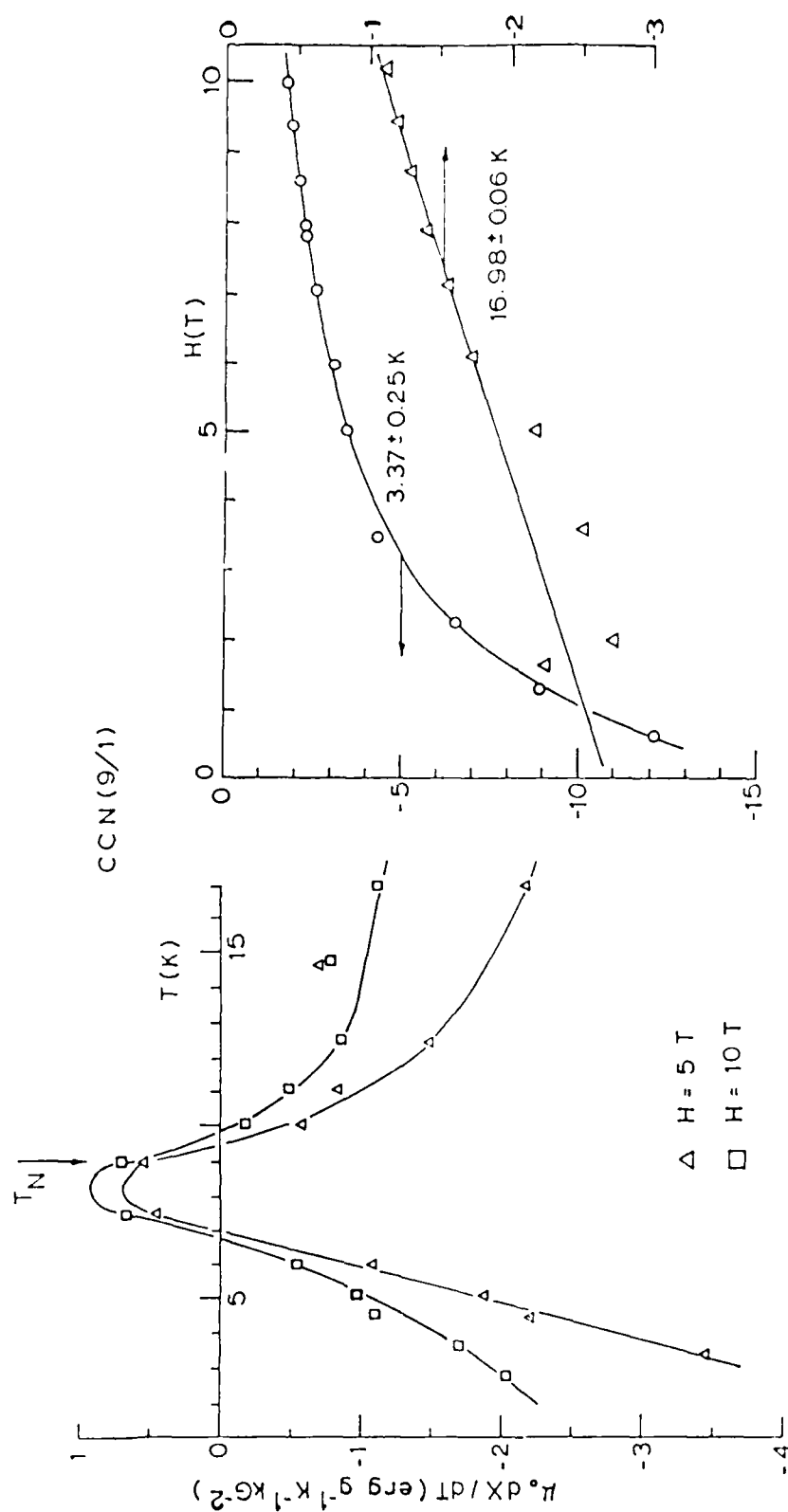


Figure 4-35. Magnetothermal phase diagrams for C50/1 according to Eq. (4-9) as functions of: (a) Temperature, and (b) Magnetic field.

data in Figs. 4-34(a) and 4-34(b) are commensurate.

The $\mu_0 dx/dT$ vs. H diagram for CCN(9/1) is shown in Fig. 4-35(b) at two temperatures above and below T_N , and once again the non-constancy of Eq.(4-9) is clearly evident.

The larger density of free spins below T_N in CCN(9/1) compared to the CdCr_2O_4 disk is clearly seen in both Figs. 4-35(a) and 4-35(b) by the much larger absolute values of dx/dT (see below, also).

ZnCr_2O_4 Disk. The $\mu_0 dx/dT$ vs. T magnetothermal phase diagram for ZnCr_2O_4 in Fig. 4-36(a) is in marked contrast to the equivalent phase diagram for CdCr_2O_4 in Fig. 4-34(a) and also does not resemble the idealized behavior in Fig. 4-33. In Fig. 4-36(a) dx/dT goes through a deep minimum at T_N at both 5 and 10 T, indicative of a near-singularity in x vs. T . At all temperatures in Fig. 4-36(a), $dx/dT < 0$, indicating that x always increases with decreasing temperature at these field strengths.

The $\mu_0 dx/dT$ vs. H magnetothermal phase diagram for the ZnCr_2O_4 disk is shown in Fig. 4-36(b), again at two temperatures above and below T_N . As in CdCr_2O_4 [Fig. 4-34(b)], dx/dT decreases very rapidly with decreasing H indicative of the importance of the higher-order terms in Eq.(4-11). Also, the appearance of saturation is seen at about 15 T.

Another striking difference between CdCr_2O_4 and ZnCr_2O_4 is seen on comparing the equivalent phase diagrams in Figs. 4-34(b) and 4-36(b). Namely, at $T \sim 2 T_N$, the dx/dT -values for ZnCr_2O_4 are substantially larger in magnitude compared to CdCr_2O_4 .

ZCN(9/1). The $\mu_0 dx/dT$ vs. T magnetothermal phase diagram for ZCN(9/1) in Fig. 4-37(a) closely resembles that for the ZnCr_2O_4 disk in Fig. 4-36(a) -- note in particular the deep minimum at T_N and the similarity of the scales.

The $\mu_0 dx/dT$ vs. H phase magnetothermal diagram for ZCN(9/1) is given in Fig. 4-37(b) for three temperatures -- above, at, and below T_N . Again the similarity to the equivalent diagram for ZnCr_2O_4 [Fig. 4-36(b)] is observed, and we note the huge

ZnCr₂O₄ Disk

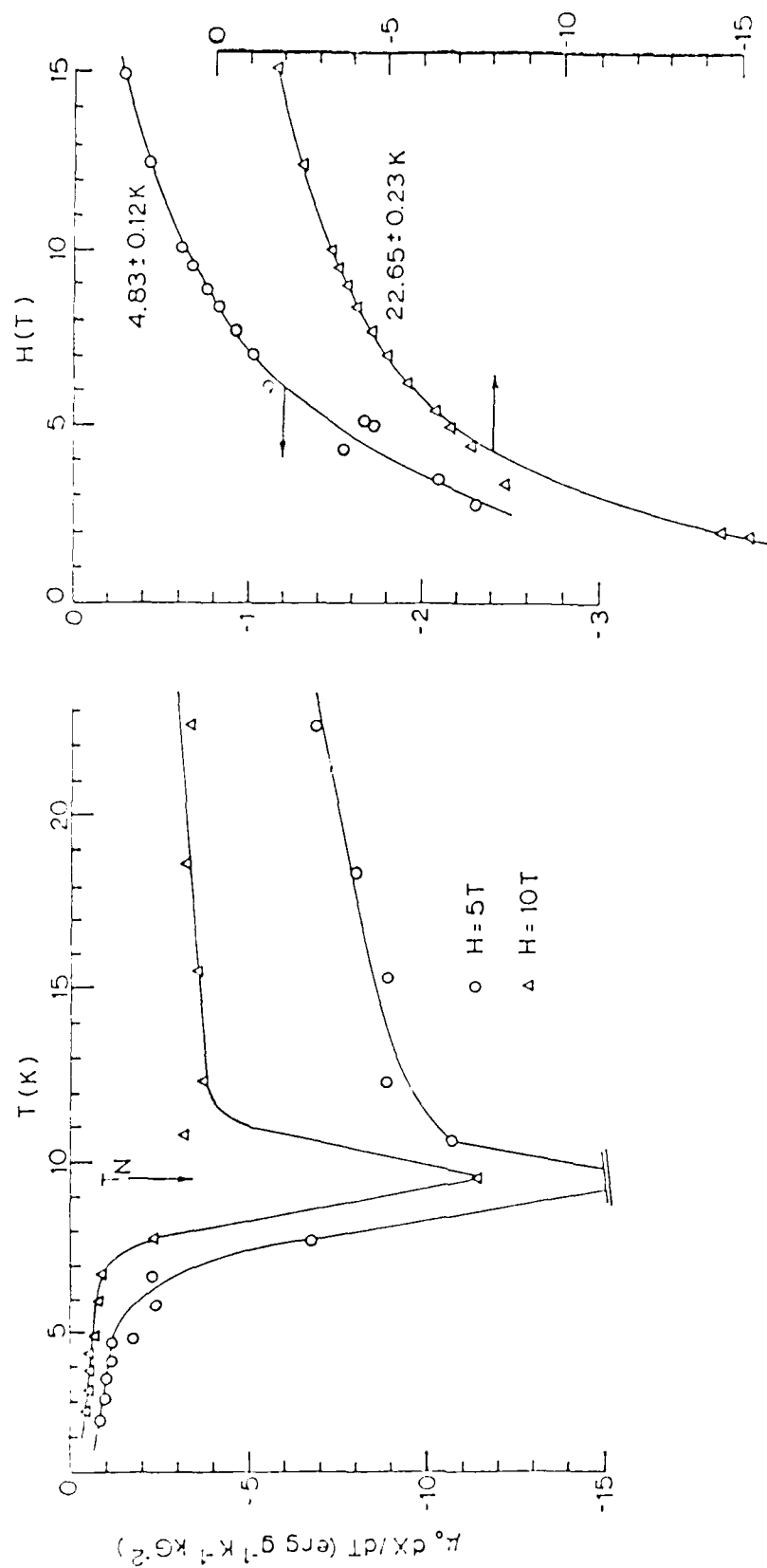
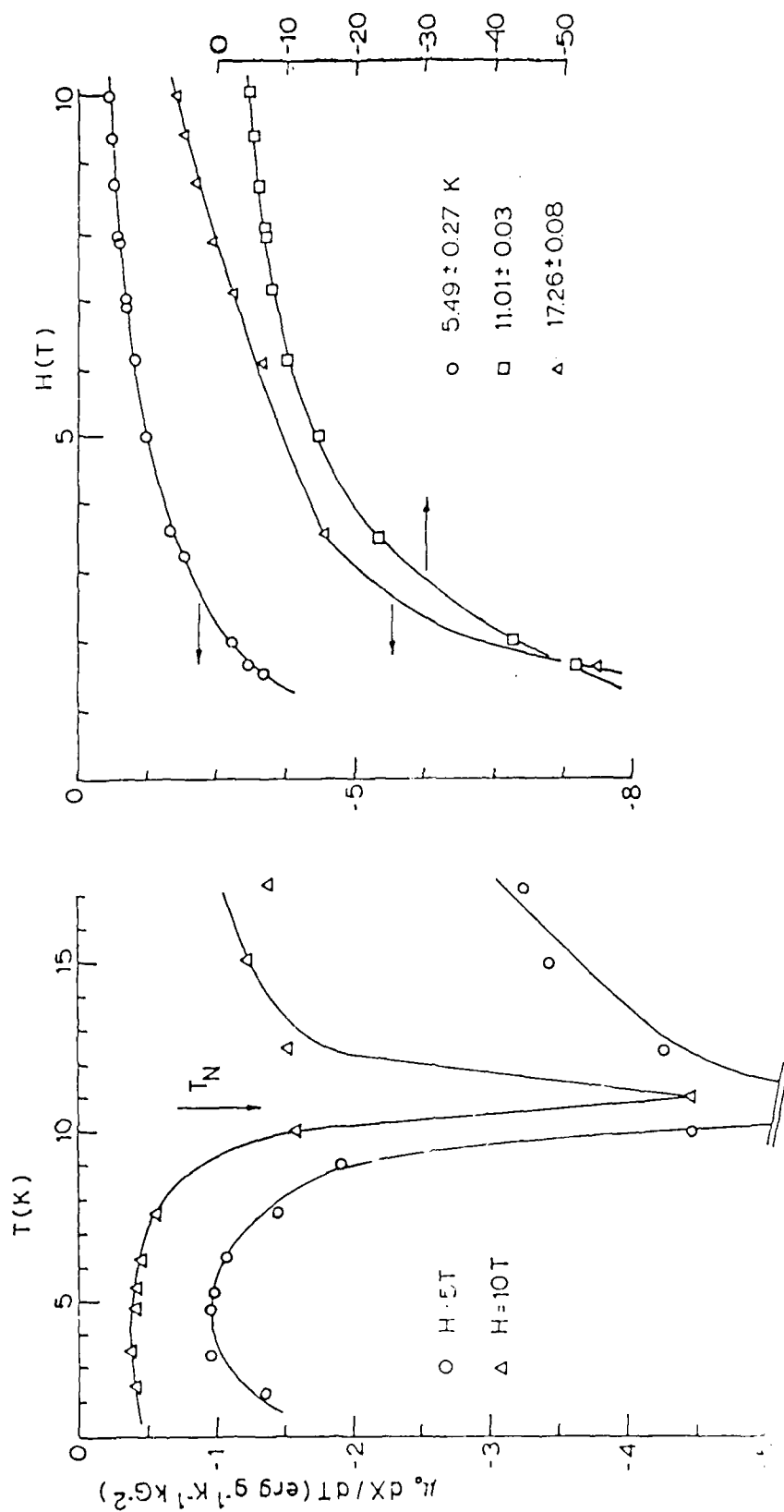


Figure 4-36. Magnetothermal phase diagrams for ZnCr₂O₄ according to Eq.(4-9) as functions of: (a) Temperature, and (b) Magnetic field.

ZCN(9/1)



(a)

(b)

Fig. 37. Magnetothermal phase diagrams for ZCN(9/1) according to Eq. (4-9) as functions of: (a) Temperature, and (b) Magnetic field.

AO-A107 240

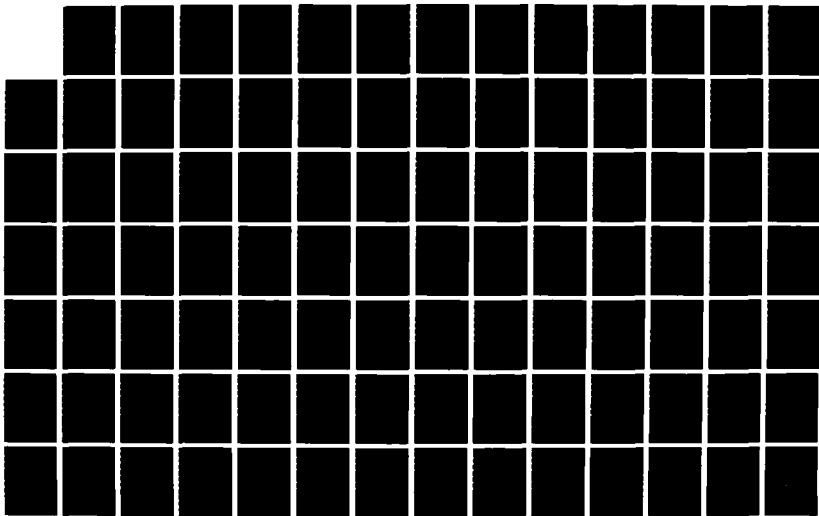
RESEARCH ON HIGH-SPECIFIC-HEAT DIELECTRICS(U)
CERAMPHYSICS INC WESTERVILLE OH M N LAWLESS ET AL.
11 MAY 87 AFOSR-TR-87-1452 F49620-86-C-0049

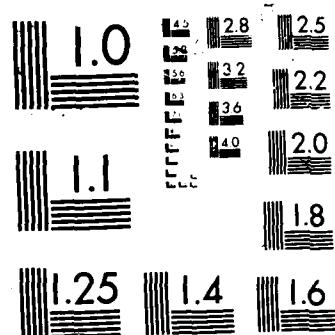
2/2

UNCLASSIFIED

F/G 11/2

NL





(absolute) values for dx/dT in ZCN(9/1) at $T \sim T_N$ in Fig. 4-37(b).

Free Spin Densities. As a final exercise, we consider the free-spin density n_p computed from Eq.(4-13). The magnetocaloric data used here to obtain ΔS_0 are taken at the highest field strength, 15 T, and the $\mu_0 dx/dT$ vs. H phase diagrams suggest that this field strength is very near the saturation level at certain temperatures. The free-ion spin value, $s = 3/2$, was used here. These computed n_p vs. T data for the four samples are shown in Fig. 4-38. Only one point each for the spinel + columbite ceramic is shown in Fig. 4-38 (i.e., at 15 T).

The n_p data in Fig. 4-38 at temperature above T_N are surprisingly consistent for CdCr_2O_4 and ZnCr_2O_4 , $n_p \approx 0.04$, but far below the expected value of $n_p = 2$. To bring these data into line with $n_p = 2$ requires $s \sim 6 \times 10^{29}$.

The data for n_p at temperatures well below T_N are also surprisingly consistent for all four samples in Fig. 4-38, $n_p \approx 0.003$ - 0.007 . The data for CdCr_2O_4 in Fig. 4-38 do not extend below 7 K because it will be recalled that there is a field-enforced crossover in the sign of dx/dT for this material at the lower temperatures.

We point out that Eq.(4-13) is not strictly valid at temperatures below T_N . Namely, in the simple two-spin model the uncorrelated free spins contribute a $dx/dT < 0$ component, the correlated spins contribute a $dx/dT > 0$ component. Consequently, n_p below T_N is a measure of the net uncorrelated spins.

E. Conclusions from Thermal Data

A large amount of experimental data have been measured on the same compacted disks of CdCr_2O_4 and ZnCr_2O_4 -- zero-field specific heat data, field-dependent specific heat data, and magnetocaloric data. The magnetocaloric data have been reduced and presented in the form of phase diagrams. The zero-field specific heat data have been analyzed in terms of Schottky and spinwave models. Finally, all the magnetocaloric data have been

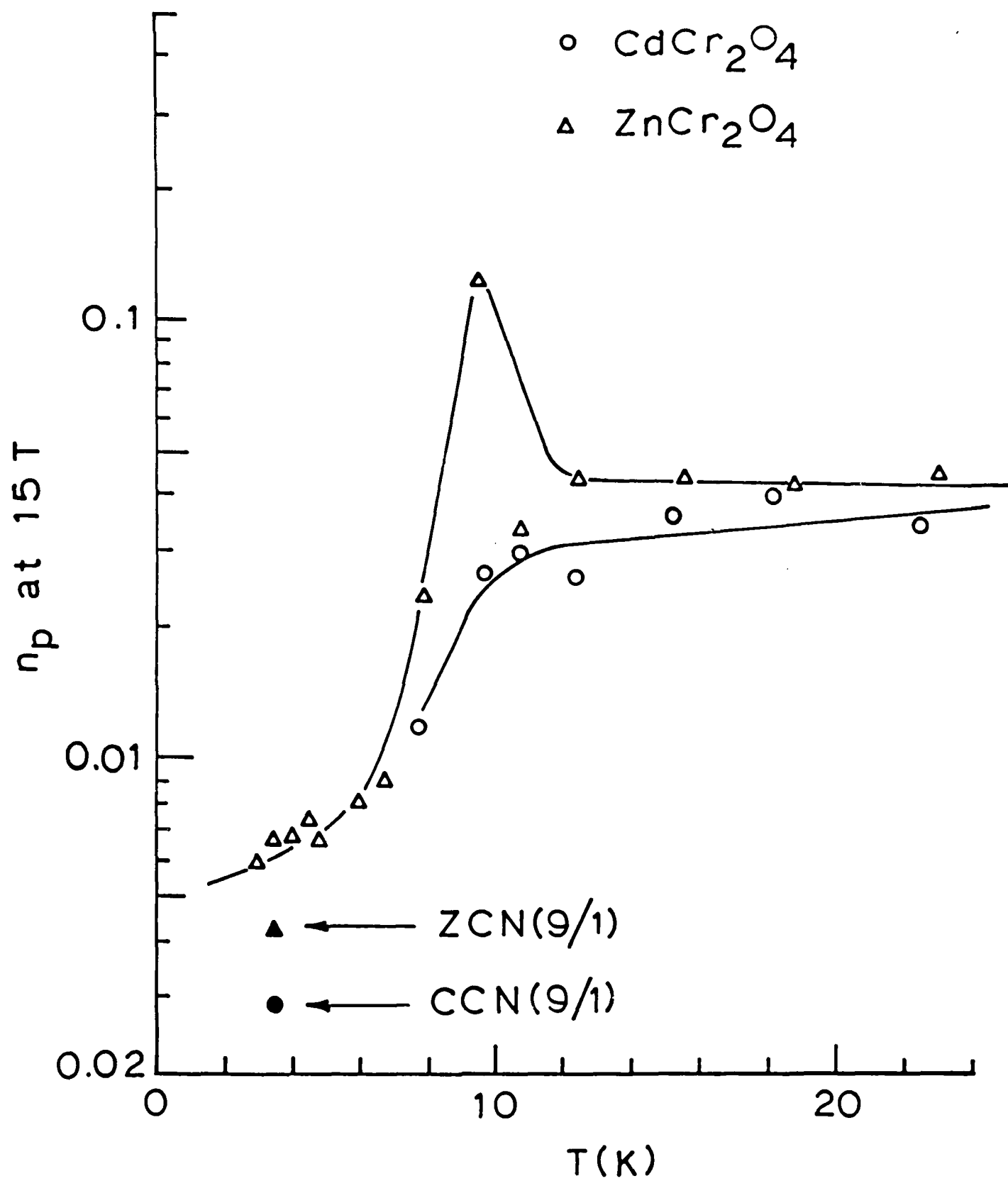


Figure 4-38. Free spin densities at 15 T as a function of temperature according to Eq.(4-13).

analyzed according to the TdS equation, making use of the specific heat data. In what follows below, the results of all these studies are summarized:

1. In contrast to ZnCr_2O_4 , $\text{CCN}(9/1)$, and $\text{ZCN}(9/1)$, the CdCr_2O_4 disk:
 - (a) Does not display a sharp maximum in the specific heat;
 - (b) Displays a field-enforced crossover between $d\chi/dt > 0$ and $d\chi/dT < 0$ below T_N ; and
 - (c) Exhibits a substantial hysteretic component below T_N in the magnetocaloric data.
2. Except at the lowest temperatures, there is a great deal of similarity in the ΔT_r phase diagrams of CdCr_2O_4 and $\text{CCN}(9/1)$, Fig. 4-25. The corresponding diagrams for the zinc spinels are not similar, Fig. 4-31.
3. Both CdCr_2O_4 and $\text{CCN}(9/1)$ exhibit magnetization cooling in a limited temperature range at and below T_N , Fig 4-25; in contrast, ZnCr_2O_4 and $\text{ZCN}(9/1)$ exhibit magnetization heating at all temperatures, Fig. 4-31.
4. Both CdCr_2O_4 and ZnCr_2O_4 show strong, nonlinear departure from the linear relation Eq.(4-9), as seen in Figs. 4-34(b) and 4-36(b). This was unexpected, given the linear M vs. H data in Fig. 2-4, and frustrates meaningful comparisons with the low-field susceptibility data in Section V below.
5. Specific heat data for CdCr_2O_4 and $\text{CCN}(9/1)$ are both consistent with a T^3 antiferromagnetic spin-wave contribution at the lowest temperatures and a $\theta_D = 420$ K acoustic-mode contribution.
6. Specific heat data for ZnCr_2O_4 and $\text{ZCN}(9/1)$ are both consistent with a T^3 antiferromagnetic spin-wave contribution at the lowest temperatures and a $\theta_D \sim 450$ K acoustic mode contribution.
7. For both the cadmium and zinc spinels, the Debye temperatures are in excellent agreement with predictions from the Lindemann equation.
8. From the $T > T_N$ Schottky fits to the specific heat data of all four samples, there is satisfactory agreement for the

number of spins partaking in the transition at T_N between CdCr_2O_4 and $\text{CCN}(9/1)$ and between ZnCr_2O_4 and $\text{ZCN}(9/1)$.

9. From the $T < T_N$ Schottky fits to the specific heat data, the densities of free spins in the disks of CdCr_2O_4 and ZnCr_2O_4 are ~ 5 - 7 times larger than in the densified ceramics $\text{CCN}(9/1)$ and $\text{ZCN}(9/1)$. This is in semi-quantitative agreement with the magnetocaloric data here based on entropy arguments, Fig. 4-38. On the other hand, the low-field dc susceptibility data below suggest that the ceramics $\text{CCN}(9/1)$ and $\text{ZCN}(9/1)$ have the larger densities of free spins.
10. From the spin-wave terms in the specific heats below T_N , the densities of the antiferromagnetically correlated spins are much larger in the disks of CdCr_2O_4 and ZnCr_2O_4 than in the ceramics of $\text{CCN}(9/1)$ and $\text{ZCN}(9/1)$, respectively. Nonetheless, the spin-wave terms do indicate that magnetization cooling should be more pronounced in the cadmium spinel than in the zinc spinel, in agreement with the magnetocaloric data [We draw attention to the assumption made in analyzing the specific heat that the zero-field splitting, etc. is the same in both forms of CdCr_2O_4 (and ZnCr_2O_4), whereas in fact different stress conditions exist in the two forms].
11. In the paramagnetic region, $T > T_N$, for both CdCr_2O_4 and ZnCr_2O_4 and for magnetic field strengths at or very near saturation (15 T), the densities of free spins estimated from entropy arguments are ~ 0.04 -- i.e., ~ 50 times smaller than anticipated, Fig. 4-38.
12. In all the thermodynamic analyses here, the field dependence of the specific heat has been ignored (i.e., $C_H \approx C_O$). This is not a serious assumption because $C_H/C_O \lesssim 35\%$ near T_N at 10 T, Fig. 4-13.

V. MAGNETIC SUSCEPTIBILITY AND RESONANCE STUDIES

Magnetic Susceptibility (χ) and EPR Studies

This section summarizes the magnetic susceptibility (χ) and EPR measurements on several CdCr_2O_4 - and ZnCr_2O_4 -based spinels, made (by the WVU group) with a view of providing new clues as to why these spinels exhibit exceptionally high heat capacities.

V.1 Experimental Methodology, Sample Preparation and Sample Notation

The χ measurements were made at the National Magnet Laboratory of MIT, using a SHE squid magnetometer. The EPR measurements, on the other hand, were made at West Virginia University with an IBM-Bruker Model ER-200D spectrometer which uses an ASPECT 2000 microcomputer for data acquisition and analysis.

The description of the samples, investigated in this report is given in Table 5.1 although measurements were made on many others as well.

Table 5.1 Investigated Samples

No.	Sample Name	Notation	Source
1	CdCr ₂ O ₄ (powder)	CdCr ₂ O ₄ (P)	Penn State (PS) Univ.
2	CdCr ₂ O ₄ (powder disk) ^a	CdCr ₂ O ₄ (PD)	PS Univ.
3	CdCr ₂ O ₄ (densified disk) ^b	CdCr ₂ O ₄ (DDCP)	Ceram Physics (CP)
4	CdCr ₂ O ₄ (densified disk) ^c	CdCr ₂ O ₄ (DDPS)	PS Univ.
5	ZnCr ₂ O ₄ (powder)	ZnCr ₂ O ₄ (P)	PS Univ.
6	ZnCr ₂ O ₄ (powder disk) ^a	ZnCr ₂ O ₄ (PD)	PS Univ.
7	ZnCr ₂ O ₄ (densified disk) ^d	ZnCr ₂ O ₄ (DDPS)	PS Univ.
8	ZnCr ₂ O ₄ (densified disk) ^b	ZnCr ₂ O ₄ (DDCP)	Ceram Physics

a. the powder compressed into a disk at 1290°C/1 hr for CdCr₂O₄ ($\rho = 4.4$ g/cc) and at 1650°C/1 hr for ZnCr₂O₄ ($\rho = 3.8$ g/cc) (Section III).

b. contains columbite

c. CdCr₂O₄ + 5% Nb₂O₅ heated at 1320°C/1 hr ($\rho = 5.3$ g/cc) (Section III).

d. ZnCr₂O₄ + 5% Nb₂O₅ heated at 1350°C/1 hr ($\rho = 4.87$ g/cc) (Section III).

V.2. Experimental Results on Susceptibility (χ)

V.2.a. χ vs. T

Figure 5.1 shows the temperature dependence of χ for the four samples of CdCr₂O₄, namely powder (P), powder disk (PD) and the densified disks (DDCP and DDPS). The high temperature ($T > 10$ K) behavior of P and PD is very nearly the same, as is also the case for DDCP and DDPS. However, the low temperature behavior (shown in detail in the inset), reflecting the cooperative, magnetic ordering, is different suggesting that sample preparation conditions do affect the microscopic spin arrangement in every sample.

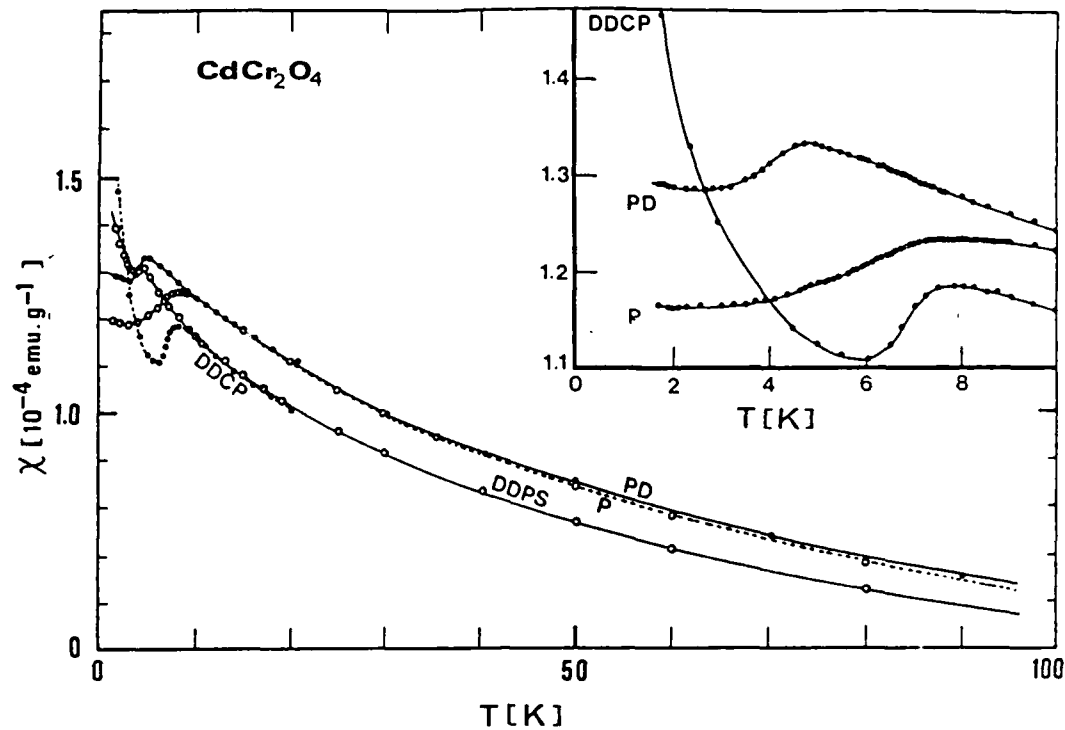


Figure 5.1 Plots of susceptibility (χ) vs. temperature (T) for the four samples of CdCr_2O_4 . The inset shows the low-temperature χ vs. T behavior.

Figure 5.2 shows the χ vs. T behavior for the various samples of ZnCr_2O_4 . It is clear that both the $T < T_N$ and the $T > T_N$ parts of the χ vs. T plots are different for different samples. All the samples except PD show a fairly well defined peak at or immediately above T_N . The PD sample exhibits a very broad peak, quite untypical of an antiferromagnetic-paramagnetic phase transition.

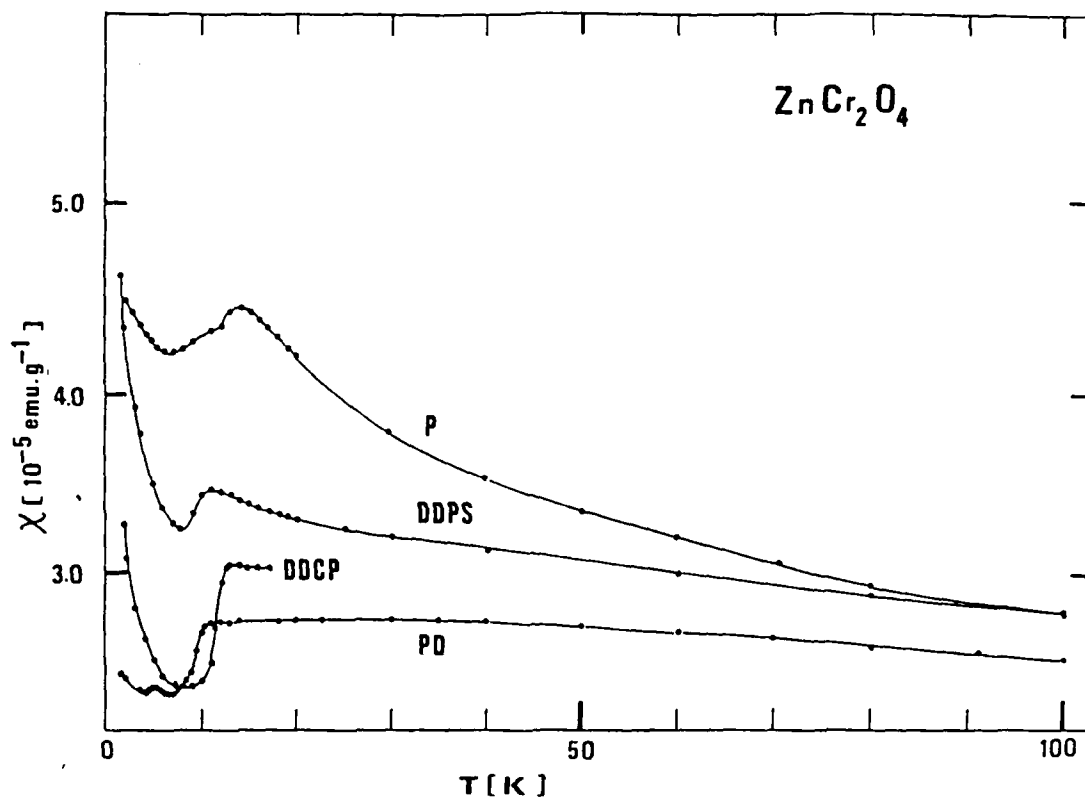


Figure 5.2. Plots of susceptibility (χ) vs. temperature (T) for the four samples of ZnCr_2O_4 .

V.2.b Magnetic field dependence of χ versus T

Figure 5.3 shows the field dependence of the χ versus T behavior for the CdCr_2O_4 PD corresponding to the applied fields of 0.2 and 20 kG. The dependence of χ on the field is quite apparent as shown by the shift in T_N towards higher temperature by ~ 0.5 K with an increase in the field from 0.2 to 20 kG; the change in the magnitude of χ being up to 5 percent. The results of χ versus T for the powder CdCr_2O_4 (P) are also shown on the same plot.

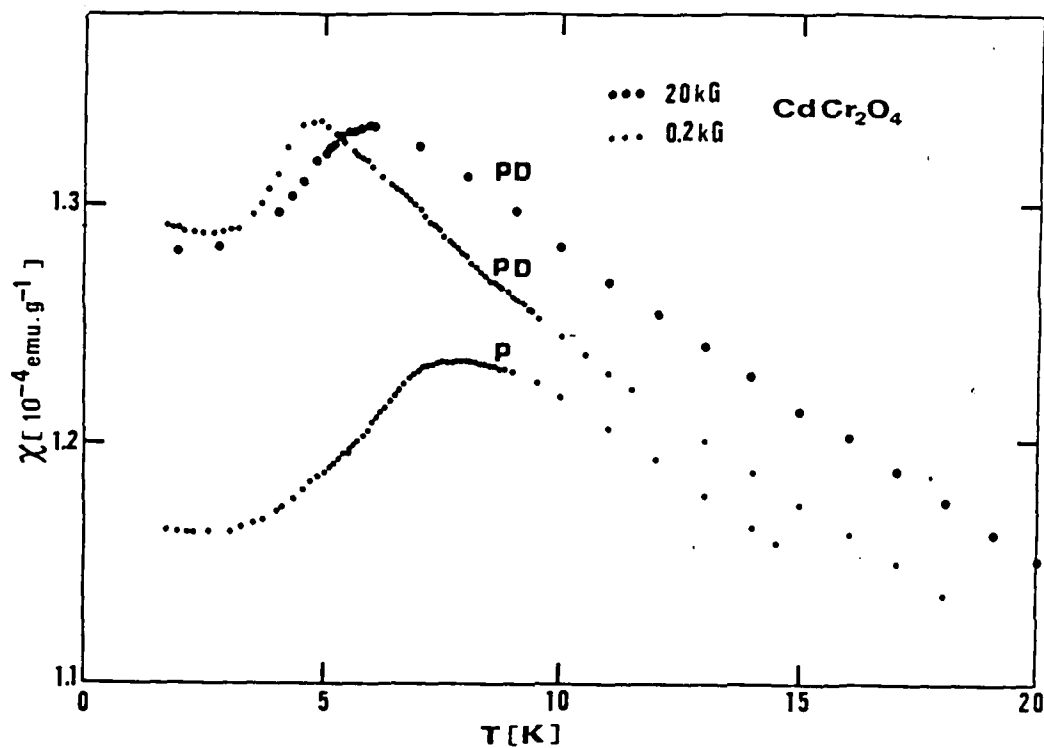


Figure 5.3. χ versus T behavior for CdCr_2O_4 (PD) in magnetic fields, of 0.2 and 20 kG. The behavior of CdCr_2O_4 (P) at 0.2 kG is also shown.

The changes in the χ versus T behavior of the ZnCr_2O_4 powder are quite dramatic as shown by the results in Figure 5.4 at the fields 0.2 and 10 kG. The features which show up markedly at 0.2 kG get suppressed considerably at 10 kG.

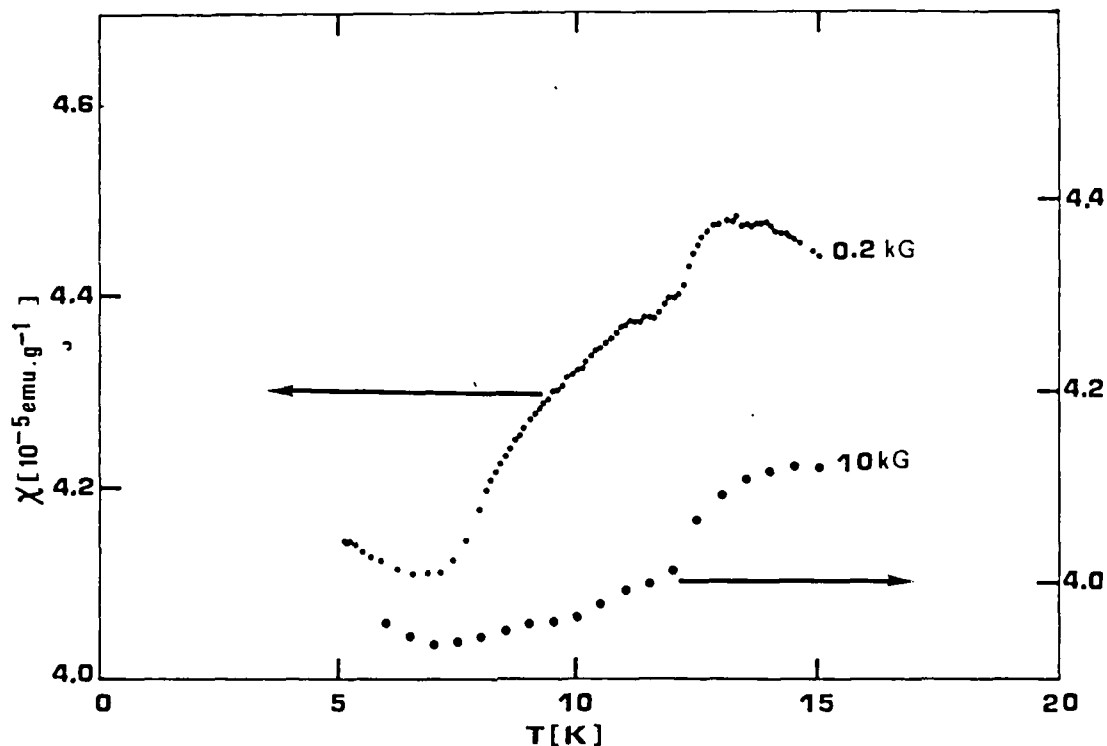


Figure 5.4. χ versus T behavior for ZnCr_2O_4 (P) in two fields of 0.2 and 10 kG.

V.2.c χ versus T in zero field cooling

Since the χ vs. T behavior was found to depend on the field, and in all the measurements the samples were field-cooled, it was decided to cool the samples in zero field for χ measurements. Results of this experiment (Figure 5.5) on ZnCr_2O_4 (PD) from 6 K to 20 K, exhibit the same behavior as that of Figure 5.2 except that the χ values for the zero-field-cooled samples are at least 25% larger in magnitude. The first derivative of χ w.r.t. T , which gives

the Neel temperature, is however at the same temperature, 9.4 ± 0.1 K (within experimental accuracy), as in the field-cooled case.

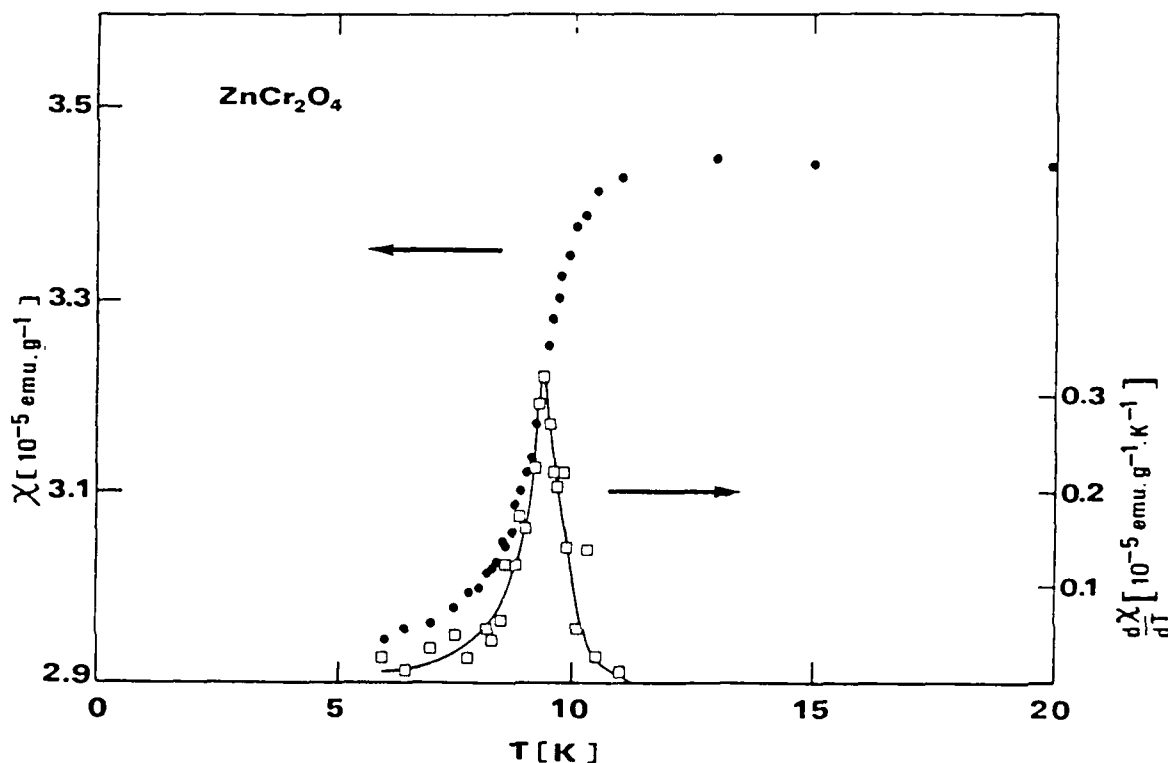


Figure 5.5. χ versus T behavior for ZnCr_2O_4 (PD) when the sample was cooled in zero field. The curve peaking at 9.4 ± 0.1 K shows the temperature dependence of $d\chi/dT$.

V.2.d Magnetic field (H) dependence of magnetization (M)

To find if these systems exhibit any spin-flop transition, the magnetization (M) was studied as a function of H, up to 45 kG. Figure 5.6 shows the M vs. H plot for a PD sample of CdCr_2O_4 , the same sample as for Figure 5.3. For this sample, a linear dependence of M on H is seen at 10 K ($T > T_N$) with no

measurable intercept on the $H = 0$ axis. At $T = 1.91$ K, however, a small but finite intercept was detected. This small value of the intercept was found to be sample dependent, since another sample examined did not yield a measurable intercept, as may be seen from Figure 5.7.

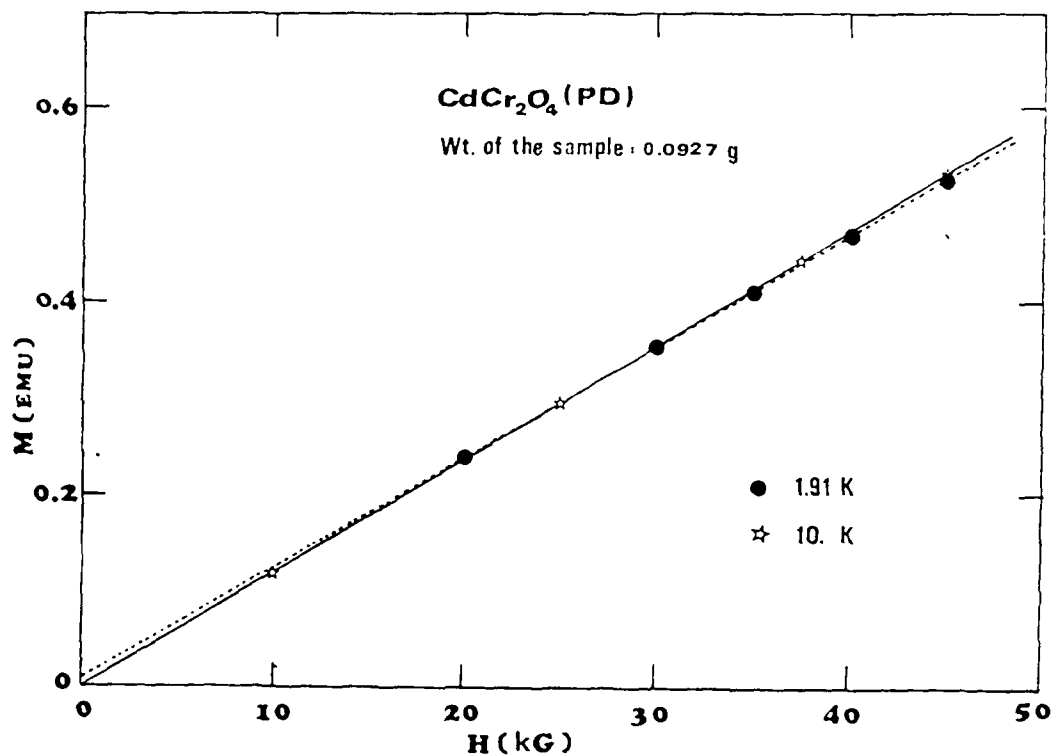


Figure 5.6. Typical M vs. H behavior for a powdered disk (PD) sample of CdCr_2O_4 .

Similar results were obtained for a powdered disk (PD) sample of ZnCr_2O_4 . The results are shown below, Figure 5.7.

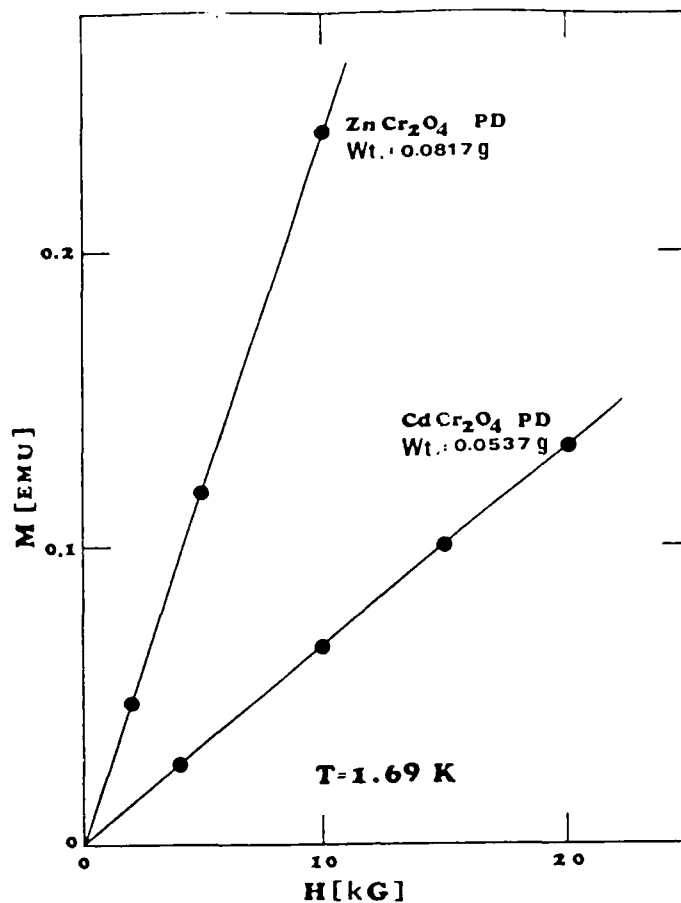


Figure 5.7. M vs. H behavior of a powdered disk (PD) sample of ZnCr_2O_4 .

V.3 EXPERIMENTAL EPR RESULTS

As the complement to the magnetic susceptibility data, EPR measurements were made above liquid nitrogen temperatures for all the samples listed in Table 5.1. For some samples, the measurements were made both in the X-band ($\sim 9.5 \times 10^9 \text{ Hz}$) and Q-band ($33.5 \times 10^9 \text{ Hz}$) regions to measure the spin dynamics.

The lineshape analysis of all the investigated samples shows the lines nearer to a Lorentzian than a Gaussian, over the temperature range 80–400 K. The lines are mainly exchange narrowed.

The EPR dependence of the peak-to-peak linewidth (ΔB_{pp}) for the powder samples of CdCr_2O_4 and ZnCr_2O_4 is shown in Fig. 5.8. This plot corresponds to

the Q-band microwave frequencies and the values for ΔB_{pp} agree with those obtained using X-band frequencies. The data for other samples (PD, DDPS, DDCP) is plotted in Fig. 5.9. The linewidth increases smoothly with decrease in temperature for all the samples except CdCr_2O_4 (DDCP) which showed a some-sort-of discontinuity around 305 K. This was shown to be due to the presence of some Cr_2O_3 which has an antiferromagnetic transition around 308 K.

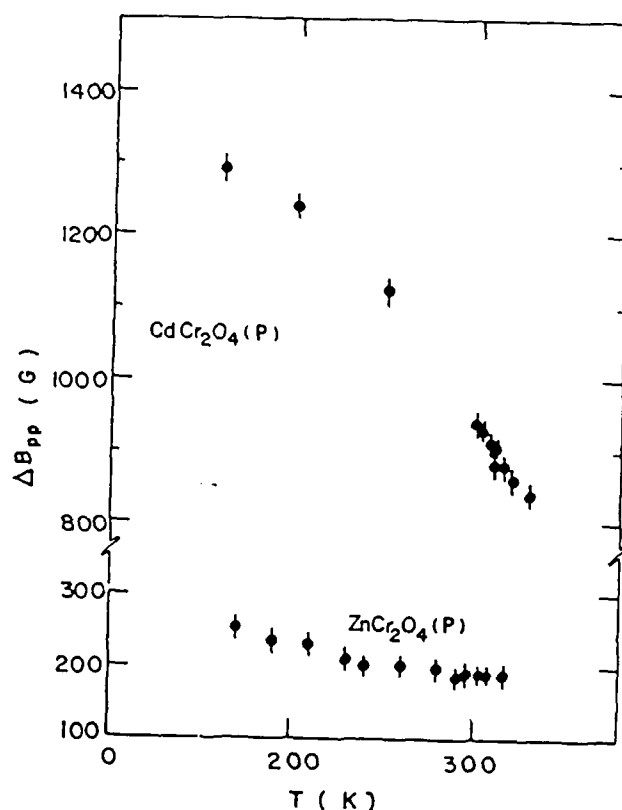


Figure 5.8 Dependence of the EPR peak-to-peak linewidth (ΔB_{pp}) as a function of temperature (T) for the spinel powders.

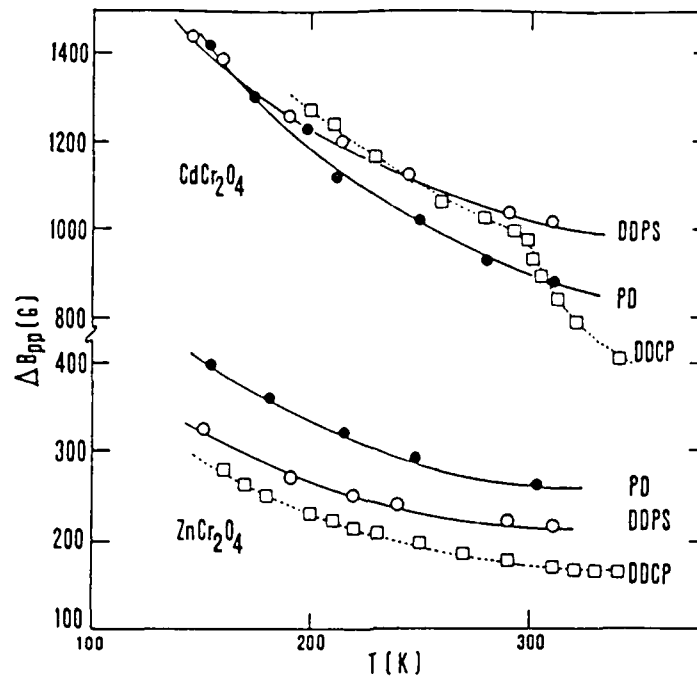


Figure 5.9 Dependence of the EPR linewidth ΔB_{pp} as a function of temperature (T) for the CdCr_2O_4 and ZnCr_2O_4 samples.

V.4 ANALYSIS OF THE χ -DATA

V.4.a Neel Temperature (T_N)

The Neel temperatures were obtained to within ± 0.1 K, as the temperatures corresponding to peaks in the $(d\chi/dT)$ vs. T plots, using the earlier discussed χ vs. T plots as the base data. Figures 5.10 and 5.11 show the $(d\chi/dT)$ vs. T plots for CdCr_2O_4 and ZnCr_2O_4 respectively.

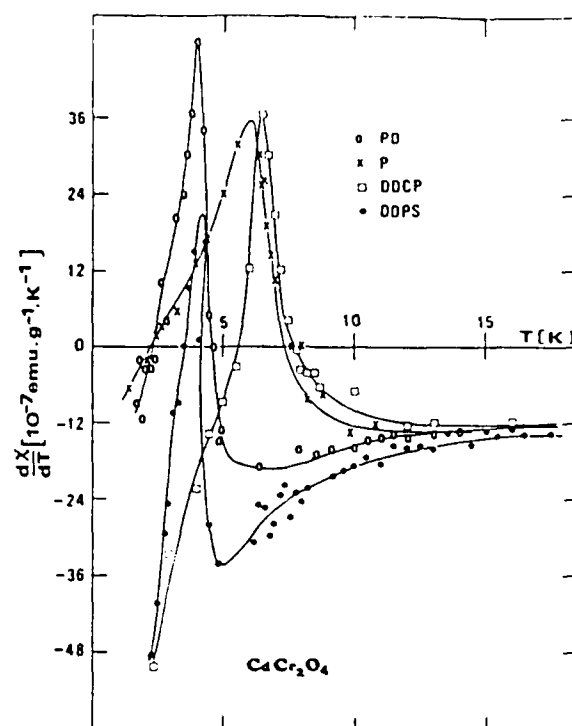


Figure 5.10. Plots of $d\chi/dT$ versus T for the four samples of CdCr_2O_4 .

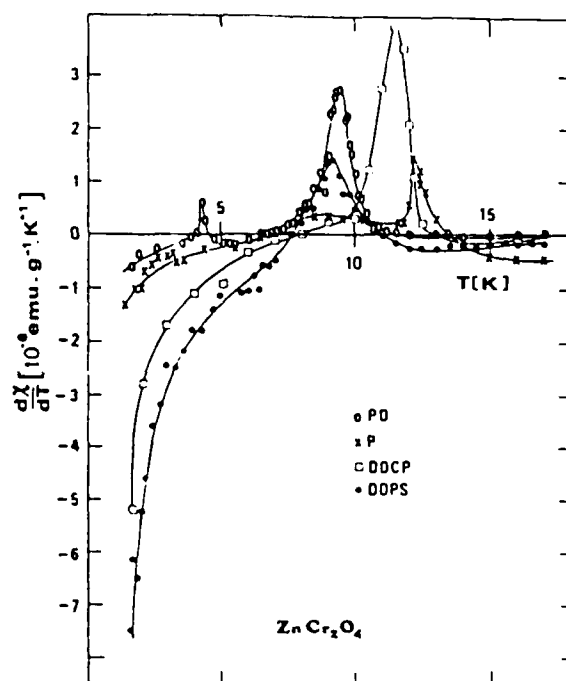


Figure 5.11. $d\chi/dT$ versus T for ZnCr_2O_4 samples.

Figures 5.12 and 5.13 summarize the Neel temperature for different samples of CdCr_2O_4 and ZnCr_2O_4 , including the available literature values (Friedberg and Burk, 1955; Baltzer et al., 1966; Lotgering, 1966; Oles, 1970; Plumier, 1977). It is not clear why the values of T_N obtained from our χ measurements are always lower by up to 2 K from those obtained via specific heat measurements.

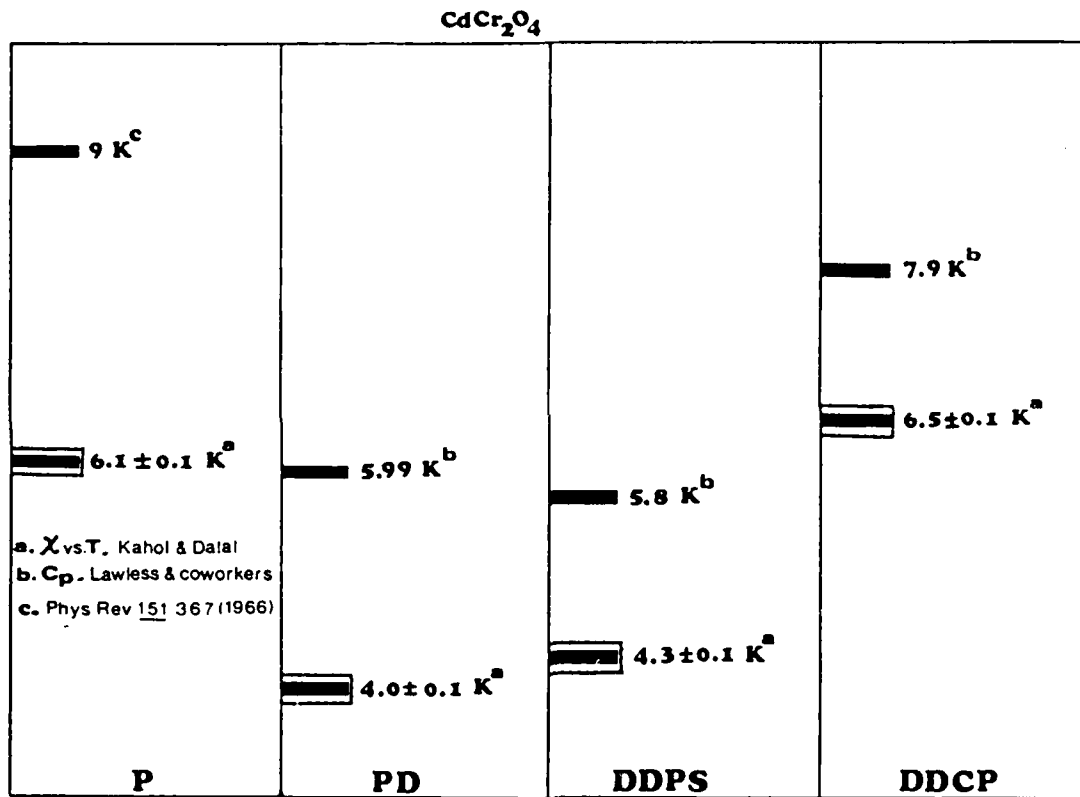


Figure 5.12. Schematic display of the Neel temperatures for CdCr_2O_4 samples.

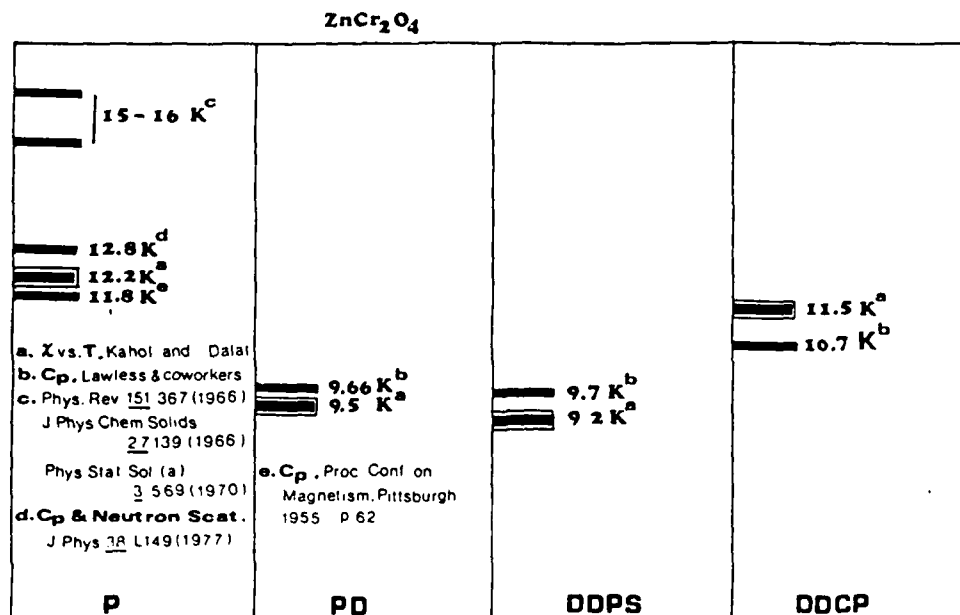


Figure 5.13. Schematic display of the Neel temperatures for ZnCr₂O₄ samples.

V.4.b Susceptibility behavior for $T > T_N$

Since CdCr₂O₄ and ZnCr₂O₄ are known to undergo antiferromagnetic orderings at T_N , the temperature dependence of χ for $T > T_N$ is expected to obey the Curie-Weiss law

$$\chi = \frac{C_{af}}{T - \theta} \quad T > T_N \quad (V.1)$$

where $C_{af} = N\mu^2/3k$ with N defined as the number of spins, μ the effective magnetic moment of the spins and k the Boltzmann constant. A plot of $1/\chi$ versus T would thus be a straight line with its slope equal to $1/C_{af}$ and the intercept equal to $-\theta/c$. Experimental results of $1/\chi$ versus T for the CdCr₂O₄ samples are shown in Figure 5.14. Linear behavior is indeed observed but only for $T > 5 T_N$.

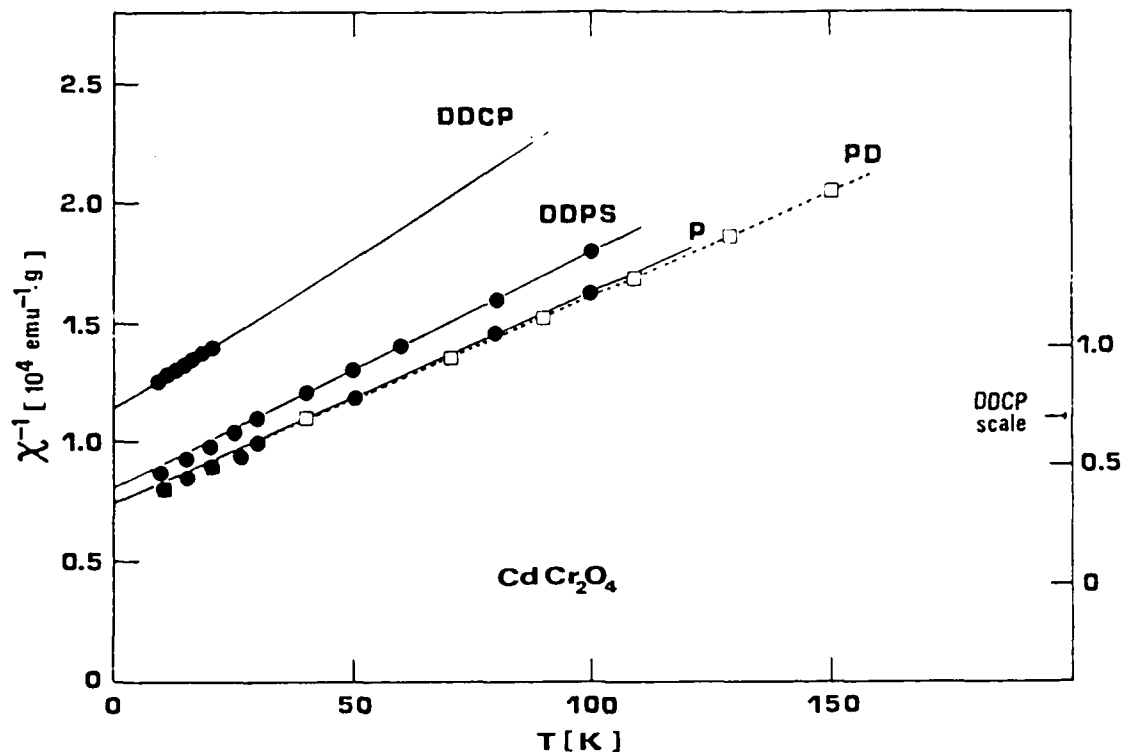


Figure 5.14. $1/\chi$ versus T for CdCr_2O_4 samples at $T > T_N$.

This result clearly implies the existence of short-range order between the spins for $T_N < T < 5 T_N$. The values of θ and C_{af} thus obtained are listed in Table 5.2.

Table 5.2. Values of the parameters C_{af} and θ obtained by fitting the $T \gg T_N$ data of CdCr_2O_4 samples to the expression $\chi = C_{af}/T - \theta$

	$C_{af} [\text{emu} \cdot \text{K} \cdot \text{g}^{-1}]$	$\theta [^\circ]$
powder	1.2×10^{-2}	-83
powder [*]	-	-83
powder disk (PD)	1.14×10^{-2}	-84
DDPS	1.10×10^{-2}	-80
DDCP	0.81×10^{-2}	-60

[*] Baltzer et al., Phys. Rev. 151, 367 (1966).

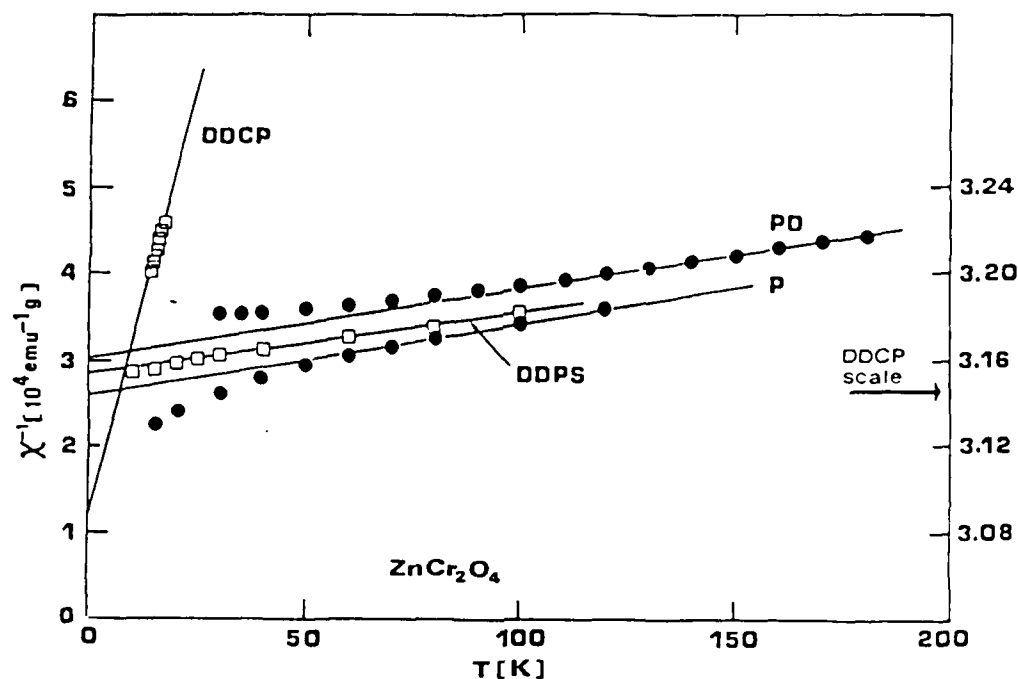


Figure 5.15. $1/\chi$ versus T for ZnCr_2O_4 samples at $T > T_N$.

The data for the various samples of ZrCr_2O_4 were also plotted as $(1/\chi)$ versus T (Figure 5.15) and yielded the parameters C_{af} and θ as given in Table 5.3. An overwhelming presence of short-range spin order can clearly be seen for all the samples.

Table 5.3. Values of the parameters C_{af} and θ obtained by fitting the high temperature data of ZnCr_2O_4 samples to the expression $\chi = C_{af}/T - \theta$

	C_{af} [$\text{emu} \cdot \text{K} \cdot \text{g}^{-1}$]	θ [K]
powder	1.17×10^{-2}	-331
powder [*]	-	-392
powder disk (PD)	1.30×10^{-2}	-396
DDPS	1.43×10^{-2}	-407
DDCP	1.26×10^{-2}	-389

[*] Baltzer et al., Phys. Rev. 151, 367 (1966).

V.4.c Susceptibility behavior below T_N

One region of particular interest below T_N is where χ increases with a decrease in temperature, the Curie-like behavior. This is believed to be due to the presence of "free" paramagnetic Curie-like spins. Assuming that the contribution to χ from the antiferromagnetically-ordered spins is independent of temperature in the range $0 \leq T < 0.5 T_N$, the experimental data can be fitted to the following expression

$$\chi = \chi_0 + C_{\text{para}}/T \quad T < T_N \quad (\text{V.2})$$

where $\chi_0 = \chi(T \rightarrow 0)$ and $C_{\text{para}} = N\mu^2/3k$. A plot of χ versus $1/T$ would thus yield C_{para} and hence the number of paramagnetic spins. The plots of χ versus $1/T$ are given in Figures 5.16 and 5.17 for CdCr_2O_4 and ZnCr_2O_4 samples, respectively. The values of χ_0 and C_{para} , obtained from the slopes of these plots, are collected in Tables 5.4 and 5.5.

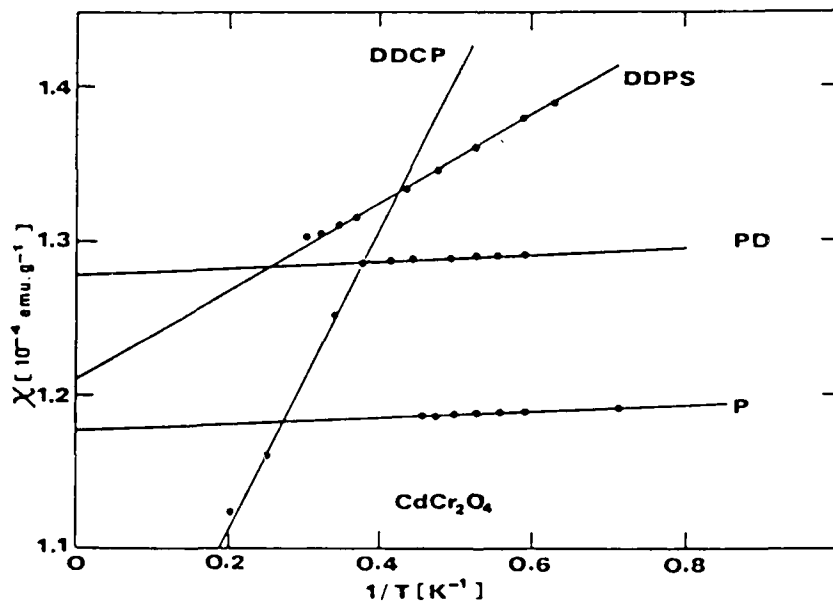


Figure 5.16. χ versus $1/T$ for CdCr_2O_4 samples.

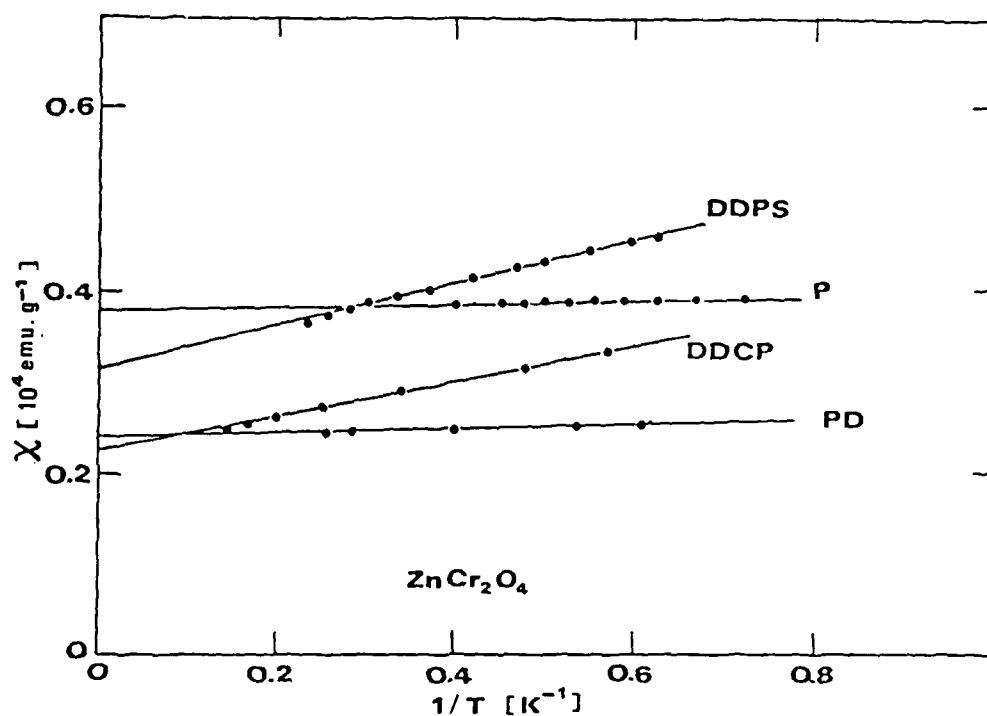


Figure 5.17. χ versus $1/T$ for ZnCr_2O_4 samples.

Table 5.4. Values of the parameters χ_0 and C_{para} obtained by fitting the low temperature data of CdCr_2O_4 samples to the expression $\chi = \chi_0 + C_{\text{para}}/T$.

CdCr_2O_4	χ_0 ($\text{emu} \cdot \text{g}^{-1}$)	C_{para} ($\text{emu} \cdot \text{K} \cdot \text{g}^{-1}$)
powder	1.18×10^{-4}	1.96×10^{-6}
PD	1.28×10^{-4}	2.14×10^{-6}
DDPS	1.21×10^{-4}	2.86×10^{-5}
DDCP	0.92×10^{-4}	9.60×10^{-5}

Table 5.5. Values of the parameters χ_0 and C_{para} obtained by fitting the low temperature data of ZnCr_2O_4 samples to the expression $\chi = \chi_0 + C_{\text{para}}/T$.

ZnCr_2O_4	χ_0 ($\text{emu} \cdot \text{g}^{-1}$)	C_{para} ($\text{emu} \cdot \text{K} \cdot \text{g}^{-1}$)
powder	0.38×10^{-4}	1.43×10^{-6}
PD	0.24×10^{-4}	2.50×10^{-6}
DDPS	0.32×10^{-4}	2.33×10^{-5}
DDCP	0.22×10^{-4}	1.92×10^{-5}

V.4.d "Free" spin concentration

An important parameter deduced from the above analysis is the fraction of the "Curie-like" or the "free" spins, as given by the ratio $C_{\text{para}}/C_{\text{para}} + C_{\text{af}}$. Tables 5.6 and 5.7 list the fraction of the "free" spins in the various samples of CdCr_2O_4 and ZnCr_2O_4 respectively. It is clear that the densified disks made by Ceram Physics have the maximum number of "free" spins.

Table 5.6. Fraction of the "free" spins in various samples of CdCr_2O_4

	$C_{\text{para}}/C_{\text{para}} + C_{\text{af}}$
PD	1.9×10^{-4}
DDPS	2.6×10^{-3}
DPCP	1.2×10^{-2}

Table 5.7. Fraction of the "free" spins in various samples of ZnCr_2O_4

	$C_{\text{para}}/(C_{\text{para}} + C_{\text{af}})$
PD	1.9×10^{-4}
DDPS	1.6×10^{-3}
DDCP	1.5×10^{-3}

V.5 ANALYSIS OF THE EPR DATA

Due to experimental difficulties in obtaining reliable data for temperatures below ~ 80 K, we did not attempt to analyze the EPR linewidths quantitatively using rigorous expressions. This must await a little longer when we expect to obtain extensive lineshape data at liquid helium temperatures.

Nevertheless, it is fairly clear from the magnitudes of the peak-to-peak linewidths (ΔB_{pp}) for the CdCr_2O_4 and ZnCr_2O_4 samples (Figures 5.8 and 5.9) that the exchange narrowing is 4-5 times more effective in ZnCr_2O_4 than CdCr_2O_4 samples. This is essentially what is expected from the susceptibility analysis above T_N , since the values of the paramagnetic temperature θ for ZnCr_2O_4 and CdCr_2O_4 samples are ~ 390 and ~ 80 K respectively. The value of J , the exchange constant, which is directly proportional to θ is thus about 5 times larger in ZnCr_2O_4 samples. The EPR results thus provide a direct support for the essential correctness of the basic model for the temperature dependence of χ in all these samples.

V.6 DISCUSSION

In this section, we make a critical evaluation of the implications of the χ -data with regard to the extensive results of the specific heat and magnetocaloric experiments. We focus our attention on two samples, PD and DDCP, for which a complete set of measurements is available.

V.6.a Magnetocaloric vs. Magnetic Susceptibility Results

ΔT_r , the reversible part of the magnetocaloric change in temperature, has been found to go through a narrow negative range (implying magnetization cooling) for both the PD and DDCP samples of CdCr_2O_4 (Section IV). Whilst the magnitude of ΔT_r in this range (magnetization cooling) is nearly the same for the PD and DDCP samples, ΔT_r is much larger for DDCP than for PD below T_N (magnetization heating). Recall that magnetization heating results from the

"free" spins whilst magnetization cooling from the "ordered" spins. The presence of ~50 times more "free" spins in DDCP than in PD, as shown by the susceptibility measurements (Table 5.3), is in line with much larger ΔT_r for DDCP than PD. As for the magnetization cooling around T_N , we can speculate that the "ordered" spins dominate the magnetization heating effects of the "free" spins and give rise to negative ΔT_r . Since the amount of magnetization cooling is nearly the same in both PD and DDCP, one would expect the same concentration of the "ordered" spins for the two cases, provided the exchange coupling constant (J) among the ordered spins remains the same. That the exchange coupling constants are not the same for PD and DDCP samples of CdCr_2O_4 can be seen from the different values of θ (Table 5.2); note that J is related to θ via the expression $|J| = 3k_B\theta/2zS(S+1)$ where z is the number of nearest neighbor spins. If the dependence of ΔT_r on J , T and the spin concentration of the ordered spins were known, the ratio of the ordered spins at T_N in PD and DDCP can be calculated. It seems, however, that ΔT_r depends rather strongly on T since the magnetocaloric cooling disappears rapidly as we go from T_N to lower temperatures.

In the case of ZnCr_2O_4 , ΔT_r does not assume negative values i.e., it shows only magnetization heating. This implies that here the free spins dominate the ordered spins. Susceptibility results (Figure 5.2) especially for PD, show clearly that around T_N significant amount of short-range order (or lack of long-range order) exists in these materials (see also Figure 5.13). This could be the explanation for the absence of magnetization cooling effects.

In a recent report Lawless and Munson (Section IV) have derived, using standard thermodynamic relationships, $(d\chi/dT)$ plots from the temperature dependence of ΔT_r . The $(d\chi/dT)$ behavior for the CdCr_2O_4 samples as obtained

from the ΔT_r measurements is that $d\chi/dT$ is negative at $T \ll T_N$, becomes positive around T_N , becomes negative for $T > T_N$, and that $d\chi/dT$ is highly field dependent. For ZnCr_2O_4 , on the other hand, $d\chi/dT$ always remains negative and shows a negative peak around T_N . These data may be compared with the $d\chi/dT$ values as obtained from direct measurements of χ and shown in Figures 5.10 and 5.11 for all the four samples (namely P, PD, DDCP and DDPS). As may be noted from Figures 5.10 and 5.11, all the samples of ZnCr_2O_4 do show a behavior similar to that for CdCr_2O_4 samples in contrast to the results from the magnetocaloric measurements. We note, however, that the susceptibility (χ) measurements were made at 200 G whilst the magnetocaloric experiments were done at much higher fields, which makes it difficult to make more definitive comments since the susceptibility behavior has been found to change significantly for the ZnCr_2O_4 powder by going from 0.2 kG to 10 kG (Figure 5.4).

V.6.b Specific Heat vs. χ Data

We now compare the χ results with those from the specific heat analysis (Section IV). As shown in Figures 5.12 and 5.13, the T_N values from the specific heat curves are always higher than those obtained from the χ data. For a simple antiferromagnetic, it is known that the magnetic specific heat is given by the Fisher relation (Fisher 1962).

$$C_m = A \frac{\partial(\chi T)}{\partial T} \quad (\text{V.3})$$

where A is expected to be a slowly varying function of T around T_N . Figures 5.18 and 5.19 show the temperature dependence of C_m for CdCr_2O_4 and ZnCr_2O_4 (PD), respectively. Here A has been assumed to be temperature

independent and has been chosen arbitrarily. The C_m versus (T/T_N) plots peak at nearly the same T as in the $(d\chi/dT)$ plots. To analyze these data we assume that (i) the Debye contribution to C_p is small up to T_N , (ii) the Schottky

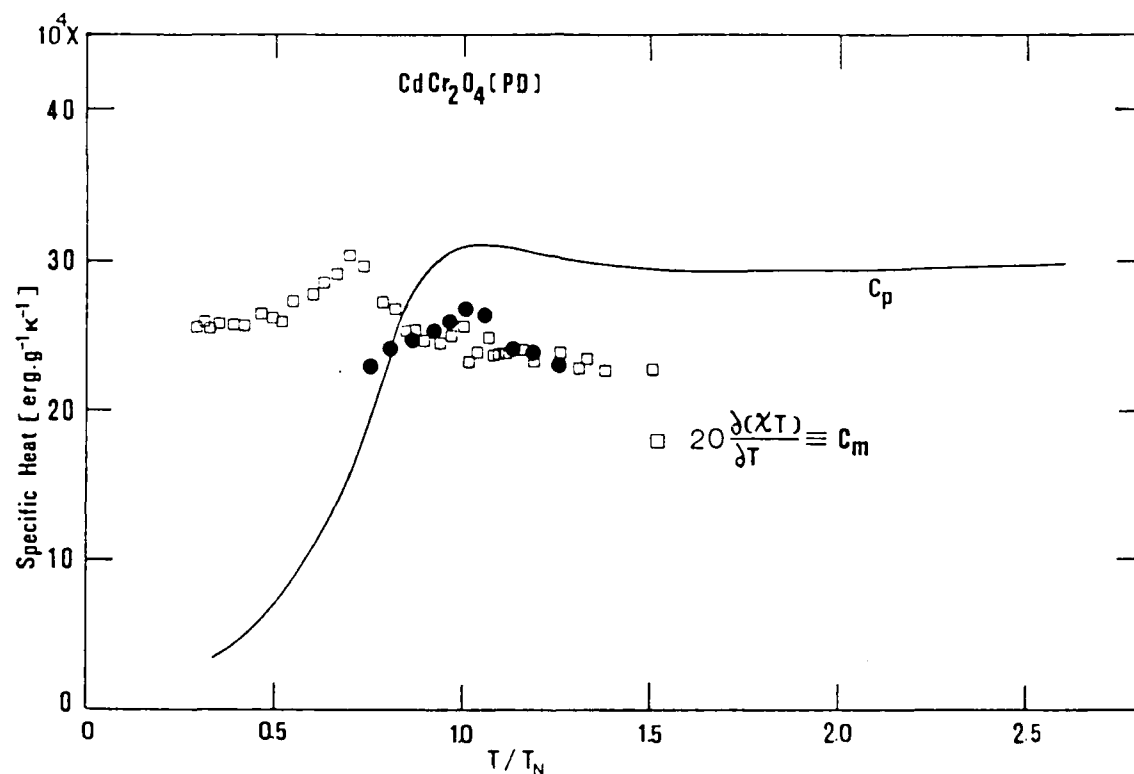


Figure 5.18. Comparison of the specific heat C_p (continuous line curve) with the magnetic specific heat C_m (open squares) for CdCr_2O_4 (PD) by setting $A = 20$. Circles denote the same data (C_m) with a different value of A and after renormalizing C_p and C_m at $(T/T_N) = 0.8$.

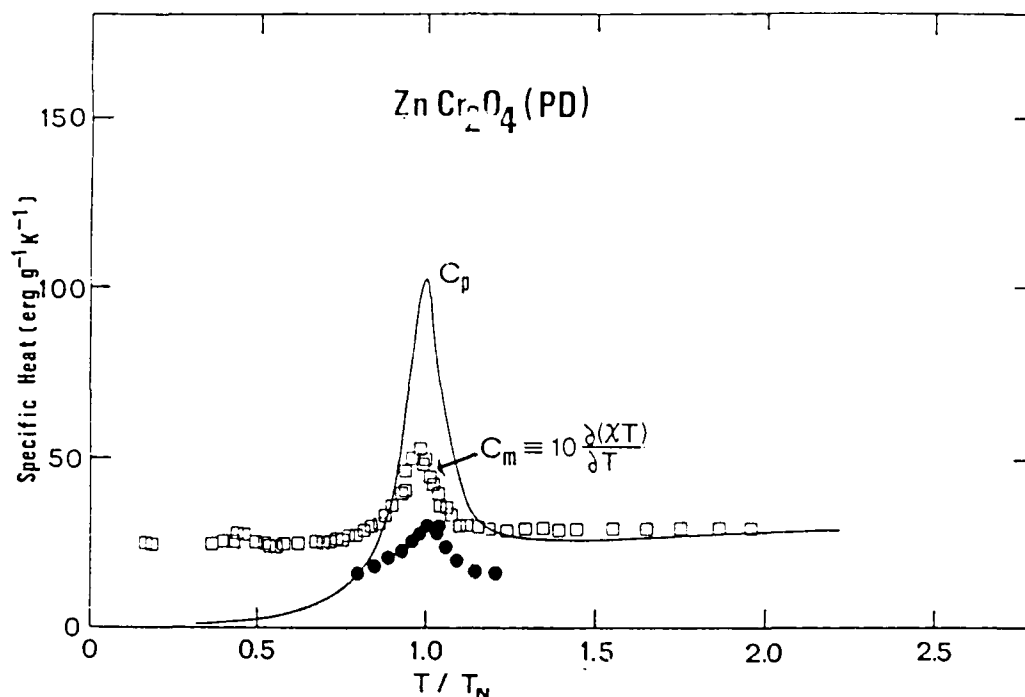


Figure 5.19. Comparison of the specific heat C_p (continuous curve) with the magnetic contribution C_m (open squares) for ZnCr_2O_4 ; the parameter A was set to 10. Circles denote the same data (C_m) with a different A and after renormalizing C_p and C_m at $(T/T_N) = 0.8$.

inversely as the square of the temperature and is small around T_N and (iii) the Fisher relation remains valid for $T/T_N = 1.0 \pm 0.2$ for a simple antiferromagnet. We further assume that at $(T/T_N) = 0.8$, $C_p = C_m$. Choosing $A = 17.64$ instead of the arbitrary number 20 and scaling the C_m data such that it peaks at $(T/T_N) = 1$ yields data points shown by closed circles. Similarly for the ZnCr_2O_4 PD, choosing $A = 5.47$ instead of 10 and scaling the C_m data the closed circles are obtained. An observed significant disagreement for the ZnCr_2O_4 sample than for the CdCr_2O_4 sample, when compared with the C_p data, indicated that the spin

ordering in ZnCr_2O_4 samples are more complicated than for the CdCr_2O_4 samples. Recalling that the $(1/\chi)$ versus T plots of Figure 5.15 indicated persistence of short-range order up to $T \approx 5 T_N$, we deduce that this postulated complicated spin ordering might be the explanation for the behaviors found in Figures 5.15 and 5.19. On the other hand, the CdCr_2O_4 PD seems to behave in a much more expected way as also reflected by the $1/\chi$ versus T plots of Figure 5.14.

Lawless (Section IV) has analyzed the specific heat data by taking into account the Debye (D), spin-wave (SW) and Schottky contributions. That is,

$$C_p = (m_{\text{SW}} + m_{\text{D}})T^3 + b/T^2 \quad (\text{V.4})$$

or

$$C_p T^2 = (m_{\text{SW}} + m_{\text{D}})T^5 + b \quad (\text{V.5})$$

Thus a plot of $C_p T^2$ versus T^5 is expected to be a straight line, and is indeed found to be so. Let us look at the implications of this analysis in the light of our susceptibility results.

A Schottky type analysis of the C_p data for $T > T_N$ (i.e. a linear plot of $C_p T^2$ versus T^5) yields b which is proportional to n , the density of the paramagnetic spins. (Note that the ordered spins behave like free paramagnetic spins above $T \approx T_N$). The ratio of b 's for the powder disk (PD) and the DDCP or equivalently the ratio of n (PD) and n (DDCP) is found to be 1.29 for CdCr_2O_4 and 1.09 for ZnCr_2O_4 samples. These values are in excellent agreement with our susceptibility data which independently yield the values 1.41 for CdCr_2O_4 and 1.03 for ZnCr_2O_4 .

Schottky analysis of C_p for $T < T_N$ does not, however, give results consistent with the susceptibility results. In the model comprising of "free" and perfectly "ordered" spins, it is reasonable to assume that the free spins

give rise to the Schottky term. With this assumption it is found that $n(\text{PD})/n(\text{DDCP}) = 6.98$ for CdCr_2O_4 and 4.72 for ZnCr_2O_4 . Note that, this ratio involves the numbers of "free" spins only, i.e., it excludes the "ordered" spins specifically. From our susceptibility analysis we find $n(\text{PD})/n(\text{DDCP}) = .022$ for CdCr_2O_4 and 0.130 for ZnCr_2O_4 . The value from the Schottky analysis is ≈ 320 times larger for CdCr_2O_4 and ≈ 35 times larger for ZnCr_2O_4 . As shown by our susceptibility plots and also suggested by Lawless (Section IV), there may be a large number of spins showing only short-range order instead of a long-range order. The contribution of these spins at $T < T_N$ might be one of the reasons for the above discrepancy. To this end, we wish to note a few points:

(i) Low temperature Schottky analysis yields linear plots only above $T \approx 3.3$ K for ZnCr_2O_4 PD, $T \approx 2.2$ K for ZnCr_2O_4 DDCP, $T \approx 1.7$ K for CdCr_2O_4 DDCP and $T \approx 2$ K for CdCr_2O_4 PD. The coefficient b which depends on n and δ^2 ($\delta \equiv$ the two-level spacing) must therefore involve fairly large δ to account for the deviations below the temperatures mentioned above.

(ii) C/T^3 versus T plots at low temperatures yield a similar behavior for the PD and the DDCP samples whilst the number of "free" spins in the DDCP samples is much higher than in the PD samples.

(iii) The Debye contribution is negligibly small for temperatures below T_N . This can be seen from the ratio of the spin-wave densities as obtained rigorously by Lawless (Section IV) and those obtained by just dividing the $(m_{\text{SW}} + m_{\text{D}})$ coefficients as shown in Table 5.8.

Table 5.8. Spin-wave Densities

Spinel	$n_{SW} (PD)/n_{SW} (DDCP)$	$(m_{SW} + m_D)_{PD}/(m_{SW} + m_D)_{DDCP}$
CdCr ₂ O ₄	5.92	5.87
ZnCr ₂ O ₄	16.7	16.00

V.6.c Shift in T_N

As shown in Figures 5.12 and 5.13, there is a clear shift in the value of T_N as the powder is subject to different heat and stress treatments. To understand this effect qualitatively we need to digress the following.

Anderson's theoretical considerations (Anderson, 1956) drew attention to the role played by the next-nearest neighbor interactions in the antiferromagnetic ordering of the B ions. The B lattice is built up from units of four nearest neighbors situated on the corners of a tetrahedron, and such a B tetrahedron shares one B site with an adjacent B tetrahedron. For only the nearest-neighbor interactions B-X-B, the ground state is determined by the condition that the spins in each tetrahedron cancel. That is, negative nearest neighbor in a completely normal spinel does not lead to antiferromagnetic long-range ordering since the ground state is largely degenerate due to the frustration of the lattice. The interactions between the B sites in different tetrahedra (B-X-X-B) can, however, give long range ordering and the Neel temperature will depend on these interactions in a complicated way. Denoting by J and K as the strengths of the nearest and next-nearest interactions, the magnetic properties can be accounted for approximately by the Heisenberg spin hamiltonian of the form

$$\mathcal{H} = -2J \sum_{ij} \vec{S}_i \cdot \vec{S}_j - 2K \sum_{ik} \vec{S}_i \cdot \vec{S}_k - g\mu_B H_z \sum_i \vec{S}_{iz} \quad (V.6)$$

The number of nearest neighbors in a perfect spinel is 6 whilst that of next nearest neighbors is 36; J and K in the above expression denote the average strengths. One can calculate T_N with this hamiltonian and study its dependence on the parameter (K/J). It is to be noted that such a philosophy has already been applied to spinels which exhibit ferromagnetic behavior (Baltzer et al. 1966). For ferromagnetic orderings, it was found that slight changes in the parameter (K/J) can shift the Curie temperature by a few degrees. It should be noted that, according to the Ohio State University group, many features of the χ - and C_p -data on these spinels can be accounted for by distorting the tetrahedra of the spinels to remove frustration (Section IV).

In short, we believe that the value of T_N is a sensitive indicator of the changes in the next-nearest neighbor interactions.

V.6.d Field dependence of χ

The magnetic field dependence of the specific heat and the magnetocaloric heat changes seem to have been established, although it has not been pursued systematically. Similarly, the field dependence of χ , although noted, has not been studied systematically. It is puzzling to find that the χ versus T behavior depends on the field. For CdCr_2O_4 PD, the magnetic field, raises the Neel temperature, contrary to expectation. We do not have any explanation for these features right now and would like to investigate this aspect to bring together the susceptibility, specific heat and magnetocaloric results. One of the possibilities is that these compounds exhibit low-dimensional

antiferromagnetic behavior. However the low temperature ($T < T_N$) neutron or X-ray diffraction studies and single crystal samples are needed to confirm this conjecture which provides a new viewpoint for the unique properties of these spinels.

VI. THEORETICAL STUDIES OF THE SPINEL LATTICE : GINZBURG-LANDAU MODEL AND MONTE CARLO COMPUTER SIMULATIONS

A. Introduction

This section is devoted to the theoretical research on the spinel materials under investigation in this contract. In particular, calculations of the specific heat, magnetic properties, and dielectric constant were carried out using a variety of complementary calculational approaches, including a phenomenological Ginzburg-Landau model, as well as first principles Monte Carlo computer simulations.

In this section we present first an overall picture for the spin ordering in the spinel lattices, then discuss the results of the Ginzburg-Landau calculation of the magnetic ordering and its effect on the dielectric constant, which enables us to explain the striking dielectric anomaly reported in section IV. Next we summarize the results of our extensive Monte Carlo calculations on the undistorted cubic phase of the spinels, and then present our calculations on the tetragonal or distorted form of the spinel in which the frustration has been reduced. Finally we describe how low temperature paramagnetic tails may arise naturally from the composite structure of the CdCr_2O_4 and ZnCr_2O_4 materials. In each part we will discuss the connection with the relevant experiments.

B. Spin Ordering in the Spinel Materials

Spinel is ferrite materials with the generic formula AB_2R_4 where R is a group VI element (O, S, Se, or Te), while A and B are metal cations as shown in Fig. 6-1. The particular spinels CdCr_2O_4 and ZnCr_2O_4 are high specific heat spinels of present interest, in which the B site elements Cr form a 3-D

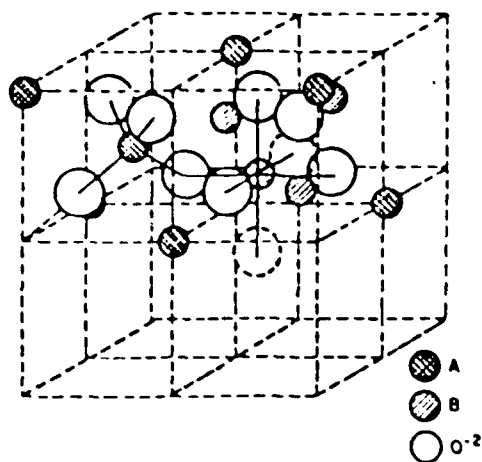


Fig. 6-1. Spinel Lattice: B-sites have magnetic Cr ions coupled by O²⁻ ions.

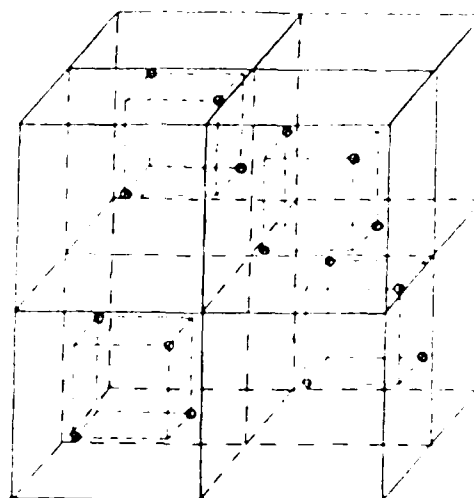


Fig. 6-2. Magnetic B-sites in lattice structure of spinel. Note chains in successive layers.

frustrated magnetic system. It has been found that there is a phase transition into an antiferromagnetic-like state at low temperature.

We start with a brief review of the salient features of the spin lattice structure of the B-site frustrated spinel lattice as shown in Fig. 6-2. The results obtained so far have suggested an attractive picture for the ordering phenomena in the B-site spinels, CdCr_2O_4 and ZnCr_2O_4 . The results have shown that at least two types of magnetic correlations are present, antiferromagnetic and paramagnetic, and that frustration and the presence of strong spin-lattice coupling play an important role in the anomalously large specific heats and thermal conductivities (Patton).

In addition the transitions in these materials were seen to have a peculiar nature in which the spins order weakly in a lattice which has a high degree of frustration. This has great importance for our understanding of

these systems, since it means that large numbers of spins can remain unordered below the transition, resulting in anomalously large specific heats, and furthermore, that distortions of the lattice, which remove the frustration, can couple strongly to the spins, thus leading to dielectric anomalies and large thermal conductivities due to spin energy being transported through the spin-phonon interaction.

More recently, the experimental work done under this current proposal has revealed much about the properties of the B-site spinels, CdCo_2O_4 and ZnCo_2O_4 . In particular, the recent work includes 1) successful fabrication and structural characterization of various ceramic phases including powder, compressed, and densified samples of CdCo_2O_4 and ZnCo_2O_4 , reported in section III, 2) experimental work on the magnetization and susceptibility which reveal an antiferromagnetic transition at $T_N \approx 9\text{-}11\text{K}$, section V, 3) experimental research on the specific heat and magnetocaloric properties, section IV, and 4) experimental work on the dielectric anomaly at T_N , which reveals a novel coupling of the spin and lattice, section IV.

The main experimental results we will focus on in connection with the theoretical calculations are the following:

- a. The fabrication experiments (III) give clear evidence that the spinel powder of nominal grain size 10 microns combines with additional mineralizers to produce a material having extra paramagnetic spins at low temperatures, among other properties.
- b. The susceptibility measurements (V) on the pure spinel powder reveal little low temperature paramagnetic Curie tail, while the grains reacted with 10% columbite or 5% Nb_2O_5 reveal a low temperature paramagnetic tail.
- c. The magnetocaloric experiments (IV) reveal no trace of hysteresis, implying the phenomena involved in the low temperature transitions in

the Zn and Cd spinels are second order in nature. The pattern of adiabatic demagnetization cooling and heating at different temperatures is indicative of antiferromagnetic ordering in the Cd samples, while all samples show evidence of low temperature antiferromagnetic spin waves.

- d. Measurements (IV) have discovered a striking anomaly in the dielectric constant at the antiferromagnetic transition, which clearly shows that the ordering of the frustrated spin system has a large effect on the structure of the lattice. The dielectric constant in large magnetic fields (Fig. 4-8) shows a clear shift in the transition for one sample.
- e. Another sample, the CdCo_2O_4 disk, did not have a sharp specific heat maximum and had a strong magnetic field dependence to $\partial\chi/\partial T$ below T_N .

In connection with results a. and b. above, in section F of our report we show that by allowing our clusters to have a finite surface area we also develop (theoretical) low temperature paramagnetic tails. Our calculations in sections D and E show that the transitions have no hysteresis, and are characterized by basically antiferromagnetic interactions as found in c. We calculate explicitly the dielectric anomaly of d. in section C and show that in general it shifts slightly in a magnetic field. Finally, our calculations in section D on the frustrated spinel material show that the transition as seen in the specific heat is broad and relatively featureless, which may explain the sample of e., while our calculations in section E show that relaxing the frustration via a tetragonal distortion that often occurs in the spinel system gives rise to an enormous specific heat singularity as seen in three of the samples.

C. Ginzburg-Landau Model and Calculation of the Magnetization and Dielectric Constant.

We start with a review of our phenomenological Ginzburg-Landau model which enables us to interpret and relate the many experimental results on specific heat, magnetic susceptibility and dielectric constant, and which has motivated much of our other calculations. In particular, this approach enables us to explain the very intriguing dielectric anomalies at the magnetic transition.

1. Dielectric Constant of Spinel

In general, the spinels exhibit extraordinarily high dielectric constants ϵ at and above room temperatures, but have rather weak temperature dependence at low temperatures. In the present case, experimental results (section IV) have revealed a large peak in the temperature derivative of the dielectric constant, $d\epsilon/dT$, at the Néel temperature (see Fig. 4-8), which suggests a coupling between the charges and the lattice.

We give first the simplest picture for the dielectric constant in an insulator and explain why it can be affected by a magnetic transition, which is very unusual. The dielectric constant arises from the polarization of the medium via virtual transitions from a filled electronic state to an empty one. Since the energy denominator in such a transition is of the order of the gap, the dielectric constant will increase as the gap decreases, becoming infinite in the limit that the gap vanishes and a metallic state is reached. A simple representation of the band structure of the spinel is shown in Fig. 6-3; the filled valence band is separated by a gap at the zone boundary $k = \pm\pi/a_0$ from the empty conduction band. The basic point is that any perturbation which affects the band structure will have an effect on the dielectric constant. The expression for the dielectric constant in an insulator may be written (Liman, 1964)

$$\epsilon(q, \omega) = 1 + \frac{4\pi e^2}{q^2} \sum_{k, G} \frac{|\langle k | e^{iq \cdot r} | k+q+G \rangle|^2}{\epsilon_{k+q+G} - \epsilon_k - \hbar\omega + i\delta} \left(f_k - f_{k+q+G} \right) \quad (6-1)$$

If we consider the static limit here, $\hbar\omega \rightarrow 0$, replace the energy denominator with an average gap Δ , and utilize the oscillator strength sum rule, then Eq. (6-1) takes the simple form

$$\epsilon(q, 0) = 1 + \frac{[\hbar\omega_p]^2}{\Delta^2} \quad (6-2)$$

where ω_p is the plasma frequency. We may use the result (6-2) to understand qualitatively what happens when the ordering of the spins couple to a distortion of the lattice. Neutron scattering experiments (Olés, et al., 1976) show a variety of patterns in the low temperature spin ordering of the B-site spinels; however, a characteristic feature is a doubling of the unit cell from a_0 to $2a_0$. If the spins couple to the lattice then a periodic potential acts on the electrons which induces bandgaps at multiples of $\pi/2a_0$ as shown in Fig. 6-4. Since the valence band in the insulator is completely filled and the

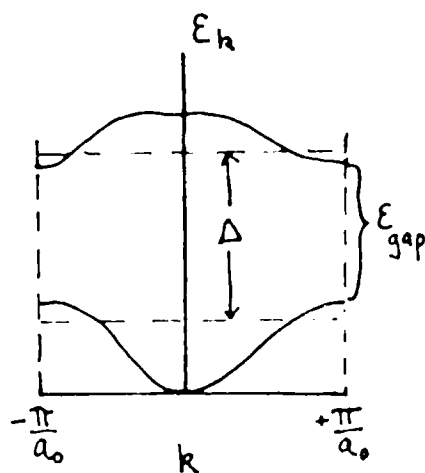


Fig. 6-3. Spinel band structure:
 $T > T_N$.

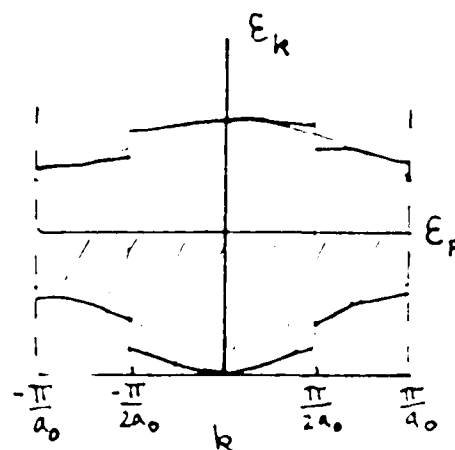


Fig. 6-4. Spinel band structure:
 $T < T_N$.

conduction band is empty, the gap induced at $\pm\pi/2a_0$ has little effect; however, the effect at the original zone boundary $\pm\pi/a_0$ is to increase the gap already present. This clearly lowers the electronic energy since occupied states are lowered in energy, while unoccupied conduction states are raised in energy. Thus it is clear that the average gap Δ is increased. We may write Δ in terms of a constant part Δ_0 and a temperature-dependent part $\delta(T)$

$$\Delta(T) = \Delta_0 + \delta(T) \quad (6-3)$$

where $\delta(T)$, due to its coupling to the magnetic order parameter, will have a temperature dependence below T_N as shown in Fig. 6-5. Taking the derivative of Eq. (6-2) then gives the result shown in Fig. 6-6 for $\partial\epsilon/\partial T$. The experiments on the dielectric constant therefore represent a very important probe of the spin and structural ordering in the spinel materials and have been pursued on all available samples.

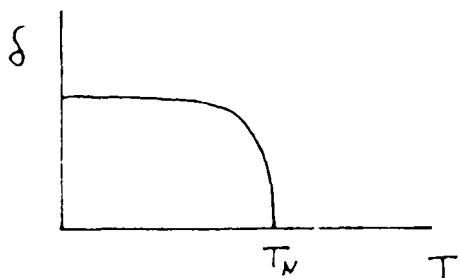


Fig. 6-5. Temperature dependence of bandgap δ arising from coupling to magnetic ordering.

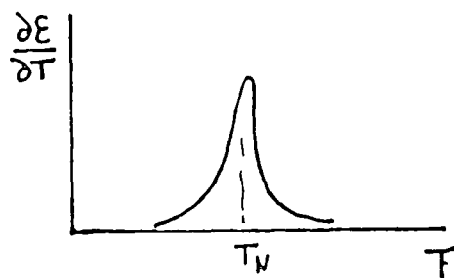


Fig. 6-6. Temperature derivative of dielectric constant vs. temperature.

2. Ginzburg-Landau Model of Spinel

In order to derive the proper Ginzburg-Landau description of the spinel materials, we note that since the experimental susceptibility (section V) and adiabatic demagnetization (section IV) are both characteristic of an antiferromagnetic system, the natural long range order parameter of the system is the sublattice magnetization. Furthermore, with both magnetic and electric fields present, then the sublattice magnetization, the total magnetization, and the polarization should all appear as relevant order parameters. We write down a Ginzburg-Landau theory with a free energy containing couplings of these order parameters and use it to analyze the system.

We start by expressing the free energy functional F in terms of the order parameters L , M , P , which are the difference of sublattice magnetic moments, the total magnetic moment, and the electric polarization, respectively:

$$F = F_{af}[L] + F_{pm}[M] + F_d[P] + F_{ap}[L, M] + F_{ad}[L, P] \quad (6-4)$$

where

$$F_{af}[L] = \int d\vec{r} \left[a|L|^2 + b|L|^4 + \xi^2 |\nabla L|^2 \right] \quad (6-5)$$

is the energy associated with the sublattice magnetization and near the Néel temperature T_N , $a = a_0(T - T_N)/T_N$,

$$F_{pm}[M] = \int d\vec{r} \left[\alpha|M|^2 - H \cdot M \right] \quad (6-6)$$

is the magnetization energy including that associated with the external magnetic field H with $\alpha > 0$,

$$F_d[P] = \int d\vec{r} \left[\lambda|P|^2 - E \cdot P \right] \quad (6-7)$$

is the dielectric polarization energy including the coupling to the external electric field E , and finally the coupling terms,

$$F_{ad}[L, M] = \int d\vec{r} G |L|^2 |M|^2 \quad (6-8)$$

$$F_{ap}[L, P] = \int d\vec{r} \left[\Gamma |L|^2 |P|^2 \right]. \quad (6-9)$$

Eq. (6-8) gives the coupling between the magnetic order parameters L and M ; we have $G > 0$ since the antiferromagnetic and ferromagnetic states tend to exclude each other. Eq. (6-9) describes the interaction between the lattice distortion involving charge displacement and the sublattice magnetization L . Both these couplings are required by 1) the behavior of the magnetic susceptibility, and 2) the experimental connection between the dielectric constant and the magnetic phase transition.

The Eqs. (6-4)-(6-9) have a rich structure even within the mean field theory approximation (MFT) in which fluctuations are neglected. Since we are concerned primarily with the equilibrium state of the system and the nature of the phase transition, this gives a reasonable first approximation. We include fluctuation effects in the next section where we consider the experimental data. In the MFT we have the following equations resulting from minimization of the free energy $F[L, M, P]$, namely,

$$\frac{\delta F}{\delta M} = \frac{\delta F}{\delta L} = \frac{\delta F}{\delta P} = 0, \quad (6-10)$$

thus

$$2\alpha M - H + 2G |L|^2 M = 0 \quad (6-11)$$

$$2aL + 2b |L|^2 L + 2G |M|^2 L + 2\Gamma |P|^2 L = 0 \quad (6-12)$$

$$2\lambda P + 2\Gamma |L|^2 P - E = 0 \quad (6-13)$$

In the case $G = \Gamma = 0$, we may identify the unrenormalized magnetic and dielectric susceptibilities, χ_{0m} and χ_{0e} , as

$$M = \chi_{om} H = \frac{1}{2\alpha} H \quad (6-14)$$

$$P = \chi_{oe} E = \frac{1}{2\lambda} E. \quad (6-15)$$

Then from Eq. (6-13) we obtain the polarization as

$$P \equiv \chi_e E = \frac{E}{2\lambda + 2\Gamma|L|^2} = \frac{\chi_{oe} E}{1 + 2\Gamma\chi_{oe}|L|^2} \quad (6-16)$$

while from Eq. (6-11) the total magnetic moment is

$$M \equiv \chi_m H = \frac{H}{2\alpha + 2G|L|^2} = \frac{\chi_{om} H}{1 + 2G\chi_{om}|L|^2} \quad (6-17)$$

The sublattice magnetization L is determined by Eq. (6-12), which gives $L = 0$ above the transition ($a > 0$), and the solution

$$a + b|L|^2 + G[\chi_m H]^2 + \Gamma[\chi_e E]^2 = 0 \quad (6-18)$$

below the transition ($a < 0$). Eq. (6-18) is a non-linear expression in $|L|^2$ due to the dependence of χ_m and χ_e on $|L|^2$ as indicated in Eqs. (6-16) and (6-17). Defining the dimensionless quantities: sublattice magnetization l , temperature t , electric field e , magnetic field h , and coupling constants γ and g

$$l^2 \equiv \frac{b|L|^2}{a_0 T_n}, \quad (6-19)$$

$$t \equiv \frac{a}{a_0 T_n} = \frac{T - T_n}{T_n}, \quad (6-20)$$

$$e^2 \equiv \frac{b\chi_{oe} E^2}{(a_0 T_n)^2}, \quad (6-21)$$

$$h^2 \equiv \frac{b\chi_{om} H^2}{(a_0 T_n)^2}, \quad (6-22)$$

$$\gamma \equiv \frac{\Gamma\chi_{oe} a_0 T_n}{b}, \quad (6-23)$$

$$g = \frac{G\chi_{om}a_0Tn}{b}, \quad (6-24)$$

we may then rewrite Eq. (6-18) for L^2 as

$$\frac{ye^2}{(1+2\gamma l^2)^2} + \frac{gn^2}{(1+2gl^2)^2} + l^2 + t = 0 \quad (6-25)$$

Solving Eq. (6-25) yields the sublattice magnetization as a function of the temperature and fields $L = L(T, H, E)$. We note that when γ is not equal to g , Eq. (6-25) is a quintic equation for l^2 , namely,

$$(l^2+t)(1+2\gamma l^2)^2(1+2gl^2)^2 + ye^2(1+2gl^2)^2 + gn^2(1+2\gamma l^2)^2 = 0 \quad (6-26)$$

The value of $|L|^2$ obtained from the solution of Eq.(6-26) determines the dielectric constant ϵ and the magnetic susceptibility χ_m as follows,

$$\epsilon = 1+4\pi\chi_e \quad (6-27)$$

where from Eq. (6-16),

$$\chi_e = \frac{\chi_{oe}}{1+2\Gamma|L|^2\chi_{oe}} \quad (6-28)$$

and

$$\chi_m = \frac{\chi_{om}}{1+2G|L|^2\chi_{om}} \quad (6-29)$$

From the solution to Eq. (6-26) it is clear that as the magnetic field increases at constant temperature, the value of L decreases. The field at which $L = 0$ defines a critical magnetic field $h_0^2 = (-t-ye^2)/g$, or

$$H_0^2 = \frac{|a|-\Gamma\chi_{oe}^2E^2}{G\chi_{om}} \quad (6-30)$$

at which the system is driven into a paramagnetic state by the external magnetic field, i.e. a kind of spin-flip transition.

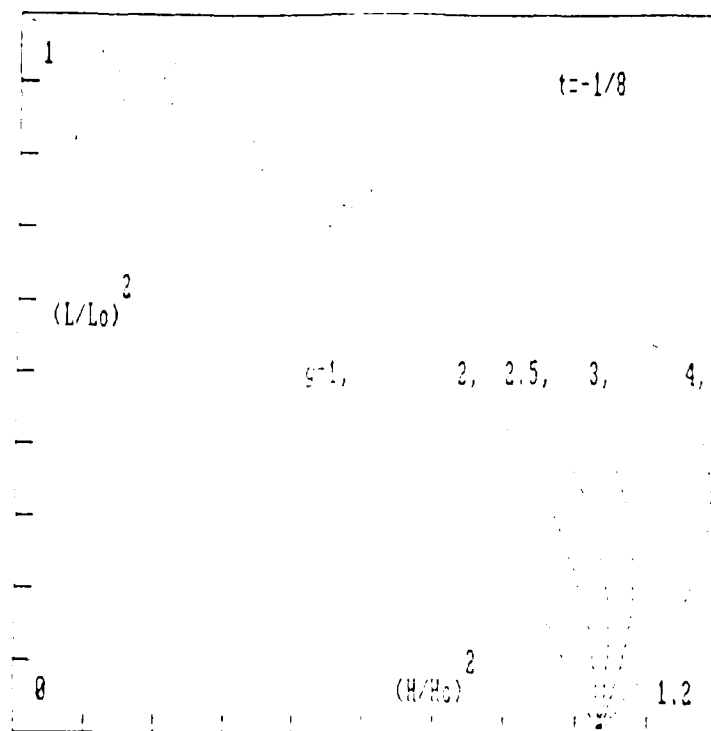


Fig. 6-7. Sublattice magnetization vs. external magnetic field at temperature $T = 7/8 T_N$ for different values of g .

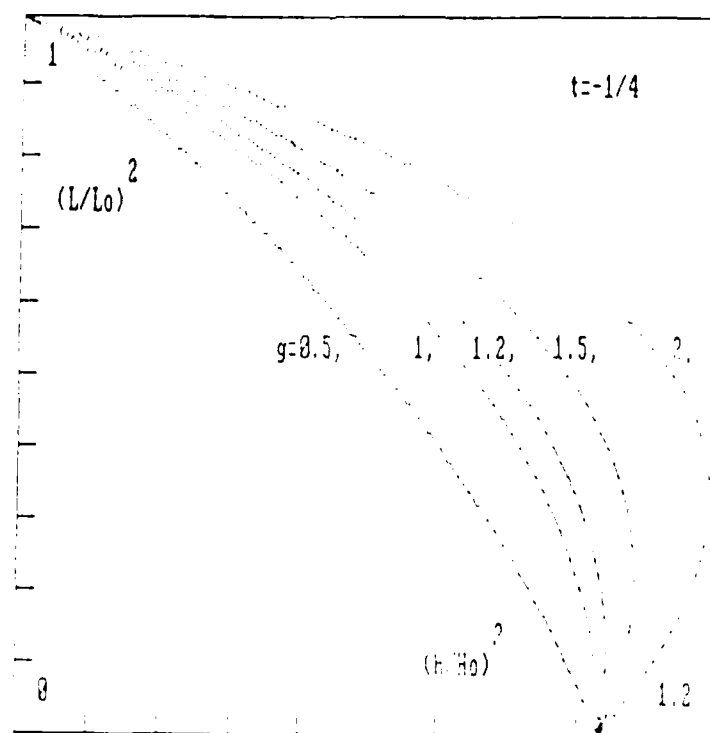


Fig. 6-8. Sublattice magnetization vs. external magnetic field at temperature $T = 3/4 T_N$ for different values of g .

As the electric field goes to zero, or if the coupling constant γ is very small, the second term of Eq. (6-26) can be dropped. Then Eq. (6-26) reduces to

$$(1^2 + t)(1 + 2g1^2)^2 + gh^2 = 0 \quad (6-31)$$

The numerical solution of Eq. (6-31) is shown in Fig. 6-7 and Fig. 6-8 for two temperatures below the transition, $t = -1/3$ and $t = -1/4$; the normalized sublattice magnetization squared $|L/L_0|^2$ is plotted versus the normalized magnetic field squared $(H/H_0)^2$ for various values of the antiferromagnetic-ferromagnetic coupling constant g where L_0 is the value of L at $H=0$ and H_0 is given in Eq. (6-30).

It is interesting to note that for larger values of g the curves show re-entrant behavior which suggests a discontinuous (first order) transition in those cases. We may determine the critical value of g , g_c , at which re-entrance appears as the value of g for which the slope of $|L|^2$ as a function of H^2 first becomes infinite at H_0 . Equivalently, we may use (6-31) to express h^2 as a function of 1^2 and require

$$\left. \frac{dh(1^2)}{d1^2} \right|_{1=0} = 0 \quad (6-32)$$

with the result that

$$g_c = \frac{1}{4|t|} \quad (6-33)$$

Thus the tendency toward a first order transition in a field increases as the temperature is lowered. Eq. (6-33) predicts a minimum value of g_c of $1/4$ at zero temperature. On the other hand, near the transition T_N , $t \gg 0$, and a second order transition in field will always occur.

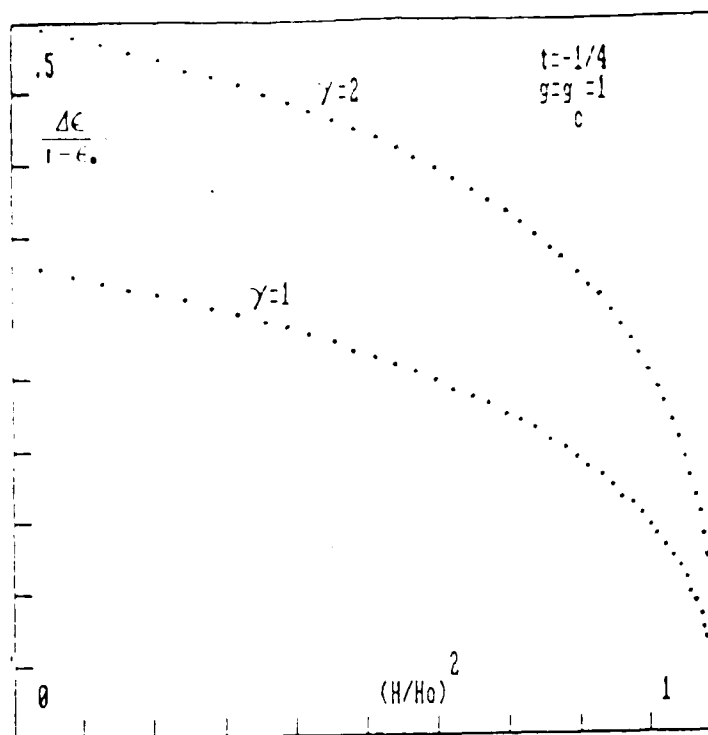


Fig. 6-9. Change of dielectric constant vs. external magnetic field at temperature $T = 3/4 T_N$ with critical $g = g_c$, and $\gamma = 1$ and 2.

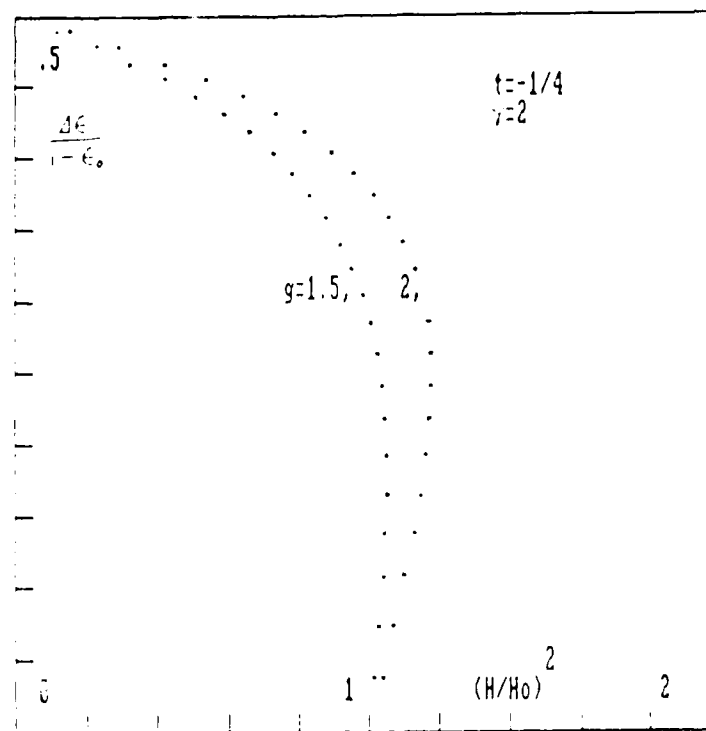


Fig. 6-10. Change of dielectric constant vs. external magnetic field at temperature $T = 3/4 T_N$ with $\gamma = 2$ and g greater than the critical g_c .

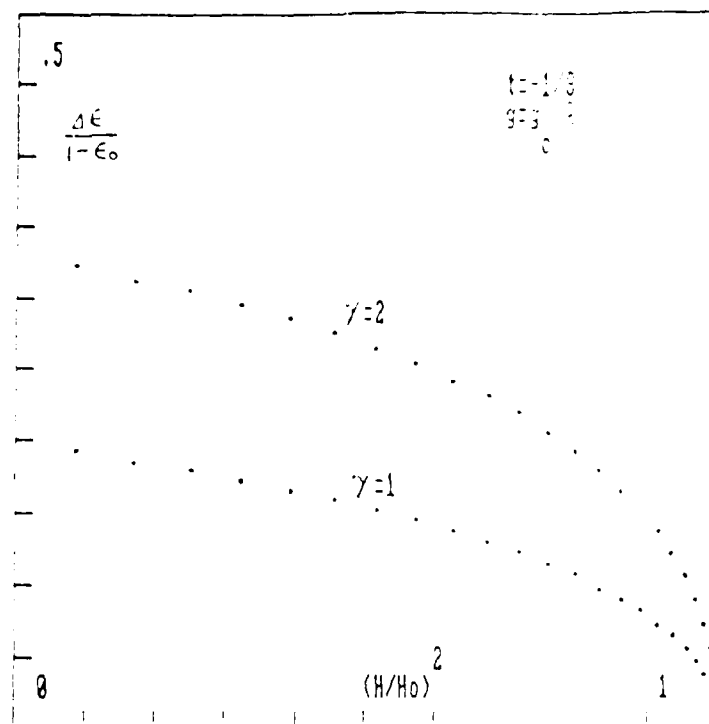


Fig. 6.11. Change of dielectric constant vs. external magnetic field at temperature $T = 7/8 T_N$ with critical g , and $\gamma = 1$ and 2 .

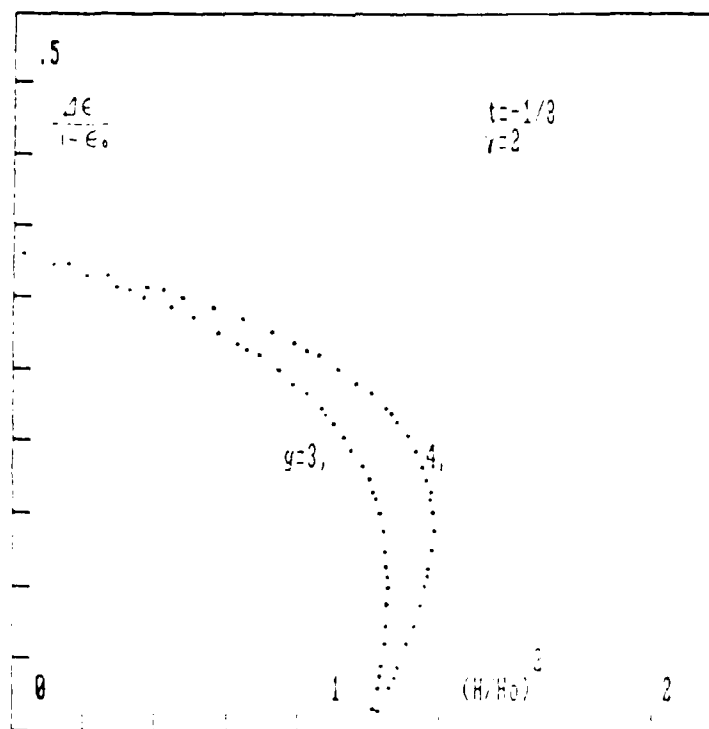


Fig. 6.12 Change of dielectric constant vs. external magnetic field at temperature $T = 7/8 T_N$ with $\gamma = 2$ and g greater than the critical g_c .

Using Eqs. (6-27), (6-28) and (6-31), we can plot $\Delta\epsilon/(1-\epsilon_0)$ vs. $(H/H_0)^2$ as shown in Figs. 6-9 through 6-12, for various fixed values of the temperature and the coupling constants g and γ . The same re-entrant behavior is found for g values greater than g_0 . We also note that at and above the critical field H_0 the dielectric constant anomaly is removed for all values of g and γ , i.e. $\Delta\epsilon = 0$. This occurs because above H_0 the magnetic field has suppressed the sublattice magnetization ($L = 0$), and thus the interaction between the charge and the lattice, $\gamma|P|^2|L|^2$, has effectively been removed.

To summarize this section, we have found a novel Ginzburg-Landau free energy which describes the unusual coupling between the dielectric constant and the antiferromagnetic transition in the B-site spinels, CdCr_2O_4 and ZnCr_2O_4 . We next consider a detailed comparison of the theory with the recent experiments in section IV on the magnetic field dependence of the dielectric constant.

3. Comparison with Dielectric Constant Measurements: Effects of Fluctuations

In order to make detailed comparisons with the experiments it is necessary to include the effects of fluctuations on the expression for the dielectric constant. This is clear from the fact that the dielectric constant starts to decrease above the actual transition, which occurs at the point of maximum slope (see Fig. 4-1).

The simplest approximation that includes fluctuations is the Hartree approximation. Consider the free energy F

$$F = a L^2 + b L^4 = (a + bL^2) L^2. \quad (6-34)$$

In the Hartree approximation, the L^4 term, which represents the interactions, is evaluated using its average value, namely, $2L^2\langle L^2 \rangle$. Eq. (6-35) then becomes

$$F = \alpha L^2 = [a + b \langle L^2 \rangle] L^2 \quad (6-35)$$

Self-consistency is imposed by calculating the average of L^2 by using Eq. (6-35)

$$\langle L^2 \rangle = (\text{Tr } e^{-\beta F} L^2) / (\text{Tr } e^{-\beta F}) = \frac{1}{\alpha} \quad (6-36)$$

Together with Eq. (6-35) this gives

$$\alpha = a + b/\alpha \quad (6-37)$$

Eq. (6-37) may be solved explicitly for α . The requirement that the limit $\alpha \approx a$ be achieved at temperature far above T_N so that L^2 approaches the mean-field result implies that the correct solution of Eq. (6-37) is

$$\alpha = \frac{a}{2} + \left[\frac{a^2}{4} + b \right]^{1/2} \quad (6-38)$$

The sublattice magnetization is thus

$$L^2 = 2/[a + (a^2 + 4b)^{1/2}] \quad (6-39)$$

In the vicinity of the transition temperature T_N , where the reduced temperature $t \equiv (T - T_N)/T_N$ satisfies $|t| \ll 1$, the Ginzburg-Landau coefficient a is given by

$$a = a_0 t \quad (6-40)$$

Although Eq. (6-40) is accurate near T_N , it gives a non-vanishing derivative for L^2 at $T = 0$ which violates the second law. A better formula which correctly interpolates between the high and low temperature limits is

$$a = a_0 [(T_N/T)^2 - 1]/2 = a_0 t [1 + t/2] \equiv a_0 t \quad (6-41)$$

thus we have as a result, in zero magnetic field

$$1^2 = \frac{2}{\tau + (\tau^2 + b)^{1/2}} \quad (6-42)$$

Rewriting the coupling constant γ in (6-23) in terms of ϵ_0

$$\gamma \equiv \gamma_1(\epsilon_0 - 1) = (\epsilon_0 - 1) \cdot [\Gamma a_0 T_N / 4\pi b] \quad (6-43)$$

and using Eqs. (6-42) and (6-43) with Eqs. (5-27) and (6-28) gives our final expression for the dielectric constant

$$\epsilon = \frac{2\gamma_1(\epsilon_0 - 1)1^2 + \epsilon_0}{1 + 2\gamma_1(\epsilon_0 - 1)1^2} \quad (6-44)$$

where in general ϵ_0 in (6-44) depends on temperature also. From fitting the experimental curve for CCN(9/1) in Fig. 4-3, we find $\epsilon_0 = 19.015 - 0.2 \, t$, $\gamma_1 = 4.33 \cdot 10^{-5}$, and $b = 0.006$. The theoretical expression from Eq. (6-44) is plotted together with the data points from experiment (from Fig. 4-1) in Fig. 6-13.

When the magnetic field is included, provided the effect of electric field is negligible, the sublattice magnetization is given by

$$1^2 = \frac{2}{\tau + (\tau^2 + 0.06)^{1/2}} - \frac{g \, (cH^2)}{1 + \frac{4g}{\tau + (\tau^2 + 0.06)^{1/2}}} \quad (6-45)$$

where H is in units of Tesla. From fitting the curve (in Fig. 4-5), g and c are determined to be $g = 3.37 \cdot 10^{-3}$ and $c = 2.67 \, \text{T}$. We note that the coupling constant g is small enough that when the magnetic field increases from 0.41 T to 15.16 T the change in ϵ is about 0.1 out of 20. The field dependence of the dielectric constant from Eqs. (6-44) and (6-45) is shown in Fig. 6-14. The theory for the magnetic field dependence is also in good agreement with the experiments, indicating that ϵ increases as the field increases.

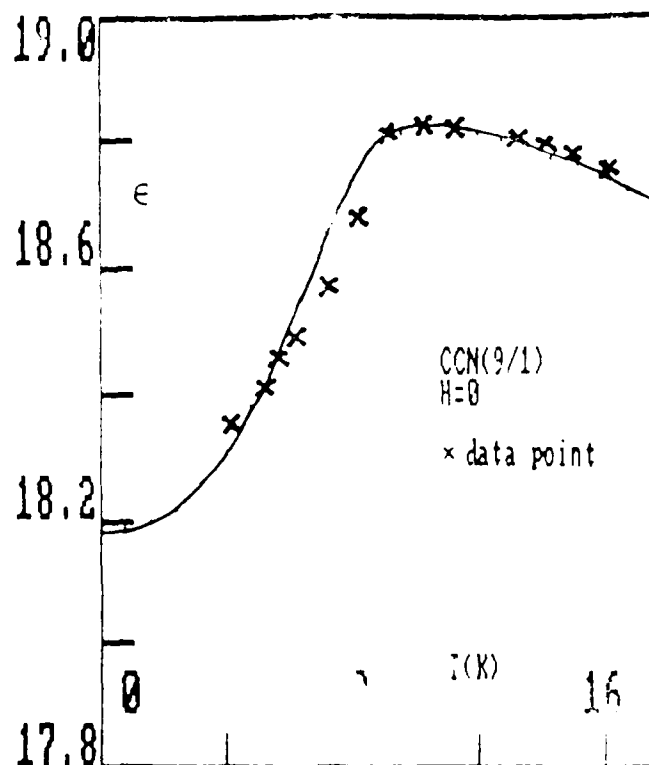


Fig. 6-13. Dielectric constant vs. temperature for CCN(9/1) spinel sample. Data from Fig. 4-1 (or 4-5) compared with theory, Eq. (6-44).

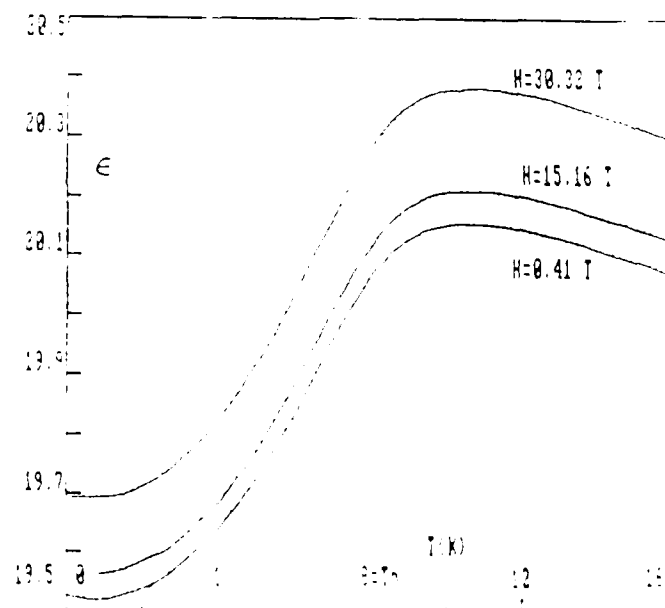


Fig. 6-14. Dielectric constant vs. temperature for typical spinel sample parameters and magnetic fields: $\mu = 0.001$, $\chi = 0.001$, and $H = 0.41$, 15.16 , and 30.32 T.

D. Monte Carlo Calculations

1. *Introduction*

The results obtained in previous work on this contract as well as the Ginzburg-Landau theory of the previous section have all suggested a picture for the ordering transitions in the B-site spinels, CdCr_2O_4 and ZnCr_2O_4 , involving two types of magnetic correlations, antiferromagnetic and paramagnetic. Frustration and the presence of strong spin-lattice coupling appear to play an important role in the anomalously large specific heats and thermal conductivities. In addition the transitions in these materials seemed to involve weak spin ordering in a lattice which has a high degree of frustration. This means that large numbers of spins can remain unordered below the transition, resulting in anomalously large specific heats, and furthermore, that distortions of the lattice, which remove the frustration, can couple strongly to the spins, thus leading to dielectric anomalies and large thermal conductivities due to spin energy being transported through the spin-phonon interaction. The most powerful way to examine these effects is through Monte Carlo simulations of the actual spin lattice. Before treating the actual magnetic ion lattice formed by the B-sites in spinels CdCr_2O_4 and ZnCr_2O_4 , we describe the computer techniques and obtain calibrations for comparison purposes on a simple cubic lattice Ising model spin system.

2. *Monte Carlo Simulations*

The Monte Carlo method uses a computer to model the thermal behavior of a physical system by simulating the random microscopic processes which give rise to the thermal equilibrium state. The Monte Carlo method and its applications in various fields have been described in detail (Binder, 1979,1984). The basic idea is to induce the system to go through a random set of points in

phase space, calculating equilibrium thermal quantities along the trajectory. Many different sampling techniques may be used. The simplest and most efficient one is called "importance sampling", which chooses random states according to their importance in the problem, e.g., according to a Boltzmann distribution in the canonical ensemble.

Choosing the Ising model as an example, the usual sampling procedure is the following:

- i. Start with an initial state at temperature T , and calculate its magnetization M and energy U ;
- ii. Select j^{th} spin to flip, calculate the "transition probability" $\exp(-\Delta E/k_B T)$, where ΔE is the change in energy associated with the spin flip;
- iii. Compare the probability with a random number x ($0 \leq x \leq 1$). If the probability is larger than x , flip the spin; otherwise do not;
- iv. Repeat ii and iii for j from 1 to N , where N is the total number of spins in the lattice, then calculate E and U again;
- v. Repeat ii, iii, and iv many times. Calculate the averages of M and U , which are just the equilibrium values.

There is some flexibility in the selection of the starting point in this procedure. The initial state can be chosen as:

- (a) an arbitrary state;
- (b) an ordered state;
- (c) the equilibrium state at a temperature close to the temperature considered.

The last one is used most often since with it leads to equilibrium faster.

The free energy F and entropy S may be obtained by integration of the following thermodynamics relations:

$$(dS/dT)_H = (dU/dT)_H/T \quad (6-46)$$

$$U = -T^2(dS/dT)/dT)_H \quad (6-47)$$

The expressions for S and F are provided in terms of integrations either from 0 to T or from ∞ to T. They are

$$S(T,H) = S(0,H) + \int_0^T (dU/dT')_H dT'/T' \quad (6-48)$$

$$\frac{F(T,H)}{k_B T} = \frac{U(T,H)}{k_B T} - \frac{S(0,H)}{k_B} - \int_0^T (dU/dT')_H dT'/k_B T' \quad (6-49)$$

or equivalently

$$\frac{F(T,H)}{k_B T} = - \frac{S(\infty,H)}{k_B} + \int_0^{1/k_B T} U d(1/k_B T) \quad (6-50)$$

$$S(T,H) = S(\infty,H) + U(T,H)/T - k_B \int_0^{1/k_B T} U d(1/k_B T) \quad (6-51)$$

Eqs. (6-50) and (6-51) are often more convenient to use because it is usually known for an s-spin Ising model that

$$S(\infty,H) = k_B \ln(2s+1) \quad (6-52)$$

Then $F(T,H)$ and $S(T,H)$ can be easily computed from $U(T,H)$.

In our calculation, the most relevant experimental quantities are the specific heat C and the magnetic susceptibility χ . We can calculate C directly as

$$C = (dU/dT)_H \quad (6-53)$$

or equivalently

$$C = (\langle U^2 \rangle - \langle U \rangle^2) / k_B T^2 \quad (6-54)$$

where $\langle U \rangle$ can be obtained from the same calculation that gives $\langle U \rangle$. In numerical applications, Eq. (6-54) usually gives a more reliable result than (6-53).

The susceptibility can be defined in two different ways. The difference susceptibility,

$$\chi = M/H \quad (6-55)$$

or the differential susceptibility,

$$\chi = (dM/dH)_T \quad (6-56)$$

The latter is equivalent to

$$\chi = \mu_B (\langle M^2 \rangle - \langle M \rangle^2) / k_B T \quad (6-57)$$

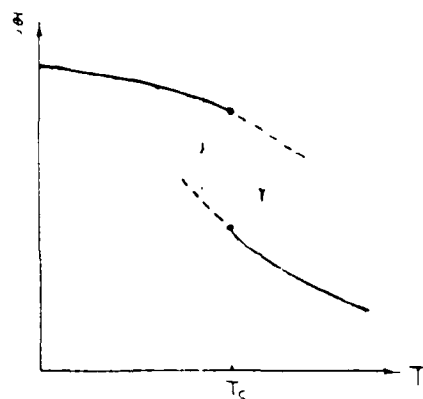
which is often more useful than (6-56) in practical applications.

In the usual procedure described above for Monte Carlo sampling, a complete cycle of steps (ii), (iii) and (iv) is called one Monte Carlo step per spin. The number of MC steps per spin needed is determined by how fast the results converge. Good convergence requires that the difference between the average quantity before and after one step is much smaller than the quantity itself. Usually the number of MC steps needed ranges from 10^3 to 10^4 for typical spin systems.

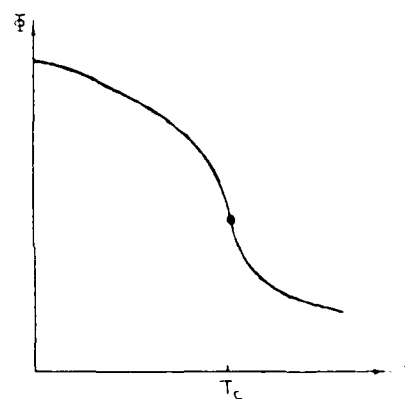
In a Monte Carlo calculation, the systems used are obviously finite, with the number of spins N usually ranging from 10^3 to 10^5 . Since a phase transition can only occur in an infinite system, we can not, strictly speaking, obtain any singular result from our calculation. With periodic boundary conditions, when the correlation length ξ gets larger than the linear dimension L of the system near the phase transition, the fluctuations become "over correlated" and the calculated results are rounded and smeared. These are called finite-size effects, and may in fact be used to determine the range of correlations. For this reason, finite-size scaling theory is an very useful tool to investigate properties near a critical point (Binder, 1984).

An important fact should be stressed here, namely, the difference in the

behavior of the order parameter obtained from a Monte Carlo calculation near a first order phase transition from that obtained near a higher order phase transition. At a first order transition, due to the existence of metastable states, the order parameter shows hysteretic behavior, while at a higher order transition it does not. As shown in Fig. 6-15, this difference is often used to distinguish the first order transition from higher order ones (Mouritsen, 1984).



a) First order transition,
dashed lines indicate
metastable states.



(b) Continuous transition.

Fig. 6-15. Order parameter Φ vs. temperature T

Compared to other methods, Monte Carlo simulations have two obvious advantages: first, the method may be used with any system with a well defined hamiltonian, and second, it is a non-perturbative method which relies on no approximations of the underlying fundamental physical laws, an approach which may bring about new and unexpected discoveries.

3. Calculations on a simple cubic lattice

To make sure our programs are correct, we first worked on a simple cubic lattice as a trial to calibrate our techniques, since the results can be compared to previous work.

The lattice we used in the present case was a $10 \times 10 \times 10$ ferromagnetic Ising ($s = 1/2$) spin array with periodic boundary conditions, although lattice sizes ranging from $5 \times 5 \times 5$ to $37 \times 37 \times 37$ were also studied. The calculations were done over a range of temperature $T = 0$ to $T = 2.0T_C$ ($4.0T_C$ for U and M), where $T_C = 4.51J$ and J is the coupling constant between nearest neighbor spins. For these calculations, we utilized a modest 100 MC steps per spin at each temperature, which proved to be adequate for approach to equilibrium in this case.

First, the energy and magnetization were evaluated directly from the average over all the configurations obtained in the random procedure at each temperature; the results are shown in Fig. 6-16 and Fig. 6-17, respectively.

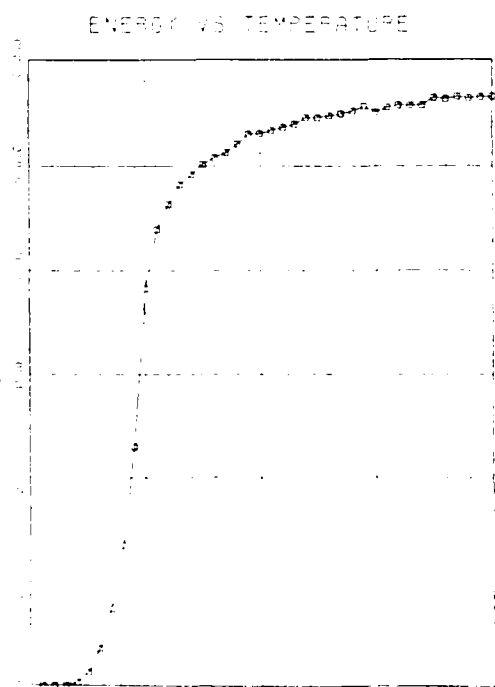


Fig. 6-16. Energy vs. temperature for $10 \times 10 \times 10$ cubic ferromagnetic Ising spin lattice.

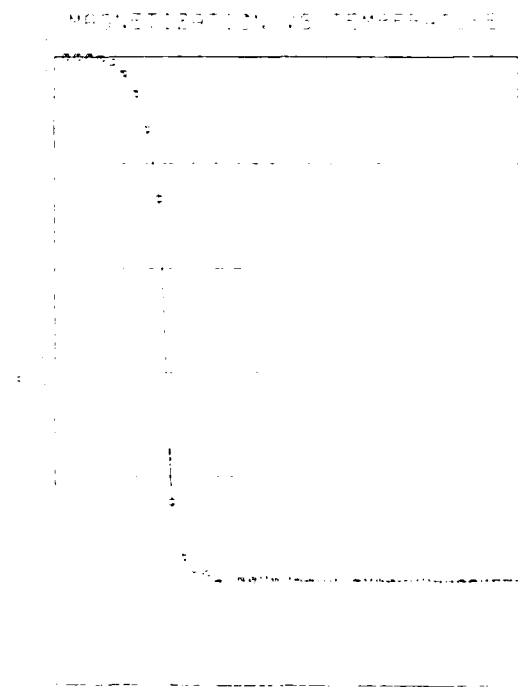


Fig. 6-17. Magnetization vs. temperature for $10 \times 10 \times 10$ cubic ferromagnetic Ising spin lattice.

As expected, the energy is equal to $-3000J$ (J times the total number of nearest neighbor bonds) at low temperature, and approaches zero at temperatures much above the transition, indicating that the spins are highly decoupled from each other. Similarly, the magnetization equals the total number of spins at low temperature, showing that all the spins are ordered in one direction, but is nearly zero at high temperature, corresponding to a completely disordered state.

From U and M at different temperatures, we computed the free energy and entropy from Eq. (6-50) and (6-51). They are shown in Fig. 6-18 and Fig. 6-19. We find a reasonable behavior for S , as well as F , from the results. At low temperature, S equals $k_B \ln 2$ since the ground state is 2-fold degenerate. At high temperature, S equals $Nk_B \ln 2$ where $N = 1000$ is the total number of spins.

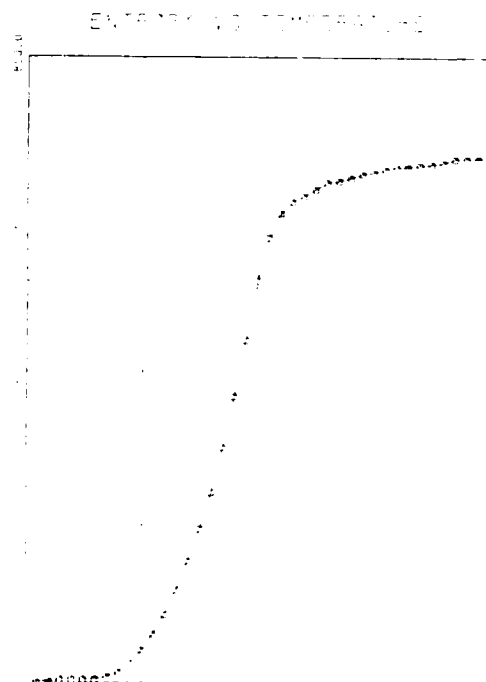
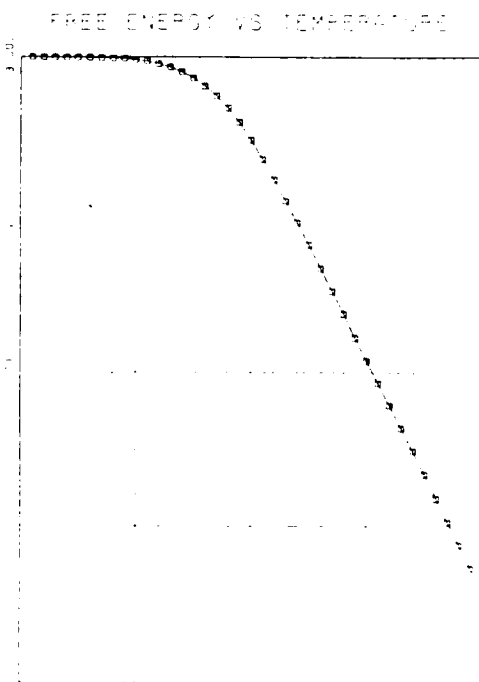


Fig. 6-18. Free energy vs. temperature for $10 \times 10 \times 10$ cubic ferromagnetic Ising spin lattice. Fig. 6-19. Entropy vs. temperature for $10 \times 10 \times 10$ cubic ferromagnetic Ising spin lattice.

To resolve the phase transition at T_C , the specific heat was calculated directly from the derivative of energy with respect to temperature. The result is plotted in Fig. 6-20, which indicates that C exhibits a peak anomaly at T_C . The divergence of C is rounded by finite size effects, as expected. A small shift of the peak to lower temperature is also seen in the results.

To investigate the order of transition, we calculated U and M both upon heating up the lattice from low temperature and by cooling it down from high temperature. The results turned out to be identical, well within the numerical uncertainty, for both directions, thus no hysteresis was observed. This indicates the

transition should be continuous instead of first order, a conclusion already known, of course, for the Ising model in three dimensions.

All the above results are consistent with previously published work in the literature 11,12,13. Therefore we can conclude from our trial calculations and analyses that the Monte Carlo method and our program are well calibrated for further studies on the magnetic spinels, whose properties can be obtained in analogy with the results reported here for the simple cubic lattice.



Fig. 6-20. Specific heat vs. temperature for $10 \times 10 \times 10$ cubic ferromagnetic Ising spin lattice, calculated using Eq. 6-53.

E. Monte Carlo Calculations on Frustrated Spinel

1. Spinel Magnetic Lattice

As discussed in previous sections, the magnetic ions on the B-sites in spinels CdCr_2O_4 and ZnCr_2O_4 form a frustrated spin system. The structure is shown in Figs. 6-2 and 6-21. Since we are focusing here on just the magnetic properties, only the magnetic atoms are drawn. We can see from Fig. 6-21 that the whole lattice is built up of interconnected tetrahedral units. Each spin is part of two adjacent units which means that for each tetrahedral unit there are two spins, with eight units in a primitive cell of the crystal.

We consider the basic loops composing the lattice triangular plaquettes which form the faces of the tetrahedral units. Around each of these loops, there is an odd number of antiferromagnetic bonds which has the consequence that spin alternation around the loop can not be perfectly satisfied, as shown in Fig. 6-22. Considering the Ising case, at least one spin in the loop can be flipped without changing the energy. This is called "frustration" in spin systems (Toulouse, 1977). The spin which can be flipped freely corresponds to

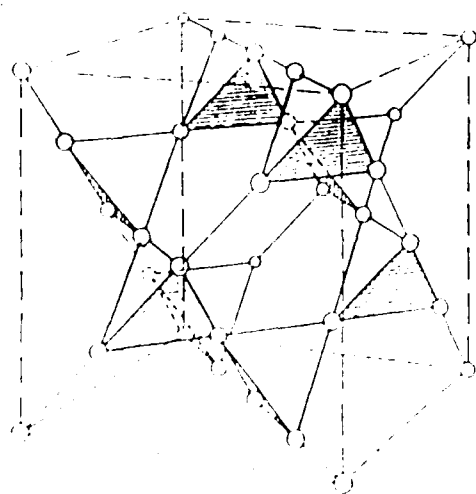


Fig. 6-21. Tetrahedral units in spinel magnetic lattice. Note chains of spins.

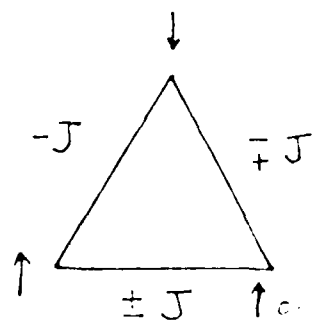


Fig. 6-22. Frustrated ordering around triangular plaquette of face of each tetrahedron.

a (paramagnetic) defect, which represents an unsatisfied bond in the ground state configuration. Disorder exists in the system since some spins can be chosen up or down randomly. Similar considerations have been applied to the spin glass phase, which has a number of unusual properties. Thus we should not be surprised to find some peculiar results arising also from the case of frustration in spinels.

We now describe the application of the Monte Carlo procedure reviewed in the previous section to CdCr_2O_4 and ZnCr_2O_4 . As mentioned before, we will use Monte Carlo simulations to investigate their magnetic properties. The lattice formed by magnetic atoms, shown in Fig. 5-2 or 6-21, is frustrated due to triangular plaquettes of the corner sharing tetrahedra. We can also think of the spin lattice as layers of spins with parallel spin chains in each layer. The Hamiltonian we will use is the Ising model with nearest neighbor antiferromagnetic interactions:

$$H = J \sum_{\langle i,j \rangle} S_i \cdot S_j \quad (6-58)$$

where $J > 0$, $\langle i,j \rangle$ denotes nearest neighbors, and the spins S_i and S_j take on the values ± 1 . We note that the Ising model appears to be appropriate to the CdCr_2O_4 and ZnCr_2O_4 systems (rather than the isotropic interaction of the Heisenberg model, for example) based on what is known of the nature of the spin ordering (Oleś et al., 1976).

The next section is devoted to the ground state properties obtained from the Monte Carlo calculations. We note in advance that although some of these results gave encouraging agreement with the experiments of sections IV and V, they did not provide evidence of a sharp transition. This suggested that the actual spinel composite materials are able to reduce the frustration in some way, which will be discussed in the next part, section F.

2. The Ground State

Since the system is frustrated, the bonds can not be all satisfied at once. However, it is clear that the lowest energy for a single tetrahedron can be achieved by setting the four spins on it as two up and two down (in six different ways). The ground state for the whole lattice is formed by putting many such tetrahedra together. The lowest energy for a single tetrahedron is $E_1 = -2J$. If there are a total of N spins, since each tetrahedron has $4 \cdot (1/2) = 2$ spins, there will be $N/2$ tetrahedra. Therefore the ground state energy E_0 is equal to

$$E_0 = \frac{N}{2} \cdot (-2J) = -NJ \quad (5-59)$$

The ground state so constructed is non-periodic and very disordered. If one looks at a single chain of spins running through the spinel lattice, it can have any pattern. Obviously the ground state degeneracy is very large. A lower bound can be obtained by setting all chains (in x-y plane) in antiparallel configurations, or in other words, satisfying all the bonds in the x-y plane, then counting the two fold degeneracy of each chain. The number of chains are $(N/2)^{2/3}$, and each chain has 2 states, yielding a lower bound of $2^{(N/2)^{2/3}}$.

The upper bound arises as follows. Divide all tetrahedra into two sets such that the tetrahedra in one set only connect to tetrahedra in the other set. Then the upper bound for the ground state degeneracy can be obtained by setting the spins on each tetrahedron in one set (which are mutually disconnected) as two up and two down; the number of possibilities comes out to be $6^{N/4}$, which is an upper bound since the spin configurations on the tetrahedra in the other set may or may not be appropriate for the ground state. If Ω denotes the ground state degeneracy, we have

$$2^{(N/2)^{1/3}} \leq D \leq e^{N/2} \quad (6-41)$$

These bounds on the degeneracy yield the following bounds on the ground state entropy per spin $s_0 = S_0/N = [k_B \ln D]/N$

$$\frac{0.437 k_B}{N^{1/3}} \leq s_0 \leq 0.896 k_B \quad (6-42)$$

A further approximate, but useful estimate for D can be obtained to within 20% (Anderson, 1956):

$$D \approx (3/2)^{N/2}, \quad (6-43)$$

which implies a ground state entropy per spin of

$$s_0 = k_B \cdot \frac{1}{2} \cdot \ln(3/2) = 0.203 k_B. \quad (6-44)$$

In all the cases considered the zero temperature entropy has a finite value as a result of the frustration of the spin ordering. As we discuss in section F below, a lattice transformation may reduce or eliminate the frustration and allow the entropy to go to zero at zero temperature.

3. Monte Carlo Calculations of the Thermal and Magnetic Properties of the Frustrated Spinel Lattice

Using Monte Carlo simulations, the thermal and magnetic properties of the system have been calculated. Most of our calculations were done on a lattice of $5 \times 5 \times 5$ unit cells containing $5 \times 5 \times 5 \times 16 = 2000$ spins, with iteration times ranging from 2000 to 20000 MC steps.

Direct averaging over many random configurations yields the magnetization $M(T)$ and energy $U(T)$ as functions of temperature. M appears to be zero (in zero magnetic field) over the whole temperature range, which is consistent with the antiferromagnetic nature of the coupling between spins. From the

the ground state entropy s_0 can be immediately calculated, which gives

$$s_0 = 0.117 k_B \quad (6-64)$$

Our Monte Carlo result (6-64) is in good agreement with the entropy obtained from the estimate of the ground state degeneracy, Eq. (6-63).

One of the most useful and interesting properties, the specific heat C , can be obtained by differentiating $U(T)$; the result is shown in Fig. 6-23. A low broad maximum in C is found at $T \approx 0.8J$ with $c_{\max} \approx 0.28$, where $c \equiv C/N$ is the specific heat per spin. Normal (unfrustrated) spin ordering transitions typically involve maximum specific heats an order of magnitude larger than this. For such a low a peak, it appears unlikely that a sharp phase transition is actually present. A low specific heat peak could also occur if the transition were first order, but near a second order critical point which

Fig. 6-23. Specific heat vs. temperature

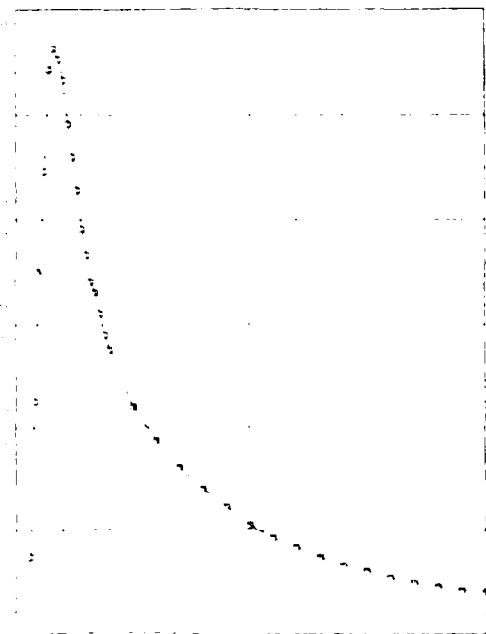


Fig. 6-23. Specific heat vs. temperature for 5x5x5x13 spin frustrated spinel lattice at $H = 0$.

Fig. 6-24. Energy vs. temperature

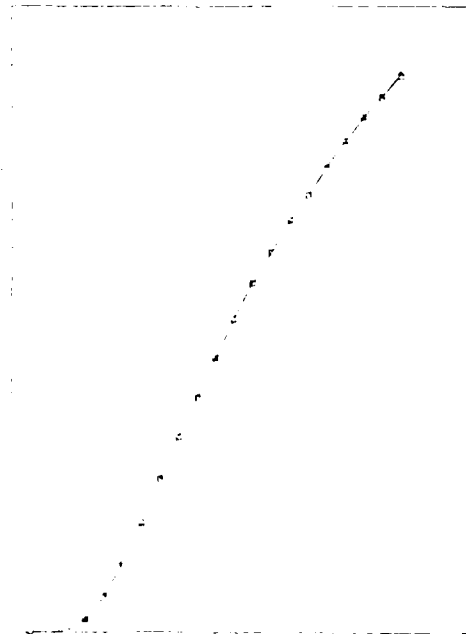


Fig. 6-24. Energy vs. temperature for heating and cooling runs at $H = 0$. No hysteresis observed.

gives weak fluctuations. However, in that case a large latent heat and hysteresis would be expected. In Fig. 6-24, plots of $U(T)$ from both heating and cooling runs are shown. No hysteresis is observed, which requires the transition, if there is one, to be second order or higher.

Another way of determining the nature of the transition in Monte Carlo calculations is to examine the magnitude of the specific heat peak as a function of the size of the lattice, using finite size scaling theory. Whether the peak value c_{\max} diverges depends on the sign of the specific heat critical exponent α , but in either case C_{\max} should vary with L . The dependence of c on size of the lattice was studied and is shown in Fig. 6-25. The results indicate that c_{\max} is almost the same for different size lattices, which also suggests that the transition is not an ordinary antiferromagnetic one.

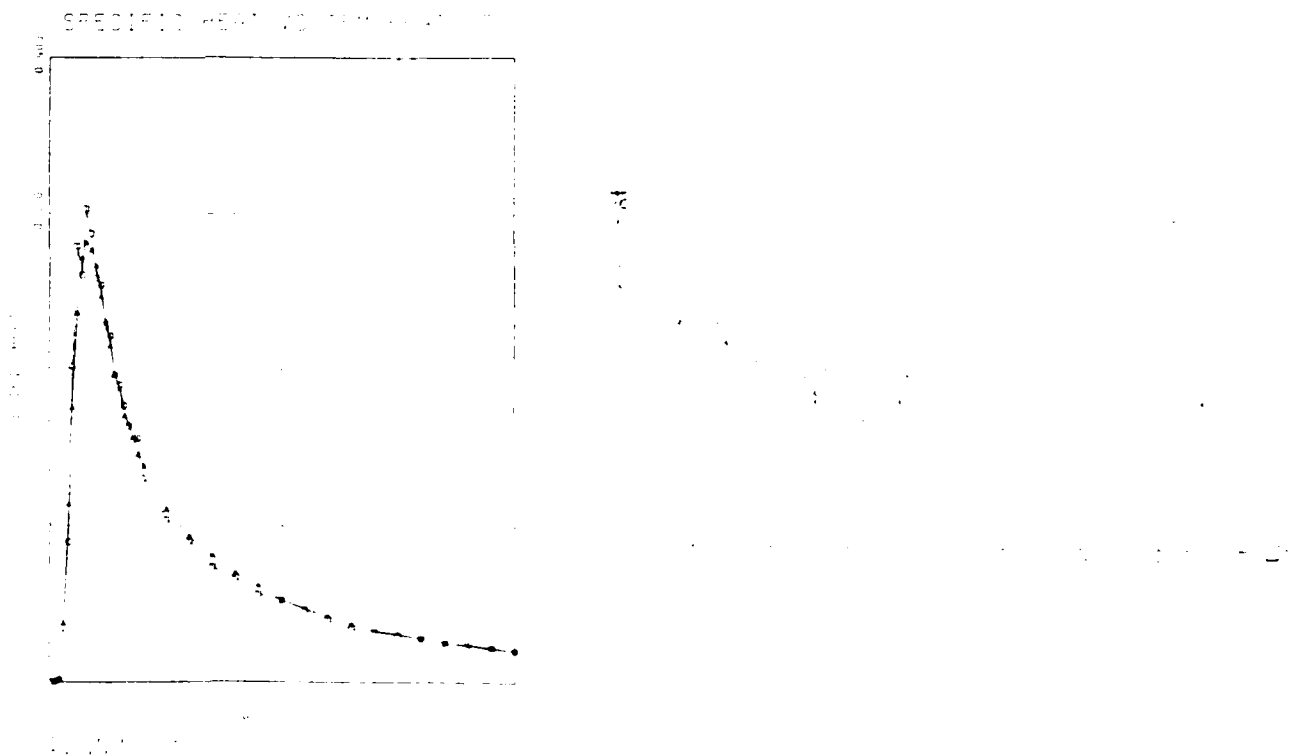


Fig. 6-25. Specific heat per spin vs. temperature for two different specific heat maximum with $L^{-1/4}$ for lattice sizes: 8×8 and 16×16 . Data are from [14] and [15].

The temperature of the specific heat maximum should also scale with the lattice size for a conventional isotropic Ising transition. If T_{max} denotes the temperature of the maximum of C , the dependence of T_{max} on different lattice sizes was calculated and the results plotted in Fig. 6-26. Surprisingly, we find good agreement with finite-size scaling theory for large L when the 3-d Ising coherence length exponent $\nu = 0.63$ is used, suggesting a continuous phase transition. It is interesting to note that T_{max} increases with L , unlike the case of the simple Ising magnet where it decreases with L . We speculate that this notable difference may arise from the frustrated nature of the spinel spin system.

Another interesting property, the magnetic susceptibility χ (in zero field) as a function of temperature, is calculated from the fluctuations in M . The results are plotted in Fig. 6-27 and show a pattern similar to that for a

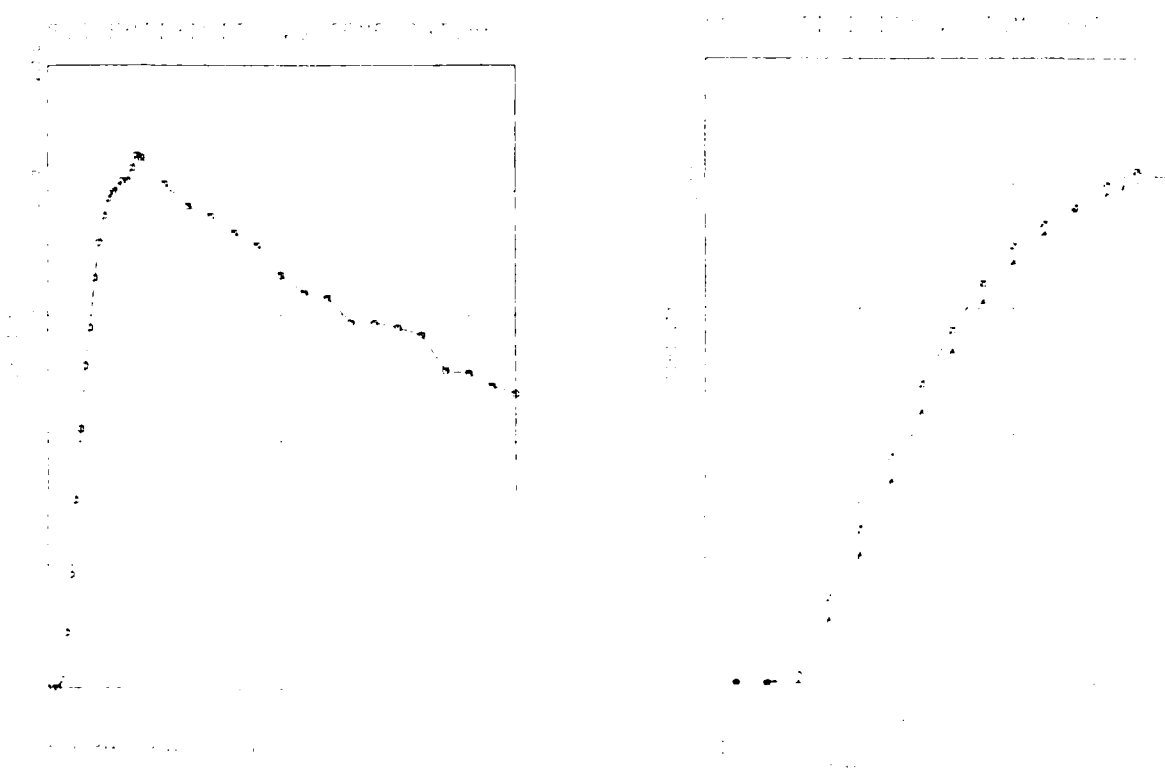


Fig. 6-27. The susceptibility vs. temperature for frustrated spinel temperature for $H = 0$ and 0.25 . $5 \times 5 \times 5$ lattice at $H = 0$. (Left) $H = 0.25$, $5 \times 5 \times 5$ lattice at $H = 0.25$.

typical Ising antiferromagnet, increasing from 0 at $T = 0$ to a maximum at T_N , but decreasing much more slowly for T above T_N , which may be an indication of local spin ordering at relatively high temperature, a result seen in the susceptibility experiments reported in section V.

The susceptibility χ in finite field H is calculated for $H = 0.4J$ and $H = 2.0J$ and shown in Fig. 6-28 and Fig. 6-29, respectively. The value of H in these and following plots depends on the value of J , which may be determined from the fitting of the experimental value of $T_N \approx 10$ K to the location of the peaks in our calculated specific heats, $T_{max} = T_N \approx 0.5-1.0 J$. From this we find $H = J \approx H_0 \approx 5-10$ T. Fig. 6-29 also compares results for the two susceptibilities M/H and dM/dH (the latter arising from the fluctuations of M). They are nearly equal to each other over the temperature range involved. Compared with χ in zero field, χ in a small field is almost unchanged, the

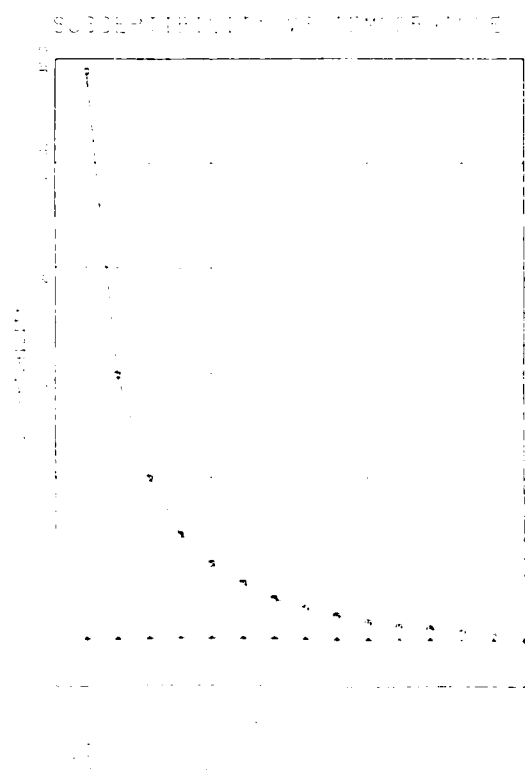


Fig. 6-28. The susceptibility vs. temperature for $H = 2.0J \approx 15T$. (Data from Fig. 6-29, $H = H_0 \approx 5T$).

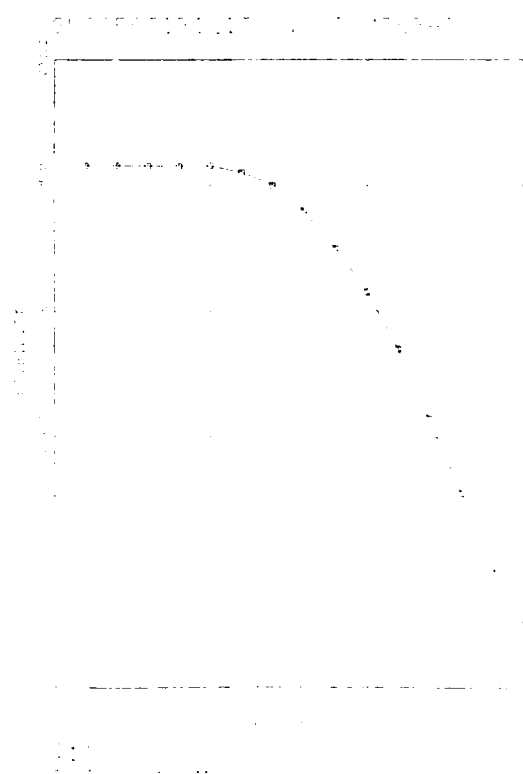


Fig. 6-29. The susceptibility vs. temperature for $H = 0.4J \approx 5T$. (Data from Fig. 6-28, expanded scale).

curve remains very slightly to lower temperature. However, Fig. 6-29 shows two totally different results for the two susceptibilities. In the upper one M/H displays a Curie type behavior since, as demonstrated below, the field $H = 3.0J$ is a critical value at which a large portion of spins are realigned. The lower curve, M/H , shown in an expanded scale in Fig. 6-30, gives the saturation magnetization produced by the field (this is more clearly seen in Fig. 6-31).

The magnetization M versus H at $T = 0.0J/kK$ is shown in Fig. 6-31. The corresponding curve expected at $T = 0$ is given by the dashed line. As T increases, the curve becomes more rounded, eventually losing its structure. The reason for the step structure in M is the following: a field H smaller than $2.0J$ is not enough to flip a spin (in the absence of thermal fluctuations). However, an H between $2.0J$ and $6.0J$ can flip a spin shared by two

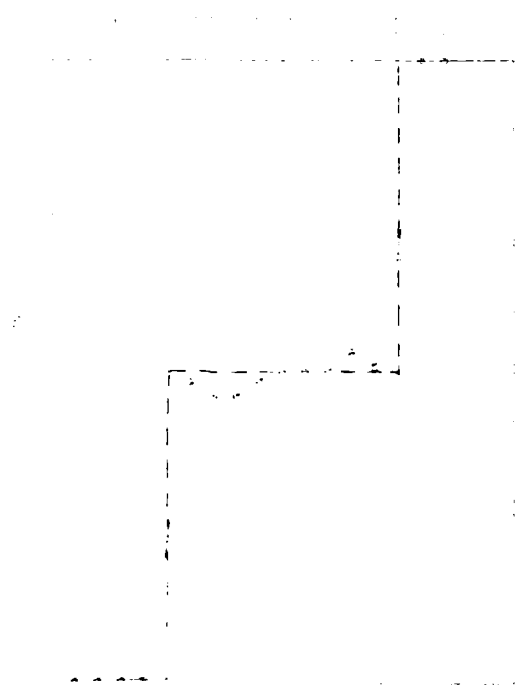


Fig. 6-31. Magnetization vs. field H for $T = 0.0J/kK$. Dotted line gives result expected at $T = 0$.

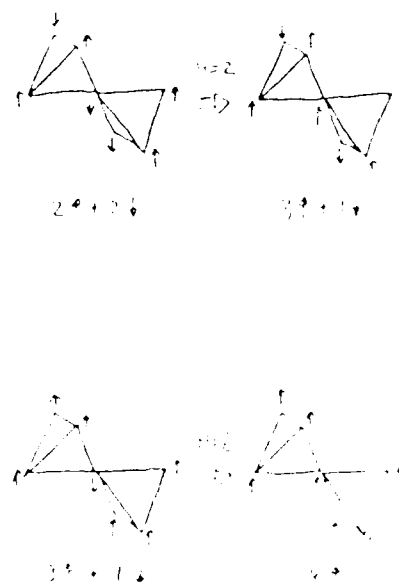


Fig. 6-32. Transitions at $H = 2J$ and $H = 6J$ in which Zeeman energy and not spin-spin coupling energy.

tetrahedra both with 2 up and 2 down spins. In this case, the increase in the spin coupling energy, which is $4J$ for the two tetrahedra, is less than the decrease in the Zeeman energy between H and the spins. H large than $6.0J$ can flip a spin shared by two tetrahedra both with 3 up and 1 down spins (for H in the positive z direction), as shown in Fig. 6-32. χ versus H , which is the slope from Fig. 6-31, is plotted in Fig. 6-33. The small peak at $H = 4.0J$ vanishes when $T = 0$ because it is the critical field to flip a spin shared by a tetrahedron with 2 up and 2 down and a tetrahedron with 3 up and 1 down. These two type of tetrahedra do not coexist at $T = 0$.

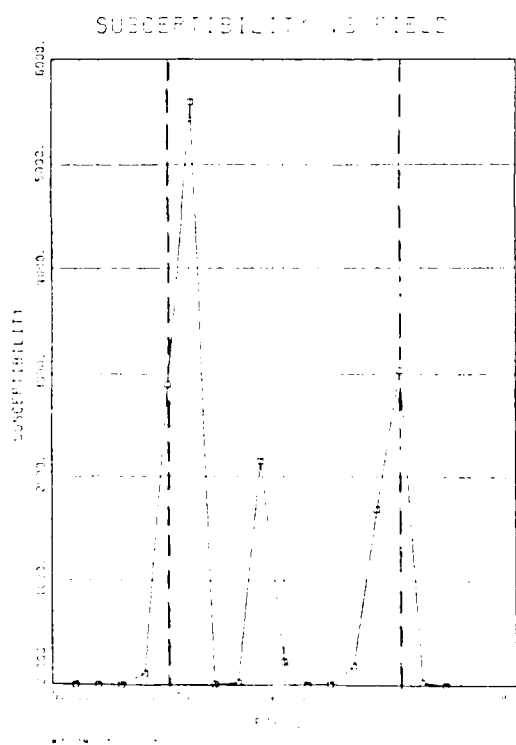


Fig. 6-33. The susceptibility $\partial M/\partial H$ vs. H at $T = 0.1J$ from Fig. 6-31. Dotted lines are $T = 0$ result.

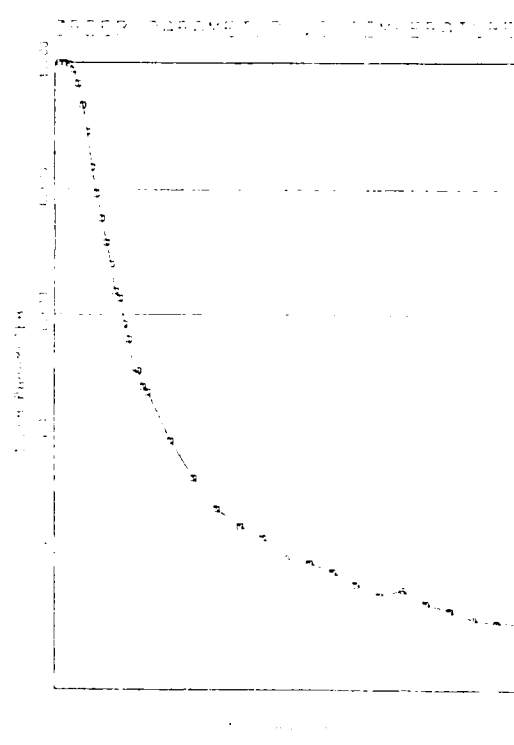


Fig. 6-34. Tetrahedral order parameter F from Eq. (6-65) vs. temperature at $H = 0$.

4. DISCUSSION

From the specific heat calculations, we do not find any evidence for a sharp transition. The specific heat in lead shows a low maximum and a slow decrease above T_N . The absence of a transition is consistent with the early conclusion of Anderson: no long range order can exist in the B-site spinels if only antiferromagnetic coupling between nearest neighbors is involved (Anderson, 1956). The large value of the specific heat above the peak, on the other hand, implies considerable local order, a result seen in some of the thermal and magnetic measurements in sections IV and V.

To try to understand what kind of order is developing we note that there is one quantity which is the same throughout the crystal at low temperatures: namely, each tetrahedron has 2 up and 2 down spins. That means, from this fact, we may extract a kind of long range ordering. Assign a number to each tetrahedron as follows: if the i^{th} tetrahedron has 2 up and 2 down spins, associate $f_i = 1$ with it; otherwise let $f_i = -3/5$. Define a "tetrahedral" order parameter F as

$$F = \frac{2}{N} \sum_i f_i \quad (6-65)$$

where we have normalized the order parameter by the number of tetrahedra, $N/2$.

At $T = 0$, each tetrahedron has 2 up and 2 down spins, so $f_i = 1$ for all i . So we have

$$F(T=0) = 1 \quad (6-66)$$

As T goes to infinity, all micro states have the same probability to appear. Thus the probability to obtain a tetrahedron with 2 up and 2 down versus that for all other type of tetrahedra is 6 to 10, or equivalently, 3 to 5. This means we have

$$F(T_{\text{tr}}) = 0$$

(6-6')

which is the reason why f_1 was weighted by $-3/5$ for all non 2 up/2 down configurations, as discussed above.

With the definition given, F looks like a typical order parameter, going to 1 at zero temperature and vanishing at high temperature. To find out what F does near the temperature T_{max} where the specific heat has its maximum, we calculated it in the Monte Carlo simulation. The result is shown in Fig. 6-34. The curve shows that F increase monotonically as the temperature decreases as expected for other order parameters, but a striking property is the extremely slow decay above T_{max} , as well as a relatively small value for T_{max} . It is hard to find a singularity in F at any temperature from the graph. Calculations of F in both heating and cooling processes also shows no hystereses, which is consistent with what happened in similar calculations for the energy U .

The long range ordering we introduced above is based on properties of small spin clusters, not on conventional magnetic moments. In some sense, it is not a typical type of magnetic ordering, as discussed by Anderson, but the ordering does have the physical meaning of being associated with the drop in entropy from 2^N for the totally disordered state to about $(3/2)^{N/4}$ for the "ordered tetrahedra". We interpret this result as evidence for strong local correlations in spin ordering over a large range in temperatures, which are difficult to classify as ordinary magnetization, but appear instead more like a spin glass type of freezing. We are not sure if F is the best or only order parameter at this moment; another definition might show a sharper phase transition. Further calculations of the correlation functions of the t_i 's would be very illuminating.

5. Conclusion

Detailed Monte Carlo calculations on frustrated spinels have provided extensive results, which show a lack of a sharp phase transition due to the complete frustration of the spin lattice, but the possibility of extensive local order. Comparison of the specific heat calculations with the experimental results, Figs. 4-9 and 4-10, indicates that the CdCr_2O_4 powder disk is in good agreement with our results for the frustrated lattice, while the $\text{CCN}(9/1)$ and the two corresponding Zn samples appear to have sharp transitions. In the next section we will see that a tetragonal distortion of the lattice, reported in ZnCr_2O_4 , but not CdCr_2O_4 , leads to a sharp phase transition.

Comparing the susceptibility from our Monte Carlo calculation with the one from experiments, Fig. 5-3, we can see the results agree qualitatively with each other except for paramagnetic tails in the data at low temperature which are especially pronounced in the powder samples. We will show in next section that if we change the periodic boundary condition used to simulate an infinite crystal to free boundary conditions appropriate to a finite sized grain, a paramagnetic tail will appear in the calculated susceptibility.

F. Monte Carlo Calculations in Distorted Spinel

1. Introduction

As mentioned in the last section, the Monte Carlo calculations on the fully frustrated spinel do not give a sharp transition, which is observed in some, but not all of the data (Fig. 3 and 4-10, for example). There are basically two ways to reduce the frustration and to have a sharp phase transition. One is to introduce second nearest neighbor interactions, the other is to allow the lattice to undergo a crystal transformation which reduces the symmetry. We do not consider the first alternative at this time because 1) there is little solid information on the nature of the second nearest neighbor interactions other than they are at least an order of magnitude smaller than the nearest neighbor interactions, and 2) neutron scattering evidence indicates that ZnCr_2O_4 and many other spinels undergo a lattice transformation below the magnetic transition temperature. The frustration in the system may be totally or partially removed, allowing ordinary magnetic long range order to be achieved. The simplest and possibly most important distortion is the tetragonal one which makes the lattice constant c in z -direction unequal to $a = b$ in x - y plane. We consider this kind of distortion since it is found in ZnCr_2O_4 (Giles et al., 1976). There are two different cases possible: $\Delta c < 0$, and $\Delta c > 0$; we find the ground state properties and carry out Monte Carlo calculations for both of these cases.

For convenience in the following discussions, let J_1 represent the coupling constant between nearest neighbors in each x - y plane and J_2 represent the one between nearest neighbors in different planes, as in Fig. 1-10. The Hamiltonian can be written as

$$H = \frac{1}{2} \sum_{\langle i,j \rangle} J_1 \mathbf{S}_i \cdot \mathbf{S}_j + \frac{1}{2} \sum_{\langle i,j \rangle} J_2 \mathbf{S}_i \cdot \mathbf{S}_j$$

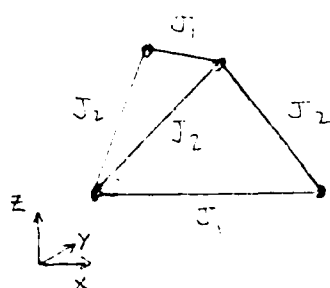


Fig. 6-35. Spinel tetrahedron: J_1 = x-y coupling; J_2 = z coupling.

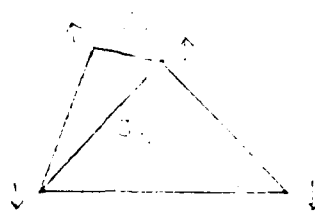


Fig. 6-36. $\Delta c < 0$ or $J_1 < J_2$ case.

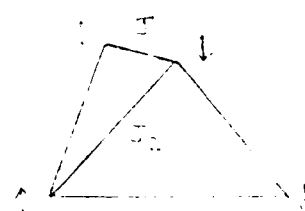


Fig. 6-37. $\Delta c > 0$ or $J_1 > J_2$ case.

where $\langle i, j \rangle$ are nearest neighbors in the same plane, $\langle i', j' \rangle$ are nearest neighbors in two adjacent planes.

2. The Ground States

In the $\Delta c < 0$ case, one expects that $J_1 < J_2$. It means that the coupling between nearest neighbors in different planes should be satisfied first with anti-parallel alignment, as shown in Fig. 6-36. Because of coupling between chains in a plane through chains in the next plane, parallel spins are required in the whole plane. So the ground state configuration is the following: spins are parallel in the same plane and anti-parallel in adjacent planes.

In this case, one can easily obtain the ground state energy without counting the bonds, which gives

$$U(T=0) = -Nz(J_2 - J_1) \quad (6-11)$$

where N is the number of spins. If all spins are fixed in the ground state

state, except for an overall flip of all spins, the ground state degeneracy equals to 2, which means the ground state entropy per spin is

$$s_0 = (k_B \ln 2)/N \approx 0 \quad (4-77)$$

The frustration has been removed from the system because the direction of each spin is uniquely determined if its neighbors are fixed.

In the $\Delta c > 0$ case, one has $J_1 > J_2$. This requires the coupling between the nearest neighbors in each plane to be satisfied first, which gives anti-parallel spin chains, as shown in Fig. 4-1. Two anti-parallel spins next to each other on one chain make a nearest neighbor spin on another chain (in the next plane) either up or down. That means the phase of a spin chain (which determines whether the first spin on the chain is up or down) is independent of the state of the other chains. Therefore, the ground state configuration is the following: anti-parallel ordered spin chains, parallel to each other in the same plane and perpendicular to each other in adjacent planes, with mutually independent phases.

The ground state energy can be estimated in a way similar to the first case. It is easy to see that bonds coupling different planes give zero net energy. All net energy comes from bonds inside planes. So we have

$$U(T=0) = -4N \cdot J_1 \quad (4-78)$$

The ground degeneracy comes from the possibility of having different combinations of phases of chains, or in other words, the possibility to choose the first spin on each chain, which equals the 1/4 of the degeneracy of the undistorted lattice. It is

$$g = 2^{N/4} \quad (4-79)$$

In this case, frustration still exists because in each triangular plaquette even with two spins fixed the third spin can be either up or down. The third spin can

still be either up or down. But only 1/3 of all spins can feel the frustration now. The ground state entropy per spin can be obtained as

$$s_0 = k_B \cdot (\ln D)/N \approx k_B \cdot (\ln 2)/(4N)^{1/3} \approx 0 \quad (14-75)$$

3. Monte Carlo Calculations

In our calculations, we set $J_1 = J$, $J_2 = 1.1J$ for the $\Delta c < 0$ case and $J_1 = J$, $J_2 = 0.9J$ for the $\Delta c > 0$ case. For the present investigation, we want to get a general indication of what happens in the tetragonally distorted lattice; in fact, the change in the J_2 is related to the magnitude of the tetragonal distortion. In future studies, various values for J_1 and J_2 could be investigated in order to find the best agreement with experimental results. The following calculations are all done on a $5 \times 5 \times 5 \times 16$ spin lattice, which was

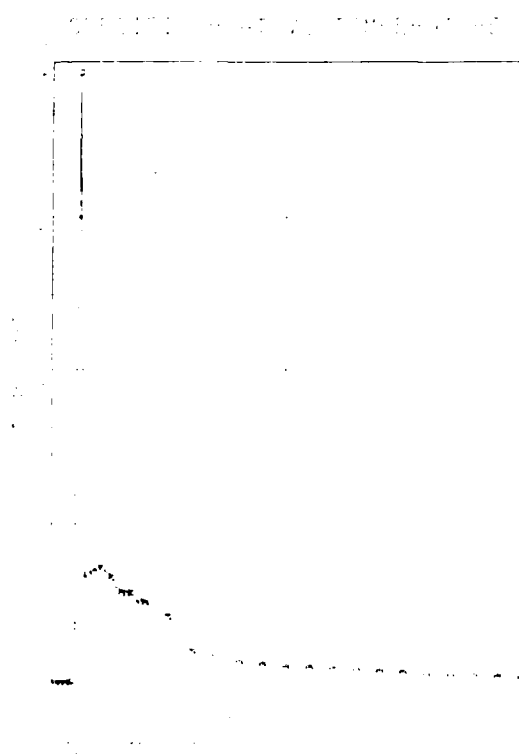


Fig. 14-76. Specific heat per spin, C , versus temperature T for the $5 \times 5 \times 5 \times 16$ spin lattice. $\Delta c = 0.05$, $J_1 = 1$, $J_2 = 1.1$.

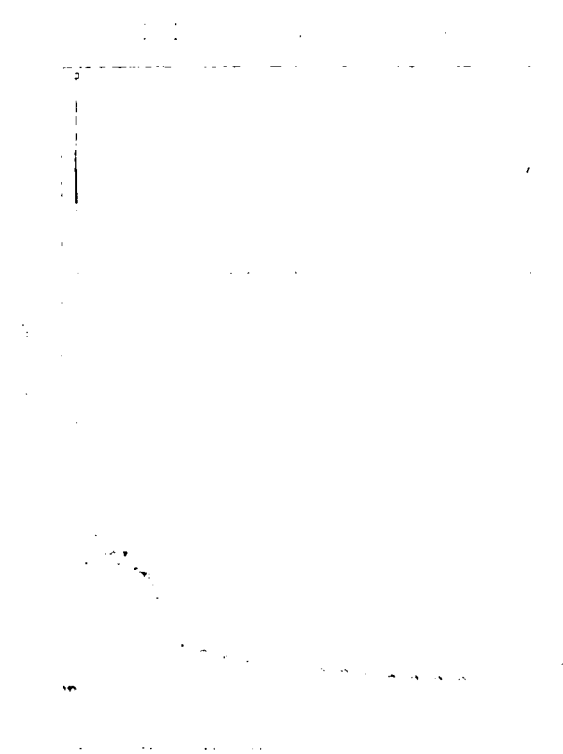


Fig. 14-77. Specific heat per spin, C , versus temperature T for the $5 \times 5 \times 5 \times 16$ spin lattice. $\Delta c = 0.05$, $J_1 = 1$, $J_2 = 0.9$.

2000 spins, with an iteration time of ~ 80 MC steps per spin.

The magnetization $M(T)$ is approximately zero for both the $\Delta_c = 0$ and $\Delta_c > 0$ cases, which is a consequence of antiferromagnetic ordering in the system. The specific heat $C(T)$ calculated from the fluctuations of M and E for two different cases, are plotted in Figs. 6-3 and Fig. 6-4. The case for the case $J_2/J_1 = 1.1$, and has a very sharp peak at $T_H = 0.1J$, with a maximum $C_{max} \approx 2$ per spin. The case for $J_2/J_1 = 0.9$ looks similar, Fig. 6-4, but has a smaller $T_H = 0.05J$ and a lower maximum $C_{max} \approx 1.5$ per spin. It should be noted that these peaks in C are indicative of genuine phase transitions and give much better agreement with the Zn samples specific heat reported in section IV, compared to the specific heat calculations for the undistorted, fully frustrated spinel lattice.

To investigate the nature of the transitions, we have calculated the

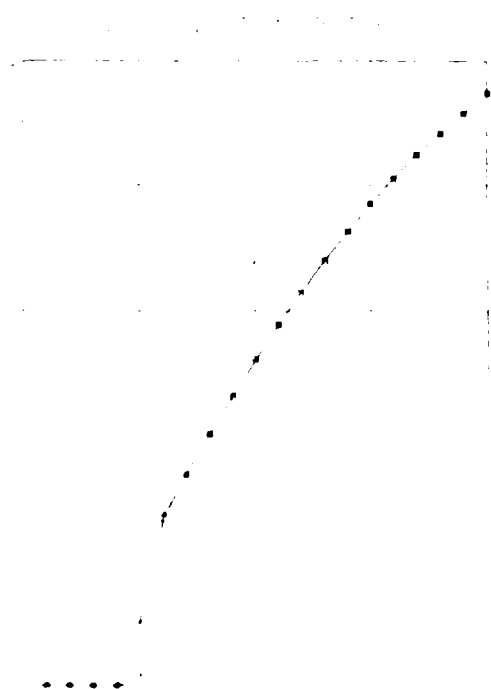


Fig. 6-3. Specific heat $C(T)$ versus temperature T/J for tetrahedral spinel lattice with $J_2/J_1 = 1.1$.

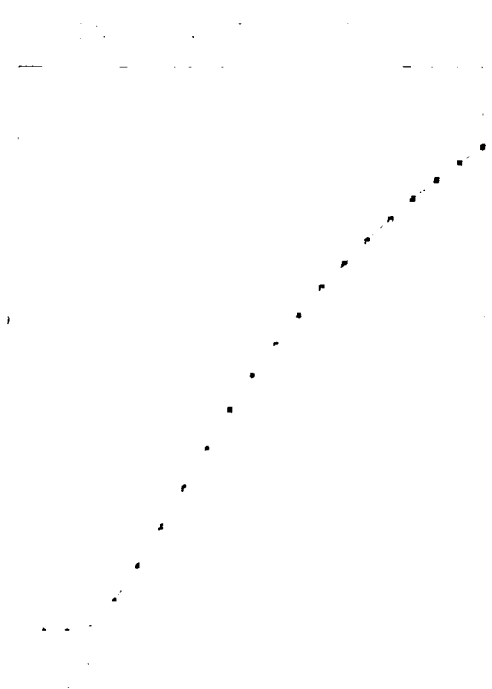


Fig. 6-4. Specific heat $C(T)$ versus temperature T/J for tetrahedral spinel lattice with $J_2/J_1 = 0.9$.

energy $U(T)$, for the two different cases, in both heating and cooling processes. They are shown in Fig. 6-60 and Fig. 6-61 respectively. Although the single spin flipping process we used may result in a long lifetime metastable state, it is still reasonable to think of the transitions as being first order or very sharp second order ones, especially in the first ($J_2/J_1 = 11$) case.

For the $\Delta\epsilon = 0$ case, since spins are anti-parallel ordered in alternating planes, we can define an antiferromagnetic order parameter L as follows: if we number all spin layers from 1 to N from top, then L is defined as the sum of spins in all layers with odd number minus sum of spins in all layers with even number, or

$$L = \sum_{i=1}^N (-1)^{i+1} S_i \quad (6-74)$$

The order parameter L is calculated for $J_2/J_1 = 11$ in Fig. 6-62.

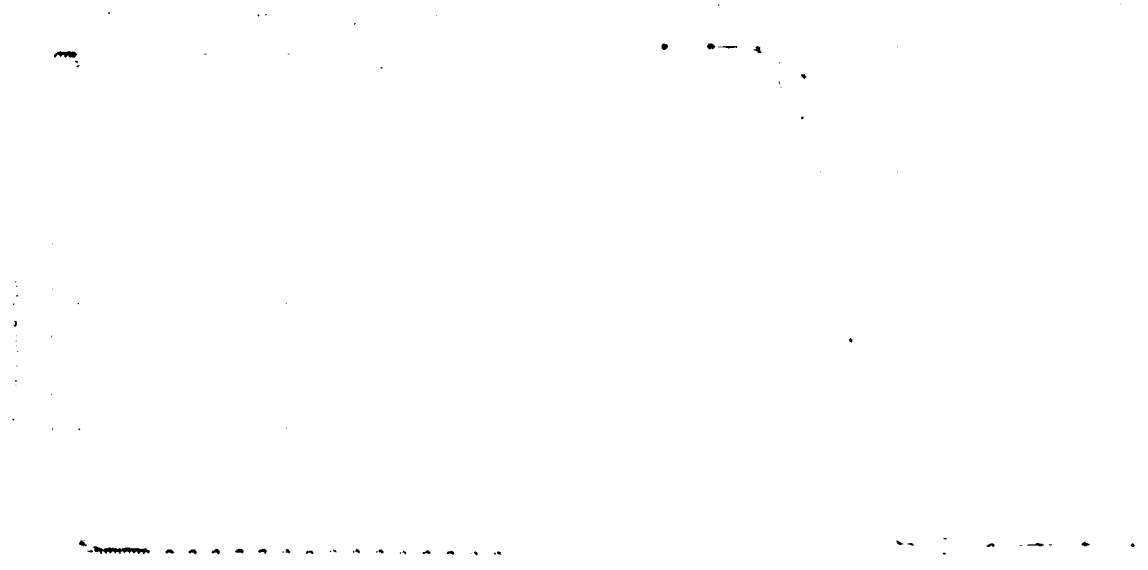


Fig. 6-62. Antiferromagnetic order parameter L versus temperature T for $J_2/J_1 = 11$.

Fig. 6-63. Antiferromagnetic order parameter L versus temperature T for $J_2/J_1 = 11$.

This case also yields a very sharp transition at the same transition temperature $T_N = 0.6J$. Near T_N , L for both cooling and heating processes are shown in Fig. 9-43. A small hysteresis is observed, in accordance with results for U , suggesting the transition is a first order or a very sharp second order one.

The susceptibility of the order parameter $\chi_L(T)$ is dL/dH at $H_S=0$, where H_S is the staggered magnetic field, is calculated from the fluctuations of L and shown in Fig. 9-44. It also gives a sharp peak at the same T_N . The curve for χ_L just above T_N is very well fitted by a power law, suggesting a second order transition. As shown in Fig. 9-45, the fit gives a critical exponent $\gamma = 1.07$, which is larger than but surprisingly close to the mean field result, $\gamma_{MF} = 1$.

Magnetic susceptibilities χ , as distinct from χ_L defined above, for the

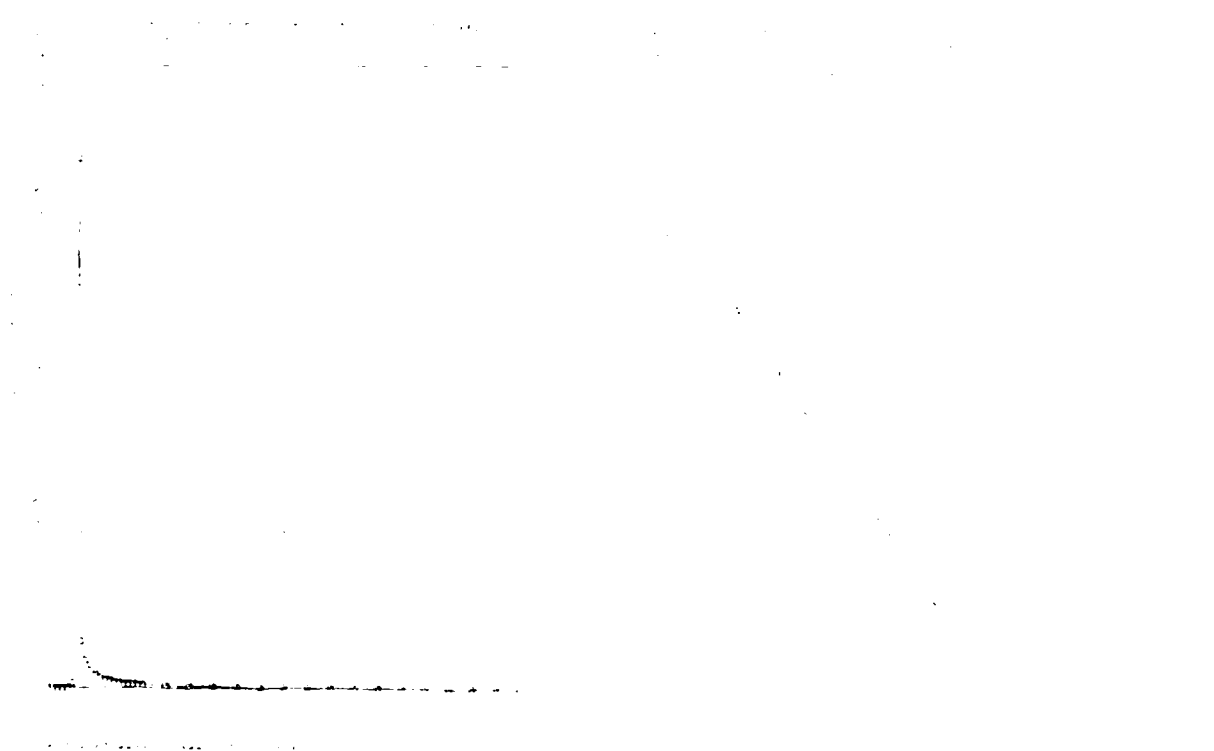


Fig. 9-44. Staggered susceptibility vs. temperature for the ferromagnetic spin-1 Ising model. The curve is calculated from the fluctuations of the order parameter L and is shown in Fig. 9-43. The curve is fitted by a power law $\chi_L \sim (T - T_N)^{-\gamma}$ for $T > T_N$, giving $\gamma = 1.07$.

$J_2/J_1 = 1.1$ and $J_2/J_1 = 0.9$, shown in Fig. 6-46 and Fig. 6-47, look almost the same as the susceptibilities in the undistorted case.

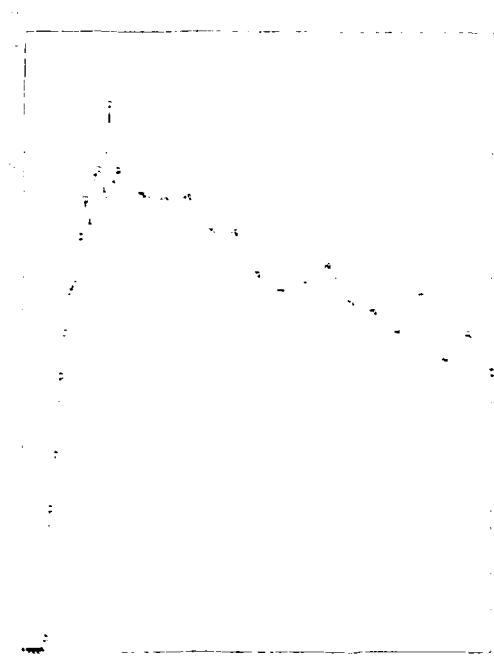


Fig. 6-46. Magnetic susceptibility vs temperature for $J_2/J_1=1.1$.

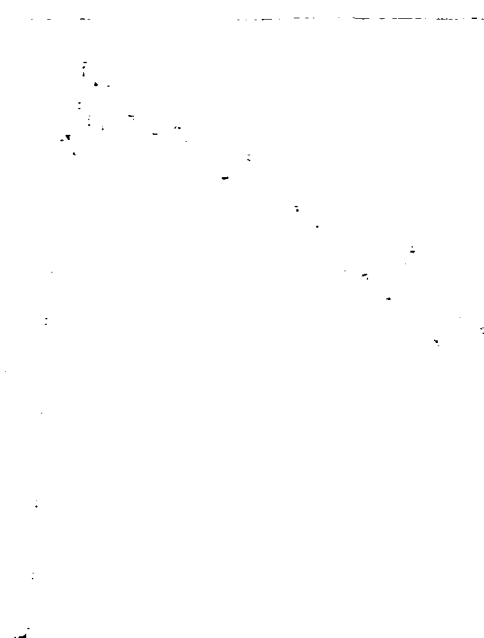


Fig. 6-47. Magnetic susceptibility vs temperature for $J_2/J_1=0.9$.

4. DISCUSSIONS

From above results, we can see that a small tetrahedral distortion in the perfect spinel lattice leads to a sharp phase transition in the system. The transition is so sharp that we can even get a small hysteresis in the energy and order parameter, which means the resultant specific heat must be very large at the transition temperature. This gives a good explanation of the unusually large specific heat observed in experiments (Section IV).

One thing should be noticed. The specific heat C_V is plotted in the $J_2/J_1 = 1.1$ and $J_2/J_1 = 0.9$ cases in Figs. 6-48 and 6-49 in the temperature range up to $4T_N$ above the transition temperature. It is not directly related to the underlying transition, but it is related to the presence of local magnetic moments. The specific heat C_V is plotted in the temperature range up to $4T_N$ above the transition temperature. It is not directly related to the underlying transition, but it is related to the presence of local magnetic moments.

situations where a large specific heat is needed over an extended range.

Comparing results on the undistorted system and the distorted system, we can see that properties involving the energy change dramatically, but properties involving the magnetization do not. If we look at the configurations for a single tetrahedron shown in Fig. 6-9b, we may see how this is possible. The two configurations shown are both ground states for the undistorted system. But for the distorted system, only one of them is still in the ground state. The other one is an excited state at a little bit higher energy (at $0.4J_1$). This is probably the cause of the transition at the critical temperature T_c . However, the two configurations make no contribution to the magnetization, just as in the undistorted system. Thus, the properties associated with the magnetization should not change too much in going from the undistorted system to the distorted one.

Although we have found good agreement with much of the experimental results, there is still one problem left. What is the origin of the low temperature paramagnetic tail in some of the experimental χ/T curves? It

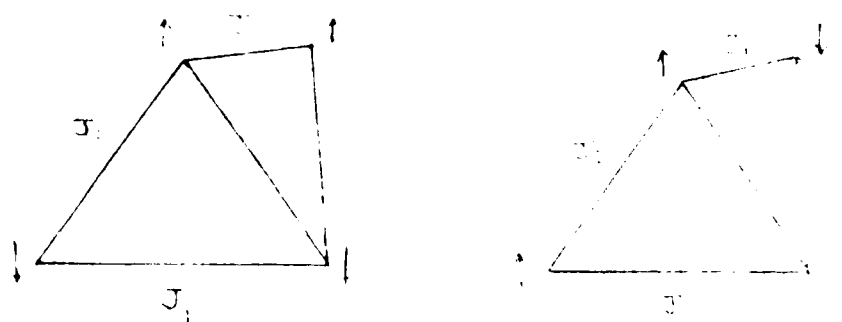


Fig. 6-9b. Two configurations of a single tetrahedron. The spins are \uparrow and \downarrow for up and down, respectively.

Fig. 6-49 we reproduce the data for the composite ZnCr₂O₄ sample from Fig. 5-1. We note that though our system may have some frustration in it, our ground state does not have any "free" spins which sit in a zero internal field. Since spins on surface are missing neighbors, the local field they see may vanish unlike in the bulk. Thus, we might expect, in a frustrated system, some free spins to exist on surface of a small grain.

The periodic boundary condition used in all our previous calculations simulates an infinite crystal with no surface spins. If we change the periodic boundary condition to a free boundary condition, which allows spins on surface to interact only with spins inside, we may simulate a finite sized grain. The resultant $\chi(T)$ is plotted in Fig. 6-50, which shows basically the superposition of the $\chi(T)$ we obtained previously plus a clear paramagnetic tail. Careful analysis shows that the number of free spins depends on how the

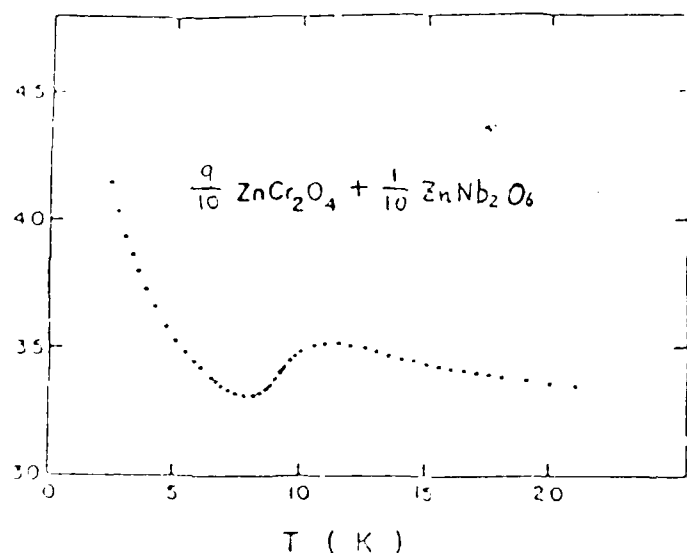


Fig. 6-49. Experimental magnetic susceptibility vs. temperature for ZNN(9/1).

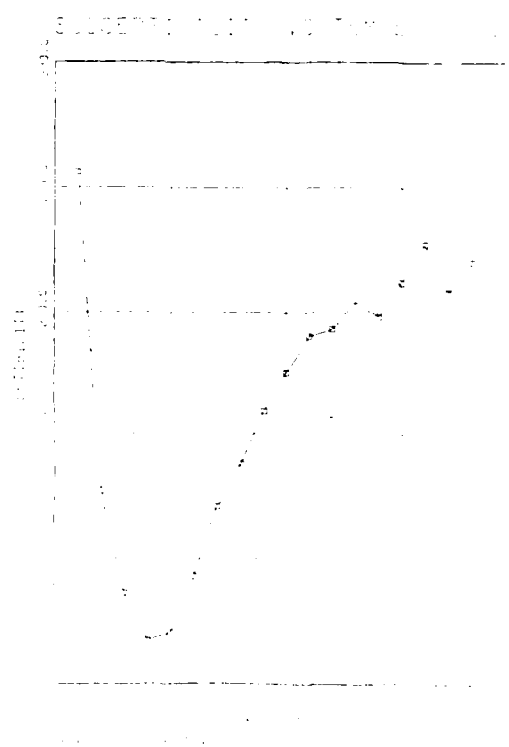


Fig. 6-50. Model calculation of $\chi(T)$ with free surfaces ($\beta = 1$).

crystal is cut: if we cut the lattice regularly along surfaces of the unit cells, each tetrahedron on the surface contributes $1/2$ "free" spin, while a more irregular cut can allow each tetrahedron on the surface to contribute 1 "free" spin. The magnitude of the Curie tail in our calculations corresponds exactly to the number of "free" spins we produce by the boundary conditions. Therefore, by using a free boundary condition instead of a periodic one, we get an additional paramagnetic tail in the magnetic susceptibility for all the cases previously calculated, in both distorted and undistorted lattices.

5. Conclusions

The study of the tetragonally transformed spinel lattice has lead to a number of further insights. A sharp thermodynamic transition occurs when the frustration is reduced in the ideal spinel lattice; the data show that samples of both distorted and undistorted nature can apparently be made. The magnetic properties are relatively insensitive to the lattice distortion, but rather depend sensitively on the surface condition of the spinel grains, compacting the grains into a denser composite material appears to reduce but not entirely eliminate the free spins left on the surface. A number of intriguing questions remain concerning the nature of the phase diagram as a function of the distortion or properties of the composite in which the grains are sintered.

VII. PROPOSED FUTURE WORK

Research the past year has concentrated on the spinels CdCr_2O_4 and ZnCr_2O_4 in the form of ceramics both with and without the respective sintering aids CdNb_2O_6 and ZnNb_2O_6 . The enormous specific heats of these spinels at ~ 10 K now appear due to frustration, but there are major discrepancies between the magnetothermal phase diagrams, the susceptibilities, and the NMR spectra. A central unanswered question is the order of the transitions in these spinels -- Monte Carlo computations predict first-order transitions for reasonable J-values, while calorimetric measurements indicate lower-order transitions. Clear evidence for free spins at the lowest temperatures has been found, but the origin of these spins remains questionable (unpaired spins are suggested). Finally, dielectric anomalies at T_N have been measured.

To date, various low temperature properties (specific heat, magnetic susceptibility, etc.) determined on ceramic samples of the cadmium and zinc chromite spinels have clearly shown a fabrication dependency. The magnetic ordering order with ceramic preparation could be due to grain size, grain size, secondary phases, or grain boundary effects, but it is yet to be determined. Thus, the following set of experiments is proposed.

- 1) To control both grain size and grain orientation, both HIP (hot isostatic pressing) and HVP (hot uniaxial pressing) will be employed to fabricate polycrystalline samples without the chromite phase.
- 2) Produce high purity, well crystalline reactive powders by the use of a) hydrothermal or b) co-precipitation chemical techniques. Of particular promise is the hydrothermal technique in which extremely fine particles (0.1 microns) that are crystalline can be produced without a calcination step and thus contamination is not required. The powders produced will also be employed in step (1).
- 3) Explore flux growth techniques to fabricate single crystals of the spinels. This process has been used to produce

tion with $\sigma = 10^{-10}$ and $\chi = 10^{-10}$. The long time scale will develop proper fluxes and growth parameters?

While the magnetic susceptibility (χ) measurements made during the current contract period have provided possible new clues to the molecular basis of the excitational specific heat exhibited by the chromite-spinel-congruents, new data are needed for a more definitive understanding. In particular, the current χ data, together with the specific heat, dielectric and magnetocaloric measurements and theoretical modeling of the spin state group show that perhaps one of the key properties for the chromites is the starting up of a new type of localized spin-cluster excitations, both well above and well below T_C . The theoretical results suggest that these excitations result from the frustrated spins on grain boundaries. To test this hypothesis, χ measurements need to be made on $ZnO_{0.5}Fe_{1.5}$ and $LiFe_{0.5}Fe_{1.5}$ samples with varying grain sizes.

The presently obtained χ -data also show that the sample magnetization depends sensitively on whether the sample is cooled with the magnetic field "on" or "off", and that T_C shifts to higher values with increasing magnitude of applied fields. This behavior suggests that the new excitations may have their origin in a "low-dimensional" magnetic spin ordering, a totally unexpected finding which may provide further data for a theoretical modeling and hence new guidelines from designing other high specific heat dielectrics with desirable temperature characteristics. Thus χ measurements on the new samples need to be made as a function of applied field.

Our currently obtained results on EPR lineshapes show extreme sensitivity to the sample preparation and magnetic field dependence. In particular there are features that can be specifically related to the "ordered spins", "Curie spins" and "clustered-spin excitations". Thus EPR measurements need to be made as a function of the grain size, sample temperature from 1.4 to 300 K, and at 10 GHz and 35 GHz frequencies. This work will provide direct verification of the susceptibility and magnetocaloric data and may yield guidelines for further theoretical

modeling and computer-aided design for new spinels.

The hierarchy of excitations in these spinels (cluster spins, free spins, and clustered spins) will continue to be explored via specific heat, magnetocaloric, and dielectric measurements on the carefully prepared samples above. Measurements in intense magnetic fields will be made at the Nat'l Magnet Lab. (MIT). A key set of measurements will be made to resolve latent heats, if any, in both zero and intense magnetic fields to resolve the order of the transitions (in both normal and densified samples).

Two new experimental approaches will be introduced: ac conductivity and thermal conductivity. The former measurement can be performed at very low frequencies (~ 0.5 Hz) to study long-time-constant effects (as suggested by the former magnetocaloric data). Thermal conductivity measurements, which depend on the availability of fully dense samples, are a sensitive probe of spin-phonon scattering rates.

Hopefully, single crystals will become available, and this would have a major impact on the research. Small crystals (~ 1 mm) could be used in all measurements except thermal conductivity. It may be too optimistic to expect large crystals, but such crystals would allow measurements of anisotropic properties.

We propose to extend and refine the Monte Carlo calculations of the spin ordering in the frustrated spinel lattice in order to give a complete picture of the unique behavior of these materials. In particular we propose to complete our calculations of the phase diagram for the distorted spinel structures so that the transition temperature can be accurately predicted for experimental systems, as well as to calculate the behavior of the specific heat and susceptibility in small and large magnetic fields.

This should enable us to relate matters such as the grain sizes and sintering conditions of the composite spinel material to the large specific heat anomalies. And in addition, we propose to calculate the thermal conductivity of the spinels, and to relate the behavior of the thermal conductivity to the other transitions occurring in the spinels.

The extent to which the... allow front-end, crystal-... single crystals become available to... following research... crystals. Conversely, the first... whether crystals are even possible.

A unique... institutions in the... capabilities in a... record of collaboration. However, the... across an... Penn State to Monte Carlo calculations at...

National Aeronautics and Space Administration
 Cost Budget for Project Apollo 11
 AFOSR Contract #17601-70-0-010

1. Direct Materials		
480 liters of liquid helium		
@ \$5.50/liter	\$2,640	
600 liters of liquid nitrogen		
@ \$0.40/liter	240	
	<u>\$2,880</u>	
2. Direct Labor		
Principal Scientist 640 hrs @ 20.04 =	\$12,826	
Senior Scientist 400 hrs @ 20.31 =	8,124	
Scientist 100 hrs @ 10.00 =	1,000	
Computer Programmer 100 hrs @ 1.00 =	100	
Technician 100 hrs @ 0.50 =	50	
	<u>\$21,100</u>	\$21,100
3. Labor Overhead		
15% of Direct Labor (#2)		\$3,165
4. Travel (2 trips to National Magnet Lab		
at MIT for P.I. and Senior Scientist)		\$300
5. General & Administrative Expense		
(20% of Items 1,2,3,4)		\$1371
	<u>TOTAL</u>	<u>\$25,936</u>

Note: Overhead and G&A rates are those currently accepted by DCAA, Columbus, Ohio

COST DETAIL

12 Month Period
Start June 1, 1967

<u>Direct Labor</u>	<u>Cost</u>
Prin. Inv. Prof. B.R. Patton 3 mos. 100% @ \$40,920/ac. yr.	\$12,270
Graduate Research Associates (2) 12 mos. 50% @ \$1,700/mo.	1,700

	\$14,040
<u>Retirement</u> @ 14% (Patton)	17,910
<u>Travel</u>	\$2,500
<u>Equipment</u>	
Sun Work Station	\$20,000
<u>Other Direct Costs</u>	
Materials & Supplies	\$1,000
Reports & Publications	\$1,500
Communications	3500

	\$3,000
 Total Direct Costs	 \$61,450
 <u>Indirect Cost:</u> 42% MTDC	 \$27,824
 Total Cost	 \$89,274

THE OHIO STATE UNIVERSITY
University Park, Ohio 43062

RESEARCH IN HIGH STRESS STATE MATERIALS

A Pricing Proposal for an 18-month period beginning on April 1, 1987
for Subcontract Support of CeramPhysics Incorporated

	First 5 Months	Next 10 Months	18-Month Totals
A. SALARIES AND WAGES			
1. Salaries, Category I:			
a. Principal Investigator, L. L. Coiro (nominal effort throughout)---			
b. Research Associate, T. R. Swartz (at 35% of a full-time effort)	\$ 3,413.	\$17,461.	\$20,874.
c. Secretarial Assistance (equivalent to 5% of a full-time effort for 12 months)	206.	1,081.	1,287.
Total Category I Salaries	\$ 3,619.	\$18,542.	\$22,161.
B. RECOVERY OF PRIOR BENEFITS (See Budget Notes)			
	\$ 1,037.	\$ 4,545.	\$ 5,582.
C. EXPENDABLE EQUIPMENT AND SUPPLIES chemicals, platinum crucibles, liquid nitrogen, compressed gases			
	\$ 500.	\$ 1,200.	\$ 1,700.
D. EQUIPMENT USAGE Use of various analytical instruments in the Materials Research Laboratory			
	\$ 200.	\$ 319.	\$ 519.
E. TRAVEL (See Budget Notes)			
a. Two trips by the Research Associate to CeramPhysics facilities at Westerville, OH	\$ 320.	\$ 320.	\$ 640.
b. Five trips by the consultant from Columbus, OH to State College, PA	\$ 385.	\$ 1,540.	\$ 1,925.
F. CONSULTANT Dr. S. L. Swartz at \$271. per day for an estimated 10 days			
	\$ 542.	\$ 2,163.	\$ 2,710.
G. COMMUNICATIONS Telephone tolls, postage, mailing and other costs for reports preparation			
	\$ 50.	\$ 250.	\$ 300.
Direct Costs (A. through G.)	\$ 6,713.	\$28,884.	\$35,597.
H. PERMANENT EQUIPMENT			
	nil	nil	nil
I. TOTAL DIRECT COSTS			
	\$ 6,713.	\$28,884.	\$35,597.
J. RECOVERY OF INDIRECT COSTS (See Budget Notes)			
	\$ 2,731.	\$ 9,122.	\$11,853.
ESTIMATED TOTAL PROJECT COSTS TO CLIENT	\$ 9,444.	\$38,006.	\$47,450.

THE PENNSYLVANIA STATE UNIVERSITY
University Park, PA 16802

RESEARCH ON HIGH SPEED CERAM PHYSICS

A Pricing Proposal for an Indirect Cost Period to be incurred

BUDGET

RECOVERY OF FRINGE BENEFITS:

Computed using the fixed rates of 30.30% applicable to Category I salaries and 7.9% applicable to Category II salaries and wages for any period between July 1, 1986, and June 30, 1987, and the fixed rates of 24.51% applicable to Category I salaries and 8.01% applicable to Category II salaries and wages for any period between July 1, 1987, and June 30, 1988.

30.30% applicable to \$ 3,619. = \$ 1,097.
24.51% applicable to \$18,542. = \$ 4,515.
Total Fringe Benefits Recovery \$ 5,612.

TRAVEL:

a. By the Research Associate:

	<u>1st Day</u>	<u>2nd Day</u>	<u>3rd Day</u>	<u>Totals</u>
University vehicle at \$.26/mile for an estimated 741 miles, RT				\$173.
Lodging (with tax)	\$45.	\$45.	—	\$ 90.
Meals (University maximum)	\$20.	\$25.	\$12.	\$ 57.
	(LD)	(BLD)	(2L)	
Estimated for each trip to CeramPhysics				\$320.

b. By the Consultant:

	<u>1st Day</u>	<u>2nd Day</u>	<u>3rd Day</u>	<u>4th Day</u>	<u>Totals</u>
Private vehicle at \$.20/mile for an estimated 700 miles, RT					\$140.
Lodging (with tax)	\$50.	\$50.	\$50.	—	150.
Meals (University maximum)	\$20.	\$25.	\$25.	\$25.	\$55.
Estimated for each trip to State College					\$385.

RECOVERY OF INDIRECT COSTS:

Computed using the fixed rates for on-campus research of 41.42% for any period between July 1, 1986, and June 30, 1987, and 31.58% for any period between July 1, 1987, and June 30, 1988. These rates are applicable to modified total direct costs (total direct costs excluding tuition, amount of subcontracts in excess of \$25,000., equipment, plant construction, and building amortization) and has been approved by the cognizant Department of Defense agency responsible for the establishment of indirect cost rates at this University.

41.42% applicable to \$ 5,713. = \$ 2,781.
31.58% applicable to \$13,884. = \$ 4,382.
Total Indirect Costs Recovery \$ 7,163.

Department of Chemistry
West Virginia University

Subject
(12 months)

	Actual Spent	Estimated
Personal Services (Salary for 12 months for one P.I. available)	15,000	15,000
Personal Services (Full time for 12 months for one hired)	15,000	15,000
Total Personnel Services	30,000	30,000
fringe Benefits (all personnel services)	4,500	4,500
Travel (WV-Perm States-Perm State)	750	750
Mat - Gas chromatography sample tubing, cryogenic supplies, liquid nitrogen, liquid helium, instrumentation maintenance and repair	5,625	5,625
Total Direct Cost	52,506	56,875
Indirect Cost (45% of TDC)	<u>23,627</u>	<u>25,582</u>
TOTAL	876,133	894,457

Signature of Nar S. Dalal (Principal Investigator):

[Handwritten Signature]

- Anderson, P.W., *Phys. Rev.* 100, 1757 (1955).
- Baltzer, P.K., *Phys. Rev. B* 15, 1071 (1977).
- Binder, K., *Monte Carlo Simulation of Statistical Physics*, Springer-Verlag, 1984, p. 1.
- Binder, K., *Monte Carlo Simulation of Statistical Physics*, Springer-Verlag, 1984, p. 1.
- Binder, K., *Applications of the Monte Carlo Method in Statistical Physics*, Springer-Verlag, 1984, p. 1.
- Bozels, P.W., Lawless, W.N., Parker, G.H., Patten, B.P., Clark, C.F., and Arenas, R.W., "High Temperature Heat Capacities and Electrical Resistance at Dielectric Boundaries", Final Report of AFOSR Contract No. F49620-83-C-0120 (1985).
- Fisher, M.F., *Philos. Mag.* 7, 1731 (1962).
- Fosdick, L.D., *Math. Comp. Phys.* 1, 245 (1963).
- Friedberg, S.A. and Burk, D.L., *Proceedings of the Conference on Magnetism*, Pittsburgh, June 1955, p. 62 (1955).
- Landau, D.P., *Phys. Rev. B* 14, 255 (1976).
- Lawless, W.N., *Rev. Sci. Instrum.* 42, 561 (1971).
- Lawless, W.N., *Rev. Sci. Instrum.* 53, 1647 (1982).
- Lines, M.E., and Glass, A.M., *Principles and Applications of Ferroelectrics and Related Materials*, Oxford Univ. Press, p. 62 (1977).
- Lotgering, F.K., *J. Phys. Chem. Solids* 27, 139 (1966).
- Mouritsen, O.G., *Computer Studies of Phase Transitions and Critical Phenomena*, Springer-Verlag, 1984, p. 23, 52 (1984).
- Niesel, U., *Ann. Physik* 10, 336 (1953).
- Oles, A., *Phys. Stat. Sol. (a)* 3, 509 (1970).
- Oles, A., Kaizer, T., Kuech, E., and Sikora, W., *Magnetic Structures Determined by Neutron Diffraction*, Wydawnictwo Naukowe, Warszawa (1976).

Chen, H. H., and H. H. Chen, 1974, *Journal of
Geology*, 82: 1-10.
Chen, H. H., and H. H. Chen, 1974, *Journal of
Geology*, 82: 1-10.

Chen, H. H., and H. H. Chen, 1974, *Journal of
Geology*, 82: 1-10.

Chen, H. H., and H. H. Chen, 1974, *Journal of
Geology*, 82: 1-10.

Chen, H. H., and H. H. Chen, 1974, *Journal of
Geology*, 82: 1-10.

END

FEB.

1988

DTic